HAL open science

Functional metasurfaces controlled by Liquid crystals

Racha Chamseddine

To cite this version:

Racha Chamseddine. Functional metasurfaces controlled by Liquid crystals. Micro and nanotechnologies/Microelectronics. Université de Lille, 2021. English. NNT : 2021LILUN030 . tel-03766339

HAL Id: tel-03766339

https://theses.hal.science/tel-03766339

Submitted on 1 Sep 2022

HAL is a multi-disciplinary open access archive for the deposit and dissemination of scientific research documents, whether they are published or not. The documents may come from teaching and research institutions in France or abroad, or from public or private research centers.

L'archive ouverte pluridisciplinaire **HAL**, est destinée au dépôt et à la diffusion de documents scientifiques de niveau recherche, publiés ou non, émanant des établissements d'enseignement et de recherche français ou étrangers, des laboratoires publics ou privés.

Université de Lille

UNIVERSITÉ DU LITTORAL CÔTE D'OPALE

Doctorate Thesis

Ph.D. in Electronics, Microelectronics, Nanoelectronics and Microwaves

In the Ecole Doctoral SPI-ENGSYS

Functional metasurfaces controlled by Liquid crystals

by

Racha Chamseddine

To obtain the title of Doctor of University of Lille

Presented and defended on 16th December 2021

Examination Committee:

Pr. Gabriel VELU, SEE, Université d'Artois	**Chairman**
Pr. Laurent DUPONT, Institut des Mines-Telecom	**Reviewer**
Pr. Gérard TANNE, STICC, Université de Bretagne Occidentale	**Reviewer**
Pr. Claire MEYER, PSC, Université de Picardie-Jules Verne	**Examinator**
Dr. Patrick ROPA, UDSMM, Université du Littoral-Côte d'Opale	**Invited Member**
Pr. Didier LIPPENS, IEMN, Université de Lille	**Thesis Supervisor**
Pr. Christian LEGRAND, UDSMM, Université du Littoral-Côte d'Opale	**Thesis Co-Supervisor**

Université de Lille

UNIVERSITÉ DU LITTORAL CÔTE D'OPALE

Thèse de Doctorat

Doctorat en Electronique, Microélectronique, Nanoélectronique et Microondes

À l'École Doctorale SPI-ENGSYS

Métasurfaces fonctionelles contrôlées par cristaux liquides

par

Racha Chamseddine

Pour obtenir le titre de Docteur de l'Université de Lille

Présentée et soutenue le 16 Décembre 2021

Jury d'examen :

Pr. Gabriel VELU, SEE, Université d'Artois	**Président de Jury**
Pr. Laurent DUPONT, Institut des Mines-Telecom	**Rapporteur**
Pr. Gérard TANNE, STICC, Université de Bretagne Occidentale	**Rapporteur**
Pr. Claire MEYER, PSC, Université de Picardie-Jules Verne	**Examinateur**
Dr. Patrick ROPA, UDSMM, Université du Littoral-Côte d'Opale	**Membre Invité**
Pr. Didier LIPPENS, IEMN, Université de Lille	**Directeur de Thèse**
Pr. Christian LEGRAND, UDSMM, Université du Littoral-Côte d'Opale	**Co-directeur de Thèse**

To my parents and my husband... ❤️

Acknowledgments

First and foremost, as an overture to this thesis, I wish to express my most sincere gratitude and thankfulness to the almighty God for giving me the strength, patience and perseverance to work through all these years so that today I can stand proudly with my head held high.

This collaborative research program started around 4 years ago between the 'Université de Lille' that granted me a PhD fellowship and the 'Université du Littoral Côte d'Opale (ULCO).

I would like to express my sincere thanks to ***Prof. Didier LIPPENS***, my supervisor from Lille University and ***Prof. Christian LEGRAND,*** my supervisor from ULCO, for supporting me thoughout my thesis. Their patience, motivation and immense knowledge, whilst allowing me the room to explore on my own, have given me the power and spirit to recover when my steps faded and the road got tough. Moreover, their guidance, exchanges and help have inspired me to excel in all the time of research and writing of this thesis.

Special thanks to ***Prof. Gabriel VELU*** for the honor he gave me to chair the defense, to ***Prof. Gérard TANNÉ*** and ***Prof. Laurent DUPONT*** for accepting to review this PhD work and to ***Prof. Claire MEYER*** and ***Dr. Patrick ROPA*** who have also kindly accepted to be part of my PhD committee. Thanks for their insightful comments and encouragement, and questions which incented me to widen my research from various perspectives.

Many thanks to ***Nicolas TENTILLIER, Redouane DOUALI, Patrick ROPA, Freddy KRASINSKI and Dharmendra SINGH*** of the UDSMM (Unité de Dynamique et Structure des Materiaux Moléculaires) Lab at ULCO for their help in the microwave characterization techniques of the LC dielectric properties, electromagnetic full wave analysis and free space scattering parameters measurements. The manufacturing of the metasurfaces was carried out at IEMN (Institute of Electronics, Microelectronics and Nanotechnology) of the FST (Faculté des Sciences et Technologies) of the Lille University as part of a RENATECH (REseau NATional des grandes centrales de TECHnology) project. Thanks to ***Karine BLARY*** and all the staff of the IEMN Micro and Nanotechnology facility for this fabrication. Special thanks to ***Nicolas FERNEZ*** and ***Véronique SADAUNE*** at IEMN for the first numerical studies devoted to the modeling of the electromagnetic behavior of LC controlled metasurfaces. And thanks to ***Prof. Przemyslaw KULA*** from the Military University of Technology in Warsaw, Poland, for providing us with the synthesized large birefringence LC 1825 for our project.

Many thanks to everyone at the UDSMM lab where the entire experimental work was performed and in particular, I thank all my fellow colleagues for all the beautiful time we have had in the last three years, ***Asmita, Hassan, Parthiban, Samah, Sarah and Sokaina.*** Thank you for making the environment familiar and warm and thanks a lot for your help, advices and scientific interactions.

My deepest gratitude to my whole family without whom nothing would've been possible. I would like to acknowledge the people who are everything to me, my parents, ***Ahmad and Nada,*** for showing faith in me and guiding me with their sincere advices throughout my entire journey. I appreciate your selfless love, care, patience and sacrifice you have and still offering to help me reach where I am now. I will forever be indebted to them and I am very lucky to have such amazing teachers in my life. A heartfelt thank you to my siblings, ***Fatima, Mohammad Ali, Souad and Zeinab,*** for their love, care, and all the smiles they drew on my face despite the distance.

And finally, I would like to express my gratitude for my husband, ***Ali,*** for pushing me to grow, for taking care of me in my time of need and for holding me when I fell apart. You are my inspiration, my strength, and my happiness. Thank you for everything.

Table of Contents

Acknowledgments 4

Table of Contents 6

General Introduction 8

Chapter 1: Scientific Context and State of Art 11

Introduction 12

1.1 Liquid crystals 13

1.1.1 Generalities on liquid crystals 13

1.1.2 Permittivity, losses and dielectric relaxation 17

1.1.3 Dielectric properties of liquid crystals 21

1.1.4 Electrical driving of liquid crystals 24

1.2 Background on Metasurfaces 26

1.2.1 Background on artificial structures (EBG-PBG, metamaterial, FSS and metasurfaces) . 26

1.2.2 Perfect absorbing layer screens 32

1.2.3 Some key papers on LC tunable metamaterials 34

Conclusion 45

Chapter 2: Operating Principle and Dielectric Properties 46

Introduction 47

2.1 Background on a PMA MTS 48

2.1.1 Micro-resonator array structure 48

2.1.2 Scattering analysis for a plane wave under normal incidence 49

2.1.3 Resonance condition 50

2.1.4 Complex reflection coefficient 51

2.2 Principle of Operation 54

2.3 Studied LC 56

2.4 “Low frequency” dielectric characterization 58

2.4.1 Experimental Setup 20 Hz – 1 GHz 58

2.4.2 Dielectric properties of studied LCs 60

2.5 Electrical driving 64

2.5.1 Experimental Setup 64

2.5.2 Experimental results 66

2.6 Microwave dielectric measurements 72

2.6.1 Experimental setup and measurements procedure 72

2.6.2 Method for Extracting Values 75

2.6.3 Microwave complex permittivity and anisotropy of studied LC 77

Conclusion 82

Chapter 3: Design of LC Tunable Metasurface 83

Introduction 84

3.1 COMSOL Design 85

3.1.1 Design rules and simulation model 85

3.1.2 Design of 50 µm thickness prototype (Prototype 1) 89

3.1.3 Design of 10 µm thickness prototype (Prototype 2) 98

3.1.4 Simulation of prototypes 1 and 2 with 1825 LC 102

3.2 TLM modeling 102

3.2.1 TLM Modeling of the metasurface without glass slide 103

Conclusion 121

Chapter 4: Realization and Characterization of LC Tunable Metasurfaces 123

Introduction 124

4.1 Fabrication and assembling 125

4.1.1 Manufacturing Techniques 125

4.1.2 Assembling Techniques 128

4.2 Characterization Techniques of the Complex Reflectivity in Free Space 132

4.2.1 Experimental set-up for free space measurements 132

4.3 Reflectivity spectra measurements for the different prototypes 140

4.3.1 5CB LC Based Tunable Metasurfaces 141

4.3.2 1825 LC Based Tunable Metasurfaces 145

4.3.3 Synthesis of the Results and Comparison with Literature 148

Conclusion 152

General Conclusion 153

Bibliography 155

Work Development 161

Abstract 162

Résumé 162

General Introduction

Metamaterial technologies and more, particularly the so-called metasurfaces, are now an interest of several research activities in electromagnetics for which the concept was introduced to acoustics or the engineering of seismic waves. In this PhD thesis, an in-depth study of the scattering of an Electro-Magnetic (EM) plane with a metasurface infiltrated by Liquid Crystals (LCs) is presented showing the possibility to dynamically control the reflection, transmission and absorption coefficients. Special attention will be paid to metasurfaces operating in the Ka (26-40 GHz) frequency band in a reflect array mode aiming to study the design and the experimental assessment of an amplitude modulator that exhibits a high contrast ratio between a high reflectivity state and quasi-total absorption. Toward this goal, it will be seen that, with respect to the previous works reported in the literature on similar topics, one of the originalities of the present work will be a dramatic reduction of the LC layer with thickness down to 10 µm and hence with typical values like one order of magnitude lower than the nominal value generally chosen in this frequency band. The other innovative feature will concern the use of high birefringent LC compounds ($\Delta n \sim 0.4$) recently synthesized that exhibit high permittivity anisotropy ($\Delta\varepsilon > 1$) along with low losses ($\tan\delta \sim 10^{-3}$) at microwave. In the frame work of this project, successful experimental demonstration of the ability to dynamically tune the reflectivity of metasurfaces with a high contrast will thus be demonstrated by characterizing the reflectance spectra of the metasurfaces in free space. For high anisotropy LC, a frequency agility of more than 5 GHz will be shown so that the reflection level of an incident wave can be modulated by more than 20 dB.

The presentation will be organized in 4 chapters:

In the first chapter, we recall first the essential characteristics of the LC technologies by focusing on the nematic compounds that will be used in practice for controlling the metasurfaces. After a presentation of their chemical and dielectric properties along with the means to control the orientation of the LC optical axis ($\vec{n}$) via the use of a magnetic induction ($\vec{B}$) or a voltage controlled electric field ($\vec{E}$), we briefly describe the Debye relaxation effects of the longitudinal and transversal permittivity tensor elements. In particular, it will be pointed out that the difference in Debye relaxation frequencies yields to a negative anisotropy ($\varepsilon_{\perp} > \varepsilon_{\parallel}$) at RF frequency bands ($\sim 1\ \mathrm{GHz}$) starting from large positive value ($\Delta\varepsilon > 0$) at extremely low frequency (ELF ~ 1 kHz) while in the microwave frequency band of interest (Ka band), the dielectric anisotropy again becomes strictly positive. In a second part, a background study is made to understand how the scattering properties of a metasurface can be controlled on the basis of the analysis of the key results published in the literature. The metasurface

subject is a broad scope topic and as a consequence we will focus our analysis of the literature mainly on the works published so far on the so-called Perfect Metamaterial Absorbers by considering the degrees of freedom to tailor and to dynamically change their scattering properties.

The second chapter is devoted first to the theoretical analysis of the complex valued reflection coefficients for a grounded dielectric substrate. This structure, that consists of a LC dielectric slab with a uniform metallic foil on the backside, cancelling any transmitted wave, is considered as the generic absorbing screen. In particular, it will be seen how implementing a micro-resonator array on top of this basic structure cancels any reflection at the resonant frequency. As a consequence, the energy of the impinging wave is totally absorbed under the condition of critical coupling. On this basis, it will be explained how the control of the orientation of the nematic LC molecules varies the effective permittivity 'probed' by the microwave EM field yielding a shift in the resonance frequency and subsequently a variation of the absorbance (reflectance) level. In a second part of this chapter, we report on the dielectric properties of the two LC compounds that were used in the present work namely the generic LC 5CB compound with a dielectric anisotropy $\Delta\varepsilon = 0.3$ and the LC 1825 that exhibits a dielectric anisotropy $\Delta\varepsilon = 1.4$ in the Ka band. In particular, we detailed an original retrieval technique based on the transfer matrix method developed at NIST (National Institute of Standards and Technology) for the determination of the complex-valued permittivity tensor deduced from the scattering parameters measurements. Prior to these measurements at microwave frequencies, we also characterize the dielectric properties of these compounds at extremely low frequency for assessing the control of the orientation of the LC molecules by an alignment rubbed surfactant or by voltage control in a quasi-static regime.

In a third chapter, we report on the design rules for achieving unit absorption at the resonance frequency of patch-like resonator periodic arrays first of all by full wave numerical analysis and then by an analytical approach based on the Transmission Line Method (TLM). In a first stage, we study the resonance frequencies by showing that they can be estimated (i) from the patch size and (ii) from the permittivity values corresponding to the polarization direction of the EM surface wave that is bouncing back and forth within the LC layers. Then, it will be shown how to satisfy the critical coupling condition that is necessary for impedance matching of the metasurface to free space for zero-reflection and hence total absorption. Full wave analysis and TLM approach will be complementary in particular for the calculation of the radiative quality factor that has to be equal to the dissipation one for perfect absorption. The results of the parametric studies performed as a function of the metal patch lateral dimension, LC thickness and pitch of the periodic array will be presented. We also addressed the corrections that have to be brought for a real device that imply to take into account a superstrate glass

slab on which the metal patches are printed, and the narrow interconnect strips for biasing all the elements of the array and the fringing field effects.

The last chapter concerns the free-space characterization of the reflectance spectra of the metasurfaces in the Ka-band. The microelectronics technologies that were employed at IEMN for the fabrication of two prototypes with LC layer thickness of 50 µm and 10 µm respectively, such as the fabrication of an optical mask patterned by E-beam lithography and the gold deposition of thin films by electron-gun evaporation is briefly discussed with emphasis about the technological choices that were decided notably with respect to the metal film thickness. Then, the free space measurement setup is commented on by justifying a bi-static configuration and by discussing the experimental far field conditions. Calibration techniques and the means to normalize the reflectance spectra complete this part devoted to the characterization methods. The results of the frequency dependence of the modulus of the reflectivity for the two LC compounds (5CB and 1825) and for the two prototypes (10 µm and 50 µm) whose scattering parameters were measured between 26 and 40 GHz are presented in the last part of this chapter. With a measured frequency shift of more than 5 GHz, the experimental results corroborate the dramatic improvement of the frequency agility afforded by high anisotropic Liquid Crystals.

Chapter 1: Scientific Context and State of Art

Introduction

In this chapter, we give a general overview of the scientific context on liquid crystal compounds (part 1) and of metamaterial technologies (part 2). For the first part, special attention will be paid to nematics and more particularly to their dielectric properties in the quasi static and microwave frequency regimes. The essential concepts that enable the orientation of the LC molecule optical axis either by surface treatment or magnetic/electric field driving will also be depicted. For the second part, after explaining the basic concepts for tailoring the scattering parameters of artificial material (Electromagnetic and Photonic Band Gap materials along with bulk - and 2D metamaterials), some of the literature key papers on metamaterials and metasurfaces are analyzed.

1.1 Liquid crystals

1.1.1 Generalities on liquid crystals

Liquid crystal properties are shown in compounds called 'mesogens' [1]. The liquid crystalline state is called "mesophase" and occurs between the crystalline solid state and isotropic liquid state. The specificity of the liquid crystalline state is that the molecules flow like liquids in addition to having physical properties that allow them to orientate in a crystal-like way. The mesogens can be found in the form of rods (calamitic LC) or disc-like (discotic LC) shapes and are of several types; thermotropic, lyotropic and polymeric. In these different types, phase transitions are respectively observed as a function of temperature, concentration (in a solvent), or the chemical composition ratio.

The widely used type is thermotropic, where varying temperature changes the mesophase of the rod-shaped liquid crystals to be, nematic, smectic, or cholesteric (Figure 1.1.1). They are characterized by several parameters, for example, short- or long-range orders, and orientational or positional distribution [1-4].

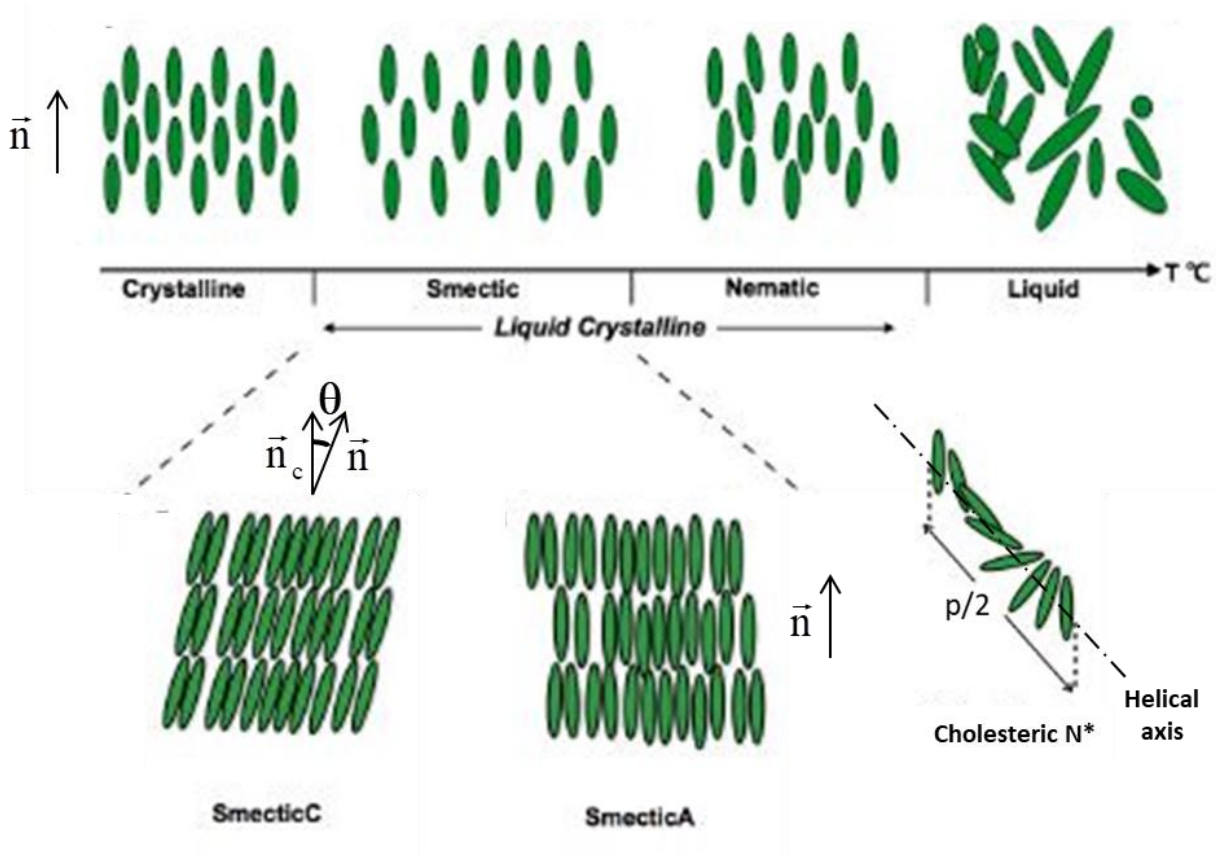

Figure 1.1.1 A schematic for the different mesophases of thermotropic rod-shaped LCs (θ and p represent the tilt angle of the SC phase and the pitch of the N* phase) [5]

Thermotropic mesophases occur because of anisotropic dispersion forces between the molecules and the interaction between them [6], and the nematic phase is the most common studied and used LC phase. As observed in Figure 1.1.1, Nematic LCs are uniaxial and have no positional order. Their molecules are free to flow and their center of mass positions are randomly distributed as in a liquid but they self-align to maintain long-range directional order [1][7]. The average direction is represented by a unit vector director (optical axis) $\vec{n}$ parallel to the molecular alignment where $\vec{n}$ and -$\vec{n}$ are the same. In the nematic phase, molecules are in the potential represented on Figure 1.1.2 where θ is the angle between the molecular axis and the director and $\theta = 0$ and $\theta = \pi$ orientations are favored.

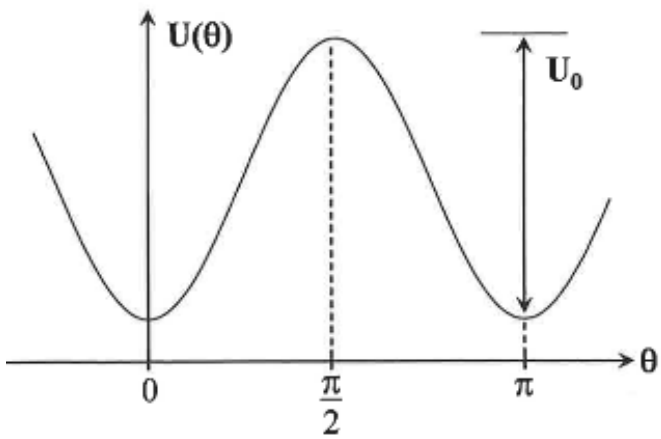

Figure 1.1.2 Nematic potential

The long range orientational order is characterized by the order parameter S:

$$S = \frac{1}{2}(3 < cos^2\theta > -1)$$

where the symbol < > represents the average on all the molecules. For a perfectly ordered nematic ($< cos^2\theta > = 1$), S=1 and for total disorder ($< cos^2\theta > = \frac{1}{3}$), S=0 (isotropic phase). A statistical model of the variation of S versus temperature T (Figure 1.1.3) has been established taking into account molecular interaction of neighboring molecules [8]. The model predicts a jump of the order parameter S from S=0 to S=0.44 at the nematic-isotropic phase transition and then the ordering increases progressively when the temperature decreases. The classical phase sequence versus decreasing temperature is Isotropic – Nematic – Smectic – Crystalline corresponding to an increase of molecular order.

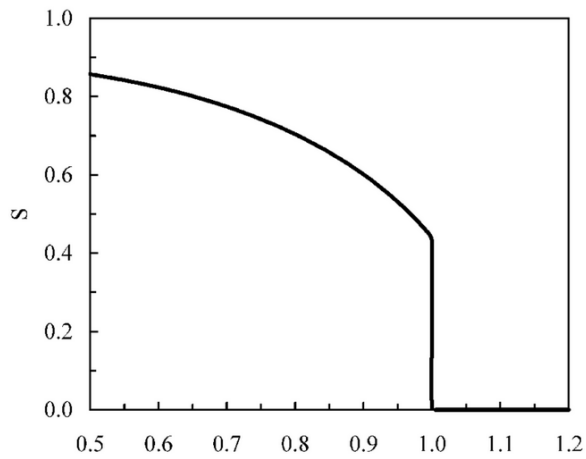

Figure 1.1.3 S(T) Maier-Saupe Curve (TNI represents the nematic-isotropic transition temperature)

The most important characteristic of LC is their anisotropy (properties depending on orientation). This property results of their ordered structure and it concerns the physical parameters: optical (birefringence), dielectric … This specific property and their fluidity allow electrical driving of nematic LC orientation. LC applications are taking advantage of this property.

In order to use these nematic liquid crystals in applications, they should be considered stable. The typical structure of rod-like liquid crystals is shown in Figure 1.1.4. It consists in a central rigid part and at least one flexible lateral chain. The other lateral chain can be flexible or a rigid group. It can also present a dipolar moment. The most stable compounds synthesized are the ones without a central linkage group, such as alkyl- cyanobiphenyl compounds (nCB, Figure 1.1.4), whereas *p*-methoxy benzylidene-*p*-*n*-butylaniline (MBBA) ends to degrade in a few days. Cyanobiphenyls compounds also present the advantage to exhibit a large dielectric anisotropy connected with the highly polar CN group.

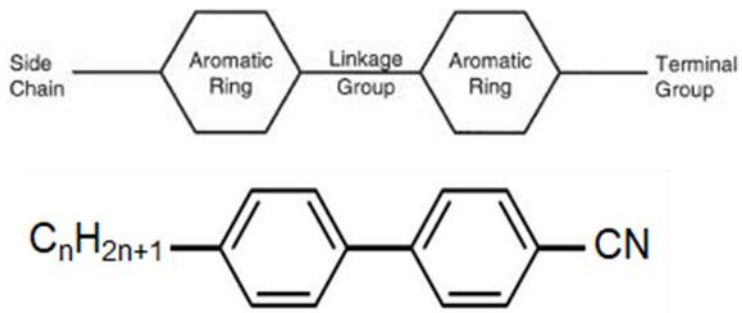

Figure 1.1.4 Typical structure of rod-like LC and example of p-n alkyl-p'-cyanobiphenyls [9]

Examples of representative cyanobiphenyls LCs like 6CB, 7CB, 8CB, 3OCB, 6OCB, and 8OCB are mentioned in Table 1 below illustrating the influence of the lateral chain length along with their

chemical composition and phase transition temperatures [9-11]. The nematic temperature range increases and the smectic A phase appears with the lateral chain length increase.

Liquid Crystal	Chemical Composition	Melting Point (°C)	T_{SAN} (°C)	T_{NI} (°C)
5CB	$C_5H_{11}CN$	22.5	-	35.3
6CB	$C_6H_{13}CN$	13.5		28
7CB	$C_7H_{15}CN$	28.5		42
8CB	$C_8H_{17}CN$	22	32.9	40.8
3OCB	C_3H_7OCN	64	-	75.8
6OCB	$C_6H_{13}OCN$	58	-	76.5
8OCB	$C_8H_{17}OCN$	50	67	80

Table 1 Different alkyl- and alkoxy- cyanobiphenyl LCs compounds (nCB, nOCB) with their chemical compositions and phase sequences.

It is important to mention that for applications, convenient properties in a large temperature range are obtained by using mixtures of several LC components. The use of mixtures allows to optimize clearing temperature, nematic temperature range and physical parameters like dielectric anisotropy, elastic constants, viscosity. E7 liquid crystal (Figure 1.1.5) is a typical example of such mixture obtained from different cyanobiphenyls LC; it shows the nematic phase between -62°C and 60°C.

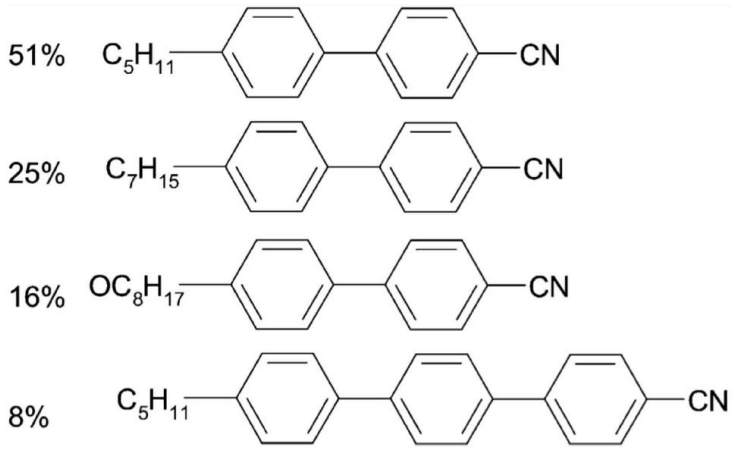

Figure 1.1.5 E7 liquid crystal composition

The alignment of the director to a certain axis is also an important point in view of applications. The alignment of nematic LC can be achieved by various methods. The first one is the alignment controlled by cell walls sandwiching the liquid crystals, and we have two ways, homogeneous (planar) or homeotropic (Figure 1.1.6). Homeotropic is an alignment perpendicular to the cell walls and is

created by treating the walls with a surfactant such as hexadecyl-trimethyl-ammonium bromide (HTAB) [4][5]. On the other hand, to achieve homogeneous (planar) alignment, there are several ways, the most commonly used method is coating the cell walls with a polymer, like polyvinyl alcohol (PVA) or polyimides, by spinning it (spin coating) in a manner to achieve a suitable thickness and then rubbing it in one direction with a velvet cloth after being cured, which helps the liquid crystal molecules' long axis to align along the rubbed direction [12][13]. Usually, the sample orientation is checked by mean of an optical polarizing microscope.

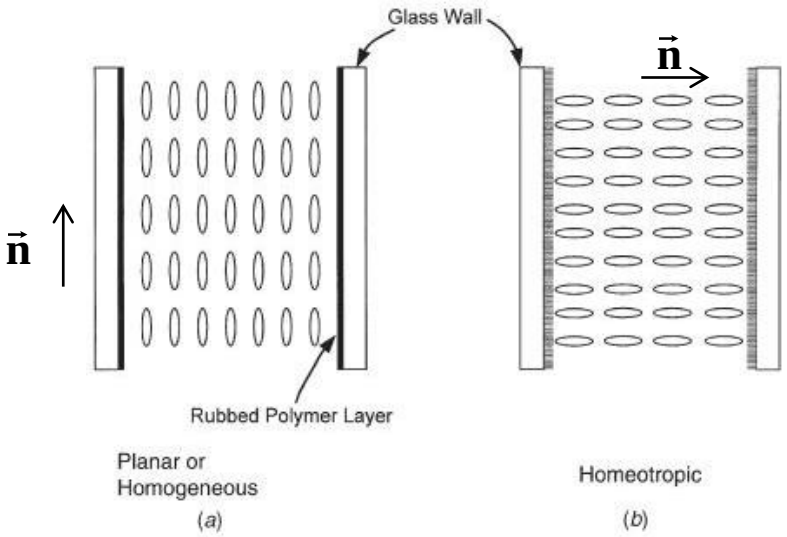

Figure 1.1.6 Nematic LCs aligned (a) homogeneously (planar), and (b) homeotropically [15]

1.1.2 Permittivity, losses and dielectric relaxation

Under electric field $\vec{E}$, a material shows a polarization $\vec{P}$; the permittivity ε translates the coupling between the applied electric field (excitation) and the corresponding polarization (response):

$$\vec{P} = \varepsilon_0 \chi \vec{E} = \varepsilon_0 (\varepsilon - 1)\vec{E}$$

$$\vec{D} = \varepsilon_0 \vec{E} + \vec{P} = \varepsilon 0 (1 + \chi)\vec{E} = \varepsilon_0 \varepsilon \vec{E}$$

Where ε_0 is the vacuum permittivity, χ the dielectric susceptibility of the material, and $\vec{D}$ is the displacement vector. The polarization is of two types: orientational polarization and induced polarization.

At the level of intramolecular bonds, the displacement of electrons from one atom to another permanently causes the molecules to have a permanent dipolar moment [15]. Under electric field, the permanent dipole follows the electric field orientation and contributes to the polarization of the material; this polarization is called orientational polarization. On the other hand, the electric field

creates displacement of atoms and orbital deformation; these two phenomena correspond respectively to atomic and electronic polarizations; both are called “induced polarization”. The induced polarization depends on the polarizability α of the molecules.

Under a sinusoidal electric field of pulsation ω, the dielectric properties of the material are expressed via the complex dielectric permittivity $\varepsilon^*(\omega)$ which links the complex polarization $P^*(\omega)$ or the complex electrical displacement $D^*(\omega)$ to the applied sinusoidal electric field E:

$$P^*(\omega) = \varepsilon_0(\varepsilon^*(\omega) - 1)E \qquad D^*(\omega) = \varepsilon_0\varepsilon^*(\omega)E\,, \quad \text{where } \varepsilon^*(\omega) = \varepsilon'(\omega) - j\varepsilon''(\omega)$$

The real and the imaginary parts $\varepsilon'(\omega)$ and $\varepsilon''(\omega)$ describe respectively the permittivity and the losses. The loss tangent $tan\delta(\omega) = \varepsilon''(\omega)/\varepsilon'(\omega)$ is also used to describe the dielectric losses.

Figure 1.1.7 illustrates the classical evolutions of $\varepsilon'(\omega)$ and $\varepsilon''(\omega)$ as a function of the frequency F; this kind of curves is called “dielectric spectra” [15] [16]. At low frequencies (Part I on Figure 1.1.7), the different polarizations are observed and contribute to the dielectric response. When the frequency increases, the orientational polarization relaxes first due to the corresponding molecular motion: the dielectric permittivity decreases progressively with increasing frequency and the imaginary part shows a maximum at a characteristic frequency F_C (critical or relaxation frequency). The induced polarization is faster than the orientational polarization; it is frequency independent for a wide frequency range but resonance phenomena appear at very high frequency (Parts II and III on Figure 1.1.7).

For some materials when there is conductivity σ, the dielectric spectra show an increase of $\varepsilon''(\omega)$ for decreasing frequency; usually this contribution is described by the following equation:

$$\varepsilon''(\omega) = \sigma/\varepsilon_0\omega$$

With logarithmic scales, the existence of conductivity traduces by a linear decrease (slope -1) of $\varepsilon''(\omega)$ versus frequency. An increase of the real permittivity $\varepsilon'(\omega)$ can also appear at low frequency; this so-called “electrode effect” results of charges accumulation at the electrodes of the measuring cell.

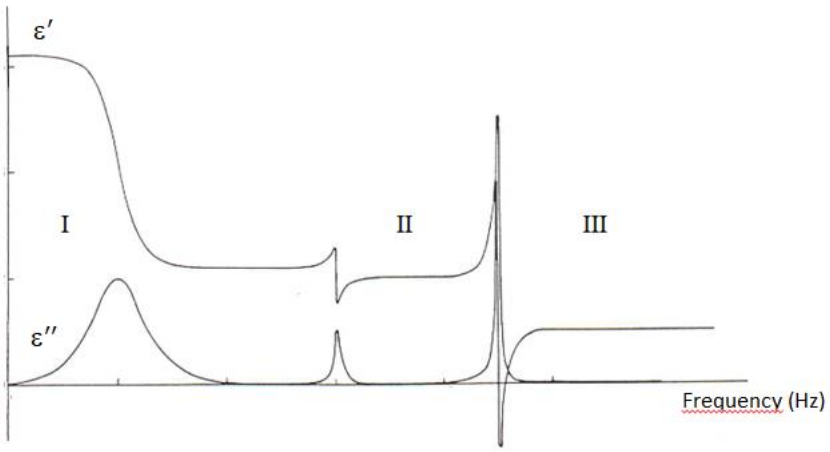

Figure 1.1.7 Dielectric spectra of a polar material: orientational (I) atomic (II) and electronic (III) polarizations

The relaxation of orientational polarization described above can be analyzed by mean of the Debye model [17]:

$$\varepsilon^*(\omega) = \varepsilon'(\omega) - i\varepsilon''(\omega) = \varepsilon_\infty + (\varepsilon_s - \varepsilon_\infty)/(1 + i\omega\tau)$$

Where ε_s is the static dielectric permittivity, ε_∞ is the value of permittivity at high frequencies where only the polarizability of the molecules plays a role, $\omega = 2\pi F$ is the pulsation of the applied field, and τ is the relaxation time. The critical frequency of the process is given by $F_C = 1/2\pi\tau$. So, we can define the real and imaginary parts of the dielectric permittivity by the following equations:

$$\varepsilon'(\omega) = \varepsilon_\infty + \frac{\varepsilon_s - \varepsilon_\infty}{1 + \left(\frac{F}{Fc}\right)^2} \quad \varepsilon''(\omega) = \frac{(\varepsilon_s - \varepsilon_\infty)\frac{F}{Fc}}{1 + \left(\frac{F}{Fc}\right)^2}$$

The difference $\varepsilon_s - \varepsilon_\infty$ represents the dielectric amplitude of the relaxation process. The peak of $\varepsilon''(\omega)$ is given by $\varepsilon''_{max} = (\varepsilon_s - \varepsilon_\infty)/2$. The loss tangent is expressed as follow:

$$tan\delta(\omega) = \frac{(\varepsilon_s - \varepsilon_\infty)\frac{F}{Fc}}{\varepsilon_s + \varepsilon_\infty(\frac{F}{Fc})^2}$$

The dielectric spectra corresponding to the Debye model are given in Figure 1.1.8. The Cole-Cole representation (ε'' versus ε') shows a semi-circle (Figure 1.1.8c).

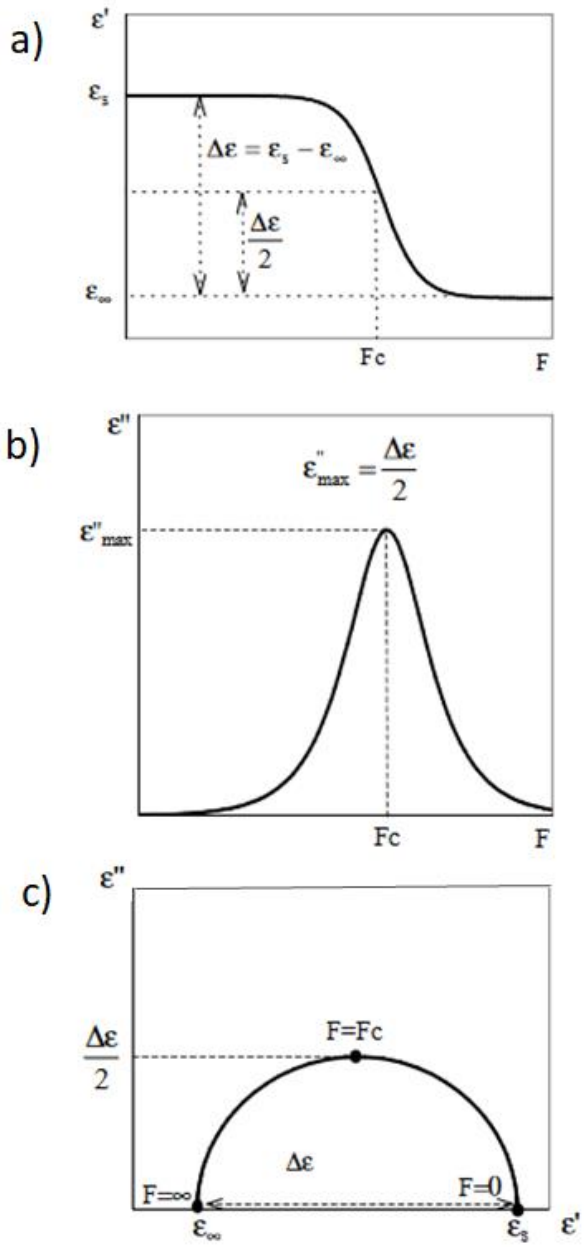

Figure 1.1.8 Frequency evolutions of the real permittivity (a) and losses (b), Cole-Cole plot (c) for a Debye relaxation process

In the general case, a distribution of the dielectric spectra can be observed due to the existence of several relaxation processes or to a continuous distribution of the relaxation frequency. The complex permittivities are the following:

N relaxation process: $\varepsilon^*(\omega) = \sum_{j=1}^{N}(\varepsilon_\infty + \frac{\Delta\varepsilon_j}{1+j\frac{F}{Fcj}})$

Cole-Cole continuous distribution: $\varepsilon^*(\omega) = \varepsilon_\infty + \frac{\varepsilon_S - \varepsilon_\infty}{1+(j\frac{F}{Fc})^{(1-\alpha)}}$

Cole-Davidson continuous distribution: $\varepsilon^*(\omega) = \varepsilon_\infty + \frac{\varepsilon_s - \varepsilon_\infty}{(1+j\frac{F}{Fc})^\beta}$

1.1.3 Dielectric properties of liquid crystals

The dielectric constant plays an important role for liquid crystals applications; it's determined by characterizing the responses to an external applied electric field [17][11][7]. Since nematic LCs are uniaxial anisotropic material, the measured permittivity depends on the direction of the applied electric field (Figure 1.1.9); we distinguish two different mean permittivities: when the measuring electric field is parallel to the director $\vec{n}$, the permittivity is noted $\varepsilon_{||}^* = \varepsilon_{||}' - j\varepsilon_{||}''$ (z axis along the director $\vec{n}$); for measurements in the perpendicular directions (x and y axis), the permittivity is noted $\varepsilon_\perp^* = \varepsilon_\perp' - j\varepsilon_\perp''$ and the complex permittivity is defined as a tensor:

$$\varepsilon^* = \begin{pmatrix} \varepsilon_\perp^* & 0 & 0 \\ 0 & \varepsilon_\perp^* & 0 \\ 0 & 0 & \varepsilon_{||}^* \end{pmatrix}$$

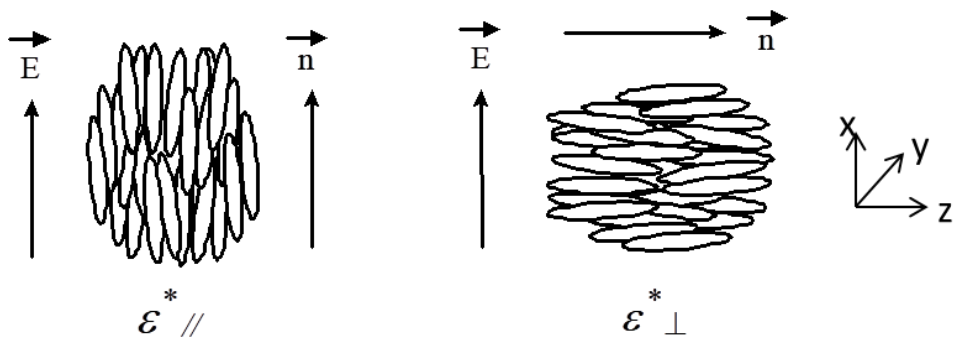

Figure 1.1.9 Parallel $\varepsilon_{||}^*$ and perpendicular $\varepsilon_\perp^*$ complex permittivities of a nematic liquid crystal

The difference between the two real permittivities is an important parameter for applications; it's called dielectric anisotropy:

$$\Delta\varepsilon' = \varepsilon_{||}' - \varepsilon_\perp'$$

The anisotropy properties also concern the dielectric losses and the conductivity which is usually ionic in liquid crystals.

The dielectric properties of the nematic phase depend on the chemical structure of the molecule; there are two important parameters:

- The permanent dipolar moment $\vec{\mu}$ of the molecule (Figure 1.1.10) resulting from the dipoles of different chemical bonding. The vector $\vec{\mu}$ contains the longitudinal μ_l and transversal μ_t components (Figure 1.1.11). The angle between $\vec{\mu}$ and the longitudinal component is noted β.

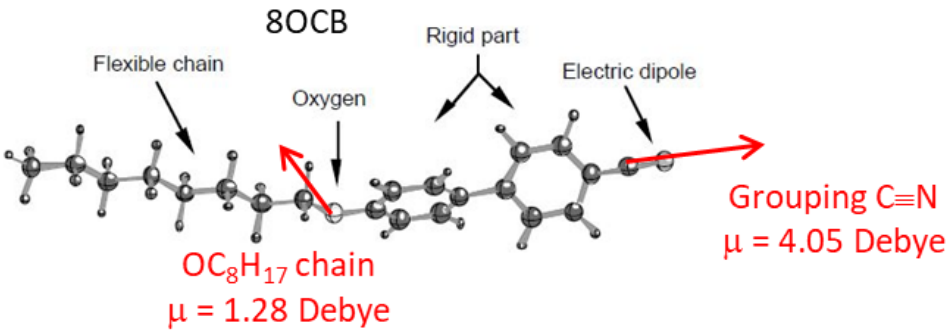

Figure 1.1.10 Example of longitudinal and transverse dipoles [15]

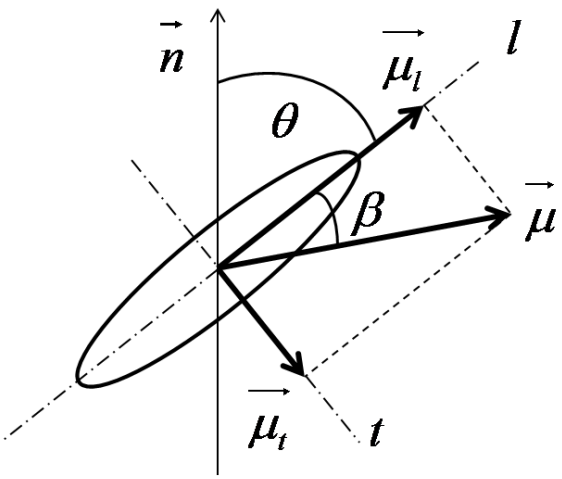

Figure 1.1.11 Schematic view of a rod-like molecule and the decomposition of the dipolar moment

- The molecular polarizability α which corresponds to the contribution of electronic and atomic polarizability of chemical bonding. The polarizability is given by:

$$\alpha = \begin{pmatrix} \alpha_t & 0 & 0 \\ 0 & \alpha_t & 0 \\ 0 & 0 & \alpha_l \end{pmatrix}$$

We can introduce the polarizability anisotropy $\Delta\alpha = \alpha_l - \alpha_t$.

At low frequency, the measured permittivity corresponds to the static permittivity and the dielectric anisotropy is called static anisotropy. The so-called Maier-Meier model gives theoretical expressions for the static parallel and perpendicular permittivities ($\varepsilon_{s//}$ and $\varepsilon_{s\perp}$) [18]:

$$\varepsilon_{s//} = \frac{NhF}{\varepsilon_0}\left\{\left(\frac{1+2S}{3}\right)\alpha_{//} + \frac{2(1-S)}{3}\alpha_{\perp} + F\frac{\mu^2}{3kT}\left[1-\left(1-3\cos^2\beta\right)S\right]\right\}$$

$$\varepsilon_{s\perp} = \frac{NhF}{\varepsilon_0}\left\{\left(\frac{1+S}{3}\right)\alpha_{//} + \left(\frac{2-S}{3}\right)\alpha_{\perp} + F\frac{\mu^2}{3kT}\left[1+\frac{1}{2}\left(1-3\cos^2\beta\right)S\right]\right\}$$

$$\Delta\varepsilon_s = \frac{NhF}{\varepsilon_0}\left[\Delta\alpha - F\frac{\mu^2}{2kT}\left(1-3\cos^2\beta\right)\right]S$$

Where,

$$h = \frac{3\bar{\varepsilon}}{2\bar{\varepsilon}+1} \qquad F = \frac{1}{1-\bar{\alpha}f} \qquad f = \frac{2\left(\bar{\varepsilon}-1\right)}{\left(2\bar{\varepsilon}+1\right)}\frac{N}{3\varepsilon_0}$$

$$\bar{\alpha} = \frac{\alpha_l + 2\alpha_t}{3} \quad \bar{\varepsilon} = \frac{\varepsilon_{//} + 2\varepsilon_{\perp}}{3}$$

N is the molecules number per volume unity. The order parameter S, the angle β and the polarizability anisotropy $\Delta\alpha$ were defined above. We can notice that depending on the value of β the static anisotropy can be positive or negative. In the isotropic phase (S=0), the simplified formula corresponds to the Onsager equation:

$$\frac{\left(\varepsilon_{is}-\varepsilon_{\infty}\right)\left(2\varepsilon_{is}+\varepsilon_{\infty}\right)}{\varepsilon_{is}\left(\varepsilon_{\infty}+2\right)^2} = \frac{N}{3\varepsilon_0}\frac{\mu^2}{3kT}$$

The coupling between the dipolar moment and an external electric field leads to different molecular motions. Usually, the molecular dynamics of nematic liquid crystals is attributed to different rotations. The model proposed by J. Jadzyn [19] considers three principal rotations (Figure 1.1.12):

- Motion (1): the rotation around the transversal axis (short axis) is connected to the longitudinal dipole moment $\overrightarrow{\mu_l}$; it's observed in parallel orientation. This rotation needs a jump over the nematic potential barrier. The relaxation frequency is about 10 MHz and strongly depends on temperature (thermally activated process).
- Motion (2): the rotation around the longitudinal axis is connected to the transverse dipole moment $\overrightarrow{\mu_t}$; the relaxation frequency is about 500 MHz and slightly depends on temperature (no jump over the nematic potential barrier).
- Motion (3): the rotation on a cone around the optical axis is linked to μ_l ; this process is observed in the two main measurement directions with higher amplitude for the perpendicular orientation. The relaxation frequency is about 100 MHz and slightly on temperature.

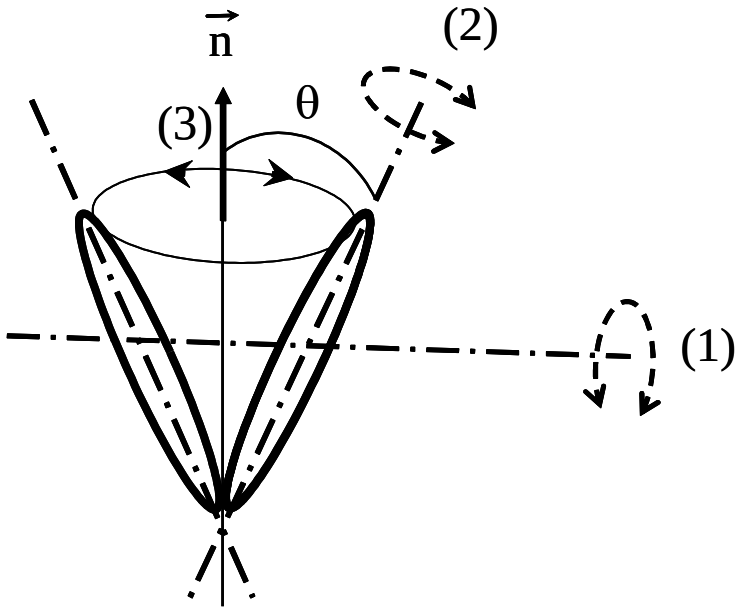

Figure 1.1.12 Molecular rotations associated to relaxation processes in nematic liquid crystals; (1) rotation around the short axis, (2) rotation around the long axis and (3) rotation around the cone.

1.1.4 Electrical driving of liquid crystals

In addition to surface treatment which allows the control of an initial orientation of the liquid crystal, it's interesting to have the possibility to change this orientation. This change of orientation can be used to modify some physical properties to obtain tunable devices. For example, in the case of liquid crystal displays the change of orientation induces a change of optical properties to obtain the "OFF" and "ON" states.

This driving of the liquid crystal orientation can be obtained by applying a magnetic or electric field. Due to the static dielectric anisotropy, a low frequency electric field with sufficiently high amplitude can reorient the liquid crystal molecules. For positive and negative dielectric anisotropy $\Delta\varepsilon'$, the long molecular axis is oriented respectively parallel and perpendicular to the applied electric field. The transition between the two extreme orientations is called Fréedericksz transition [20-22]. To describe this transition, we have to take into account the competition between elastic and electric energy; the global energy is given by:

$$U = \frac{1}{2}K\left(\frac{d\theta}{dz}\right)^2 - \frac{1}{2}\varepsilon_0\Delta\varepsilon' E^2 sin^2(\theta)$$

E is the applied electric field (*E=V/d*) and θ is the angle between the long molecular axis and the substrate; K represents the elastic constant. By minimizing the energy, we can determine the evolution of the angle θ versus the amplitude of the electric field. For low values of *V*, the voltage does

not affect the initial orientation. From a threshold value V_{th}, the orientation starts to change progressively:

$$V_{th} = E_{th}d = \pi\sqrt{\frac{K}{\varepsilon_0 \Delta\varepsilon'}}$$

V_{th} is independent from the thickness of the cell. In Figure 1.1.13 we present a schematic view showing the progressive effect of the voltage on the liquid crystal orientation; we can distinguish three regimes: region 1 corresponds to low voltages with unchanged orientation, region 2 with a modified orientation especially in the middle of the cell; the complete homeotropic orientation is obtained for a high voltage corresponding to region 3.

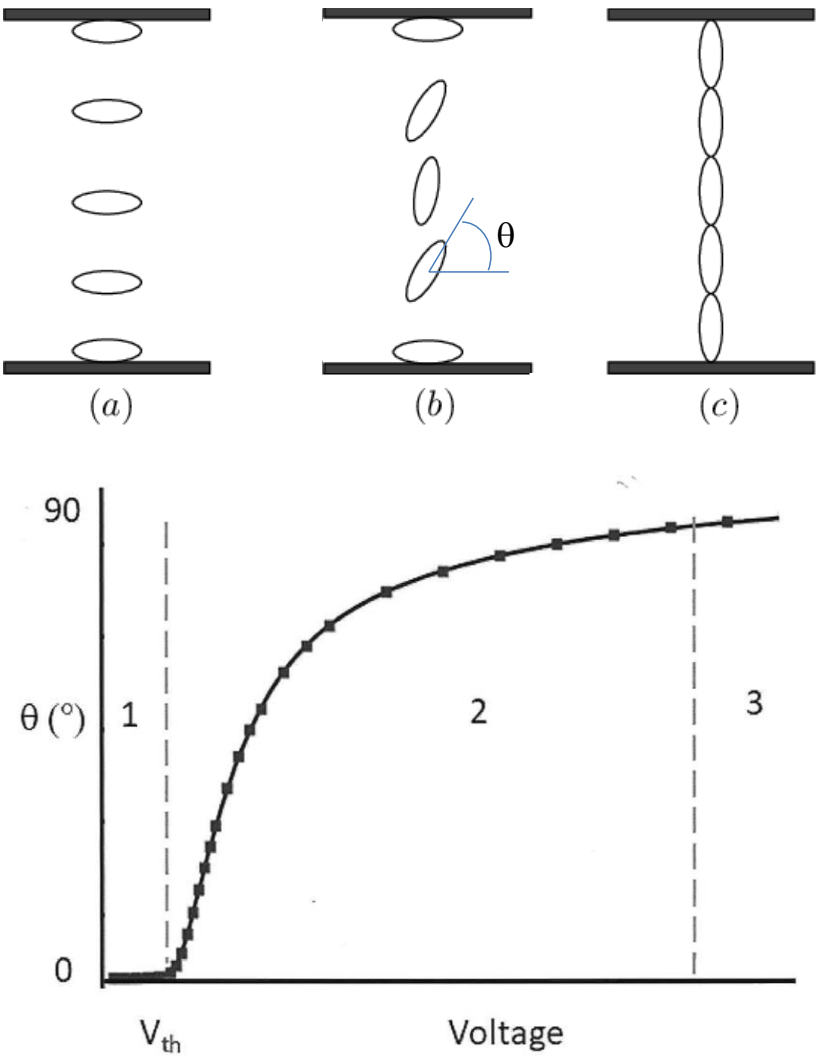

Figure 1.1.13 Schematic representation of progressive switching between planar and homeotropic orientations under voltage for positive dielectric anisotropy LC

For applications, it's important to have a fast change between these two orientations. The time response of the liquid crystals depends on the viscosity γ; we can distinguish two different response times; τ_{ON} corresponds to the switching time after applying high voltage and τ_{OFF} is the response time when the voltage is stopped:

$$\tau_{ON} = \frac{\gamma d^2}{\varepsilon_0 \Delta\varepsilon' (V^2 - {V_{th}}^2)}$$

$$\tau_{OFF} = \frac{\gamma d^2}{\pi^2 K}$$

Let us notice that τ_{ON} decreases with increasing voltage and dielectric anisotropy. τ_{OFF} is higher than τ_{ON} because there is no electric field to support the switching from ON to OFF state. The switching times decrease with viscosity and cell thickness.

The driving can also be achieved using a high magnetic field and a threshold is also defined as [1]:

$$B_{th} = \frac{\pi}{d}\sqrt{\frac{\mu_0 K}{\Delta\chi}}$$

$\Delta\chi$ is the magnetic susceptibility anisotropy. Liquid crystals molecules are diamagnetic and the molecules orientates in the direction of the magnetic field which has to be high.

1.2 Background on Metasurfaces

1.2.1 Background on artificial structures (EBG-PBG, metamaterial, FSS and metasurfaces)

In this section which aims to introduce the metasurface concept, we will briefly address some of the main ideas that were proposed over the past for tailoring the scattering properties of artificial materials.

1.2.1.1 EBG-PBG technologies

Let us first consider the so-called Electromagnetic Band Gap (*EBG*) technology by using the acronym that was generally used for the microwave part of the electromagnetic spectrum. Whereas in the optical range, the term Photonic Band Gap (*PBG's)* or Photonic Crystal (*PC's*) is used. These various terms indicate that a material is structured by reproducing the *periodic* arrangement of a crystal and that such structuring, in a full-dielectric approach (case of a dielectric with air holes in

optics) or with metal-dielectric compositions (case for instance of the multilayered metal-dielectric wave guide at microwave) yields to *band gaps* (forbidden frequency band in which there is no propagation). As a consequence, the EM waves are evanescent in these forbidden gaps and it is possible to *trap and confine* or to *guide* an EM wave in a specific region of space by means for instance of defects in the crystal lattice.

On the other hand, unique electromagnetic properties [23] such as the reversal of the group velocity $v_g = \frac{\partial\omega}{\partial k}$ with respect to the phase velocity $v_\varphi = \frac{\omega}{k}$ can also be achieved in the second band structure. These abnormal properties are illustrated in Figure 1.2.1 for an air hole array in a semiconductor medium manufactured at IEMN and operating at Near infrared. It can be noticed that in the second band plotted in red the slope of the $\omega - k$ curve is negative ($\frac{\partial\omega}{\partial k} < 0$) while the ratio $\frac{\omega}{k}$ is positive involving *backward wave* propagation.

However, it is essential to understand the necessary conditions for achieving such effects (confinement, guiding, backward wave propagation). First of all, the relevant dimensions implemented in the structuring have to be *comparable to the wavelength* ($d \sim \lambda$). Under this condition, destructive interferences effects induce band gaps in the dispersion diagram ($\omega - k$) tailoring the electromagnetic properties and subsequently the scattering properties. Secondly, the formation of such band gaps requires a sufficient number of basic cells. As a consequence, the structure can be considered as periodic despite its finite dimension.

From a practical point of view and notably for the miniaturization of the component, it is important to note that both conditions ($d \sim \lambda$, and large number of basic cells) can give rise to severe limitations to the application of these principles to devices that are operating in the microwave spectrum.

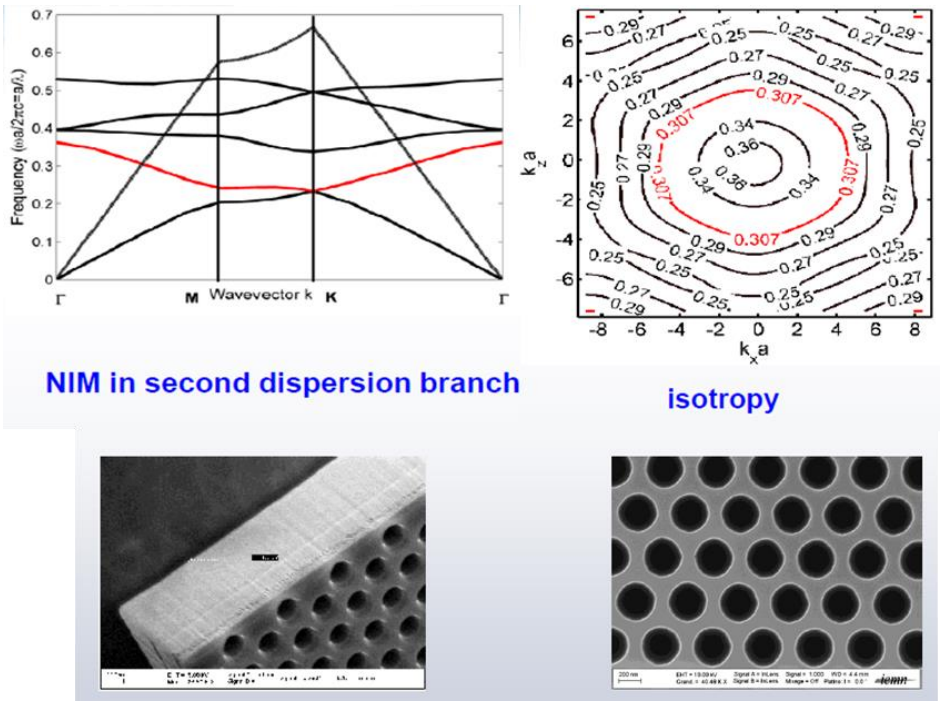

Figure 1.2.1 Illustrations of Photonic Crystal (PC) technologies used for tailoring the dispersion diagram with here negative index at the operating wave length of 1.55 µm (NIR) by drilling an air hole periodic array in a semiconductor matrix [23]

1.2.1.2 Metamaterial technology

The second key approach is the so-called *metamaterial* technology. The prefix meta means 'beyond'. Therefore, the term metamaterial is often used to design artificial materials that exhibit unusual properties *beyond* those presented by natural materials. The most representative example of singular properties afforded by structuring metal-dielectric structures is the possibility to obtain negative values of the *effective* refractive index ($n_{eff} < 0$) by for instance alternating Split-Ring-Resonators (*SRR*) with a negative effective permeability $(\mu_{eff} < 0)$ called MNG (Mu-NeGative) media and metal-strip periodic arrays with negative permittivity ($\varepsilon_{eff} < 0$) termed ENG (Epsilon NeGative) media. Where the parameters ε_{eff} and μ_{eff} describe the electromagnetic properties of an effective media. When MNG and ENG constituents of the artificial material exhibit *simultaneously* negative values for μ_{eff} and ε_{eff}, the effective refractive index, n_{eff} is negative in the corresponding frequency band.

In Figure 1.2.2 we illustrated the scattering properties of an *omega-type metamaterial* that was designed by full wave simulations, manufactured by Printed Circuit Board (PCB) technology and experimentally assessed in a scattering chamber (made of two parallel large plates with TEM propagation mode mimicking the condition of free space) at IEMN. It can be shown that such an omega pattern satisfies the aforementioned conditions for a DNG media with the intuition that the core and

the arms of the Ω motif are responsible of the magnetic and the electric responses respectively that can be confirmed by more in-depth study.

The effective medium condition for observing such unique effects is that the relevant dimensions have to be much lower than the operating wave length ($d \ll \lambda$ with typically $\frac{d}{\lambda} < 10$). From a practical implementing point of view, we would like firstly to stress that this long wavelength regime achieved for *deep subwavelength* dimensions can be difficult to satisfy. In addition, the exotic properties that were achieved for instance here with negative value of n_{eff}, can also lead to tricky issues. This is notably true for satisfying the impedance matching condition at the air/dielectric interface in the aforementioned example with positive and negative constitutive parameters, that is necessary to achieve high transmission efficiency. For instance, in the omega array taken here as an example around 10 dB losses can be noted in the pass-band transmission spectrum.

Moreover, as for EBGs, the metamaterial concept applied to negative index material also requires to multiply the number of basic elements in the propagation direction so that the incident magnetic field induces a *negative* magnetic response ($\mu_{eff} = -\frac{|\vec{B}|}{|\vec{H}|}$). Indeed, for that case, it is imperative that the incident H-field orientation is along the Ω central axis (grazing incidence with respect to the printed substrates).

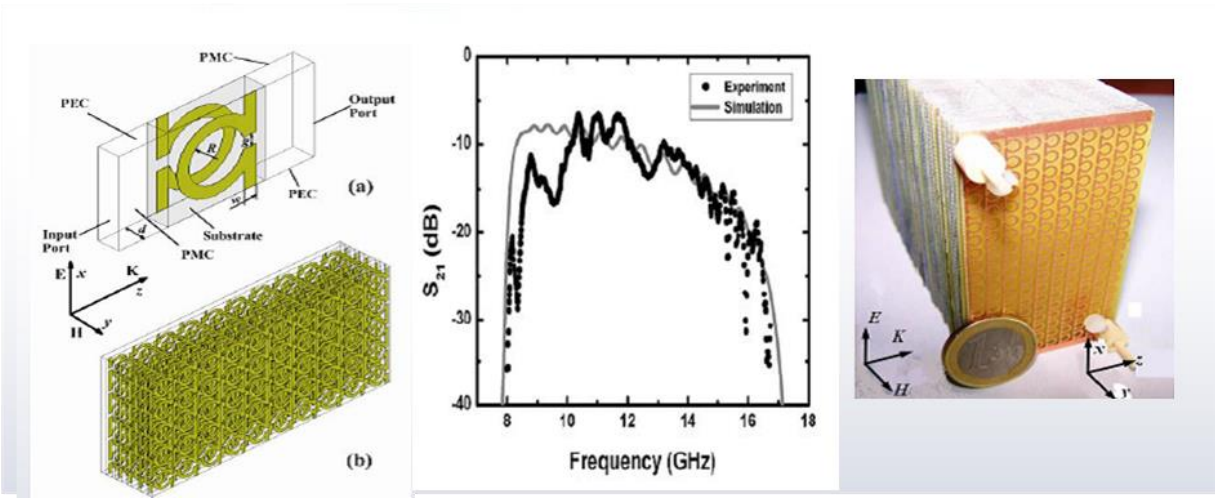

Figure 1.2.2 Illustrations of the transmission properties of omega-type DNG metamaterial [24]. Note the H-vector orientation along the Omega central axis [25]

All these reasons have motivated the development of the *metasurface* concept and hence a 2D electromagnetic structure instead of a bulk one. Also, let us note that as a first analysis, a metasurface can be compared with the so-called Frequency Selective Surface (FSS) by remembering that FSS have been used for many decades in radiating systems operating in microwave frequency.

1.2.1.3 Frequency Selective Surfaces

Here, the acronym (FSS) gives first indications about the specificity of the scattering properties of such a surface with an impinging plane wave. In fact, by printing onto a dielectric substrate either metal patches (capacitive patterns) or narrow strips (inductive geometries) or combining them as illustrated in Figure 1.2.3, it appears possible to introduce frequency selectivity.

The design rules are depending on the specificities of the targeted applications which are based on the frequency selectivity of the transmission. They were mainly used as hybrid randoms, band stop filters, dichroic reflector, Circuit Analog Absorbers [26]. Also, they can bring some control of the polarization of the transmitted wave that depends on the printed pattern symmetries. In particular, high degree of symmetry permits one to design filtering structure that are *insensitive* to the direction of *linear* polarized waves. By associating inductive and capacitive motifs, it is also possible to induce resonant responses with half-wavelength typical dimensions for the dominant resonance modes. Such hybrid FSSs can be considered to be part of the so-called metasurface technology based on resonant effects.

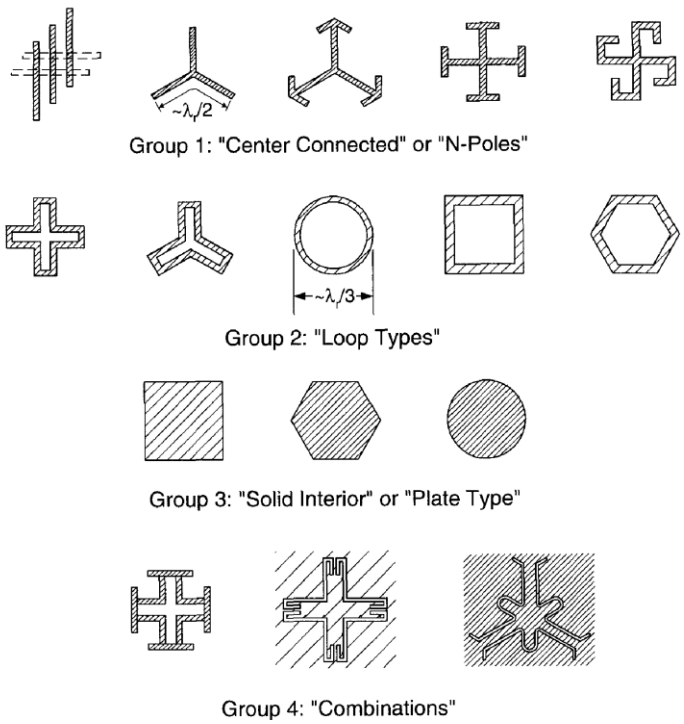

Figure 1.2.3 Examples of FSS pattern drawn from [26]

1.2.1.4 Metasurface technology

What we call a metasurface is not, strictly speaking, a pure 2D system as it would be the case for a graphene sheet. This is however the case of a FSS with a finite substrate thickness provided that

it has no real impact on the electromagnetic properties primarily determined by the metal pattern layout. Here again, the criterion for speaking of metamaterial-inspired technology is that the relevant dimension, for considering the artificial material as 2D systems, is much lower that the operating wave length (typically $\frac{d}{\lambda}$ <100 in the ideal case). It will be seen in the following section, devoted to absorbing screens that metasurfaces consist generally of an ultra-thin dielectric layer sandwiched between two patterned metal layers placed on the top and back sides.

One of the motivations for developing such a bi-layered structure is the following: we indicated that the achievement of a magnetic response with bulk metamaterial technologies implies an orientation of the incident magnetic field in a direction normal to the metal printed substrate. This condition is only satisfied for a *grazing* incidence of the impinging wave with respect to multilayered substrate and not under *normal* incidence. To overcome this difficulty, one solution is to use two patterned or uniformly metallized plates facing each and stacked along the incident wave propagation direction. In fact, this bi-layered metal configuration allows to induce a magnetic response resulting from conduction and displacement current loops. Figure 1.2.4 gives some examples of basic cells that were developed for the metamaterial technology [27] with a schematic of the two metallic facing plates and illustration of conduction and displacement currents in Figure 1.2.4h.

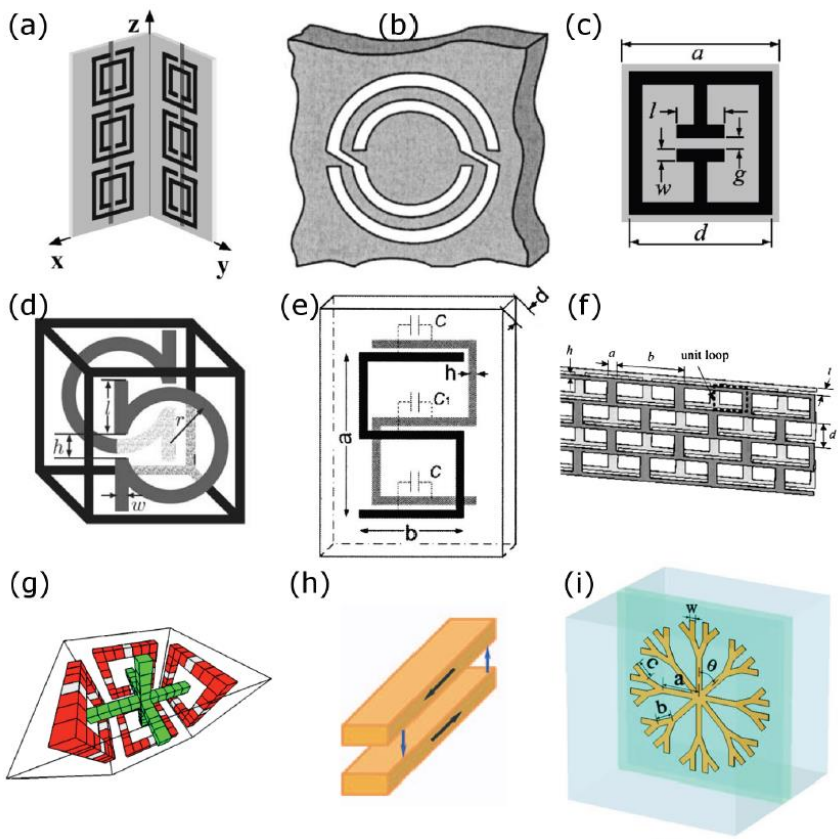

Figure 1.2.4 Examples of basic cells used for bulk metamaterial and metasurface technologies [27]

After this brief presentation of the key structuring techniques with emphasis on the relevant dimensions, let us now consider the basic concepts for perfect absorption of an incident wave notably on the basis of the literature references on the absorbing layers known as Dällenbach, Salisbury or Jaumann Screens.

1.2.2 Perfect absorbing layer screens

We outline in this section the various solutions that were developed and reported in the literature for absorbing screens aiming for *low-profile* total absorbers. In fact, it is well known that the most efficient absorbers, such as those that are used in an anechoic chamber, are pyramidal shaped foams with conductive particles (will be used for the free space experiment reported in Chapter 4). A proper design of the characteristics of the pyramid enables firstly the optimization of the trapping of the incident energy that is spread in several directions at the air/foam interface and subsequently dissipated by the conductive particles within the pyramids. For this first example, it can be noted that one requirement for full absorption is the lack of reflection and trapping of the energy here in the volume of the pyramids.

Targeting now a low-profile absorber in the sense that its thickness is much less than the operating wave length, one can contemplate to start from the same underlying ideas that are implemented in the Dallenbach, Salisbury and Jauman screen technologies.

The structure of a Dallenbach screen is a lossy magneto-dielectric slab onto a metal plate [28]. Zero reflection can be achieved at the interface between the air and the screen with the equality of the relative permeability and permittivity with thus a unit ratio and a surface impedance surface equal to the 377Ω ($Z_s = Z_0\sqrt{\frac{\mu_r}{\varepsilon_r}}$). For this screen, a quarter-wavelength thickness is often chosen for the dielectric layer.

The Salisbury screen, patented in 1952 [29], is a structure that is composed of (i) a back-side metal layer, that acts as a ground Perfect Electrical Conductor (PEC), (ii) a dielectric spacer with a thickness $d = \frac{\lambda}{4}$ and (iii) a purely resistive sheet with a surface resistance (R_s) that can be properly chosen for matching the free space impedance ($Z_0 = 377\Omega$). One can interpret the lack of reflection at the interface between air and absorbing screen by using a transmission line approach that will be explained in further details in Chapter 3. Indeed, by the choice of a quarter wavelength condition for the dielectric substrate thickness, one can note that the equivalent impedance at this interface is given by the parallel association of the impedance of the grounded dielectric layer ($Z_d \rightarrow \infty$, $d = \frac{\lambda}{4}$) and the sheet resistance (R_s) with thus $Z_{eq} = Z_d // R_s = R_s$= 377Ω.

Interestingly, the Jauman screen is an extension of the Salisbury screen allowing the design of broad band absorbers by stacking several sheet resistance-dielectric bilayers. Generally, for the sake of simplicity in the design, the dielectric thickness is, here again, chosen as quarter wave length slab and the optimization of the various sheet resistance values can be also performed by using a transmission line method. By this stacking, it is possible to improve the absorption bandwidth that is broadened by the existence of more rejection dips in the reflection spectra. Therefore, the Jauman approach is mainly applied for the design of broad band absorber by the multiplicity of impedance matching condition and not by using high losses material that would also decrease the frequency selectivity of absorbing mechanisms.

For the three kinds of absorbing screens outlined above, *quarter-wave length* dielectric layers were chosen (half wave length for a bi-layered sheet resistance/dielectric Jaumann screen). It results from this relatively high absorber thickness that it does not satisfy the low-profile criterion generally required for total absorbers and notably at microwave.

A means to alleviate such a drawback is to implement FSS structures on top of a basic grounded dielectric (substrate onto a metal film) instead of a sheet resistance. By this means it is thus possible to cancel the imaginary part resulting from the grounded substrate by the imaginary part of the FSS. In the transmission line formalism, it is well known that the equivalent impedance of a loss-less grounded substrate is:

$$Z_s = Z_c \tan \beta d$$

In this expression, Z_c, β and d are the characteristic impedance of the transmission line, that describes propagation of the TEM wave in the dielectric layer, the propagation constant and the dielectric thickness respectively.

For thin dielectric ($\frac{d}{\lambda} \ll 1$), Z_s is equivalent to the impedance $(Z = jL\omega)$ of an inductive element (L) with $L = \mu_0 \times d$. For $d \ll \lambda$ it is thus possible to cancel this inductive term by the equivalent capacitance that results from the integration of a capacitive FSS structure for instance by implementing patch-like patterns.

In that case of substitution of the resistive sheet (conventional $\lambda/4$ Salisbury screen) by a FSS with a drastic reduction of the dielectric slab, it is worth noting that the dissipation of the incident waves takes place in the dielectric layer (low-loss layer with a loss tangent of a few percent).

In Chapter 3 part 2, devoted to the analytical description of *deep-subwavelength* Perfect metamaterial absorbers controlled by the orientation of LC, the Transmission Line (TL) formalism applied to a FSS placed in front of a grounded substrate (TL loaded by a short circuit) has to take the coupling effects between the FSS and the ground plane into account.

On the basis of these backgrounds about the various artificial structures and the total absorbing screens, we will now comment the key papers on LC tunable metamaterial that were published in the frame work of a previous PhD thesis work performed by Fuli Zhang at IEMN, this work being made in collaboration with the Tsinghua University [30].

1.2.3 Some key papers on LC tunable metamaterials

We will start with the first paper published in 2008 entitled *Magnetic control of negative permeability metamaterials based on liquid crystals* [31], (Figure 1.2.5).

In this paper, the authors used two facing Split Ring Resonators (double C shaped strip with a back-to-back direction to avoid a magneto electric response). This configuration is named broad side coupled SRR for suppressing the electrical response. This is the same underlying idea that was used in edge coupled resonators as proposed by Pendry in its seminal work. The current component induced by the electric field cancel due to their reverse orientations keeping the current induced by the magnetic field as the sole current contribution. The metal patterns are printed onto the surface of fiberglass slabs with voids that were infiltrated by LC 5CB. The fact of using an *isolated* C pattern means that such an artificial structure can be compared to a MNG with a stop band transmission characteristic.

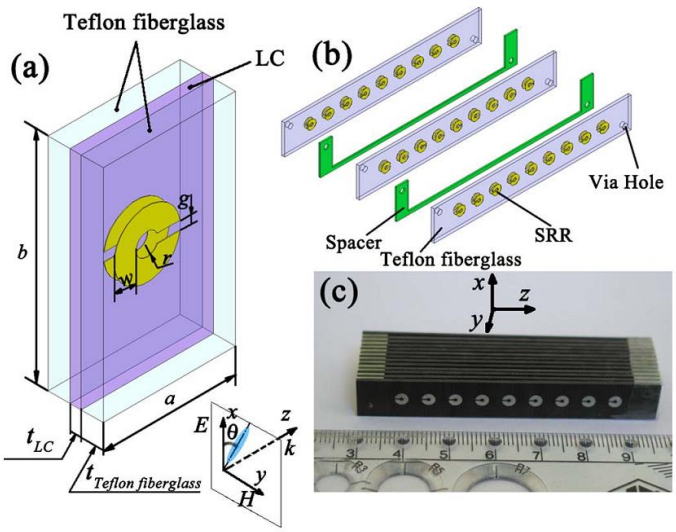

Figure 1.2.5 3D view of a broad-side coupled SRR periodic array [31]

In Figure 1.2.6 we show the results of the transmission spectra as a function of the orientation of the LC molecule. It is assumed that the electric field of the incident beam is polarized along the *x* direction and the magnetic field of the incident beam is polarized along the *y* direction with illumination of the structure along *z*. We emphasize that such a grazing incidence of the incident wave with respect to the multilayered surface is necessary for inducing a magnetic response. As expected from the respective signs of the effective constitutive parameters with $\varepsilon_{eff} > 0$ and $\mu_{eff} < 0$, the frequency dependence of the S_{21} parameters calculated by a full wave analysis (CST microwave studio) shows a rejection dip at the resonant frequency that can be dynamically varied by controlling the orientation of the molecules within the LC slab. The electric field map that is also displayed in this figure confirmed the localization of the E-field between the two facing metal plates.

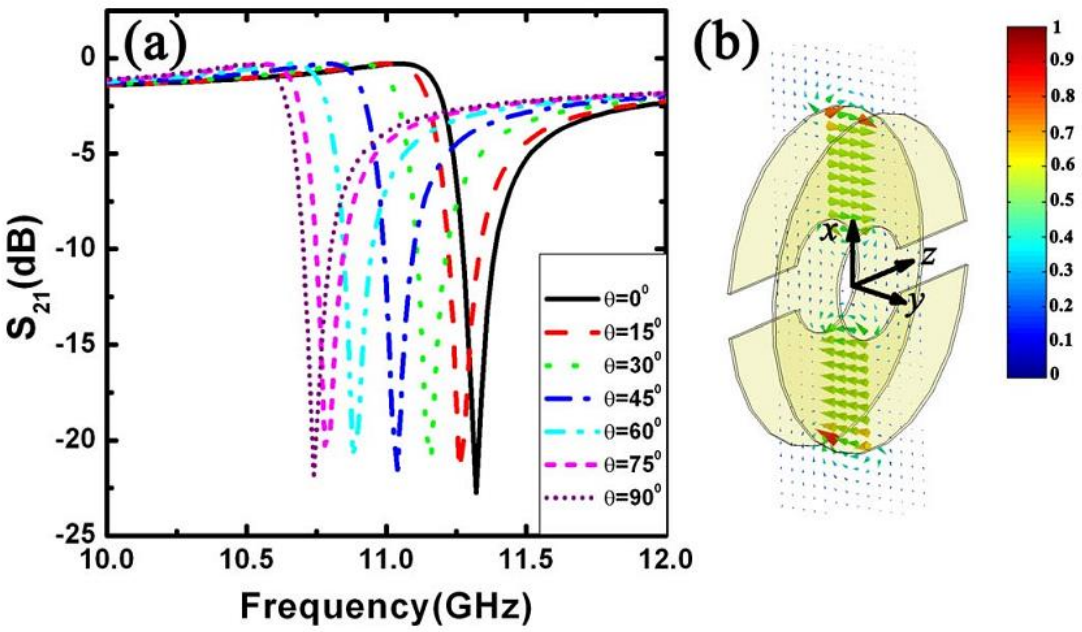

Figure 1.2.6 Frequency dependence of the scattering parameter S21 for various orientations of the LC optical axis with (a) E-field plot at resonance [31]

Turning now to the experimental assessment of the frequency shift resulting from the LC re-orientation, we report in Figure 1.2.7 the result of the S_{21} measurements when the LC molecules are *magnetically* aligned compared with those calculated.

A shift toward lower frequency is well predicted in agreement with the experimental data. However, it can be noticed that the frequency shift recorded in the transmission spectra are relatively weak, a few percent. In the present paper, the author used 5CB as LC compound with a relatively modest dielectric anisotropy. And hence it will be one of the motivations of the thesis work to drastically increase this frequency shift by using higher anisotropy LC compounds.

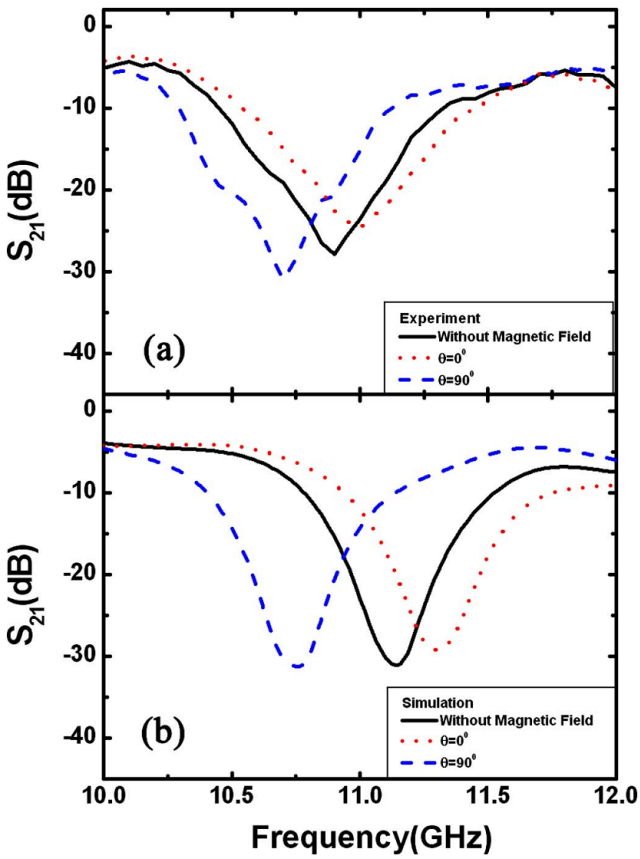

Figure 1.2.7 Comparison between the experiment and the simulation for the C–shaped [32]

Recently, this previous work that was published in 2008 in APL, was revisited in particular by comparing isotropic and anisotropic approaches [32]. The results of this comparison drawn from this reference published in 2021 are shown in Figure 1.2.8. The authors used exactly the same C-shaped structure and same dimensions as noted in this figure and the same assumptions with respect to the Electric field orientation.

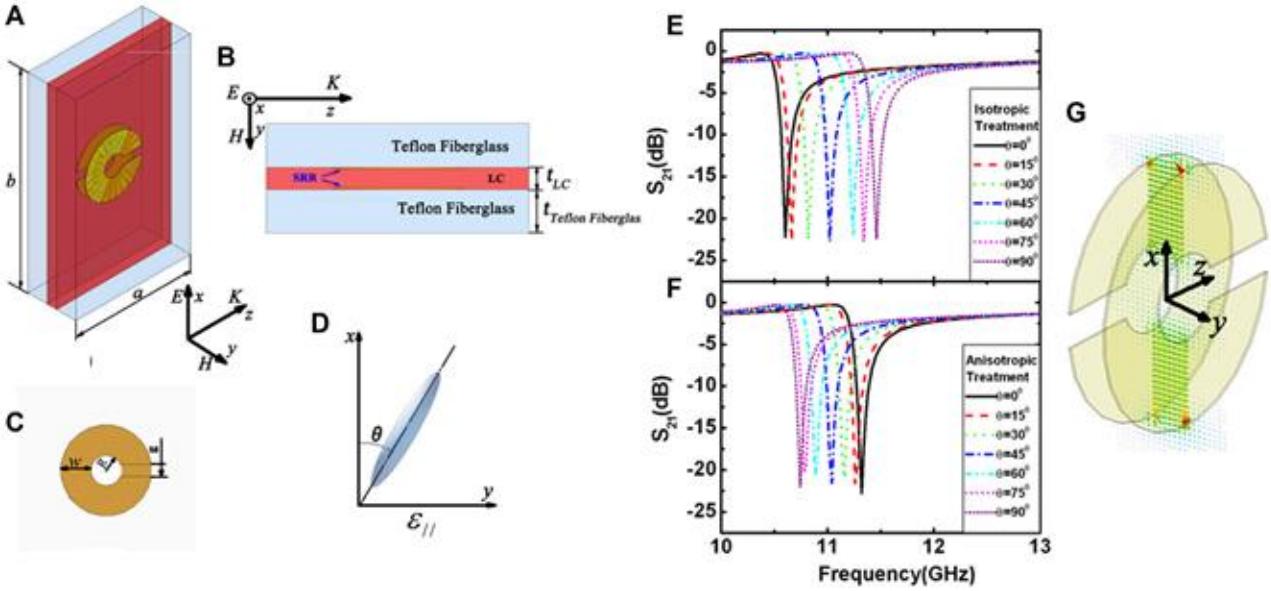

Figure 1.2.8 Broadside coupled SRR metamaterial infiltrated with 5CB (A) top view of the basic cell (B) and front view (D). Schematic showing the optical axis orientation (D) Transmission spectra as a function reorientation angle isotropic and anisotropic treatments (E) Electric field distribution within the SRR in the x-y paned at resonance (G) [32]

For the isotropic case, the LC layer is considered as a homogeneous isotropic material [33]. For aligned nematic liquid crystal, the electric field is polarized along the *x* direction and the LC dielectric constant is approximately:

$$\varepsilon = \frac{\varepsilon_{\parallel}\, \varepsilon_{\perp}}{\varepsilon_{\parallel}\, sin^2\theta + \varepsilon_{\perp}\, cos^2\theta}$$

Where $\varepsilon_{\perp}$ and $\varepsilon_{//}$ represent the permittivity for the polarized beam perpendicular and parallel to the director axis *n* and θ denotes the rotation angle of the molecular director with respect to the x axis.

For the second approach used in this paper, a tensor description for the LC layer was introduced [34]:

$$\varepsilon = \begin{pmatrix} \varepsilon_{\perp} + \Delta\varepsilon\, cos^2\theta & 0 & \Delta\varepsilon\, cos\theta\, sin\theta \\ 0 & \varepsilon_{\perp} + \Delta\varepsilon\, sin^2\theta & 0 \\ \Delta\varepsilon\, cos\theta\, sin\theta & 0 & \varepsilon_{\perp} \end{pmatrix}$$

From Figure 1.2.8, for the isotropic treatment when the LC orientation varies from 0° to 90°, the resonance frequency of the SRR i*ncrease*s from 10.9 to 11.4 GHz. On the contrary, the *resonance frequency decreases* for the anisotropic treatment.

As a consequence, the authors concluded that an isotropic treatment is no longer valid. On the basis of this important conclusion, in the following chapters of this dissertation, all the simulations that will be performed will be conducted by assuming a *tensor approach.*

The SRR-type pattern allows the design of a single negative medium with a magnetic response. Let us now consider the case of an omega–type multilayered structure that was also studied by the same research group and that was published in 2009 in Optic Express [35] entitled *magnetically tunable metamaterials by liquid crystal orientation*.

Let us first consider Figure 1.2.9 whose illustrations were drawn from this reference. Instead of an isolated C-shaped metal pattern, the periodic array that was designed, manufactured by PCB technology and experimentally assessed in free space in the X band, is here composed of *omega-type* basic cells *interconnected* by metal strips. In the case of omega array, we previously learned (overview of the metamaterial technology) that omega pattern shows a *magnetic response* through the current loop in the C shaped motif but also an *electric response* via the arms attached.

Therefore, one can expect a pass-band and not a stop-band transmission characteristic owing to the fact that the artificial material can be compared to a Double NeGative medium (DNG). This assumption is confirmed by the calculation of the S_{21} parameter and their measurements in the X band for the prototype displayed in Figure 1.2.9. Looking at the numerical results, it is seen that the pass–band can be tuned toward lower frequencies, here again, of a few percent according to the choice of a moderate anisotropy LC. This behavior is assessed by the experimental results with however a much broader transmission window and hence less pronounced frequency shift. Anyway, for both transmission characteristics, experiment and simulation, it can be noticed that the maximum of transmission is much less below full transmission with quasi-unit S_{21} values. As a consequence, the same conclusion pointed out in the omega–type *bulk metamaterials* section, namely a relatively poor transmission still holds. This can preclude the application of the tunability concept by LC technology in a practical functional device, such as an amplitude modulator.

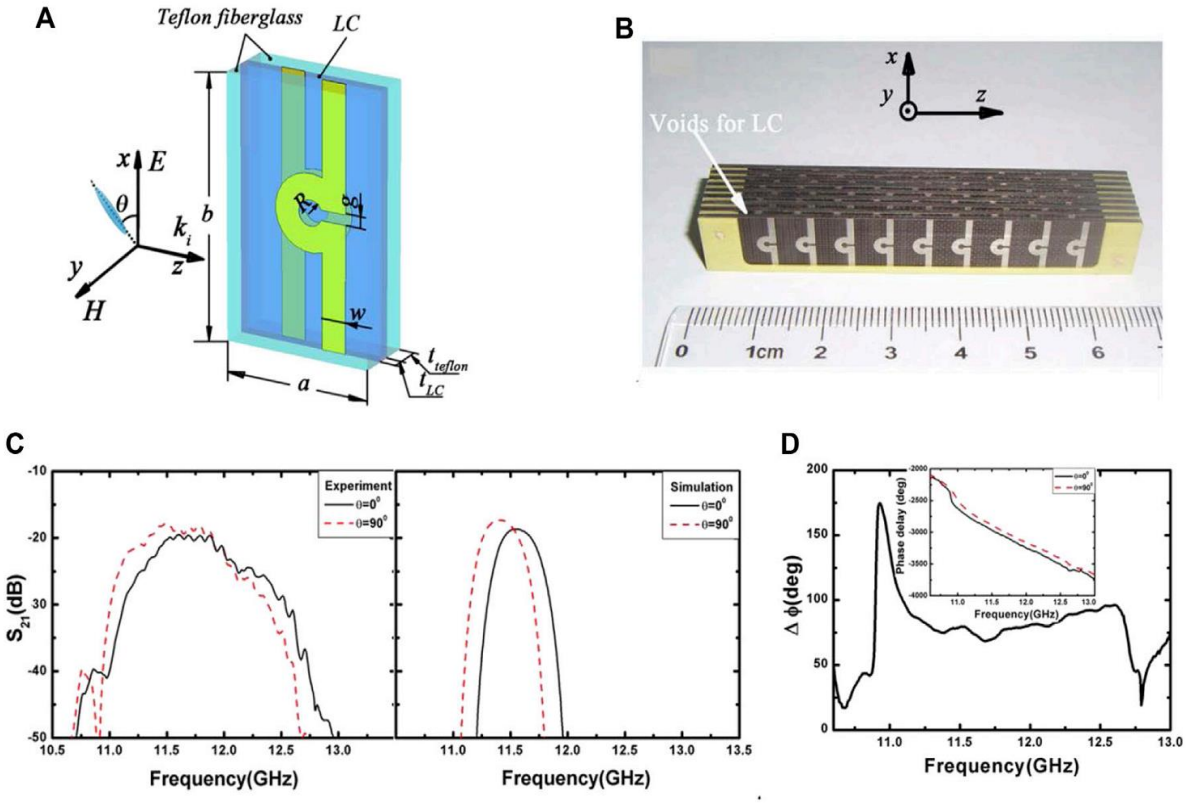

Figure 1.2.9 (A) Schematic of the basic cell the inset illustrating the orientation of the LC molecule in the x-y plane (B) photo of the multilayered structure (C) comparison of the transmission spectra measured and calculated. (D) result of phase shift measurement for ϕ = 0° and 90° [35]

We will end this part devoted to tunable metamaterial technology at microwave by quoting two others references of this research group published in 2010 [36] and 2011 [37] respectively:

For the former, the authors report an experimental demonstration on voltage tunable *short wire pair* metamaterial with *negative permeability* at microwave frequencies. Figure 1.2.10 illustrates the structure that was designed and experimentally characterized in this publication. The structure is composed of two copper parallel plates with the incident EM wave impinging *under normal incidence*. (Inset in this figure with the orientation of the incident wave vector (k_i). The geometrical parameters are as follows: W= 4.00; L= 9.00, $P_x = 11.00$, P_y= 6.00 and the thickness of the Teflon Fiberglass is t_{Teflon}= 1 (unit mm). The most relevant parameter notably for the saturation voltage is $t_{LC} = 0.6\ mm$. On the other hand, the copper bar used for the interconnection is 1 mm wide. The permittivity of the Teflon fiberglass is 2.65 for a loss tangent of 0.001.

In this work, a commercial LC TEB30A with a birefringence Δn =0.1703 at optical range was employed. However, owing to the dielectric characteristic dispersion, a smaller birefringence was measured at 10 GHz with n_0= 1.65 and n_e =1.73 and hence with Δn= 0. 08.

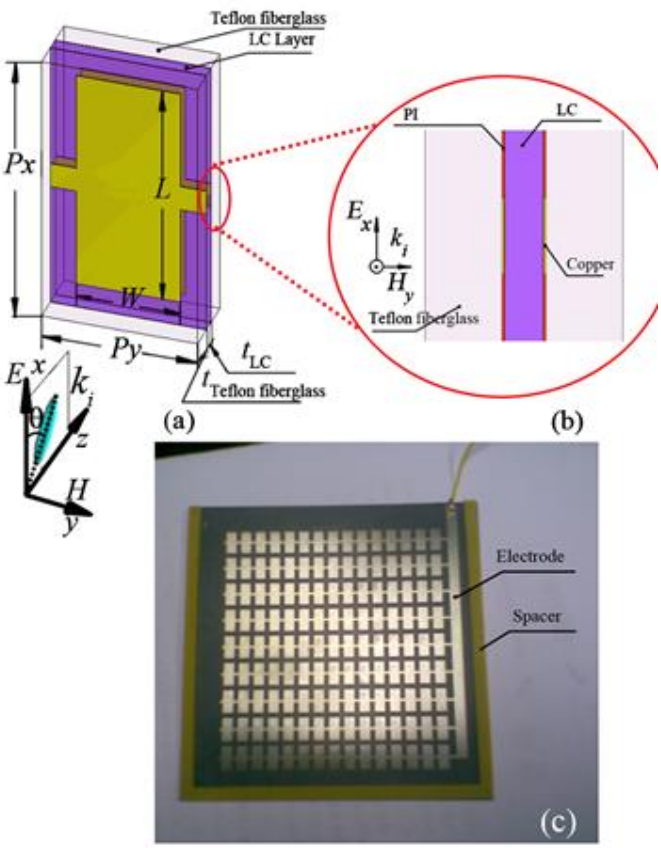

Figure 1.2.10 3D-Schematic of the short wire pair array (a) cross section indicating notably the direction of incidence (b) and photograph of the manufactured sample [36].

Figure 1.2.11 compares the complex valued S_{21} characteristics versus frequency in the X band (8-12 GHz) that can be calculated by using a full wave numerical code and those measured by varying the controlling applied voltage between 0 and 120 V. The results, displayed in this figure, show that magnetic resonance can be *continuously* shifted from 9.91 GHz down to 9.55 GHz by increasing the applied voltage from 0 to 100V. Commenting on these results, here again it can be noted that the frequency shift resulting from the LC orientation is weak and more importantly, it requires the application of a voltage up to 120 V to observe some saturation in the S_{21} frequency variations. However, on the contrary to the results reported in 2008 on bulk metamaterial with a *grazing* orientation of the impinging EM wave, one can notice a dramatic increase in the transmission level opening the way to use such a double pair structure in practical applications.

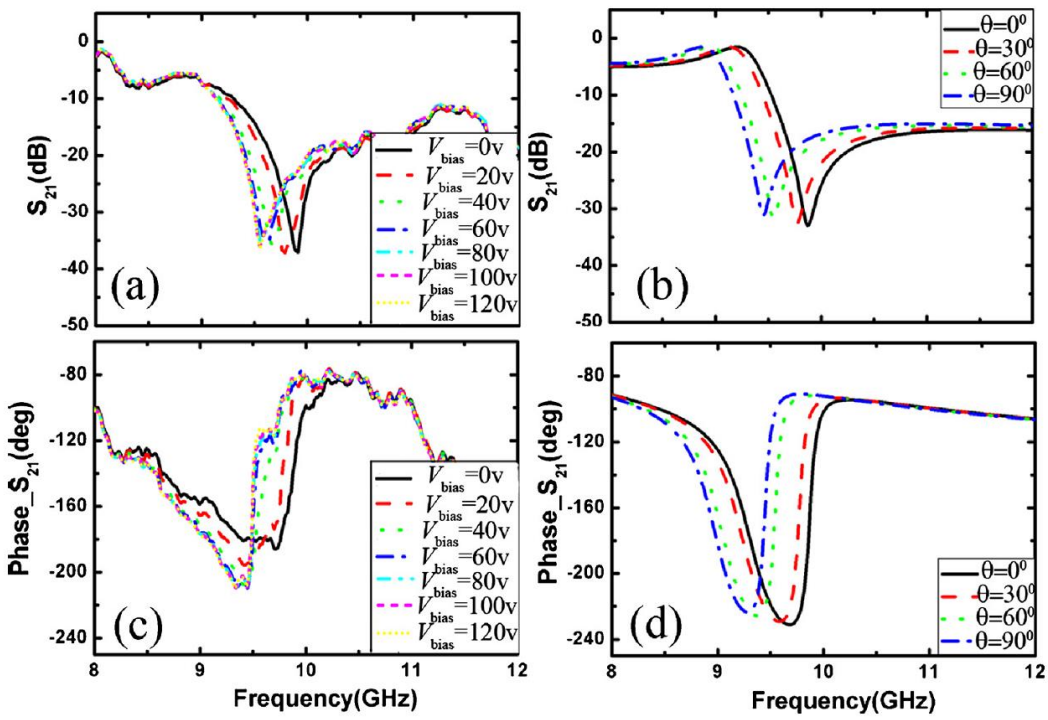

Figure 1.2.11 Comparison of the transmission spectra (S_{21}) calculated and measured by varying the applied controlling voltage between 0 V and 120 V [36]

In this publication, the authors also interpreted their results in terms of effective permeability that was retrieved from the theoretical scattering parameter calculation. The frequency dependence of the real part of the *retrieved effective permeability* is displayed in Figure 1.2.12.

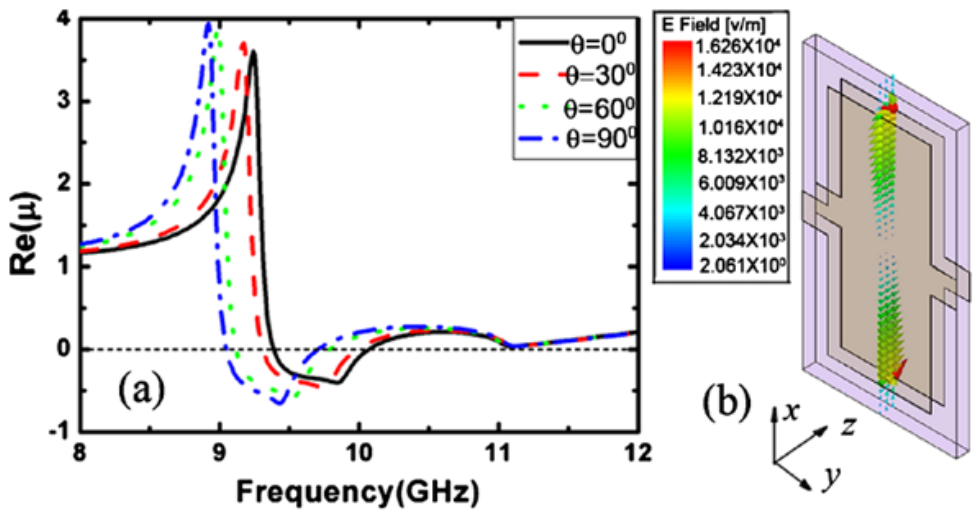

Figure 1.2.12 Retrieval of the effective relative permeability for various values of θ along with the electric field map at resonance.

A magnetic resonance effect is clearly evidenced with a continuous down shift of the resonance frequency. At resonance, it also can be noted from the E-field map that is displayed in inset of this figure, that the extrema of the modulus of the E-field are at the edge of the wider dimension of

the metal plates. In the framework of this thesis, it will be shown that that such E-field configuration is typical of resonant patch-like metal patterns.

The paper published in 2011 was entitled Electrically controllable fishnet metamaterial based on nematic liquid crystal [37].

In this publication, a variable *index* metamaterial was demonstrated by embedding nematic liquid crystals inside fishnet layers void at microwave frequencies. In contrast, with respect to the aforementioned article using cut wire, the authors introduced the concept of an effective properties indicating that the wave propagates within the artificial medium and are not evanescent. Indeed, in the case of single negative medium, the product of the effective permittivity ε_{eff} and of the permeability μ_{eff}, whose root square defines the index ($n = \sqrt{\varepsilon_{eff}\mu_{eff}}$), is negative. It results from this an imaginary index and hence an evanescent wave rather than a propagating wave seen in the following equation:

$$n = \sqrt{\varepsilon_{eff}\mu_{eff}} = \sqrt{-|\varepsilon_{eff}||\mu_{eff}|} = j\sqrt{|\varepsilon_{eff}||\mu_{eff}|}$$

In the dispersion diagram of such a DNG media, some bands show a left-handed character (propagation of backward waves with negative index) or a conventional band structure (positive index) termed right-handed.

In this publication, the authors showed that the left-handed pass band can be reversibly shifted from 9. 14 GHz to 8. 8 GHz with an external electric field, whereas the upper right-handed passband is nearly unchanged. It is also explained that that magnetic resonance is shifted to a lower frequency owing to the permittivity increase between fishnet structures, leading to an effective index change of 1.1 within negative index regime.

Figure 1.2.13 below illustrates the structure of the periodic array that was used for this demonstration of the tunability of the left-hand dispersion band according to the LC orientation in (a) a cross section and in (b) a 3D view of the multilayered metal LC slab and here again Teflon Fiber glass as substrates on which the metal pattern by PCB technology was structured.

The geometrical dimensions of the unit cell are quite comparable to those used in the article on short pair with W=8.00, L= 12, Px= 15, Py = 10.00 t_{LC}= 0.5 and t_s= 1.00 unit:mm). The Teflon fiberglass has a relative permittivity of 2.65 with $tan\delta$= 10^{-3}. The copper layer thickness is 0.03 mm. The same LC compound (TEB 30 A) with a moderate birefringence Δn= 0.8 at 10 GHz was employed.

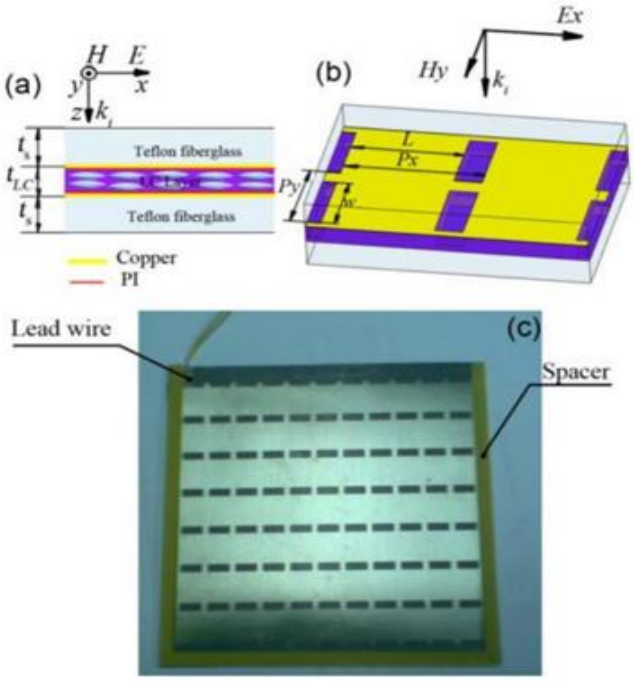

Figure 1.2.13 Side view of the multi-layered structures, 3D views indicating the relevant dimensions and photograph of the Fishnet structure designed by numerical analysis (HFSS commercial code) fabricated by conventional Printing Circuit Board technology and experimentally characterized in X band [37]

Figure 1.2.14 shows the comparison between the frequency dependence of the transmission that was calculated numerically by using the commercial software HFSS (High Frequency Structure Simulator) and the results of the characterization in free space by varying the applied voltage between 0 and 60 V corresponding to the saturation value, resulting from the relatively thick-LC layer (0.6 mm). In agreement with the electromagnetic behavior of a DNG, a pass-band transmission characteristic was achieved for both numerical and experimental data with an anti-resonance-dip/resonance peak that is a characteristic of the transmission spectra of DNG materials. Moreover, it can also be seen that the transmission loss around 9 GHz is moderate with a peak around -5 dB below the maximum of transmission that was reached around 11 GHz with quasi unit transmission level.

As for the short metal pair publication, the authors also showed the effective permittivity and permeability parameters as a function of frequency that can be retrieved from the scattering parameters. They are plotted in Figure 1.2.15 along with the effective index. In agreement with theory in the frequency band where the effective permittivity and permeability are negative simultaneously, the effective index is negative.

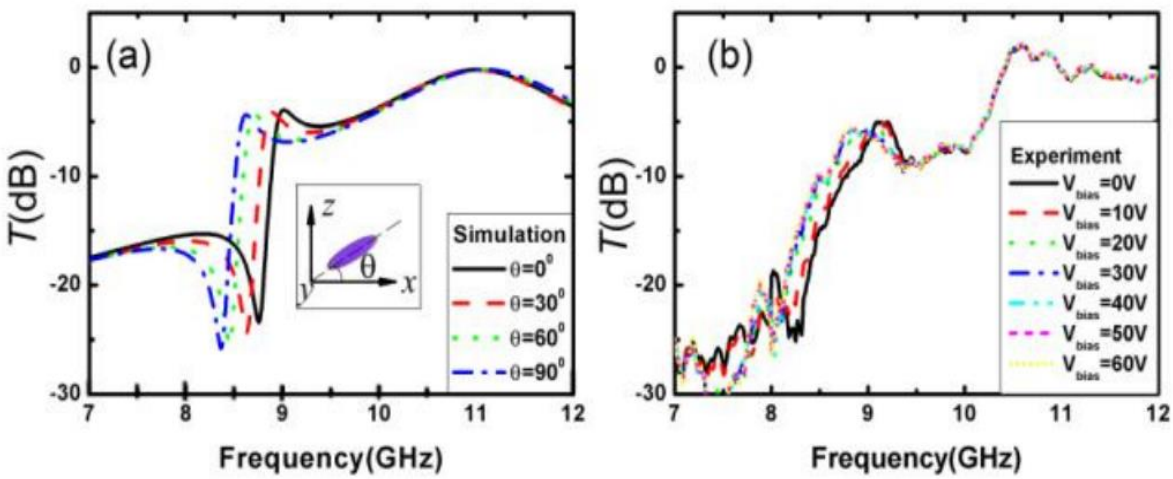

Figure 1.2.14 Comparison between numerical simulation and experiment for the fishnet structure published in [37]

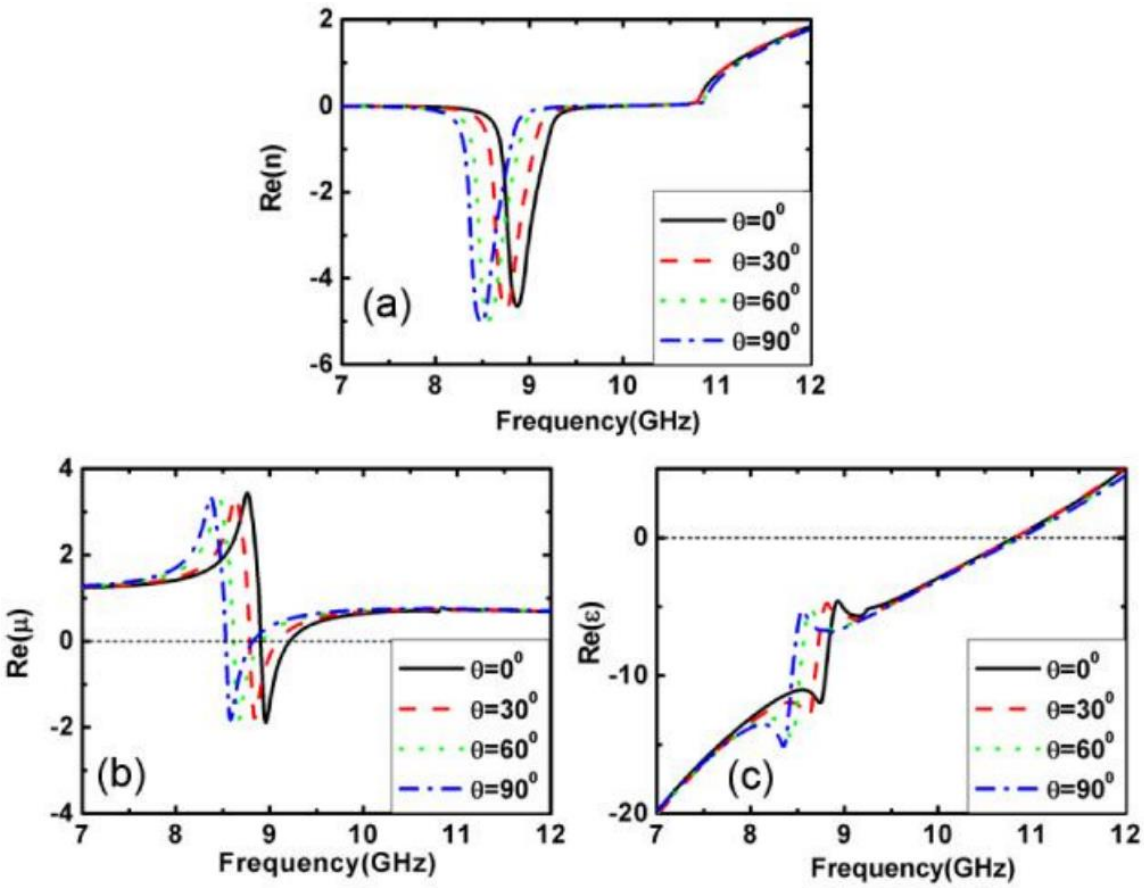

Figure 1.2.15 Effective parameters retrieved from the scattering measurements that were calculated numerically

Conclusion

In this introductory chapter, we first reported the basic concepts of Liquid Crystal technology aiming at the dynamic control of the scattering properties of electromagnetic metasurfaces. More specifically, the various possibilities to induce such a control were pointed to be via the orientation of the optical axis of high dipolar moment nematic LC either by means of an electrical driving force that results of an extremely low frequency controlling ac voltage or a high magnitude dc magnetic field. Both methods will be employed in the framework of this thesis work for experimentally determining the permittivity tensor of high anisotropy LCs and to validate the first principle of an amplitude modulator.

In the second part of this chapter, devoted to the introduction to metasurface technology, we first reviewed the various structuring techniques (EBG-PBG, Metamaterials, FSS metasurfaces) that allow tailoring the transmission and reflection coefficients and the absorption characteristics owing to the energy conservation. In particular, we showed that such a scattering parameter control can be obtained by introducing Bragg-type band gaps in the dispersion diagram or resonance effects yielding to negative value effective constitutive parameters. In a second stage, we analyzed some of the key papers published in the literature on this research field. From this brief outline, the solution of a patch-like metasurface printed onto an ultra-thin LC grounded substrate operating in a reflect array mode will be retained in the following chapters. The main objective will be to a have a first experimental assessment of the possibility to switch from a high reflectivity state to a quasi-unit absorption state by voltage controlling the LC optical axis orientation.

Chapter 2: Operating Principle and Dielectric Properties

Introduction

In Chapter 1, the analysis of some of the key articles in the field of metasurfaces (MTS) has shown the potentialities of such microstructures for the Electro-Magnetic wave front manipulation (magnitude, phase and polarization states). In particular, some proof of concepts of frequency agility on the basis of liquid crystal technology have been already reported in the literature in the microwave range essentially in a transmit array mode.

In the present Chapter 2, the condition to achieve $A \cong 1$ while *R= T=0* for a metasurface that is grounded by a uniform metal plate will be first explained, by using a Perfect Electrical Conductor (PEC). This will be demonstrated by the analysis of the literal expression of the *complex reflection coefficient* of a metasurface expressed as a function of the so-called *dissipative* and *radiative* quality factors. They are the key parameters to be optimized by seeking their equality at the metasurface resonance frequency. In addition, an analytical formula of the resonance frequency will be also proposed on the basis of a simplified description of the metasurface interaction with an impinging EM wave under normal incidence.

In a second section, it will be explained how the control of the orientation of the LC molecules yields some frequency agility in the absorbance or equivalently of the reflectance spectra. In particular, the figure of merit aiming at a *high dynamic* transition between a high to a low reflectivity state will be emphasized. In addition, the main properties of LCs 5CB and 1825, that will be used in Chapter 4 for the reflectance measurement in the Ka band (26-40 GHz) will be presented in a third section.

In a fourth section, the “low frequency range” (up to 1 GHz) dielectric characterization of the two LCs is reported. Measurements are performed in the two main directions using a high magnetic field to orient the LC optical axis (optical axis parallel and perpendicular to the measuring electric field). Results analysis gives the conductivities and the static anisotropy which is an important parameter for electrical driving.

The fifth section concerns the study of electrical driving of the LCs by performing impedance measurements (C(V) and G(V) characteristics in a *quasi-static regime* with a probing E-field in the kHz range).

And in the last section, the frequency dependence of the complex valued permittivity tensor of LC 5CB in the Ka band will be reported. They were retrieved from the scattering parameters measurements by Vector Network Analysis (VNA) by using a waveguide cell infiltrated by magnetically oriented LC 5CB molecules.

2.1 Background on a PMA MTS

2.1.1 Micro-resonator array structure

A 3-D schematic view of the Microstructure array that will be used throughout this thesis work is illustrated in Figure 2.1.1a. It consists of a dielectric substrate with a back-side uniform metal plate that suppresses any transmission. On top, a printed periodic patch-like resonator array appears more suitable than other patterns notably this making used of the so-called split ring resonator (SRR) array in the framework of Electrically controlled LC technology. For polarization insensitivity to a plane wave impinging on the metasurface *square-shaped* patches arrayed with a *square lattice* were chosen. However, it is worth-mentioning that the design rules deduced here on the basis on underlying physical mechanisms are quite general. They can be applied to other similar polarization insensitive patterns such as round-shaped metal patch array with a triangular lattice.

Figure 2.1.1b shows a cross-section of this structure and the relevant *geometrical* and *material* parameters. The dielectric substrate is characterized by its complex relative permittivity ($\varepsilon_r = \varepsilon_r' - j\varepsilon_r''$) with two key parameters namely its relative permittivity (ε_r') that will determine the wavelength of the *surface waves* propagating within the dielectric layer while the dielectric losses are taken into account by means of the loss tangent ($tan\delta = \frac{\varepsilon''}{\varepsilon'}$) (the tunability of the scattering parameters will be afforded by the infiltration of Liquid Crystal molecules between the top and ground metal plate). Indeed, as seen in the following, the loss tangent ($tan\delta = {Q_d}^{-1}$) will appear as one of the key settings in critical coupling criterion. Depending on the operating frequency and on the technology employed, metal losses have to be also considered. However, in the Ka band of interest here and for the macro-electronics techniques used for the manufacturing of the MTS, dielectric losses will be found as the dominant contributor.

With respect to the geometrical parameters, one of the most important parameters is the *dielectric thickness* (t_d) that plays a major role in the resonance quality, which is quantified by the radiative quality factor. The other key parameters are the gap between resonators arrayed with a period (*p*). For square-shape and square-lattice array, this distance corresponds to the *slot width* (*w*) in Figure 2.1.1b. In the following it will be seen that the array's resonance frequency varies with the inverse of the patch side noted (*a*). It will be the main degree of freedom for adjusting the resonance frequency for a given dielectric substrate defined by its relative permittivity (ε_r'). For parametric studies notably for multi-size patterns it is also convenient to also introduce the array pitch depending on both patch side and slot width ($p = a + w$). At last, to be quite general notably with respect to the loss terms, it can be relevant to introduce the metal layer (t_m). Most of the calculations in the

microwave regime can be conducted however by assuming a Perfect Electric Conductor (PEC) for the back-side ground plane and by assuming infinite conductivity for the micro-structured top layer.

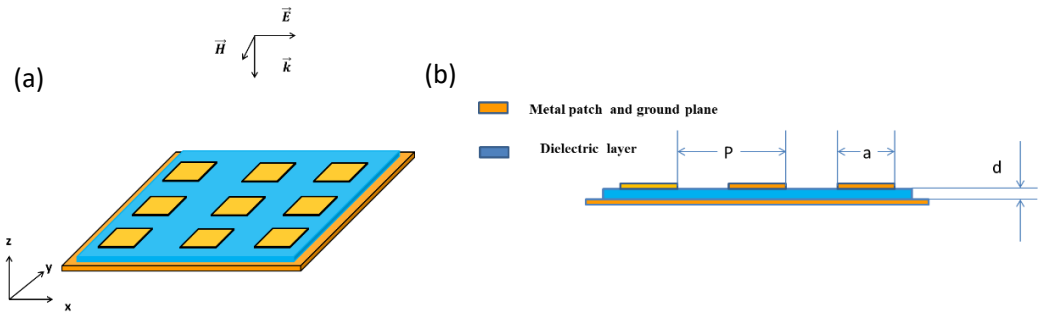

Figure 2.1.1 (a) 3D view of the square-shape and square lattice patch-type, (b) cross-section illustrating the relevant material (complex relative permittivity $\varepsilon_r = \varepsilon_r'(1 - jtan\delta)$) and the geometrical parameters with the patch side a, the slot between patches s, the period of the array $p = a + w$ and the thickness of the dielectric layer t_d

2.1.2 Scattering analysis for a plane wave under normal incidence

Let us consider that a plane wave is impinging onto the metasurface under normal incidence and hence with the $\overrightarrow{k}$ vector normal the metal layers. The incident $\vec{E}$ chosen here polarized along the **x** direction (see Figure 2.1.1a) induces charges on the top metal plate thus acting as an elementary dipole patch like antenna. For ultra-thin dielectric substrate with t_d << a, charges of opposite signs are also created on the ground metal plate. Therefore, in terms of circuit element, the dielectric slab sandwiched between the two metal plates is thus equivalent to a capacitance along the transverse direction. It results from this tight coupling, with opposite charges on the top and bottom metal plates, an *electric quadrupole* with the charge extrema at the edges of parallel plate-type structure. Such a quadrupole moment explains the formation of a current loop with antiparallel configuration of the *conduction currents* on the metal plates and *displacement current* inside the dielectric layer, as illustrated schematically in Figure 2.1.2. As a consequence, while the electric field vector shows *an out of plane* orientation, this current loop induces a magnetic dipole with an *in-plane* component. These coupling mechanisms, through magnetic and electric dipole interactions, explain the EM-field transition between a plane wave propagating in free space along the normal direction, to a *surface wave* that is now propagating along the transverse directions. The incident wave, if not fully reflected due to strong mismatch at the air/metasurface interface, is thus *trapped* in the ultra-thin dielectric layer with an in-plane Poynting vector showing a vortex-like pattern in the dielectric plane.

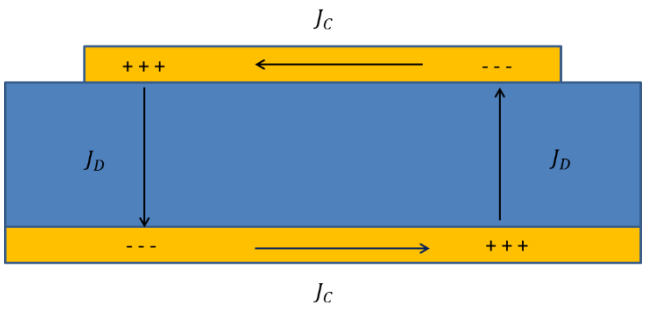

Figure 2.1.2 Illustration of a magnetic moment resulting from the excitation of electrical dipoles in antiparallel configurations in the top and bottom metal layers tightly coupled via an ultra-thin dielectric substrate.

This patch array can thus be viewed as an array of micro-antennas that allows the frequency selective trapping of the incident energy. It also allows the conversion of the incident plane wave with a normal k-vector ($\overrightarrow{k_n}$) in surface waves that are now propagating as in parallel plate waveguides with a transverse k-vector ($\overrightarrow{k_t}$).

2.1.3 Resonance condition

In a first approximation, the resonance condition will correspond to the matching of *half of the wavelength* of the EM wave propagating in a parallel plate waveguide configuration as seen before. The propagating structure is however segmented with slotted metal plates yielding to *localized surface waves*. Therefore, one can see the resonance mechanism as a surface wave *propagating back and forth* in the transverse directions that was initially determined by the E-field polarization in each elementary micro-resonator. This explains the choice of square patterns with equivalent relevant dimensions in the parallel directions. On the other hand, it can be noted that the polarization properties of the reflected wave could also be tailored for instance by using rectangular rather than square patterns.

The parallel plate propagation mode is illustrated in Figure 2.1.3 for half of the guided wavelength $\left(\frac{\lambda_g}{2}\right)$ equal to the side of the patch a. Extrema of the out-of-plane Electric field (here along the z direction) and maxima of the in-plane magnetic field are achieved at the edge of the patch.

Using the resonance criterion $\frac{\lambda_g}{2} = a$ the resonance frequency condition can be written:

$$f_0 = \frac{c}{2a\sqrt{\varepsilon_r'}}$$

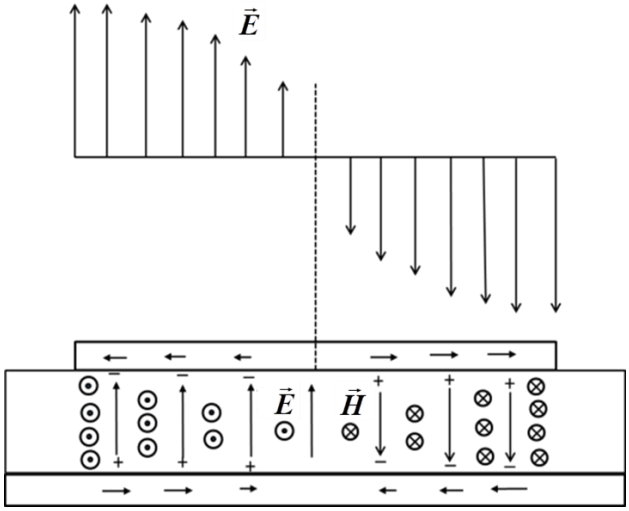

Figure 2.1.3 Schematic illustration of the EM field pattern for an EM wave trapped within the parallel metal plate structure under the patch.

The wave is propagating back and forth along the transverse direction explaining the half-wave length matching of the guided wave to the patch side.

This round trip of the EM wave explains how the energy is dissipated within the ultra-thin dielectric layer as it is the case in the so-called low profile Perfect Metamaterial Absorbers (PMA) in contrast to bulky conventional absorbers such as the Salisbury or Jauman screens.

On the other hand, as the resonance frequency is inversely proportional to the square root of the dielectric permittivity, it can be understood how to dynamically tune this resonance frequency using a Liquid crystal (LC) dielectric slab. Indeed, the effective permittivity 'seen' by the transverse electric field with transverse components can be varied by controlling the orientation of the elongated LC molecules with different values of the permittivity tensor along the ordinary and extraordinary directions. Due to the out-of-plane E-field configuration illustrated in Figure 2.1.3, the permittivity tensor term 'seen' by the EM wave corresponds to the orientation being normal to the metal plates. Hence, by changing the LC molecule orientation, the permittivity value used in the resonance frequency expression corresponds either to $\varepsilon'_{\perp}$ or $\varepsilon'_{||}$ of the LC permittivity tensor.

2.1.4 Complex reflection coefficient

The basic equation that gives the reflection coefficient noted by *r* is [1-3]:

$$r = -1 + \frac{2/\tau_r}{-j(\omega - \omega_0) + 1/\tau_a + 1/\tau_r}$$

In this expression, τ_a and τ_r are the *lifetimes* of the EM waves due to *absorption* inside the micro-resonator and *radiation* to the far field respectively. One can interpret τ_a and τ_r as the characteristic times of the dissipation process of the energy strictly confined in a closed resonator and of the radiative mechanism that allow the EM wave to *escape* from the micro-resonator.

If the resonant system is weakly coupled to its environment, the characteristic time τ_r is very long. In the limit $\tau_r \to \infty$ and hence ${}^{1}/_{\tau_r} \to 0$, one finds $r = -1$ (the microstructure metasurface is equivalent to a uniform metal plate). In that case, whatever the dissipation term and the operating frequency are, one finds the characteristic unit modulus with a phase shift of π of the reflected wave on a uniform metallized plate.

If there is no intrinsic dissipation source with thus $\tau_a \to \infty$, the incident wave is again fully reflected since there is no means to absorb the incident energy that cannot be transmitted on the other hand owing to the back-side metal plate.

For a direct application of this formula notably on the basis of the material properties, it can be more convenient to introduce the quality factors as:

$$Q_d = \frac{\omega_0 \tau_a}{2} \qquad \text{(Dissipative)}$$

$$Q_r = \frac{\omega_0 \tau_r}{2} \qquad \text{(Radiative)}$$

Where ω_0 is the resonance angular frequency ($\omega_0 = 2\pi f_0$), recalling that the dimensionless quality factors are defined as the ratio of the energy stored and of the energy lost in the system during one cycle. For strict confinement in a closed dielectric resonator, this ratio does not depend on geometrical parameters (same volume for the calculation of the energy stored and dissipated). In that case the Q factor is simply related to the material properties with $Q = (\tan\delta)^{-1}$.

As a function of the quality factors (Q_d, Q_r) and of the resonance angular frequency (ω_0), the complex reflection coefficient can be written as:

$$r = -1 + \frac{Q_d}{\frac{Q_d}{2} + \frac{Q_r}{2} + jQ_r Q_d \left(\frac{f_0}{f} - 1\right)}$$

At the resonance frequency ($f = f_0$) the reflection coefficient has no imaginary part and reads:

$$r = -1 + \frac{Q_d}{\frac{Q_d}{2} + \frac{Q_r}{2}}$$

Or expressed in terms of lifetime:

$$r = -1 + \frac{2/\tau_r}{1/\tau_a + 1/\tau_r}$$

From these equations, one can note that satisfying the resonance condition *is a necessary condition* for the cancellation of the imaginary part of reflection coefficient but *not sufficient* to achieve $r = 0$.

In contrast for the so-called *critical coupling* condition $Q_d = Q_r = Q$ or in terms of lifetimes $\tau_a = \tau_r = \tau$, one finds:

$$r = -1 + \frac{Q}{\frac{2Q}{2}} = 0$$

$$r = -1 + \frac{2/\tau}{1/\tau + 1/\tau} = 0$$

At this stage, it can be interesting to discuss of the resonance broadening that is related to quality factor via the following relations:

$$Q_d = \left(\frac{\omega_0}{\Delta\omega}\right)_a$$

$$Q_r = \left(\frac{\omega_0}{\Delta\omega}\right)_r$$

Where $\Delta\omega$ with index *a* or *r* defines the broadening (at 3 dB in logarithm scale or the Full Width at Half Maximum (FWHM) in linear scale) of the reflectance spectra resulting from the absorption mechanisms and from the coupling of the micro resonator to its environment. The total quality factor (Q_t) by taking these two sources of broadening into account obeys the following equations:

$$\frac{1}{Q_t} = \frac{1}{Q_d} + \frac{1}{Q_r}$$

Or equivalently:

$$Q_t = \frac{Q_d Q_r}{Q_d + Q_r}$$

When the critical coupling condition ($Q_r = Q_d$) is met one thus obtains:

$$\frac{1}{Q_t} = \frac{2}{Q_d}$$

As seen previously in the microwave regime and for generic technologies, the dielectric losses dominate. As mentioned before, the dissipation quality factor becomes:

$$Q_d = (tan\delta)^{-1}$$

And the Fractional Bandwidth (FBW) can be defined as $FBW = (Q_t)^{-1} = 2\tan\delta$.

Such an equation gives some preliminary indications on the resonance properties for a given structure whose resonance frequency can be, on the other hand, deduced from wavelength matching considerations (see the resonance frequency section). For instance, for dynamically tuned metasurfaces, as it will be considered in the following infiltrated with liquid crystal, typical loss tangent ($\frac{\varepsilon_r''}{\varepsilon_r'}$) values are $tan\delta = 2.5\times10^{-2}$ giving a fractional bandwidth ($\Delta\omega/\omega_0$) of 5 %. Aiming for a transition between a high reflective state ($|r| \cong 1$) and a zero-reflection state with total absorption ($|r|$= *0*) as discussed in introduction, this means that the frequency phase shift resulting from the dielectric anisotropy of the LC layer has to be in excess of the intrinsic broadening of the resonance.

2.2 Principle of Operation

To sum up the aforementioned considerations, based on the underlying physical mechanisms and analytical expressions of the resonance frequency and of the complex reflectivity, the front patch-like and back side uniform metallic layers form a resonant cavity. As the back ground plane cancels all transmission through it, the impinging EM wave is totally absorbed at the resonance frequency in the absence of reflection. Conduction currents are induced by the incident wave in the metal plates and displacement currents in the dielectric layer are created between the front and rear face metal layers both with an antiparallel configuration as shown in Figure 2.1.2. The resonance frequency is controlled by the *width of the patch* and the permittivity of the dielectric layer, not by the dielectric thickness which can be expressed in the following equation:

$$f_r = \frac{c}{2a_{eff}\sqrt{\varepsilon_r}} \quad (1)$$

Where a_{eff} is the effective patch side that can be determined by taking the edge effect into account (In chapter 3, these edge effects will be analyzed in detail, where they influence the resonance frequency of a few percent (< 6 %) for a ratio between the dielectric thickness (50 µm) and the patch side (2.5 mm) of $\frac{2500}{50} = 50$ and hence can be neglected in a preliminary analysis). As illustrated in Figure 2.2.1,

taking into account the edge effects depend on the thickness of the dielectric layer with respect to the patch side can be performed with the following expression $a_{eff} = a + 2h$.

In equation 1, ε_r is the real part of the complex value of the permittivity tensor that depends on the LC molecule orientation.

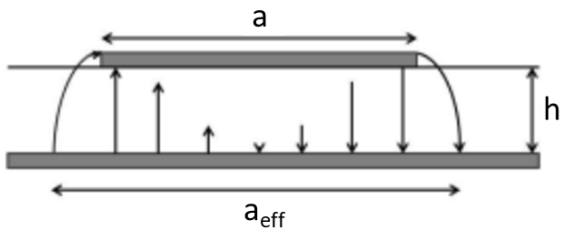

Figure 2.2.1 Illustration of the edge effects by a schematic plot of the E field map at the resonant frequency with quasi-round shaped field lines at the two edges justifying the relation $a_{eff} = a + 2h$

In practical applications, the thickness of the dielectric layer has to be limited as far as possible to minimize the LC volume, decreasing the controlling voltage and the response time during the LC molecule orientation.

In the present work, the tuning of the various cells is uniform over the whole area and not local as it would be the case for a pixelated MTS. The application of the same bias voltage to all the basic cell is realized by using a grid of very narrow (w≈150 µm) interconnection strips for avoiding coupling of adjacent patches through these interconnecting elements. This bias voltage (a low frequency (KHz) varying voltage is applied as it will be seen in section 2.4) results in an external electric field that re-orientates (homeotropic direction) the LC molecule initially aligned by surface treatment (polyimide deposition and rubbing). As a consequence of this reorientation of the molecule optical axis, the real part of the complex valued permittivity changes from perpendicular to parallel.

When the resonance effects are sufficiently selective with a full width at half maximum (FWHM) that is lower than the frequency shift induced by the LC reorientation a transition between high reflective states and high absorption states. The dynamic for this transition is directly related to the ratio between FWHM and voltage-controlled frequency offset.

Finally, to adjust the level of absorption at the resonance, it is essential to satisfy the condition of matching the impedance of the metasurface to that of air. The total quality factor (Q_{total}) is given by the following equation:

$$\frac{1}{Q_{total}} = \frac{1}{Q_{rad}} + \frac{1}{Q_{diss}} \qquad (2)$$

Where Q_{rad} is the radiative quality factor coefficient describing the coupling between the incident plane wave and the micro-resonator array which is a function of the period *(p)* and the size (*a*) of the patch and the LC layer thickness (t). Q_{diss} is the dissipative quality factor which is equal to 1/tanδ in a first approximation where tanδ that describes the dielectric losses that also depend on the orientation of the optical axis of the LC infiltrated in the metasurface.

Our first work was to show feasibility of LC tunable metasurface for reflectance applications.

2.3 Studied LC

Two LC were studied to show feasibility of LC tunable metasurface for reflectance applications.

The first one that was already generally mentioned in Chapter 1 is a commercial and largely studied liquid crystal 4-Cyano-4'-pentylbiphenyl (5CB). The phase sequence and molecular formula of 5CB are recalled in Figure 2.3.1. 5CB was chosen for many reasons. It is a commonly used - near room temperature - nematic LC and commercially available (Apollo Scientific). Its molecular structure shows a good chemical stability at the middle link having the chemical formula of $C_{18}H_{19}N$. The interesting property of 5CB is its large dielectric anisotropy at low frequency which shows us its ability to be electrically driven with moderated electric field [4]. The large dielectric anisotropy of 5CB is connected to a high $\varepsilon_{\parallel}$ due to its large longitudinal dipole moment of C≡N group (app. 4 Debye - strong). In addition, its microwave anisotropy gives us an idea about the resonance frequency shift that we are going to obtain noticing that only a few studies are performed on 5CB in the microwave frequency range.

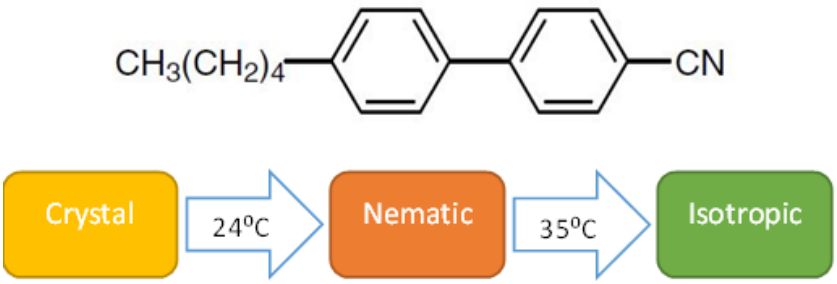

Figure 2.3.1 Phase sequence and Molecular structure of 5CB (p-n pentyl-p'-cyanobiphenyl)

The second LC is a large birefringence nematic mixture reference 1825 and synthetized at the Institute of Chemistry of the Military University of Technology in Warsaw, Poland [5].

1825 LC is a mixture of isothiocyanates (Figure 2.3.2). This mixture is nematic at ambient temperature and exhibits this phase in a very large temperature range (-12°C to 136°C). Its constituents

present a large longitudinal dipole obtained thanks to NCS polar end group and lateral fluorine groups (X) which reinforce the longitudinal dipole. Tulane groups and NCS groups increase the parallel polarizability of the molecule explaining the large birefringence of 1825 material which is the highest of a series of mixtures. This results in a large dielectric permittivity at microwave frequency corresponding to the specification for our tunable metasurfaces.

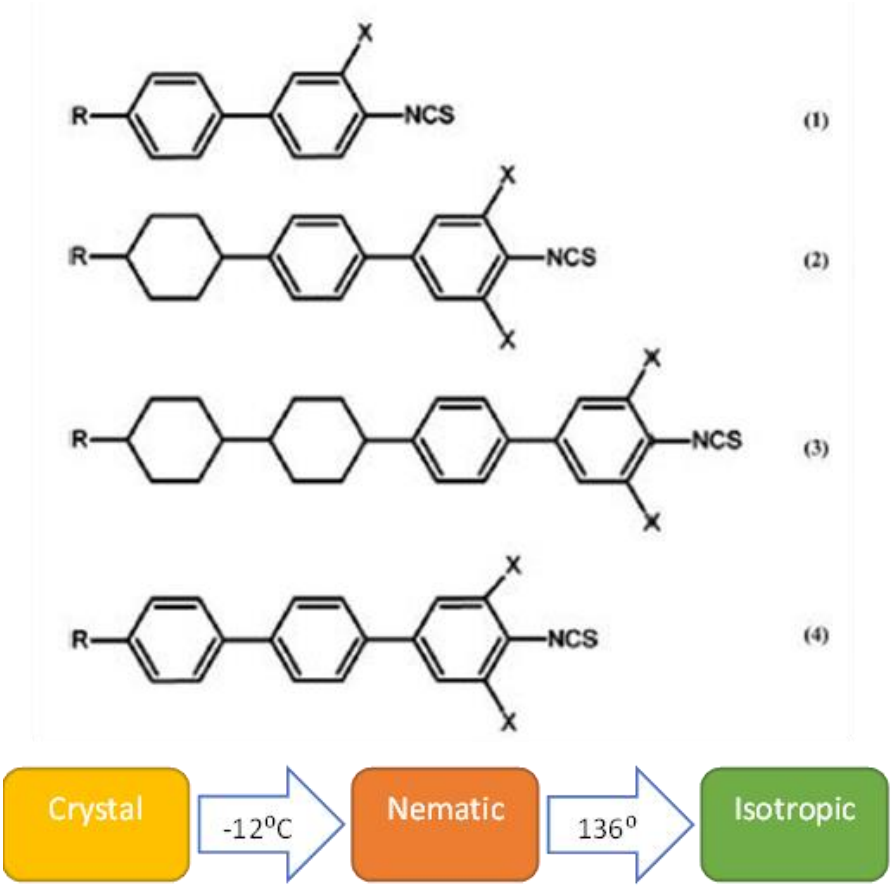

Figure 2.3.2 Phase sequence and liquid Crystal components used for the formulation of the mixture 1825.

In Table 2, we give the estimated value of different parameters of 1825 that were reported in recent papers [6][7], where it is indicated that it has an anisotropy more than 17 and a birefringence between 0.38 and 0.43 in the THz range. These values can be compared to the static anisotropy of 5CB which is 9, and having a birefringence between 0.15 and 0.22 in the THz range [8].

Reference	Frequency	$\varepsilon \parallel$	$\varepsilon\perp$	$\Delta\varepsilon$	Δn	K_{11}	K_{33}
[6]	0.5 THz	21.7	4.7	17	0.38	12.5	32.1
[7]	Infrared	25.6	5	20.6	0.43	20.1	32.1

Table 2 Reported values for some dielectric properties of LC 1825

2.4 "Low frequency" dielectric characterization

The first characterization concerns dielectric measurements of the two studied liquid crystals in the frequency range 20 Hz - 1 GHz. We successively describe the experimental set-up and the results obtained in the two main directions (parallel and perpendicular) at room temperature.

2.4.1 Experimental Setup 20 Hz – 1 GHz

As shown in Figure 2.4.1, the experimental set-up is made of two coupled commercial impedance analyzers (Keysight HP E4990A-120 and HP4192A) working respectively in the frequency range 20 Hz - 120 MHz and 1 MHz - 1.8 GHz. The switching between the two impedance analyzers is carried out using a controlled coaxial switch (SMA standard); this allows automatic measurements in the whole frequency range between 20 Hz - 1.8 GHz (8 decades). Measurements and switching between analyzers are controlled via the Agilent VEE software.

The common frequency range (1 MHz – 120 MHz) allows to check the data overlapping from the two analyzers.

For frequencies up to 1 GHz, a specific measuring cell was developed for LC dielectric characterization [9]. In order to characterize anisotropic material such as nematic LC, it is necessary to orientate the optical axis of the LC according to the measuring electric field (optical axis parallel and perpendicular to the measuring electric field). For this reason, the measuring cell is made of two planar capacitors (uniform electric field) with a thickness of about 100 µm and connected via a coaxial line (APC7mm standard, Figure 2.4.2). The capacitors constitute of the "active" part of the cell and the LC is introduced by capillarity (sample volume 4.5 mm^3). Connection between the cell and the switch output is made via a APC7mm/SMA transition. The cell is inserted in the gap of an electromagnet (Figure 2.4.1); where the available magnetic field is sufficiently high to orientate the LC molecules (1 Tesla for a 3 cm gap). The electromagnet or the cell can be rotated to obtain the two orientations.

The active part is characterized by the active capacity C_a and the residual capacity C_r (Figure 2.4.2). The values of C_a and C_r are determined from standard liquids measurements (C_a=5.46 pF and C_r=0.5 pF). After a preliminary calibration procedure (short-circuit, open-circuit and matched load (50Ω) measurements), the reflection coefficient $\rho_m(f)$ at the input of the cell is measured by the impedance analyzers. The complex permittivity is finally calculated from the admittance $Y_e(f)$ obtained after subtracting the contribution of the coaxial line:

$$\varepsilon'(F) = \frac{C(F) - C_r}{C_a} \qquad \varepsilon''(F) = \frac{G(F)}{C_a\, 2\pi F}$$

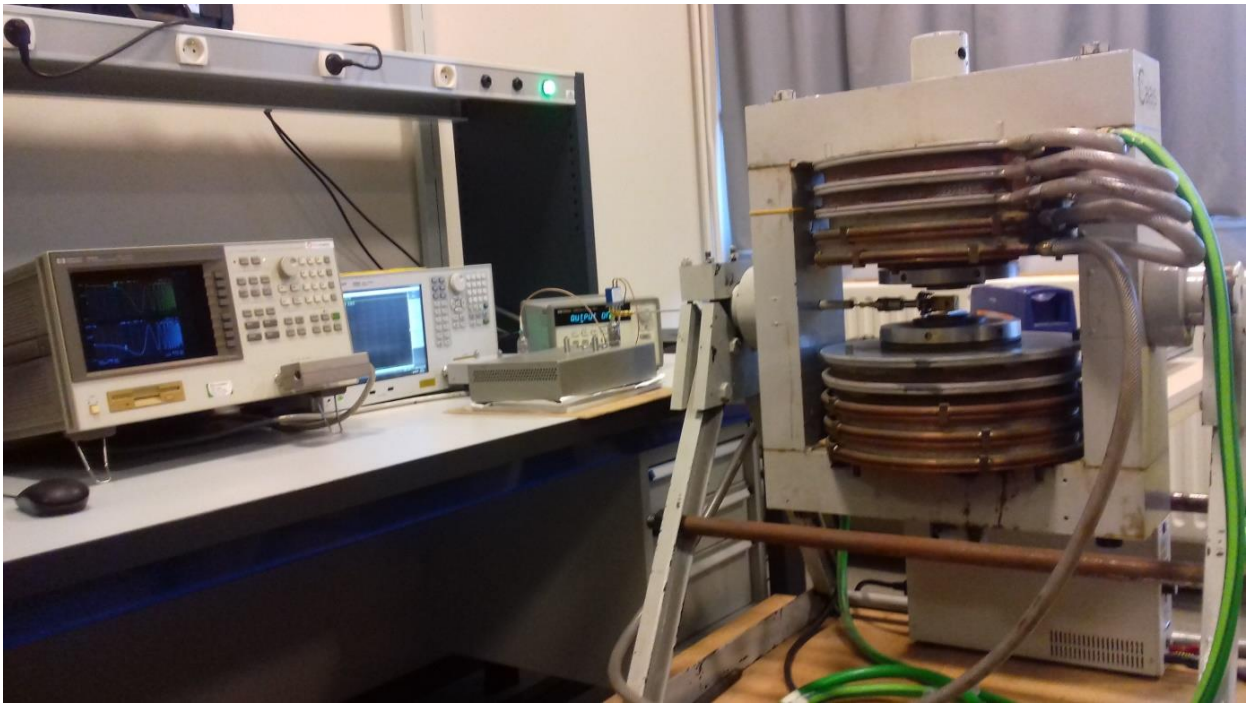

Figure 2.4.1 Experimental set-up for dielectric measurements in the frequency range 20 Hz - 1 GHz

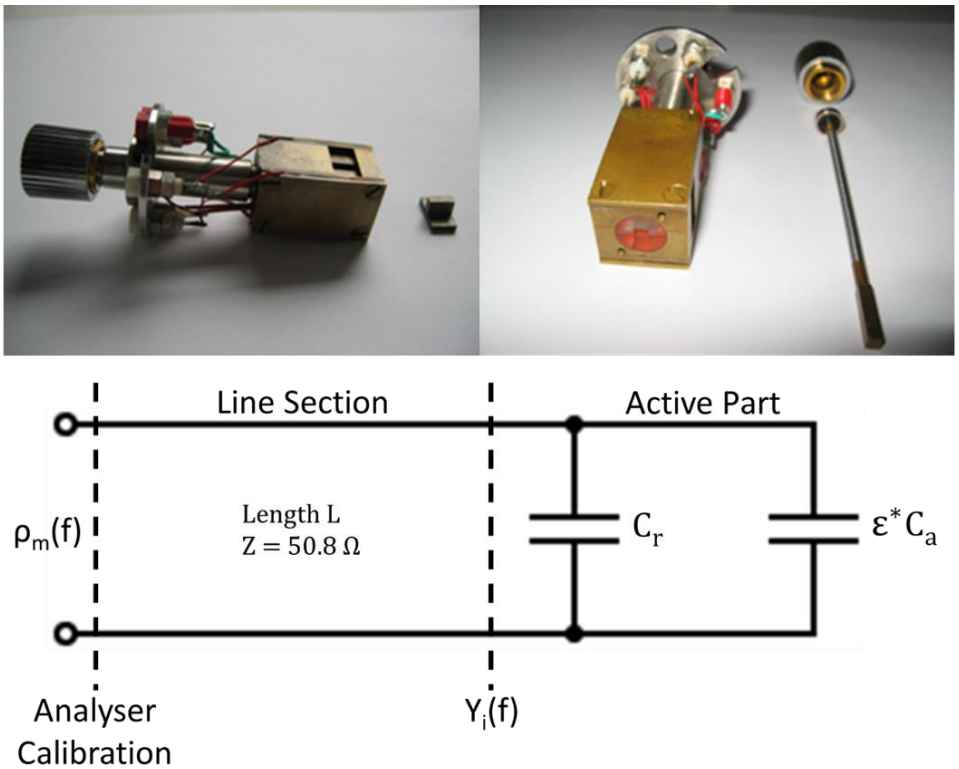

Figure 2.4.2 Experimental set-up for dielectric measurements in the frequency range 20 Hz – 1 GHz

2.4.2 Dielectric properties of studied LCs

Dielectric spectra obtained for 5CB and 1825 are compared for parallel (Figure 2.4.3) and perpendicular (Figure 2.4.4) orientations. The spectra clearly show differences between dielectric properties in the two directions due to the anisotropy. The spectra also show the different phenomena described in 1.1.3.

At lower frequencies, we can observe the contribution of ionic conductivity: the dielectric losses strongly increase with decreasing frequency with a slope -1 (log-log scale) and the permittivity increases due to electrode effect (charges accumulation at the electrodes). It is possible to deduce the static conductivities using the equation given in Section 1.1.3 where the values are reported in Table 3.

	$\sigma//$ $(\Omega m)^{-1}$	$\sigma\perp$ $(\Omega m)^{-1}$
5CB	$1.2*10^{-6}$	$1.57*10^{-7}$
1825	$8.3*10^{-7}$	$9.3*10^{-8}$

Table 3 Static conductivities for the molecules' two main orientations of the two studied LCs

One can notice that the conductivity of 1825 is lower than that of 5CB (the ratio is about 10). For both liquid crystals, the conductivity is higher in the case of parallel orientation. This positive conductivity anisotropy is generally observed in nematic LC [10].

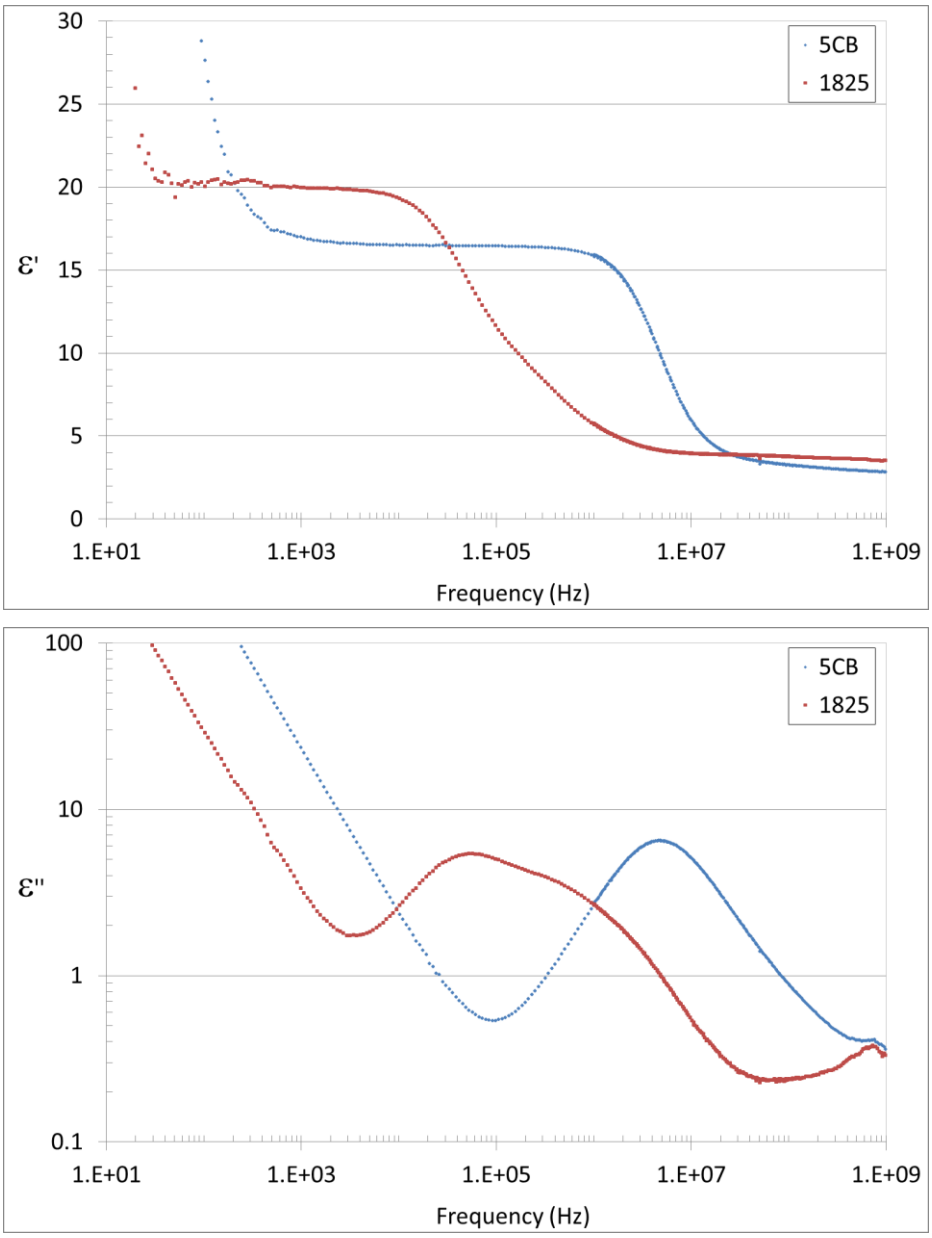

Figure 2.4.3 Dielectric spectra for the parallel real permittivities and dielectric losses of 5CB and 1825

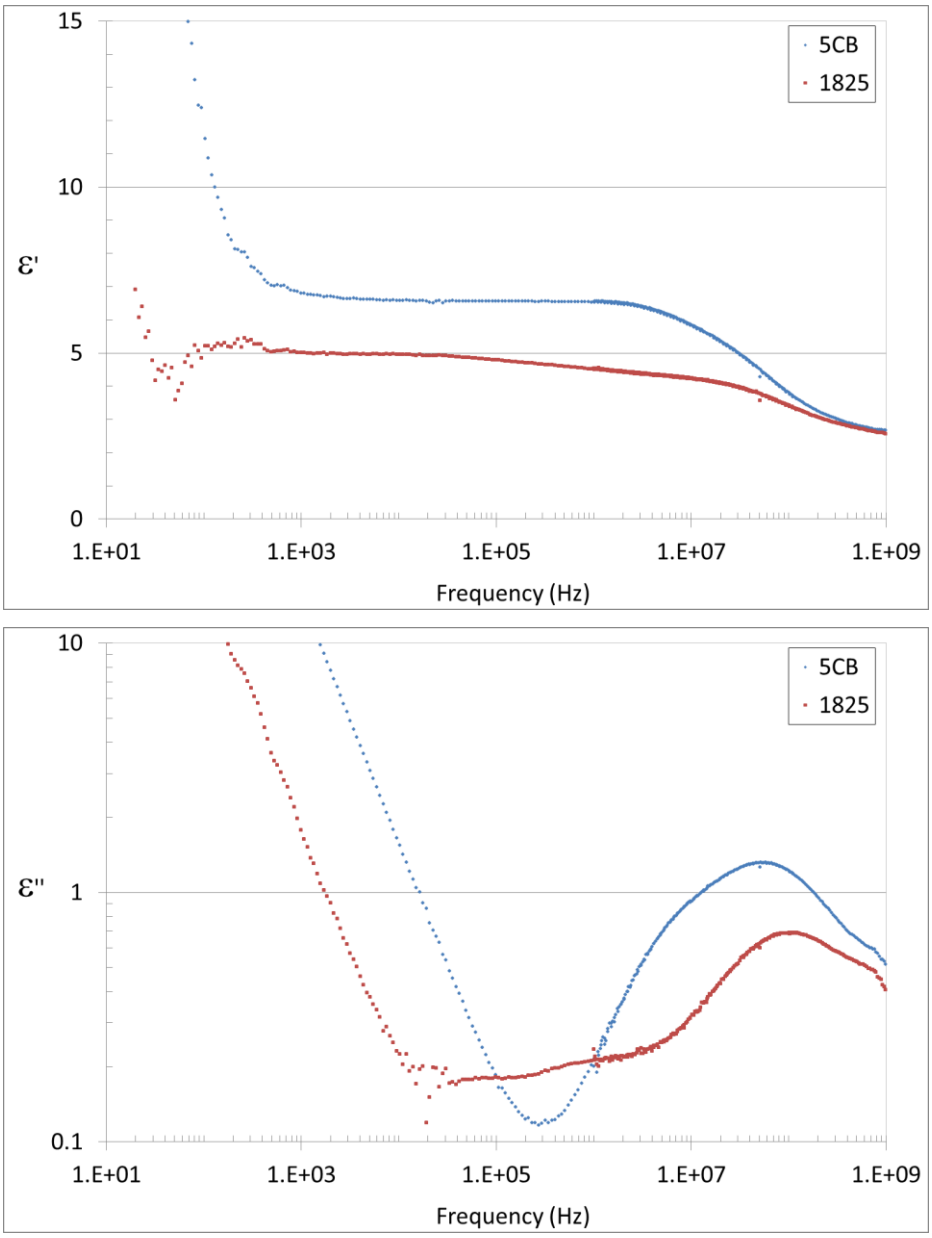

Figure 2.4.4 Dielectric spectra for the perpendicular real permittivities and dielectric losses of 5CB and 1825

On the real part of the dielectric spectra (Figure 2.4.3 and Figure 2.4.4) and at the end of the electrode effect, we can distinguish a frequency range with a constant value of the permittivity; it corresponds to the static dielectric constant. In the parallel orientation, the static dielectric constant is of 16.6 for 5 CB and 20 for 1825; the values are observed in the frequency ranges 1 kHz - 1 MHz and 30 Hz and 10 kHz respectively. In the perpendicular orientation, the permittivities are respectively 6.5 (1 kHz - 3 MHz) for 5CB and 5 (1 kHz - 30 kHz) for 1825. From these data, we can extract the static dielectric anisotropy ($\Delta\varepsilon_S$ = 10.1 and 15 for 5CB and 1825 respectively).

	$\varepsilon_{s\parallel}$	$\varepsilon_{s\perp}$	$\Delta\varepsilon_s$
5CB	6.5	16.6	10.1
1825	5	20	15

Table 4 Static permittivities and dielectric anisotropies for the two studied LCs

For frequencies sufficiently high (after the plateau corresponding to the static permittivity), the real part ε' decreases due to dipolar relaxations [10-12]:

- On the parallel orientation (Figure 2.4.3), the 5CB liquid crystals show one relaxation process visible on the real and imaginary parts of the dielectric spectra; this process was widely studied and attributed to the rotation around the short molecular axis. The contribution of the rotation around the cone is not clearly detected. The 1825 LC shows more than one relaxation process; the contributions are more visible on the imaginary part: one peak around 80 kHz and another one around 1 MHz. The different molecules constituting the 1825 mixture could explain the different relaxation frequencies.

- On the perpendicular part (Figure 2.4.4), both liquid crystals exhibit two relaxation processes. For 5CB, the critical frequencies are about 10 MHz and 100 MHz; in the case of 1825 (about 1 MHz and 100 MHz) the two frequencies are more spaced. The corresponding molecular dynamics is linked to rotations around the long axis and around the cone.

Finally, the frequency dependent dielectric properties in the two directions lead to a frequency dependent dielectric anisotropy. As shown in Figure 2.4.5, the dielectric anisotropy is largely positive and frequency independent at low frequencies (without electrode effect contribution); it becomes negative around 10 MHz and again slightly positive at higher frequencies.

The static dielectric anisotropy is used to drive the LC orientation from planar to homeotropic orientation and this induces a change of high frequency permittivity. The change in the microwave frequency range constitutes the basic parameter in microwave tunable devices [14, 15]. At 1 GHz, the anisotropy of 5CB and 1825 are respectively 0.19 and 0.96 (ratio 5).

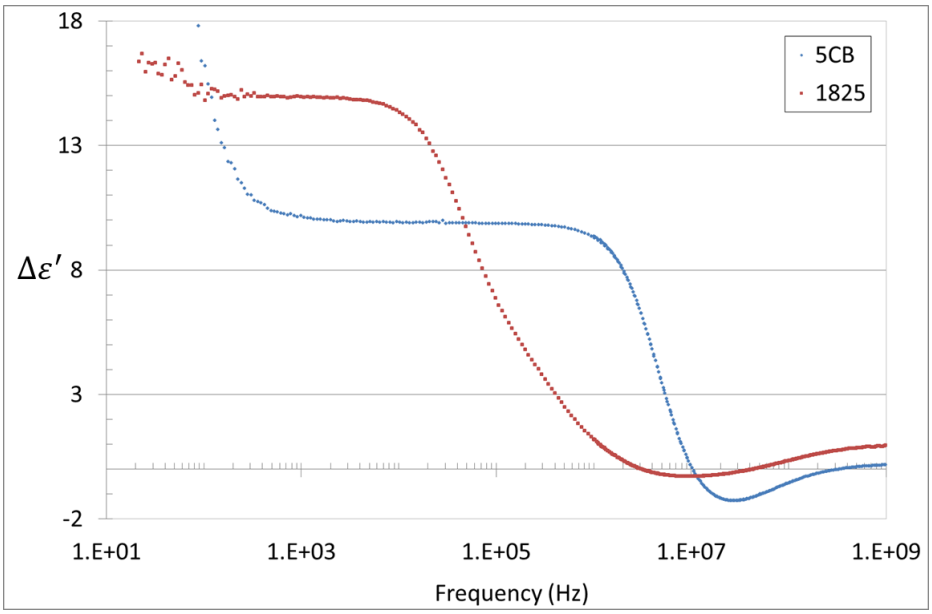

Figure 2.4.5 Dielectric anisotropy versus frequency of 5CB and 1825

2.5 Electrical driving

In this part, we studied the electric field influence on the sample orientation. Initially, the LC is in planar orientation and an electric field is applied to switch the sample in a homeotropic orientation (Section 1.1.4). In this objective, we studied the voltage dependence of the static dielectric permittivity which varies from perpendicular to parallel for voltage varying from 0 V to sufficiently high values. For this study, it's necessary to use a sinus-shaped voltage with a low frequency to avoid charge accumulation at electrodes as it is the case when using a static voltage. We describe below the experimental setup used to measure static dielectric permittivities for different voltage.

2.5.1 Experimental Setup

In this part, it was necessary to measure the impedance by varying the amplitude of the measuring voltage in a large range. For this reason, we used the HP4284A LCR meter that has a frequency range of 20 Hz to 1 MHz and a measuring voltage range of 10 mV_{eff} to 20 V_{eff}.

The LC is introduced to specific commercial cells (AWAT from Poland) to obtain the initial planar orientation (Figure 2.5.1). These cells constitute of 2 glass slides glued to each other having spacers (wires) between them to have a specific thickness. The LC molecules are initially orientated along the surface (planar orientation) which has an ITO layer used as a conductor for voltage application. ITO layers are etched so that they intersect in the center with an area of 5x5 mm, in addition to the 2 offset blades on each side for contact. The planar orientation is obtained using an

adequate surfactant (polyimide SE 130 from NISSAN Chemicals). Due the resistance in the ITO layers (10 Ohm/square) we have a limited frequency range (about 1 MHz).

The measuring cell is first measured empty for capacitance C_0, then it is filled with LC (in isotropic phase) by capillarity. This cell is placed in a specific cell holder with SMA connectors to connect it to the impedance analyzer; the cell holder is also connected to a temperature controller.

In order to acquire and analyze the data given by the impedance analyzer, the instrument is controlled via an IEEE bus using the Keysight HPVEE software. The dielectric data are calculated from the measured impedance and the equations given in Section 2.3.1. Let us notice that there is no residual capacitance C_r with the cells in the configuration used in this part; the active capacity corresponds to the empty cell capacity C_0.

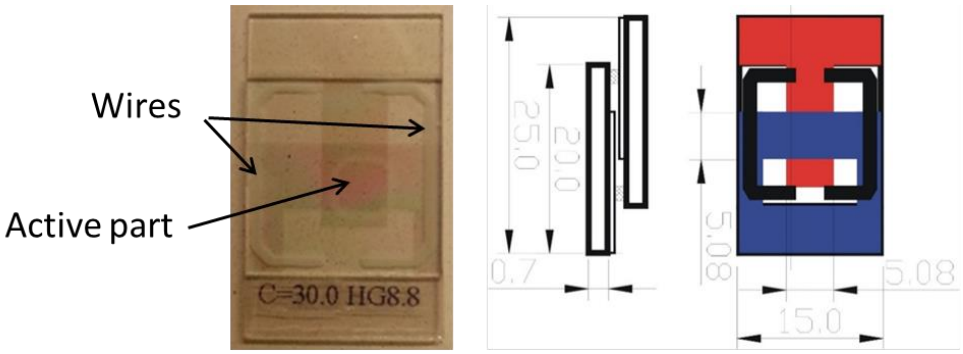

Figure 2.5.1 Schematic presentation of commercial cell from AWAT.

In order to test cells with thickness higher than 20 µm, non-commercial cells are used. They are unbuilt cells (Figure 2.5.2) that use mica as spacers and are built by hand without glue in a special cell holder that can hold the glass slabs with etched ITO electrodes and then filled with LC after placing it inside [9].

These glass slabs are thoroughly cleaned and coated with a solution of Polyvinyl Alcohol (PVA) in distilled water (from Aldrich company, 1 %/ml) as a surfactant to initially orientate the LC after rubbing and filling.

When mounted, a surface of 5x5 mm is obtained in the center with ITO on the upper and bottom sides, and is filled from the gap of the cell holder (Figure 2.5.2) which is connected by SMA connectors to the impedance analyzer.

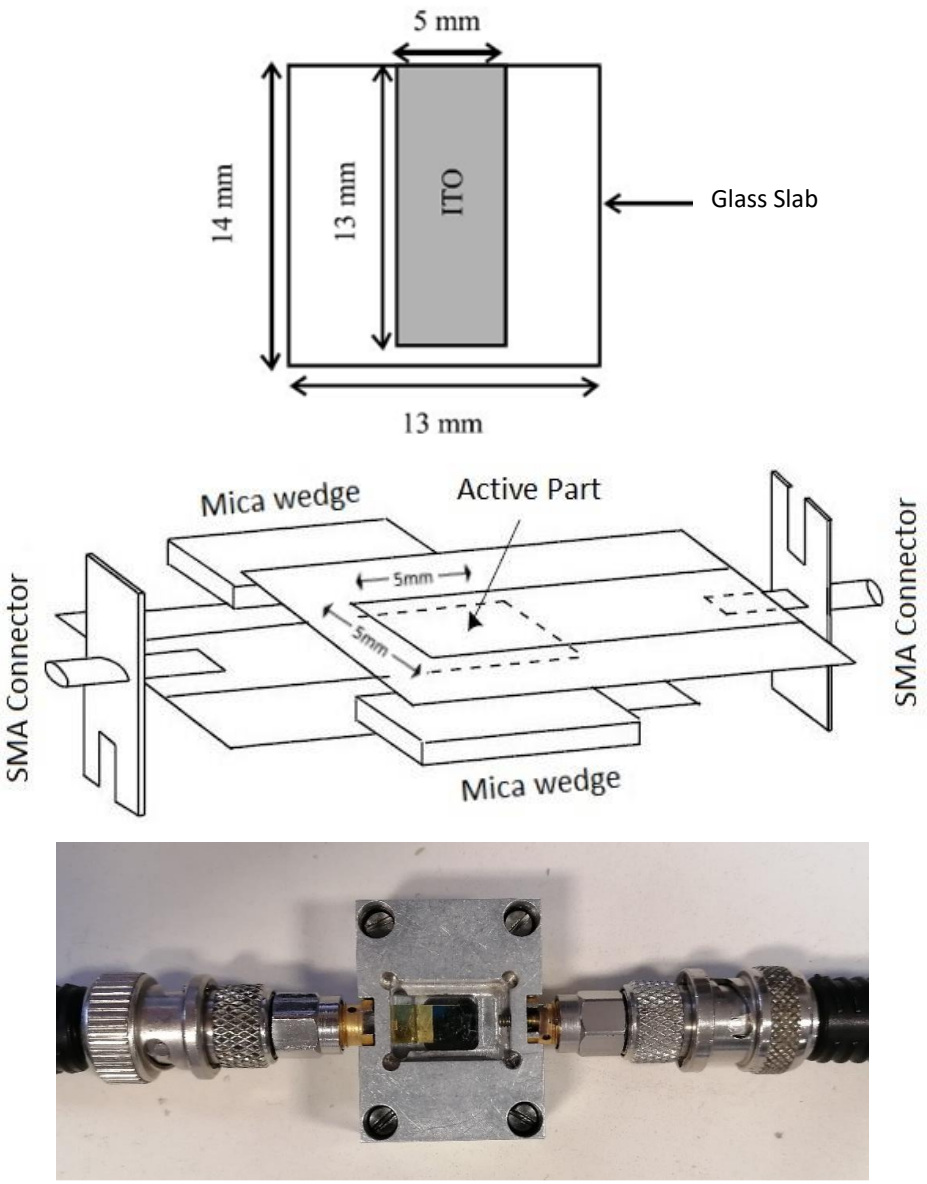

Figure 2.5.2 Schematic of the non-commercial cell and the cell after being built inside of the cell holder

Moreover, during the measurements, a polarized microscope was used in transmission or reflection modes in order to check the orientation of the LC molecules by observing the change in color that happens when applying voltage to the cells, where it becomes pitch black when fully orientating along the applied electric field.

2.5.2 Experimental results

The measurements were made for cells of different thicknesses, 5 µm, 9.2 µm, and 20 µm. These values given by AWAT were checked from the measured empty capacitance C_0 and the active surface S. As shown below, the estimated thicknesses are different from that given by AWAT. The difference is in the range 15-20 %.

	5 µm	9.2 µm	20 µm
C_0	51.5 pF	29.9 pF	13.8 pF
Estimated thickness	4.3 µm	7.4 µm	16 µm

Table 5 Measured empty capacity and estimated thickness of the different AWAT cells

The cells are filled and measured from very low voltage (100 mV_{eff}) to high voltage (20 V_{eff}) for 2 cycles at a frequency of 10 kHz. As explained in Chapter 1, we will observe progressive orientation of LC molecules from homogeneous (parallel) to homeotropic (perpendicular) orientations; this progressive switching is associated to a change of the measured permittivity (Figure 2.5.3) and a change of color observed by polarized optical microscopy (Figure 2.5.5).

The voltage dependent permittivity for 5CB is given in Figure 2.5.3 in comparison with the value in isotropic phase (obtained by heating the cell) and for a thickness of 5 µm. This figure shows that the real permittivity of 5CB is changing between 6.3 and 16.3 which results in a dielectric anisotropy of 10 with an isotropic permittivity of 10.3. For increasing voltage, the measured capacitance (permittivity) starts to increase for the threshold voltage V_{th}. To quantify V_{th}, we define it as the voltage where the initial capacitance increases by 5% of its total variation; the threshold voltage is found around 1 V_{rms} and the same for 5 µm, 9.2 µm and 20 µm (Figure 2.5.4) in agreement with Section 1.1.4. The corresponding value of elastic constant deduced from the formula given in Section 1.1.4 is K_{11}=18 pN. Similarly, we define the driving voltage V_{dr} as the voltage where the initial capacitance increases by 95% of its total variation. The driving voltage is: V_{dr}= 6.1 V_{rms} (8.6 V amplitude) for 5 µm, 9.2 µm and 20 µm.

Let's notice that no hysteresis is observed between the two measuring cycles showing that the LC returns to its initial orientation.

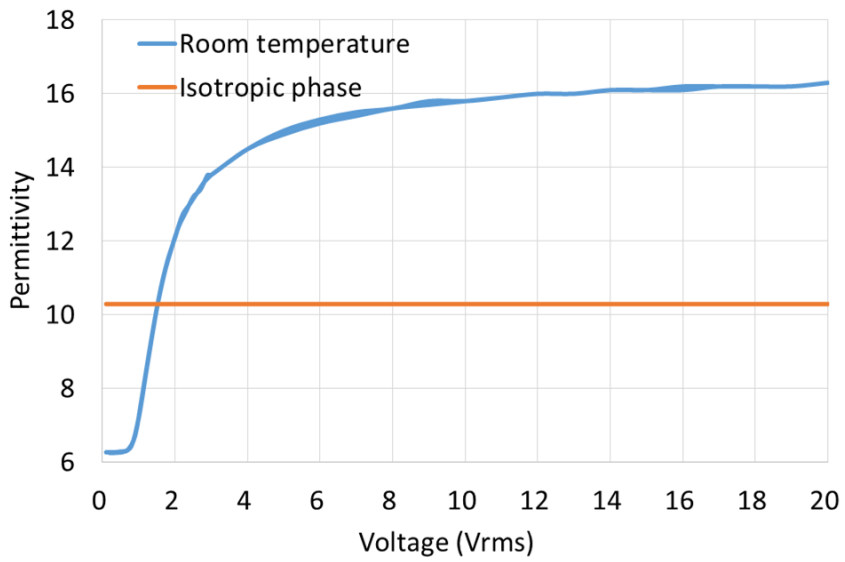

Figure 2.5.3 Evolution of the permittivity versus driving voltage for 5µm/5CB/AWAT cell

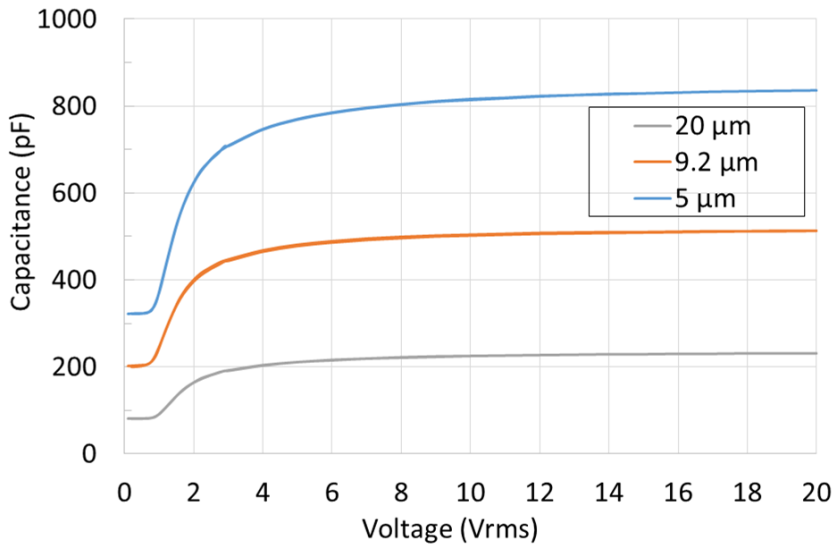

Figure 2.5.4 Comparison of the evolutions of the capacitance versus driving voltage for 5, 9.2 and 20 µm thickness 5CB/AWAT cells

In Figure 2.5.5 we can see the evolution of the reflected color from light pink to totally black indicating the change of the orientation of the LC. We can see that at the previously determined driving voltage (8.6 V amplitude), the color is black for 5 µm, dark grey for 9.2 µm. This indicates that this voltage, the LC molecules are quasi-fully orientated parallel to the applied external field. This is not the case for the 20 µm cell which becomes black at higher voltage. Let us notice that by varying the thickness of the cell, the sample color observed by polarized optical microscopy changes due to the change of intensity of reflected color wavelength.

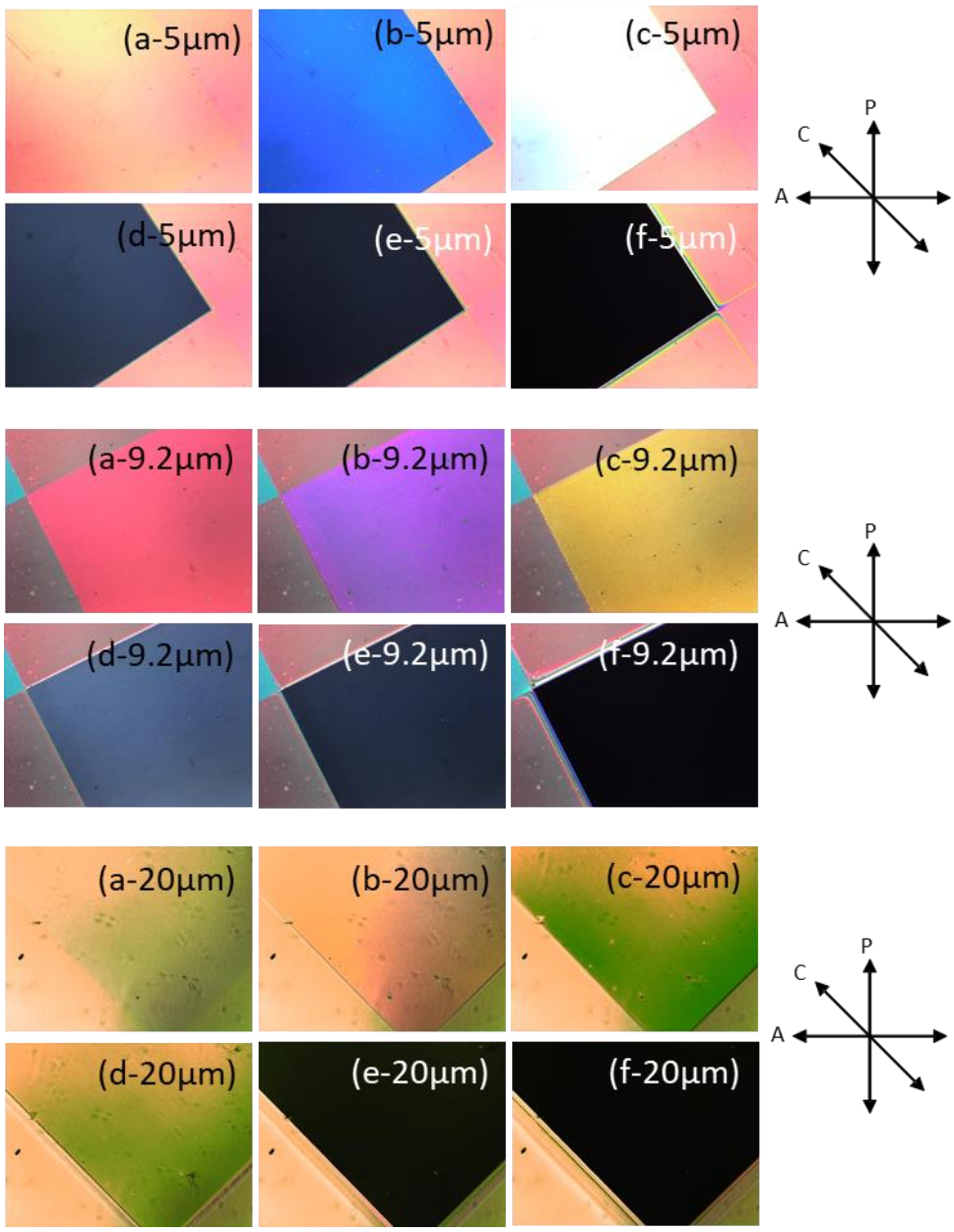

Figure 2.5.5 Optical observation under polarizing microscope of the cells 5, 9.2 and 20 µm at different driving voltages: a) 10 mVrms, b) 1 Vrms, c) 2 Vrms, d) 5 Vrms, e) 10 Vrms, f) 20 Vrms

For the 1825 LC, the voltage dependent permittivity given below (Figure 2.5.6) leads to V_{th}= 1 V, K_{11}= 27 pN and V_{dr}= 9.1 V_{eff}. These data are obtained using a commercial AWAT cell with a given thickness of 20 µm and a corresponding estimated thickness of 14.6 µm. As for 5CB, no hysteresis is observed between the two measuring cycles.

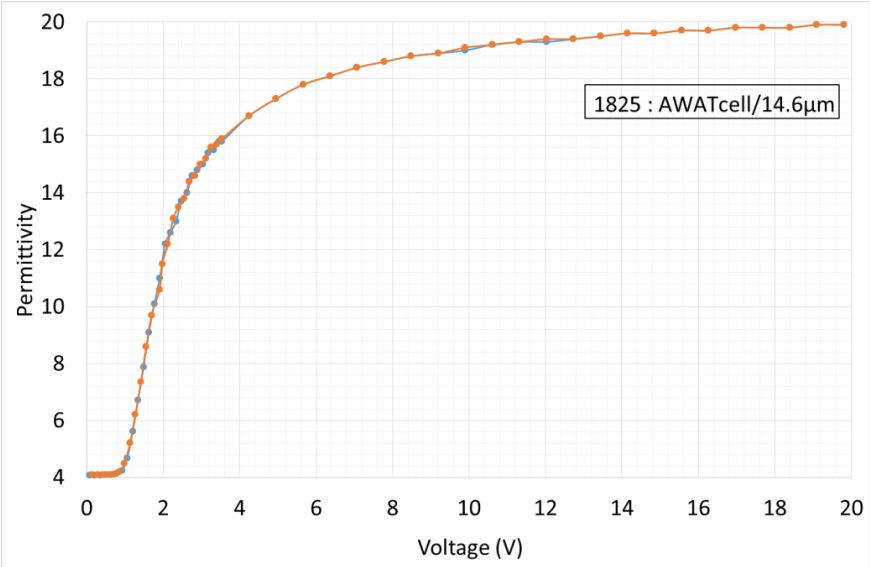

Figure 2.5.6 Evolution of the permittivity versus driving voltage for 1825/AWAT/14.6 µm cell

For 1825, in addition to measurements in commercial cells, we realized complementary measurements using cells built by hand and using mica spacers. These measurements allow to check the influence of another surfactant (PVA: Polyvinyl Alcohol) and gold electrodes that will be used for the prototypes' realization and also to test higher thickness.

For comparison with commercial cells, we first prepared cells with ITO/ITO electrodes and mica spacers (Meta fix) with thickness of 10 µm. The thickness is estimated to 17 µm from the empty capacitance. The PVA solution was prepared just before cell building and filling with 1825. This cell is called ITO/ITO/PVA/17 µm. Figure 2.5.7 shows that this built cell gives results globally similar to that obtained from ITO/ITO/14.6 µm AWAT cell (Figure 2.5.6). However, the following differences can be noticed:

- the curve starts from a permittivity value of 5 at 0 V whereas the value is of 4.1 in the 14.6 µm AWAT cell; it means that the initial orientation is not completely planar.

- the shape of the curves is different at a very low voltage: for the built cell, the measured permittivity increases progressively from 0 V while it seems to be quasi-constant up to 1 V in the case of the commercial cell.

- a small hysteresis also appears between the two measuring cycles for the built cell.

These differences can be explained by a weaker anchoring of LC molecules on the PVA layer.

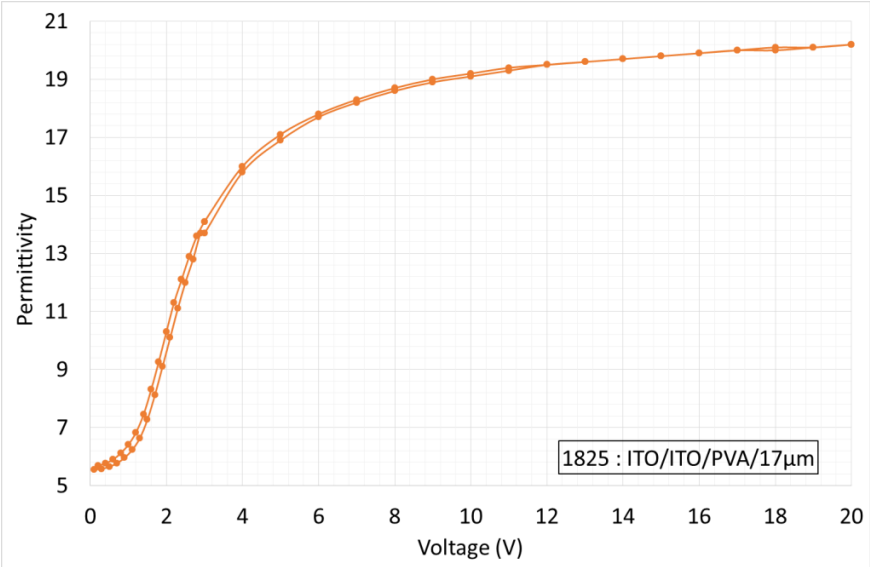

Figure 2.5.7 Evolution of the permittivity versus driving voltage for ITO/ITO/PVA/17 µm cell

On the next step, we prepared ITO/ITO/PVA/50 µm cell to check the influence of thickness higher than that available values from AWAT cells. The figure below (Figure 2.5.8) shows a behavior completely different from that observed with ITO/ITO/10 µm cell. For a thickness of 50 µm and from the first cycle, the initial value of permittivity (at 0 V) is of 6.5 and higher than that measured with 10 µm; this means that the anchoring between LC and PVA is weaker in the case of 50 µm. For decreasing voltage during the second cycle, the permittivity value obtained at 0 V is of 9; this value is higher than that obtained at the beginning of the cycle and this means that the orientation is different. This observation is in agreement with a weaker anchoring between the LC and the PVA layer whose effects are reinforced at higher thickness.

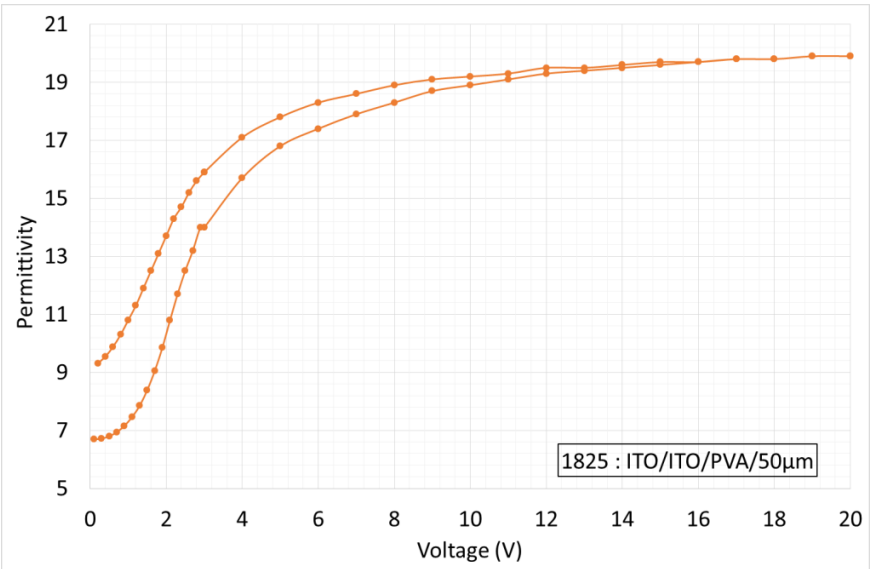

Figure 2.5.8 Evolution of the permittivity versus driving voltage for ITO/ITO/PVA/50 µm cell

Finally, we prepared a Gold/Gold/PVA/50 µm cell; except for the electrode nature, the conditions are the same as for the ITO/ITO/PVA/50 µm cell. The figure below (Figure 2.5.9) shows that the initial value of permittivity (4.5) and the permittivity after the first cycle are lower than those obtained with ITO/ITO/PVA/50 µm (6.5). This means that the PVA layer promotes the planar orientation more due to a better anchoring and this means that the gold electrode is favorable for a best effect of the PVA layer on LC planar orientation.

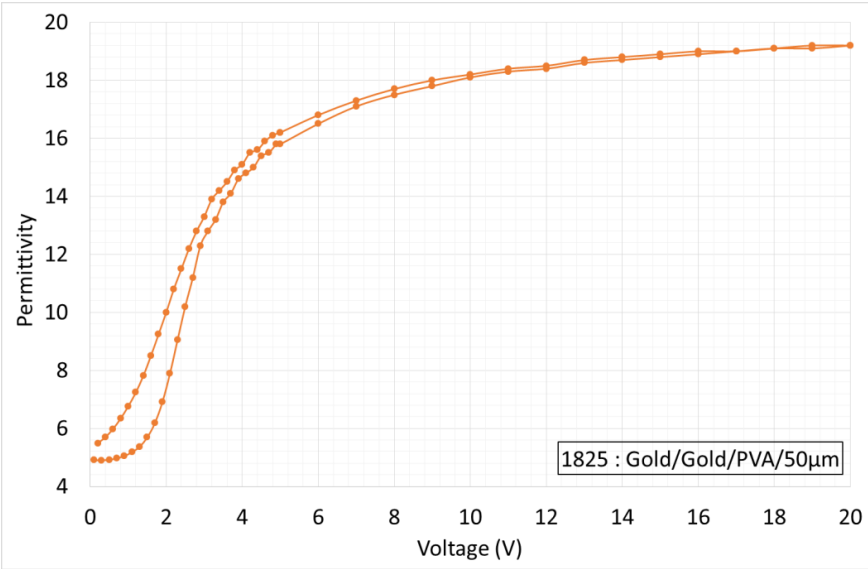

Figure 2.5.9 Evolution of the permittivity versus driving voltage for Gold/Gold/PVA/50 µm cell

2.6 Microwave dielectric measurements

2.6.1 Experimental setup and measurements procedure

Microwave dielectric measurements are based on scattering parameters measurements. These measurements are performed using a network analyzer (Keysight "AT PNA E8361C" 10 MHz - 67 GHz) in the frequency range 26 - 40 GHz (Ka band); it corresponds to the working frequency range of our prototypes presented in Chapter 4.

For the microwave dielectric measurements, we used a rectangular waveguide measuring cell filled with the sample [16]. A uniform electric field is obtained in the sample with the dominant transverse electric mode TE_{01} (Figure 2.6.1 and Figure 2.6.2). As for "low frequency measurements", the optical axis of the LCs is oriented according to the direction of the measuring electric field. For this reason, the cell is inserted in the gap of an electromagnet; the available magnetic field is sufficiently high to orientate the LC molecules (1 Tesla for a 3cm gap, Section 2.3.1). The electromagnet or the cell can be rotated to obtain the two orientations (Figure 2.6.3).

The different elements of the measuring cell are shown in Figure 2.6.1 before and after mounting. The rectangular waveguide cell has dimensions of 7.112 mm x 3.556 mm x 2.48 mm. These dimensions are sufficiently low to insert the cell in the gap of the electromagnet (gap of 3 cm). The LC is introduced to the cell through a specific slot as shown in Figure 2.6.1 by a syringe to prevent bubbles from forming. The length of the cell is 2.48 mm and the filling volume is of 63 mm^3. The cell length is sufficiently low to avoid resonance in the cell; this phenomenon can affect measurements' accuracy [17]. In addition, the use of mica spacers is indicated in the figure to close the sides of the cell gap to prevent the LC from entering the waveguide. Let us notice that the mica spacers disturb the wave propagation; to minimize its influence, we used micas of thickness 10 µm. The measuring cell is attached to the waveguides on each side, which are then connected to the network analyzer by Ka band coaxial cables and two coaxial-waveguide adapters.

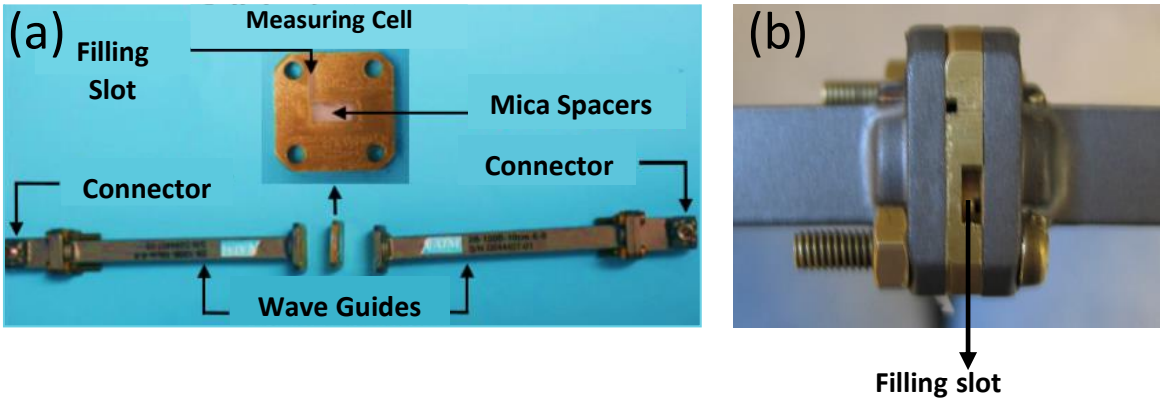

Figure 2.6.1 Different elements of the measuring cell before and after mounting

The method of extraction (described below) does not need calibration; however, we noted that some devices (especially those of recent design (since about 2000)) gave us better results with calibration with more smooth/fit curves. We believe this is due to the use of the manufacturer's algorithms, maybe to improve the dynamic measurements of the VNA. So, before the start of measurements, calibration of the network analyzer was done at the end of the waveguides; for this, the *TRL* (*Thru-Reflect-Line*) method is used and the measuring cell constitutes the *Line* in this method having a delay of approximately 8.3 ps.

In order to extract the LC microwave anisotropy, we need to do three measurements: the first measurement is the empty cell with mica spacers on each side; then the second and third measurements are made in the two orientations with the filled cell. As this explanation shows, there is no need to mount and unmount the measuring cell throughout all the experiment, making it easier to measure and decreasing the margin of error.

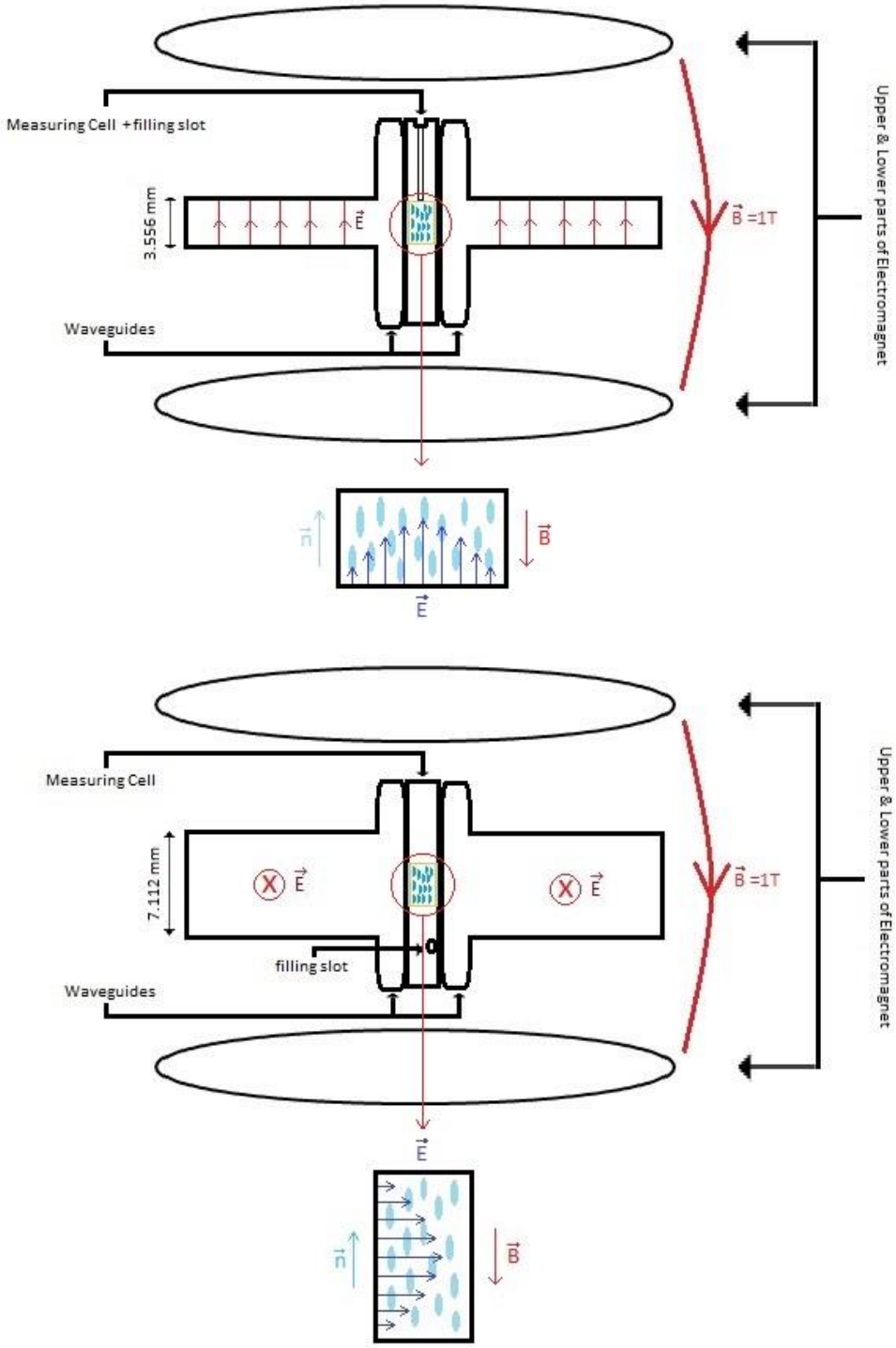

Figure 2.6.2 Parallel and perpendicular orientations of LC molecules with respect to the direction of the magnetic field obtained by rotation of the measuring cell – Electric field is in the measuring cell (TE_{01} mode)

The general experimental setup is shown in Figure 2.6.3. The whole setup is fixed in place so that we can move the electromagnet to envelope the cell after filling.

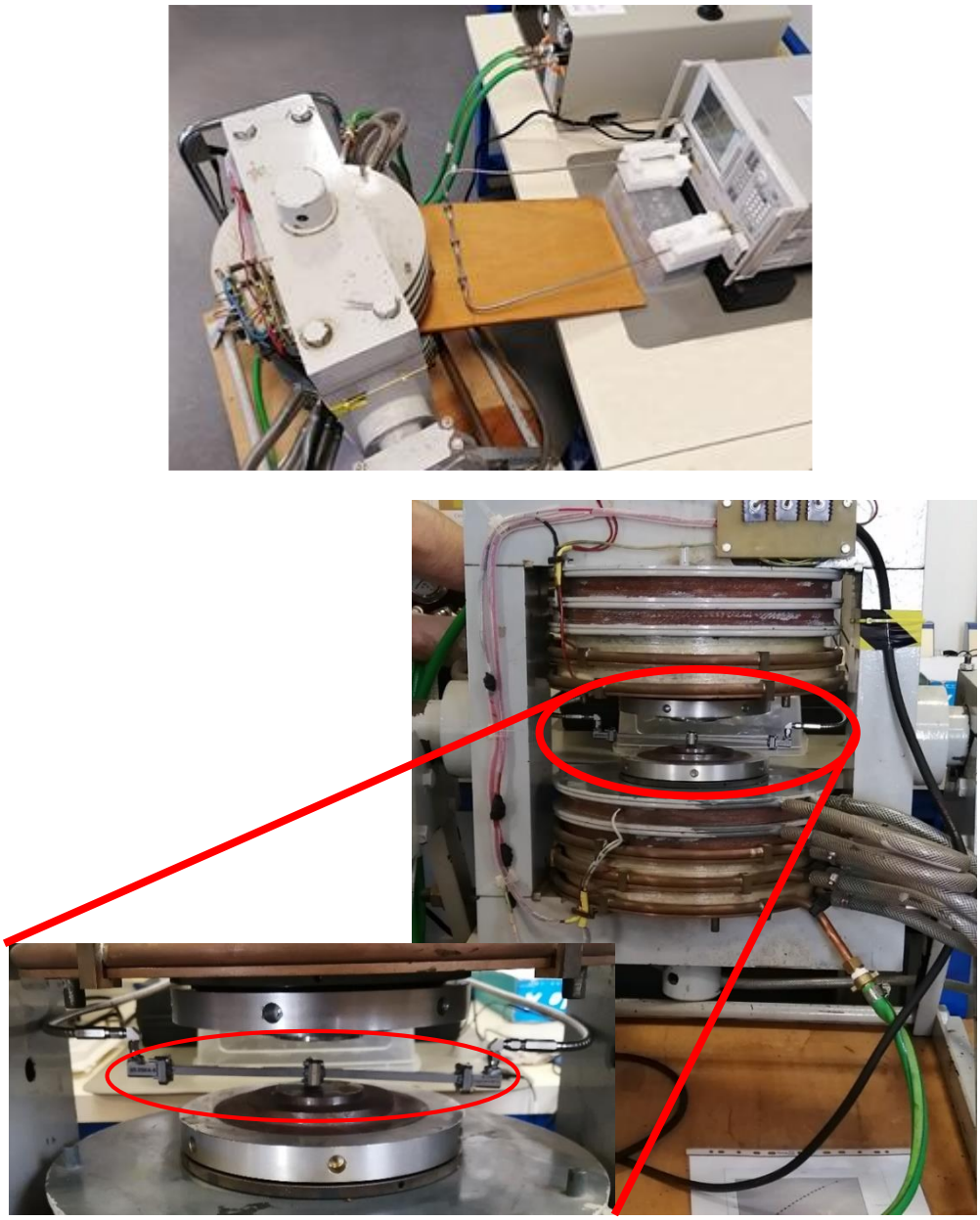

Figure 2.6.3 General microwave dielectric measurements set-up and demonstration of the measuring cell position inside the magnet

2.6.2 Method for Extracting Values

The retrieval method used to extract the complex permittivity from measured S-parameters is a method developed by N. Tentillier in his PhD thesis [16]. This method is called *Delta-Gamma* method $\Delta\gamma$ and is based on the retrieval technique published by NIST [18]; this technique is based on the use of two samples of different length but it requires mounting and disassembling.

In the delta gamma method reported below, the length *L* of the measurement cell is fixed and the propagation constant γ varies. Upon this remark, the main interest of this method is measurement without unmounting the cell.

As mentioned before, two measurements are required to use this method, first the measurement of the empty cell (measured scattering matrix S_1) and then the measurement of the filled cell with the material we want to study (measured scattering matrix S_2). The change of the propagation constant γ results from the propagation of the electromagnetic wave either in an empty or filled rectangular waveguide. This method is applied to dielectric materials; we thus assume the relative permeability value μ_r is equal to 1.

First, S_1 and S_2 scattering matrices are transformed to T_1 and T_2 transmission matrices also termed as ABCD Matrix [19] using the following transformation formula:

$$T(S) = \begin{pmatrix} -\frac{|S|}{S_{21}} & \frac{S_{11}}{S_{21}} \\ -\frac{S_{22}}{S_{21}} & \frac{1}{S_{21}} \end{pmatrix}$$

The T_1 and T_2 transmission matrices can be expressed as follow:

$$T_1 = T(S_1) = e_1 T_{vac} e_2$$

$$T_2 = T(S_2) = e_1 T_{\varepsilon^*} e_2$$

The matrix T_1 and T_2 results from the transmission matrix of the empty T_{vac} or filled cell T_{ε^*} and the contribution of errors represented by the matrices e_1 and e_2 due to connections and mica slabs; theses error matrices do not change between the two measurements as the cell is not unmounted.

The reference impedance is taken equal to that presented by the empty cell. As a consequence, the transmission matrices of the empty and filled cell are given by the following equations:

$$T_{vac} = \begin{pmatrix} e^{-j\frac{2\pi F}{c}L} & 0 \\ 0 & e^{j\frac{2\pi F}{c}L} \end{pmatrix}$$

$$T_{\varepsilon^*} = T_\Gamma \begin{pmatrix} e^{-j\frac{2\pi F}{c}\sqrt{\varepsilon^*}L} & 0 \\ 0 & e^{j\frac{2\pi F}{c}\sqrt{\varepsilon^*}L} \end{pmatrix} {T_\Gamma}^{-1}$$

With $T_\Gamma(\varepsilon^*) = \begin{pmatrix} \frac{1}{1-\Gamma(\varepsilon^*)} & \frac{\Gamma(\varepsilon^*)}{1-\Gamma(\varepsilon^*)} \\ \frac{\Gamma(\varepsilon^*)}{1-\Gamma(\varepsilon^*)} & \frac{1}{1-\Gamma(\varepsilon^*)} \end{pmatrix}$, where $\Gamma(\varepsilon^*) = \frac{1-\sqrt{\varepsilon^*}}{1+\sqrt{\varepsilon^*}}$

In the above equation, the coefficient $\Gamma(\varepsilon^*)$ corresponds to the first reflection at the interface between air and a medium of complex permittivity ε*. In addition, T_{vac} and T_{ε^*} can be calculated at each frequency *F* knowing the cell length *L* and the permittivity ε*.

We can also write: $T_2 {T_1}^{-1} = e_1 T_{\varepsilon^*} e_2 {e_2}^{-1} {T_{vac}}^{-1} {e_1}^{-1} = e_1 T_{\varepsilon^*} {T_{vac}}^{-1} {e_1}^{-1}$

This relation shows that $T_2 {T_1}^{-1}$ and $T_2 {T_{vac}}^{-1}$ are similar matrices; so, as a consequence, these two matrices have same eigenvalues, same eigenvectors and same determinants.

The resolution of the previous equation consists of varying the complex permittivity ε* to make the matrix $T_{\varepsilon^*} {T_{vac}}^{-1}$ similar to $T_2 {T_1}^{-1}$; this calculation is performed numerically using appropriate methods and software.

The previous equations are valid for TEM propagation. As mentioned before, we use rectangular waveguide cells, so we have to take into account the dispersion characteristics of the dominant TE_{10} propagation. The determined complex permittivity is an effective value $\varepsilon_{eff}{}^*$, the complex permittivity of the material is given by:

$$\varepsilon^* = \left[1 - (\frac{\lambda_0}{\lambda_c})^2\right] \varepsilon_{eff}^* + (\frac{\lambda_0}{\lambda_c})^2$$

λ_0 and λ_c are the vacuum wavelength and cut-off frequency of the propagated mode.

We used Mathcad software for all the iterative mathematical treatment.

2.6.3 Microwave complex permittivity and anisotropy of studied LC

An example of calibrated S parameters obtained for the empty and the filled cell for the two orientations of the LC is given in Figure 2.6.4. The frequency evolutions of reflection and transmission coefficients are those classically obtained for low losses dielectric material [17].

The extracted permittivities and losses for the two LCs are given in Figure 2.6.5.

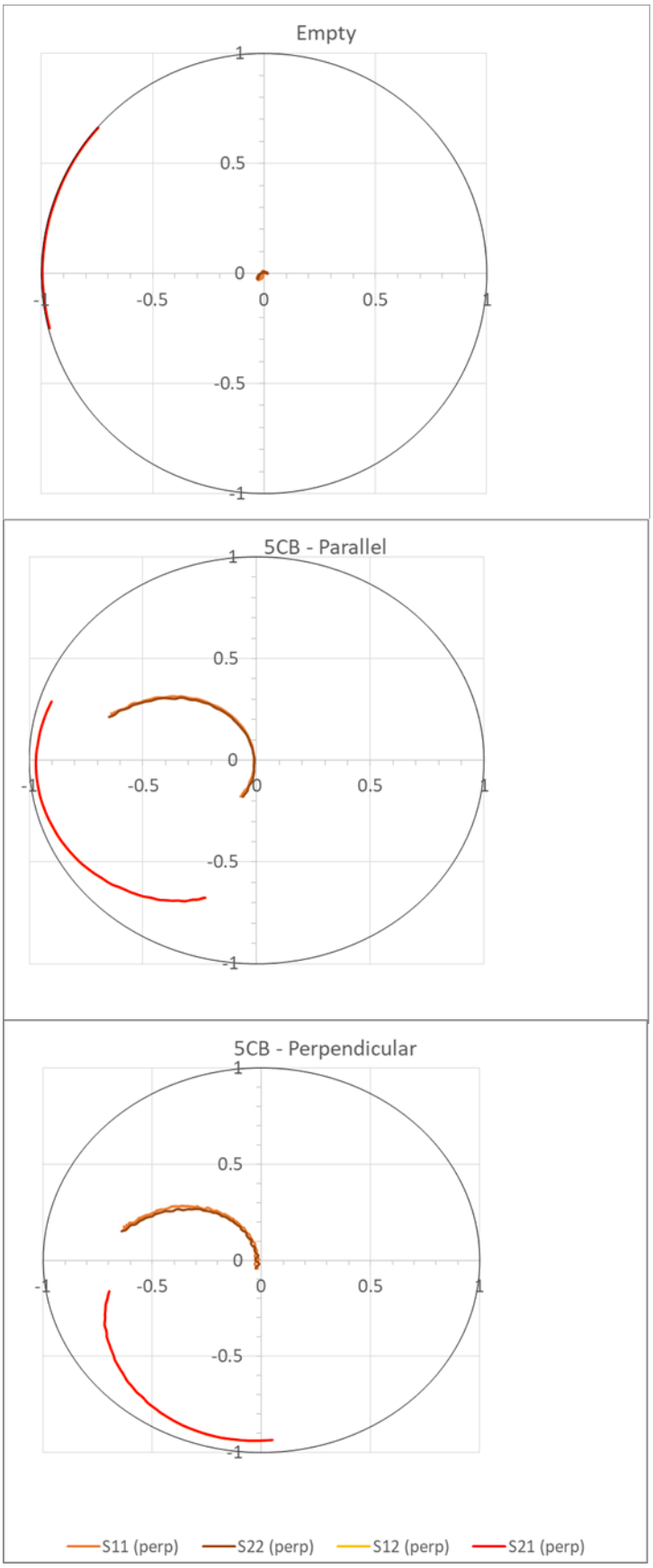

Figure 2.6.4 The measured S-parameters of the measuring cell while being empty and when filled with 5CB while having perpendicular and parallel orientations (calibrated measurements)

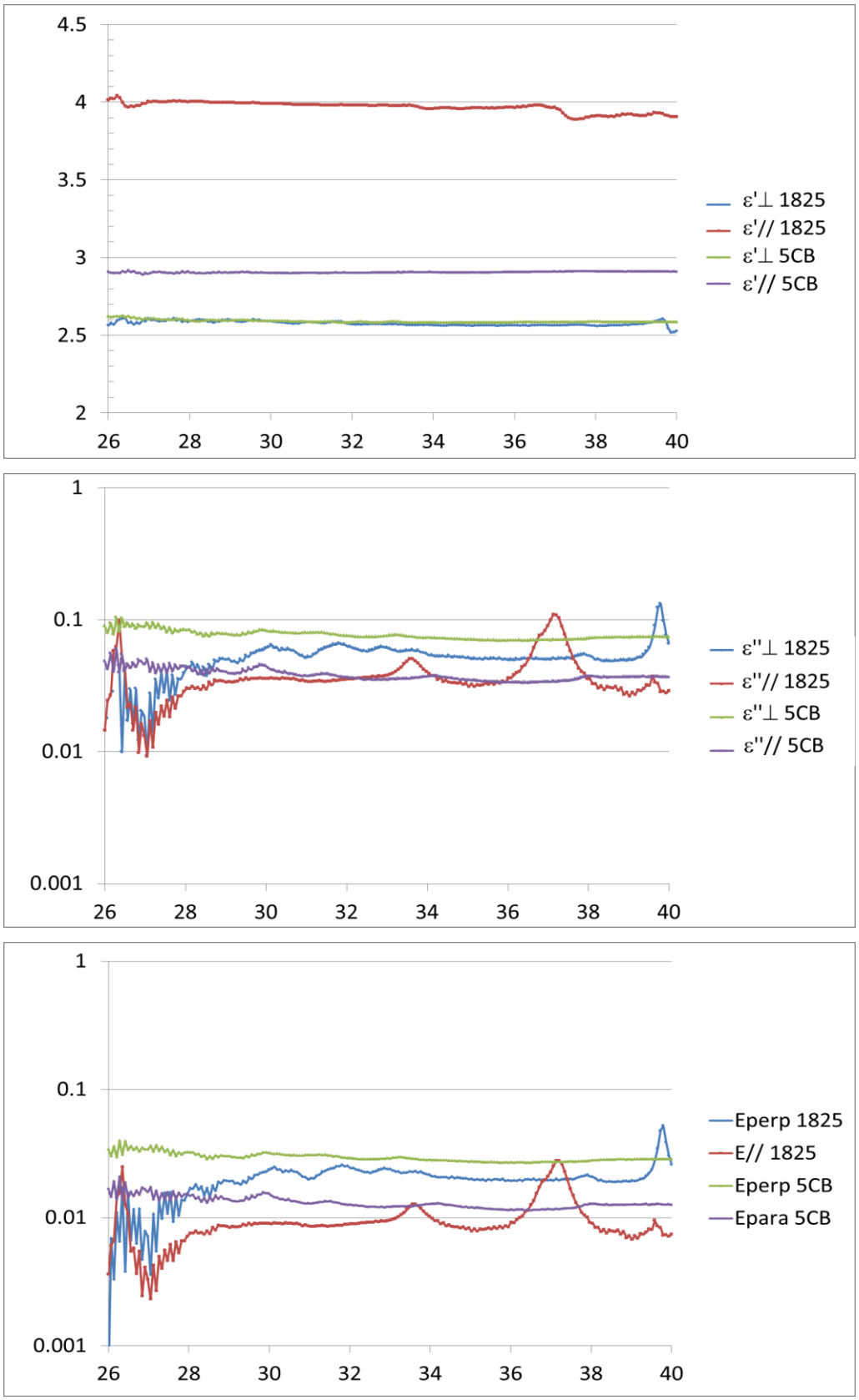

Figure 2.6.5 Extracted complex permittivity with respect to frequency with (a) the real part of ε_r^* and (b) the imaginary part of ε_r^* and (c) the loss tangent $\frac{\varepsilon''}{\varepsilon'}$.

The experimental results show that dielectric permittivities are frequency independent and are much lower than static permittivities. The $\varepsilon'_{\perp}$ permittivities of the two liquid crystals are the same. The losses are small ($\varepsilon'' < 0.1$) and the perpendicular losses are two times higher than parallel losses (negative losses anisotropy).

Contrary to low frequency range (F < 1 GHz), there is no observed relaxation process in the microwave region. Very slight decreases of the permittivities and losses are observed in the measurement frequency range (excepted for the $\varepsilon'_{\perp}$ permittivity of 5CB). They can be attributed to the "end" of low relaxation process contribute to the complex permittivity in the microwave frequency range. This explains the behavior observed for 5CB and 1825 LC.

The frequency evolutions of the microwave dielectric anisotropy are compared for the two LCs in Figure 2.6.6. The microwave anisotropy of 5CB slightly increases. This is explained by the small decrease of $\varepsilon'_{\perp}$ whereas $\varepsilon'_{\parallel}$ is frequency independent. This is not the case for the microwave anisotropy of 1825 which is frequency independent in all the frequency range.

The tunability factor for a material is defined by the ratio of the dielectric anisotropy and average permittivity: $t = \frac{\Delta\varepsilon'}{\overline{\varepsilon}}$ with $\overline{\varepsilon} = \frac{\varepsilon'_{//} + 2\varepsilon'_{\perp}}{3}$

An important result in terms of tunability is that the microwave dielectric anisotropy of 1825 is about 4.5 times higher than that of 5CB.

The tunability factor of 1825 is 46% that is four times higher than this of 5CB (Table 6).

This microwave anisotropy can be used to manipulate the resonance frequency with electrical driving by taking into consideration that the resonance frequency is inversely proportional to the square root of the permittivity. The relatively low dielectric losses observed in the two directions is also of interest for our applications especially for reflectivity modulation due to the frequency resonance shift. Too low losses would degrade absorption and high losses degrade the selectivity.

The extracted permittivities and losses in the microwave range for the two LCs are given in Table 6.

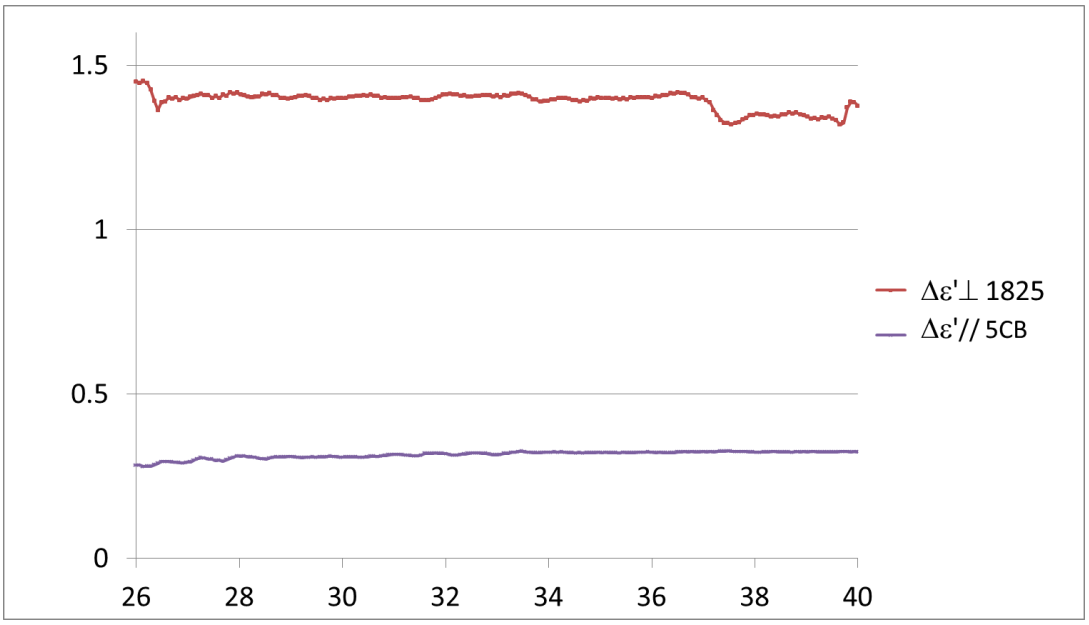

Figure 2.6.6 Microwave dielectric anisotropy of 5CB and 1825 versus frequency

Liquid crystal	$\varepsilon'_{\parallel}$	$\varepsilon'_{\perp}$	$\Delta\varepsilon'$	$\tan\delta_{\parallel}$	$\tan\delta_{\perp}$	$\Delta\tan\delta$	$\overline{\varepsilon'}$	t (%)
5CB	2.9	2.59	0.31	0.012	0.029	-0.017	2.7	11.5
1825	3.98	2.57	1.41	0.0095	0.024	-0.0145	3.04	46.4

Table 6 Extracted data from the microwave dielectric characterization of 5CB and 1825

Conclusion

This chapter consists of two parts. The first one was devoted to the study of the electromagnetic properties of a patch-like grounded (rear uniform metal plate) metasurface with notably the determination of the literal expression of the complex-valued reflection coefficient. The relevant dimensions (patch side and inter-patch gap) along with the key material parameters (real permittivity part and loss tangent of the LC compounds) were pointed out by targeting a unit absorption at the resonant frequency of the periodic patch array. It was shown that the singular properties afforded by structuring the composite metal-dielectric tri-layered structures on a sub-wavelength scale is not a related to Bragg effect but to the electromagnetic response of the elemental patch element (in other words, the array period determines the inter-patch gap and hence the coupling of the electromagnetic wave to the micro-resonator array). Also, despite the fact that we will focus our attention in the next chapter on the modulus of the reflection coefficient via reflectance spectra measurement, the analysis of the argument of the reflection coefficient reported here will also help us for a depth analysis of the surface impedance of the array that has to be matched to the free space based on a transmission line approach and that is reported in Chapter 3.

The second part concerns the experimental study of the dielectric properties of the two nematic compounds that were used in the present work for controlling the metasurface. The originality of this section with respect to the literature is mainly the experimental determination of the real and imaginary parts of the parallel and perpendicular dielectric constant in the operating frequency band (26 – 40 GHz) of a high birefringence nematic compound (LC 1825). To this goal, we used a waveguide measurement technique with magnetic orientation of the LC molecules and a transfer matrix retrieval technique that was previously developed in UDSMM laboratory. This method was here successfully applied to LC 1825 supplied by MUT (Military University of Technology) in Warsaw in the framework of a collaborative work with this lab. The method is inspired from the technique that was initially developed at NIST (National Institute of Standards and Technology) by avoiding the calibrating stage owing to the comparison of the scattering parameters (S_{ij}) for two different lengths of the waveguide's measurement cell. For avoiding disassembly that is measurement error sources and for preserving low LC volume, we compared the S_{ij} when the measurement cell with a constant length was first empty and then filled. Compared to the dielectric properties of 5CB that was also characterized as a reference compound, a dramatic improvement was shown of the microwave anisotropy of LC 1825 in the Ka band with $\Delta\varepsilon = 1.4$ that compares very favorably to the value $\Delta\varepsilon = 0.3$ of 5CB.

Chapter 3: Design of LC Tunable Metasurface

Introduction

In this chapter, we report the two methods that were employed for the design of LC controlled patch-like metasurface. The first one is based on full wave numerical simulation of the scattering of a plane wave with the metasurface using COMSOL software, while the second part is devoted to the so called TLM approach for which the propagation of the EM wave within the grounded dielectric substrate infiltrated by LC is described by means of a transmission line loaded by a short circuit and the printed metal array in terms of equivalent circuit.

3.1 COMSOL Design

Although there are many efficient and commercial softwares to be used such as “ANSYS HFSS” and “CST Studio Suite” [1], EM full wave simulations of the metasurface design in the microwave range were executed by the software “COMSOL Multiphysics” [2]. All three softwares are 3D-EM high frequency simulators based upon different computational techniques, where HFSS utilizes a 3D full-wave Finite Element Method (FEM) field solver [3] while CST is based upon the Finite Integration Technique (FIT) dealing with integral equations [4]. COMSOL is similar to HFSS where it is a cross-platform finite element analysis, solver and multiphysics simulation software. It allows conventional physics-based user interfaces and coupled systems of partial differential equations (PDEs). The choice of using COMSOL was first based on using a frequency domain solver due to being less time consuming for elementary structures like unit cells and FSS, and secondly because of its friendly interface and ease of using the different functionalities in the software. In addition, in COMSOL, we can add different modules other than RF, for example to make low frequency simulations we can use an AC-DC module.

3.1.1 Design rules and simulation model

As shown in Figure 3.1.1 and Figure 3.1.2, our simulation model presents the device described in Section 2.1. This 3D model of a basic cell consists of a glass slab, a square metal patch with interconnections, a very thin dielectric layer at the bottom representing the LC layer and a back side with PEC condition mimicking the uniformly metalized layer in real devices. In addition, the different parameters are also defined in the figures. A square patch was used to reduce the sensitivity of the model to the linearly polarized EM plane wave assumed along the x-axis with a normal incidence along the z-direction. Therefore, the E-field was defined in the simulation as:

$\vec{E_i} = E_i e^{-i.\overrightarrow{k_0}.\vec{z}}\vec{x}$, where $k_0 = \frac{2\pi}{\lambda_0} = \frac{2\pi F}{c}$ and c is the light speed in vacuum.

(Where $\vec{x}$ represents the unitary vector along Ox axis)

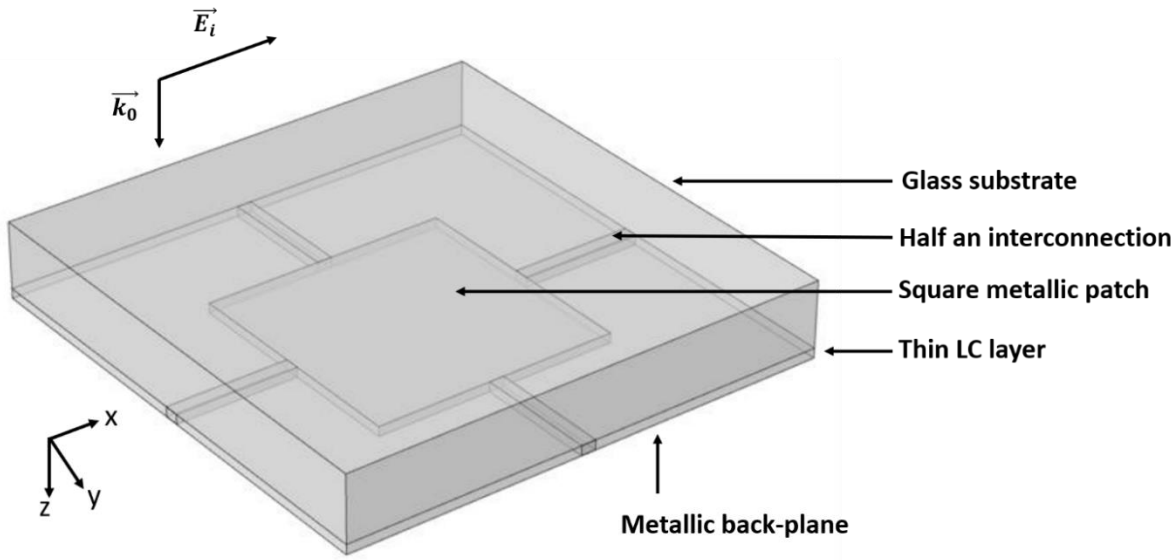

Figure 3.1.1 3D model of a unit cell of the prototype where all the different parts are demonstrated. The polarization direction of the incident electric field E_i is shown to be along x

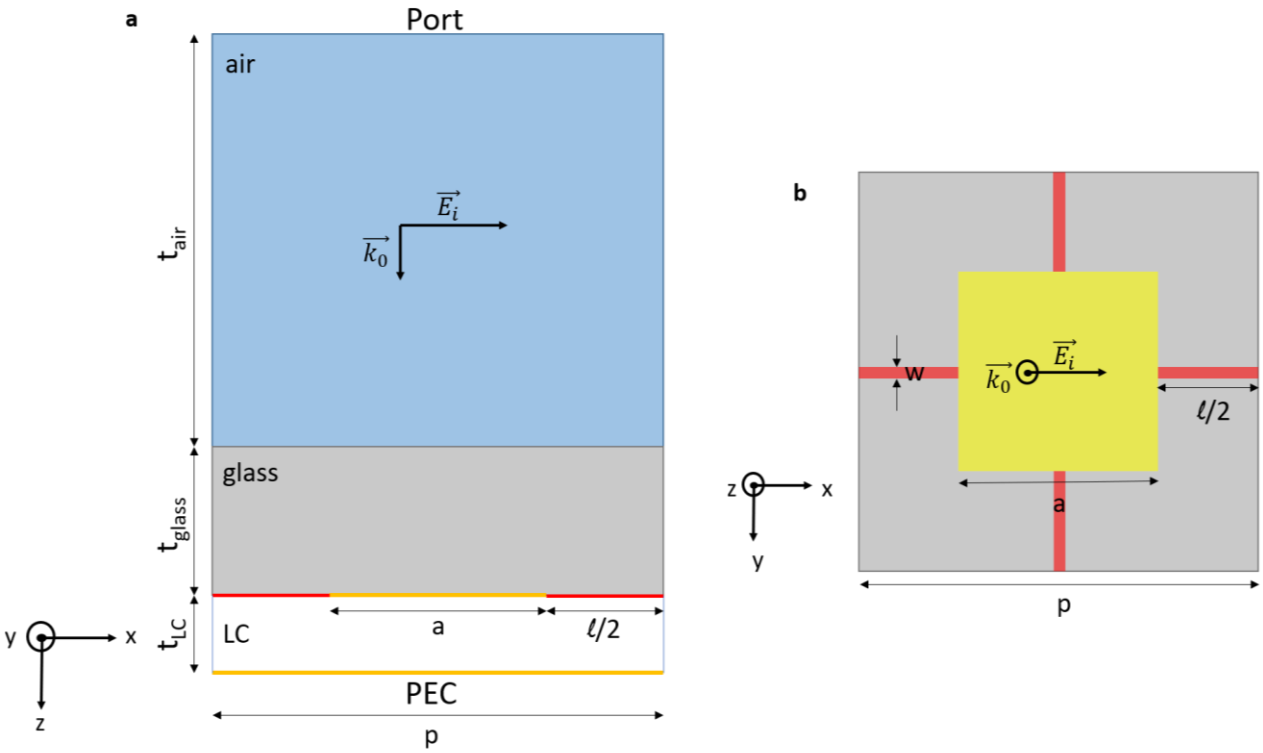

Figure 3.1.2 (a) Cross-section of the simulated unit cell model in the middle of the patch indicating the thickness of the different layers (air, glass, and LC) in addition to the boundary, and (b) top view of the model showing the patch and interconnections, where *p* is the period, *a* is the size of the patch, *w* and *l* are the width and length of the interconnections

Since our prototype is a periodic and symmetrical structure, periodic boundary conditions were used to simulate a single unit cell.

In addition, all simulations will be conducted under normal incidence for symmetrical metasurface patterns. Hence, instead of using the master-slave boundary conditions, we decided to use Perfect Electric Conductor (PEC) and Perfect Magnetic Conductor (PMC) [5, 6] which were defined in the x and y directions respectively (Figure 3.1.2 and Figure 3.1.3).

PEC boundary conditions are used to specify boundaries that behave as a Perfect Electric Conductor such as metals. For such a boundary, the component of the electric field parallel to the boundary and the component of the magnetic field perpendicular to the boundary are both zero. PEC boundaries are perfectly reflecting, allowing no energy to escape the simulation volume along that boundary. PMC boundary conditions are the magnetic equivalent of the PEC. The component of the magnetic field parallel to a PMC boundary and the component of the electric field perpendicular to a PMC boundary are both zero.

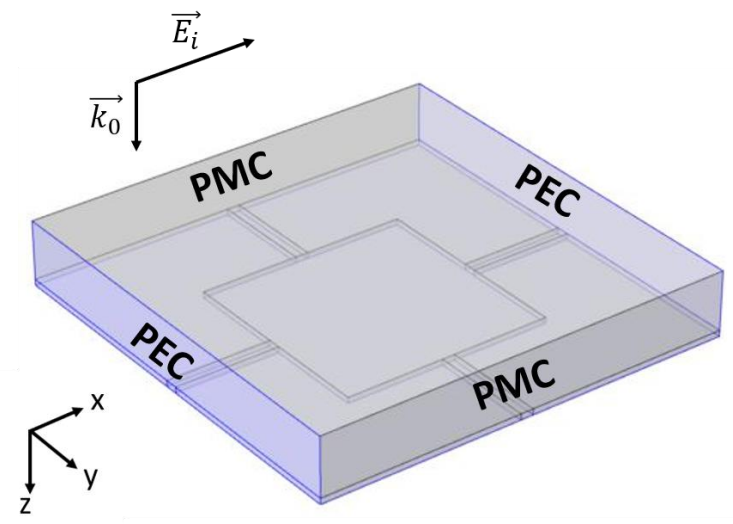

Figure 3.1.3 In addition to the incident electric field indicating the direction of the PEC condition, assignment of periodic boundary conditions to the unit cell are shown

In addition, taking into account simulation accuracy, calculation time, and memory size, a detailed mesh is used as shown in Figure 3.1.4. It can be seen that the number of points is much increased in the regions where there is absorption of electric field in the LC under the patch and interconnections. This ensures to have a quasi-perfect calculation of the desired frequency response of the system according to the designated areas.

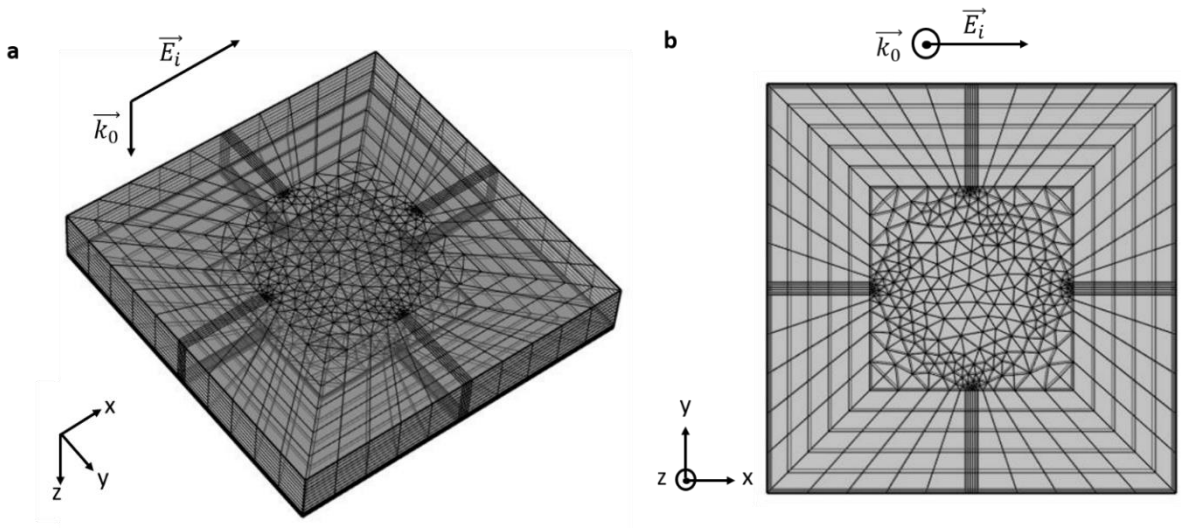

Figure 3.1.4 (a) Mesh pattern through each part of the unit cell where it appears to having more points in the desired areas (above and under the patch and interconnections) as shown in (b) the top view of the model

In order to simulate the model with and without voltage, the permittivity of the dielectric LC layer had two configurations as shown in Figure 3.1.5, where it explains that the LC molecules keep their initial planar orientation in the areas outside the patch. To define each configuration, let's recall as presented in Section 2.1 Figure 2.1.3, the operation of the prototype is connected to the microwave electric field under the patch which is orientated perpendicular to the patch and the metallic back plane (O_z direction). As a consequence, at V = 0, the permittivity seen by the microwave electric field is the LC perpendicular microwave permittivity $\varepsilon_{\perp}^{*}$. On the other hand, at V ≠ 0, the molecules orientate and the permittivity seen by the microwave electric field becomes the LC parallel microwave permittivity $\varepsilon_{\parallel}^{*}$. Therefore, the configuration of V = 0 is:

$\varepsilon_x = \varepsilon_{\parallel}(1 - i\tan\delta_{\parallel})$, $\varepsilon_y = \varepsilon_{\perp}(1 - i\tan\delta_{\perp})$, $\varepsilon_z = \varepsilon_{\perp}(1 - i\tan\delta_{\perp})$ which is the same on all the surface,

Whereas for the configuration of V > $V_{threshold}$, there are two parts, the first one is under the patch and interconnections where the LC molecules rotate to obtain a homeotropic orientation, and the second one is outside the patch and interconnections where the molecules' orientation does not change. So, the configuration would be:

$\varepsilon_x = \varepsilon_{\perp}(1 - i\tan\delta_{\perp})$, $\varepsilon_y = \varepsilon_{\perp}(1 - i\tan\delta_{\perp})$, $\varepsilon_z = \varepsilon_{\parallel}(1 - i\tan\delta_{\parallel})$ for under the patch and interconnection,

and $\varepsilon_x = \varepsilon_{\parallel}(1 - i\tan\delta_{\parallel})$, $\varepsilon_y = \varepsilon_{\perp}(1 - i\tan\delta_{\perp})$, $\varepsilon_z = \varepsilon_{\perp}(1 - i\tan\delta_{\perp})$ for outside the patch.

Notably, for simulations, when the interconnections are taken into account, the LC orientation conditions with and without bias under strips, is the same of that under the patch.

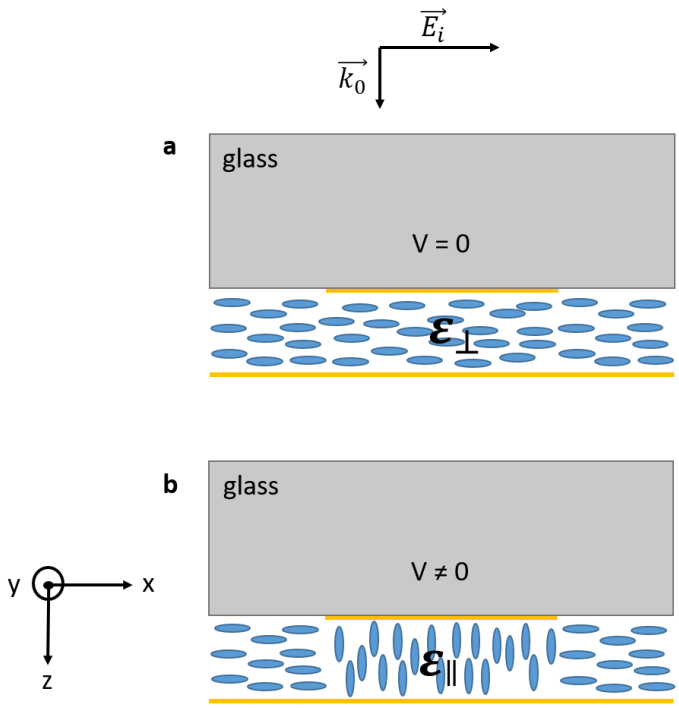

Figure 3.1.5 LC molecule orientation and tensor permittivity values in a simplified unit cell (without interconnections), under the patch and around it, (a) without and (b) with bias (voltage).

As the molecules' alignment follows the E-field lines at the edges of the patch, it can be expected to have a transition region where the molecules have an intermediate orientation underneath the patch and in the outside regions. The transition between the patch and the surrounding region is assumed here abrupt, and as a consequence, the fringing field effects [7] in the LC layer are not fully taken into account in the simulations. We will see in the comparison between simulation results and experiments that it will be necessary to introduce an effective patch dimension that is slightly greater than the physical one.

3.1.2 Design of 50 µm thickness prototype (Prototype 1)

To start the simulations, we have fixed some parameters:

- The LC used is 5CB, with microwave permittivity tensor terms and losses defined as: $\varepsilon_\perp$=2.64, $\varepsilon_\parallel$=2.98 and assuming the same loss value of tanδ=0.014 for both.

- The glass substrate that will be used for manufacturing prototype 1 is of thickness 0.68 mm and a relative permittivity of 5 by assuming low losses in the 10^{-3} range for the ratio of the imaginary to the real part of the complex permittivity.

The targeted operating frequency is around 33 GHz, the mid-frequency of the Ka Band.

- The choice of the thickness is also dictated by the volume of the LC used. So, to obtain acceptable control voltage, response time and filling volume, we choose a LC thickness of 50 µm. This thickness also makes it easier for us to assemble the prototype as the spacers are chosen depending on LC thickness and the LC is filled by capillarity.

Finally, only two parameters have to be adjusted that are the patch size *a* and the period *p*.

Having these material parameters in mind, we report the following parametric study in order to satisfy (i) the resonance and (ii) the critical coupling conditions. Where the latter, when satisfied at the resonance frequency, corresponds to the free space impedance matching. Under this criterion, total absorption is achieved for the incident energy fully trapped in the micro-resonator array without reflection. This impedance matching criterion depends on geometrical parameters such as the patch side, the pitch array and the LC dielectric thickness- and the material parameters, such as the LC complex permittivity tensor.

This parametric study will be quite general and we will see what are the degrees of freedom in the design when for instance we fix the LC thickness at 50 µm for prototype 1 infiltrated with 5CB.

3.1.2.1 Influence of different parameters

3.1.2.1.1 Influence of patch side *a*

With respect to the geometrical parameters, the first choice is the patch size. It determines notably the lower limit of the array pitch (period) (p>a).

The principle of operation of the prototype was explained at the beginning of Chapter 2. Let's recall the following equation which explains the resonance condition of the MIM structure (patch-LC-ground plane) that corresponds to the matching of the half wavelength of an EM wave propagating

in the LC layer, having a real permittivity ε_r, here assumed to be averaged over the 3-D directions, to the patch dimension noted *a*.

$$\varepsilon_r = \frac{\varepsilon_{\parallel} + 2\varepsilon_{\perp}}{3}$$

$$f_r = \frac{c}{2a\sqrt{\varepsilon_r}}$$

Using the previous equations at V = 0, and considering the permittivity ε_r used is that of 5CB where $\varepsilon_\perp$=2.64 and $\varepsilon_\parallel$=2.98, the size a of the patch is calculated to be 2.74 mm by targeting an operating frequency in the middle of the Ka Band at approximately 33 GHz.

For the preliminary studies, we first consider the prototype without DC bias interconnections and without the glass substrate between the air medium and the patch. In order to observe the effect of different patch sizes, the period is fixed at 5 mm.

As seen in Figure 3.1.6, by increasing the patch side *a* from 2.3 mm to 2.8 mm, the resonance frequency decreases while the reflectance dip increases slowly. And to obtain a resonance frequency around 33 GHz, the size of the patch must be between 2.7 and 2.8 mm as calculated previously.

As observed in Figure 3.1.7, there is a relatively good agreement between calculated and simulated $f_r(a)$ with only a 2% error which can be explained by two effects neglected up to now: the fringing effect on the upper and lower sides of the patch, and the effective permittivity. This phenomenon will be explained in the next section about TLM [7].

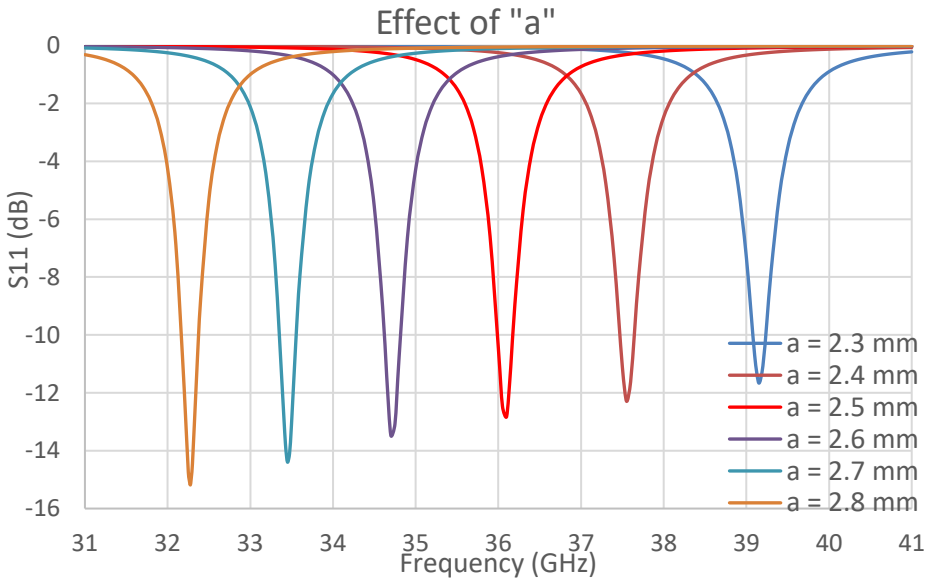

Figure 3.1.6 Influence of patch size *a* on the resonance frequency of the model having no glass or interconnections, with LC 5CB (t_{LC}=50 µm, $\varepsilon_{r\perp}$=2.64, tgδ=0.014) and p=5 mm

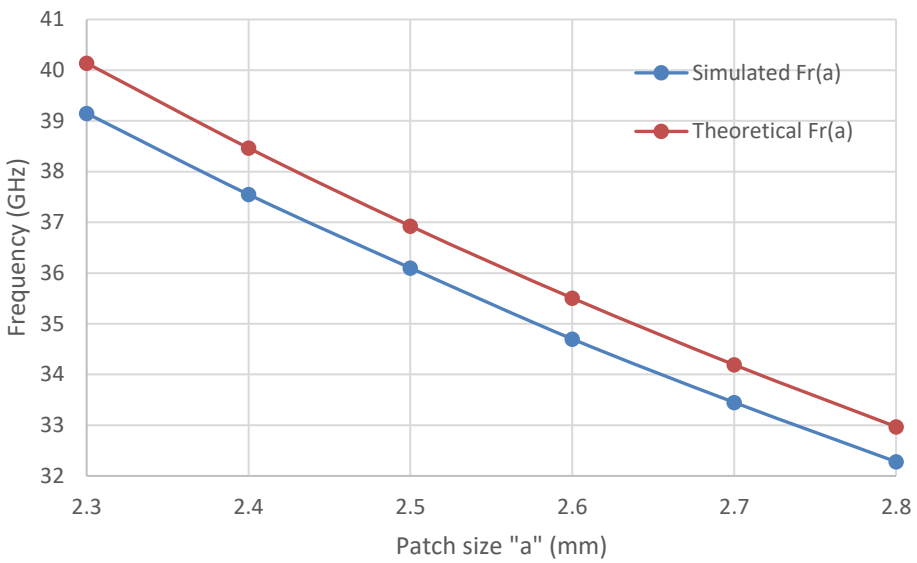

Figure 3.1.7 Resonance frequency of the metasurface versus the patch size. Comparison between simulated and calculated (theoretical) $f_r(a)$ of the model having no glass or interconnections, with LC 5CB (t_{LC}=50 µm, $\varepsilon_{r\perp}$=2.64, tgδ=0.014) and p=5 mm

3.1.2.1.2 Influence of interconnections

Before introducing the glass layer in the basic cell model, it is interesting to test the influence of the interconnections on the resonance frequency. The width of these bias interconnections has been chosen to be equal to 150 µm where the period is fixed to be 5 mm.

As shown in the following Figure 3.1.8, the evolutions of the resonance frequency and of the maximum absorption versus the patch size are preserved, but compared to the case without interconnections, the resonance frequency slightly increases and the absorbance decreases.

This can be understood by considering that the equivalent model of the patch alone is an LC resonant circuit and that the model of the interconnection is an inductor of an inductance L_i due to its width being very small compared to its length. L_i is given as:

$$L_i = \mu_0 t \frac{l_{int}}{w_{int}}$$

Where for t=50 µm, a=2.5 mm, p=5 mm, and w=150 µm we obtain:

$$\mu_0 t = 62.8\ pH, \qquad l_{int} = p - a = 2.5\ mm, \qquad \frac{l_{int}}{w_{int}} = 16.7, \qquad and\ L_i = 1\ nH$$

Where w is the width of the interconnections and l_{int} is their length and it is equal to $p - a$ so that when p is fixed and a decreases, l_{int} will increase which will increase L_i.

By modelling the prototype in an LC equivalent circuit (Section 3.2), this supposes that the inductance L_i is in parallel with the inductance L of the equivalent circuit of the patch, the inductance of the circuit becomes $L \parallel L_i$ so the resonance frequency f_r increases.

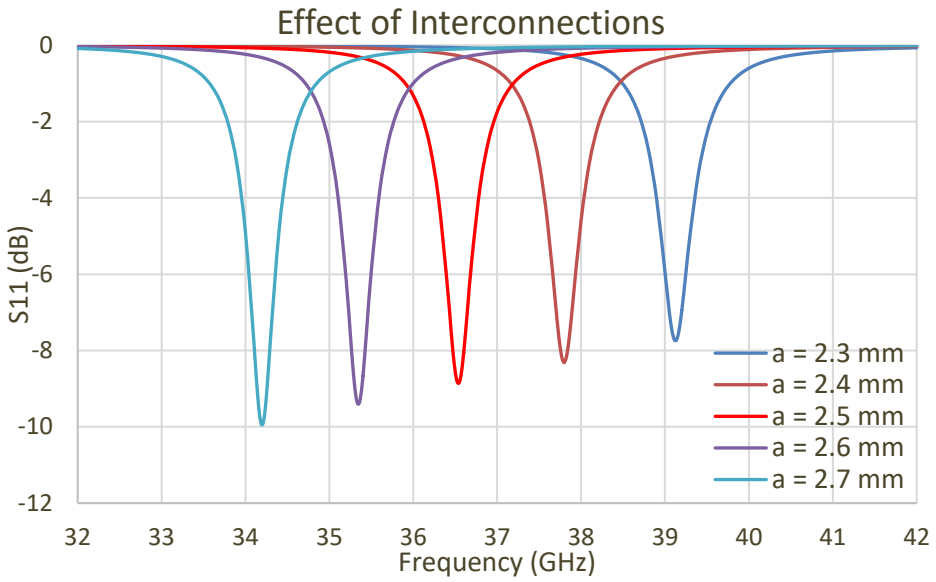

Figure 3.1.8 Influence of the interconnections on the reflectance spectra with different values of a, having no glass, with LC 5CB (t_{LC}=50 µm, $\varepsilon_{r\perp}$=2.64, tgδ=0.014), p=5 mm and w_{int}=150 µm

3.1.2.1.3 Influence of glass

To complete our model, we added a glass substrate between the air and the patches with a thickness of 0.68 mm and a standard permittivity of 5 without losses. The role of the glass is to create a physical support for the deposition of metal layers and to create a cavity where the LC is infiltrated.

Figure 3.1.9 shows us that the resonance frequency has strongly decreased from before. For example, for a=2.5 mm, the frequency value was 36.1 GHz without glass and interconnections which decreased to 33.7 GHz after adding both the glass and interconnections. These results show that the glass side has an opposite effect on resonance frequency to that of interconnections.

In addition, an important observation is that the reflectance level is almost the same in all the cases of different patch sizes and has increased to be about -14 dB.

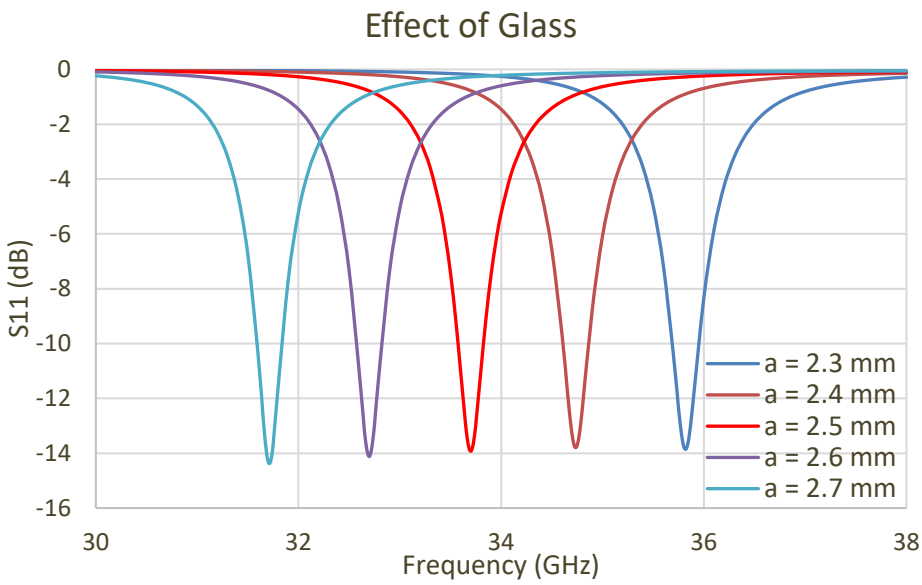

Figure 3.1.9 Influence of the glass substrate on the frequency response of the model with glass and interconnections. LC 5CB (t_{LC}=50 µm, $\varepsilon_{r\perp}$=2.64, tgδ=0.014), p=5 mm, w_{int}=150 µm, t_{glass}=0.68 mm and ε_{glass}=5

At this point of the study, it is possible to decide the value of the patch size *a*. According to the previous simulated parameters, the best choice of patch with interconnections and glass is to be 2.5 mm in order to achieve an operating frequency of 33 GHz taking into account that this frequency will decrease under voltage application.

3.1.2.1.4 Influence of LC thickness t

After the observation of the influence of the FSS and glass, we are interested to see the influence of the thickness of the dielectric material we want to used. All parameters were fixed and we varied the thickness *t* of the LC in a manner where there is no voltage applied. The results of these simulations are given in Figure 3.1.10.

This study shows the strong shift of the resonance frequency with the variation of *t* in addition to the change in the absorption. This effect is attributed to the increase of the effective permittivity with the LC thickness and highlighted by the effect of the glass substrate.

The simulation gives the best option to be t=30 µm to have a total absorption for a period of 5 mm. However, the LC thickness being fixed to 50 µm, the critical absorption condition will be obtained in adjusting the period of the prototype.

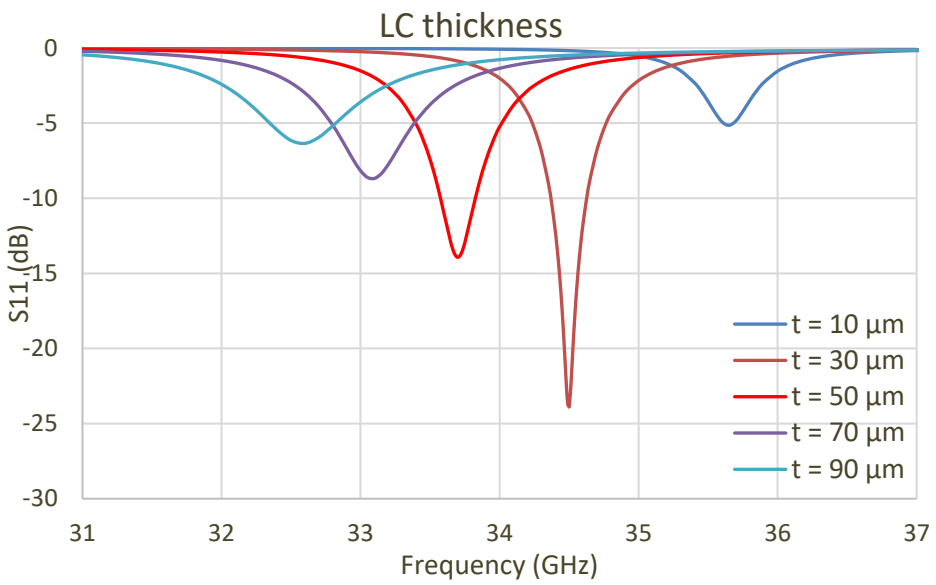

Figure 3.1.10 Influence of LC thickness on the resonance frequency of the model. LC 5CB ($\varepsilon_{r\perp}$=2.64, tgδ=0.014), p=5 mm, w_{int}=150 µm, t_{glass}=0.68 mm, ε_{glass}=5 and a=2.5 mm

3.1.2.1.5 Influence of LC losses

Here, if the LC thickness is fixed at 50 µm, the choice of the loss angle also makes it possible to obtain the optimum coupling but also varies the selectivity of the response as can be seen in Figure 3.1.11. We can notice that the resonance frequency is independent from the value of the dielectric losses, while the selectivity is not. As the losses increase, the selectivity increases making it reach near unity at the value of 0.035. The graph explains how the quality factor increases with tanδ where finally it was fixed to 0.014 complementing the value that was obtained in the microwave measurement of 5CB's permittivity.

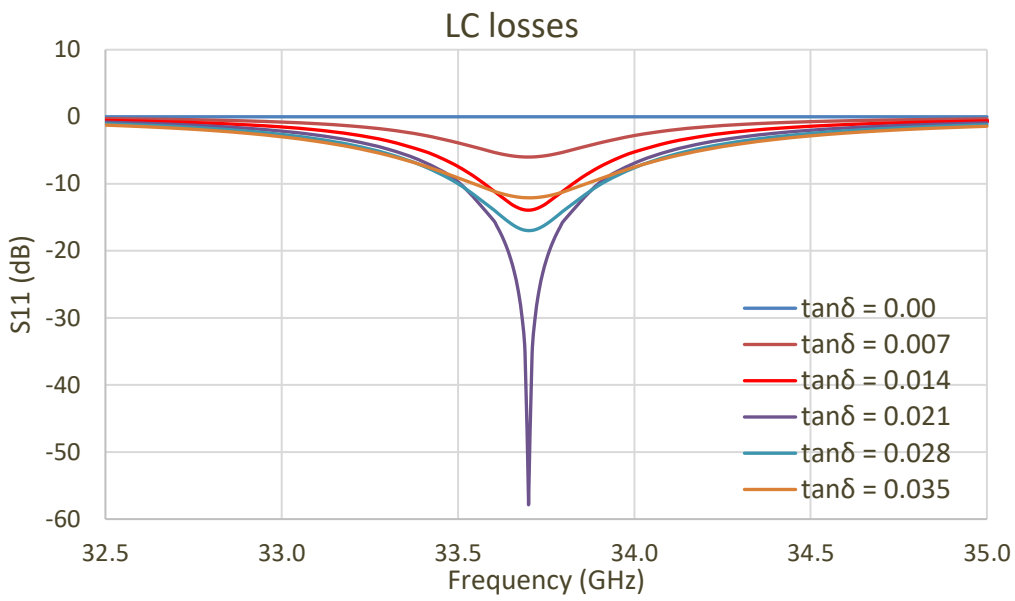

Figure 3.1.11 Influence of the LC's dielectric losses on the resonance frequency of the model. LC 5CB (t_{LC}=50 µm, $\varepsilon_{r\perp}$=2.64), p=5 mm, w_{int}=150 µm, t_{glass}=0.68 mm, ε_{glass}=5 and a=2.5 mm

3.1.2.1.6 Influence of period *p*:

At last, to optimize the absorption of the model, we varied the period *p*.

The influence of the period is studied in two cases, the first case is when the LC molecules are aligned perpendicular to the electric field under the patch, simulating the case when there is no applied voltage. The second case is when the LC molecules are aligned parallel to the electric field under the patch, simulating the case when we have an applied threshold voltage.

As we can see in Figure 3.1.12 and Figure 3.1.13, total absorption and critical coupling is obtained at V = 0 and V ≠ 0 for the optimum period of 5.5 mm. Also, high absorption is obtained for close values of p=5 mm and 6 mm. But at the end the value 5 mm was chosen in order to have better surface efficiency of the metasurface resulting in a greater number of patches under which the orientation of LC molecules can be electrically controlled.

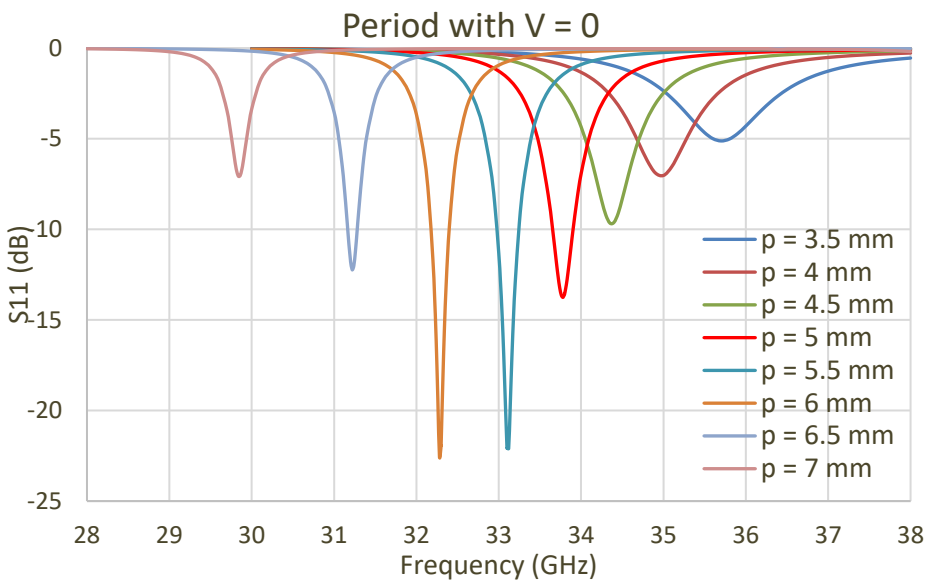

Figure 3.1.12 Influence of the period on the frequency response of the model when V = 0. LC 5CB (t_{LC}=50 µm, $\varepsilon_{r\perp}$=2.64, tgδ=0.014), w_{int}=150 µm, t_{glass}=0.68 mm, ε_{glass}=5 and a=2.5 mm

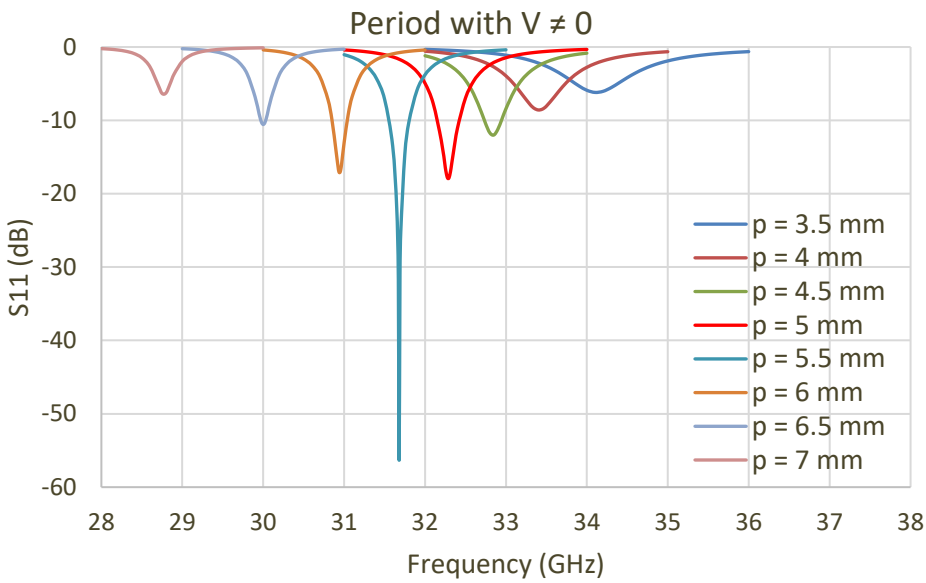

Figure 3.1.13 Influence of the period on the frequency response of the model when V ≠ 0. LC 5CB (t_{LC}=50 µm, $\varepsilon_{r\perp}$=2.64, tgδ=0.014), w_{int}=150 µm, t_{glass}=0.68 mm, ε_{glass}=5 and a=2.5 mm

3.1.2.2 Prototype 1 Optimization

After choosing the best parameter values for the final model, we perform a simulation for the model with and without voltage. The chosen parameters are:

p	5 mm
a	2.5 mm
w	150 µm
t	50 µm
LC	5CB

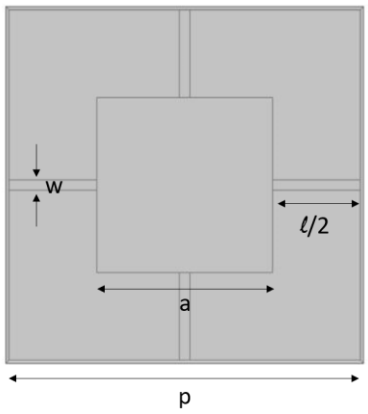

Figure 3.1.14 shows us the response of the model when whether we apply a voltage or not on the electrodes. The width at half height of the absorption is about 500 MHz for a resonant frequency of around 33 GHz which shows us that we have a good total quality factor. In addition, the birefringence of the LC generates a resonant frequency shift of 1.5 GHz which makes it possible to go from total absorption to total reflection by the application of the control voltage causing the LC molecules to orientate.

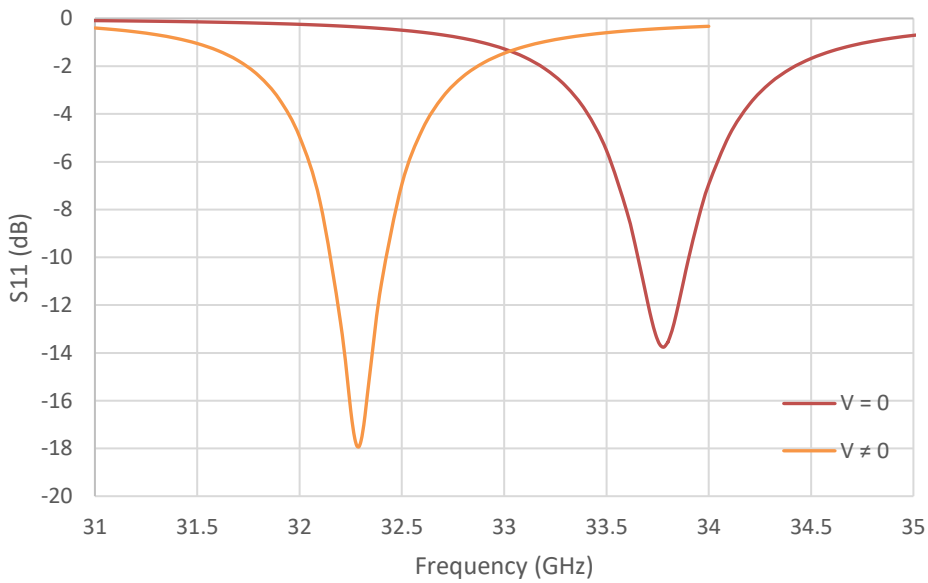

Figure 3.1.14 The frequency response of the final model with and without voltage of prototype 1 with 5CB LC (t_{LC}=50 µm, $\varepsilon_{r\perp}$=2.64, tgδ=0.014), w_{int}=150 µm, t_{glass}=0.68 mm, ε_{glass}=5 and a=2.5 mm

3.1.3 Design of 10 µm thickness prototype (Prototype 2)

From experience in the simulations with Prototype 1, in order to design Prototype 2, we keep the parameters used before the same since we are aiming to operate at the same frequency, which is 33 GHz, the middle of Ka Band, meaning, the permittivity of the LC and the patch side are fixed to 2.64 and 2.5 respectively, in addition to the LC losses of 0.014 and the interconnections' width being 150

µm. As for the other parameters, the thickness of the LC was decreased to 10 µm, and the glass was changed to have a thickness of 1.1 mm and a permittivity of 5.7 (from Verre Industrie).

Firstly, we studied the effect of the period on this model, which its result is presented in Figure 3.1.15, showing that the optimization of absorption is still possible.

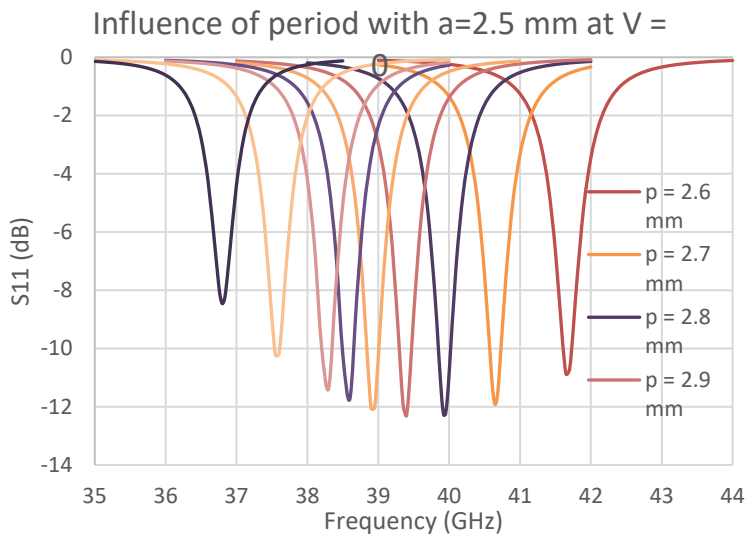

Figure 3.1.15 Influence of the period on the frequency response of the model when V = 0. LC 5CB (t_{LC}=10 µm, $\varepsilon_{r\perp}$=2.64, tgδ=0.014), w_{int}=150 µm, t_{glass}=1.1 mm, ε_{glass}=5.7 and a=2.5 mm

As shown in Figure 3.1.16, we have maximum absorption being more than 12 dB with a period between 2.8 mm and 2.9 mm. The problem is with the high resonance frequency (39.4 GHz) which has to be decreased. So, an optimization has been made to this result by increasing the patch size with a quick calculation using the expression of resonance frequency giving a new value of 2.9 mm.

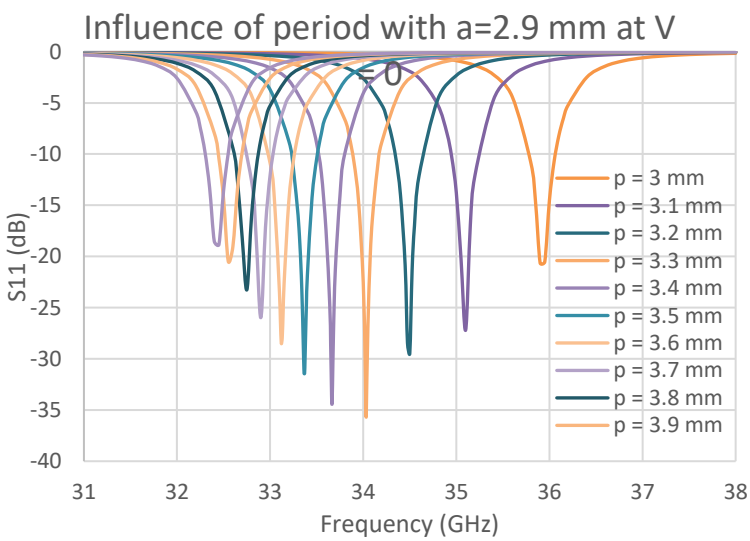

Figure 3.1.16 Influence of the period on the frequency response of the model when V = 0. LC 5CB (t_{LC}=10 µm, $\varepsilon_{r\perp}$=2.64, tgδ=0.014), w_{int}=150 µm, t_{glass}=1.1 mm, ε_{glass}=5.7 and a=2.9 mm

The simulations with a=2.9 mm versus the period are given in Figure 3.1.17. The results show that the resonance frequency has decreased effectively to be in the predicted frequency range. A maximum absorption of 35 dB is obtained for a lower period of 3.3 mm.

As a conclusion, in order to obtain an optimal prototype in the working frequency range when decreasing the LC thickness, it is necessary to increase the patch size and to decrease the period leading to a strong decrease in the gap size (interconnections' length) l_{int} between the patches.

Moreover, to complete this study, it was decided to use another method to decide which patch size and period to use for this prototype. This new approach is a new method of study aiming to see the effect of patch size and period on the level of absorption of the model at a specific frequency. The chosen resonance frequency for this study is 34 GHz. The results given in Figure 3.1.17 show that the condition with the most absorption and a good quality factor is the one having a patch size of 3 mm and a period of 3.2 mm (length of interconnections is 0.2 mm). These values of the patch size *a* and the period *p* are chosen for the prototype 2.

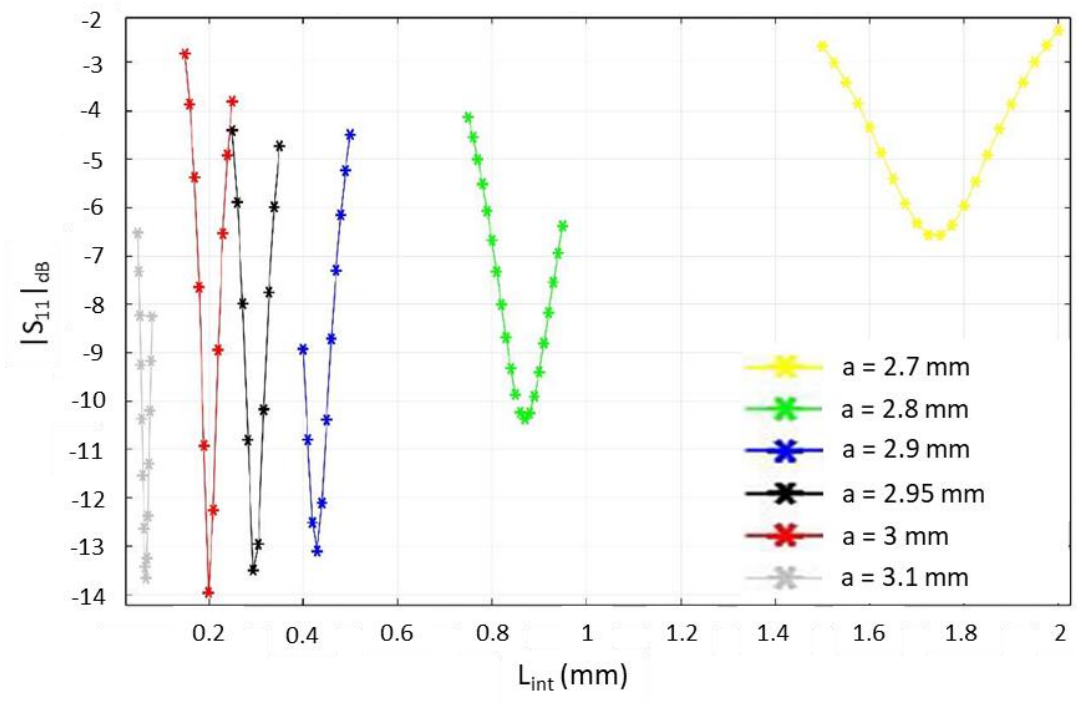

Figure 3.1.17 Dependence of the modulus of S11 versus the interconnections' length l_{int} taking the patch size *a* as a parameter for an operating frequency of 34 GHz. LC 5CB (t_{LC}=10 µm, $\varepsilon_{r\perp}$=2.64, tgδ=0.014), t_{glass}=1.1 mm, and ε_{glass}=5.7

3.1.3.1 Prototype 2 Optimization

After choosing the best parameter values for the final model, we perform a simulation for the model with and without voltage. The chosen parameters are:

p	3.2 mm
a	3 mm
w	150 µm
t	10 µm
LC	5CB

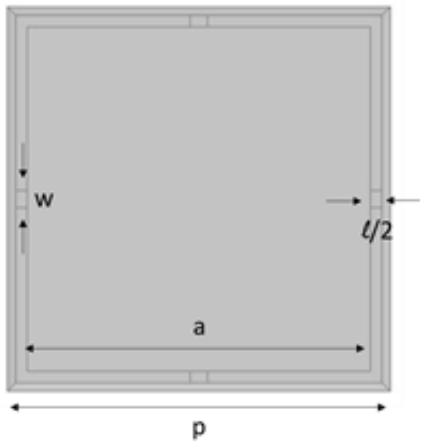

Figure 3.1.18 shows us the response of the model when whether we apply a voltage or not on the electrodes. The width at half height of the absorption is about 700 MHz for a resonant frequency of around 34 GHz without voltage and is 300 MHz for a resonance frequency of 32.15 GHz which shows us that we have a selective resonance. In addition, the birefringence of the LC generates a resonant frequency shift of 1.85 GHz which is greater than that of prototype 1. The different functionalities of prototypes 1 and 2 are presented in Table 7

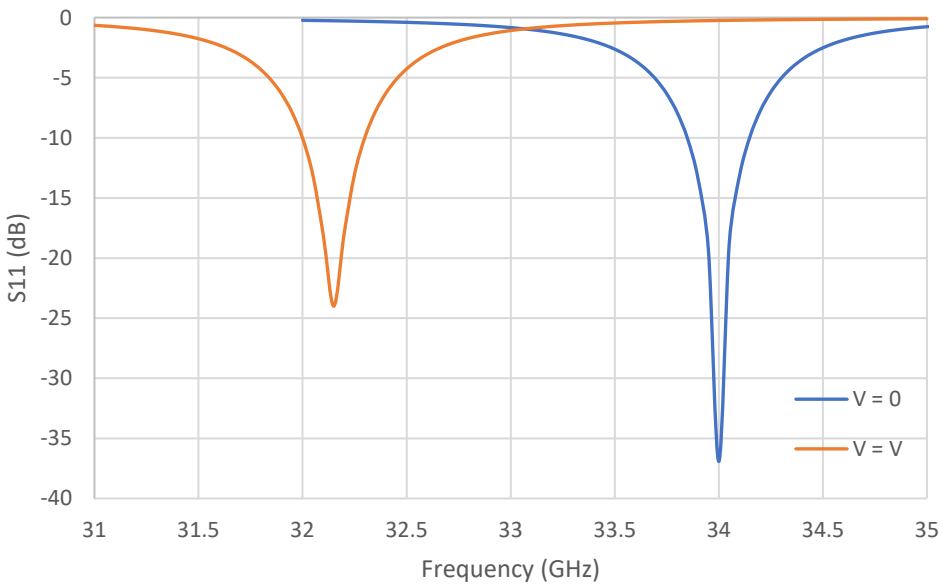

Figure 3.1.18 The frequency response of the final model with and without voltage of prototype 2 with 5CB LC (t_{LC}=10 µm, $\varepsilon_{r\perp}$=2.64, tgδ=0.014), w_{int}=150 µm, t_{glass}=1.1 mm, ε_{glass}=5.7, a=3 mm and p=3.2 mm

Functionality	f_r(GHz) at V = 0	f_r(GHz) at V ≠ 0	Tunability Δf_r(GHz)	Absorption (dB) at V = 0	Absorption (dB) at V ≠ 0
Prototype 1	33.78	32.29	1.49	13.76	17.93
Prototype 2	34	32.15	1.85	36.92	24

Table 7 Comparison between the different functionalities of prototypes 1 and 2 filled with 5CB

3.1.4 Simulation of prototypes 1 and 2 with 1825 LC

Prototypes 1 and 2 filled with the high anisotropy 1825 LC will also be studied in Chapter 4. In Figure 3.1.19, the frequency evolution of the reflection coefficient of prototypes 1 and 2 filled with 1825 LC are given. These results will be used in Section 4.3 to compare simulated and measured reflectivity of these prototypes. The different functionalities of prototypes 1 and 2 are presented in Table 8.

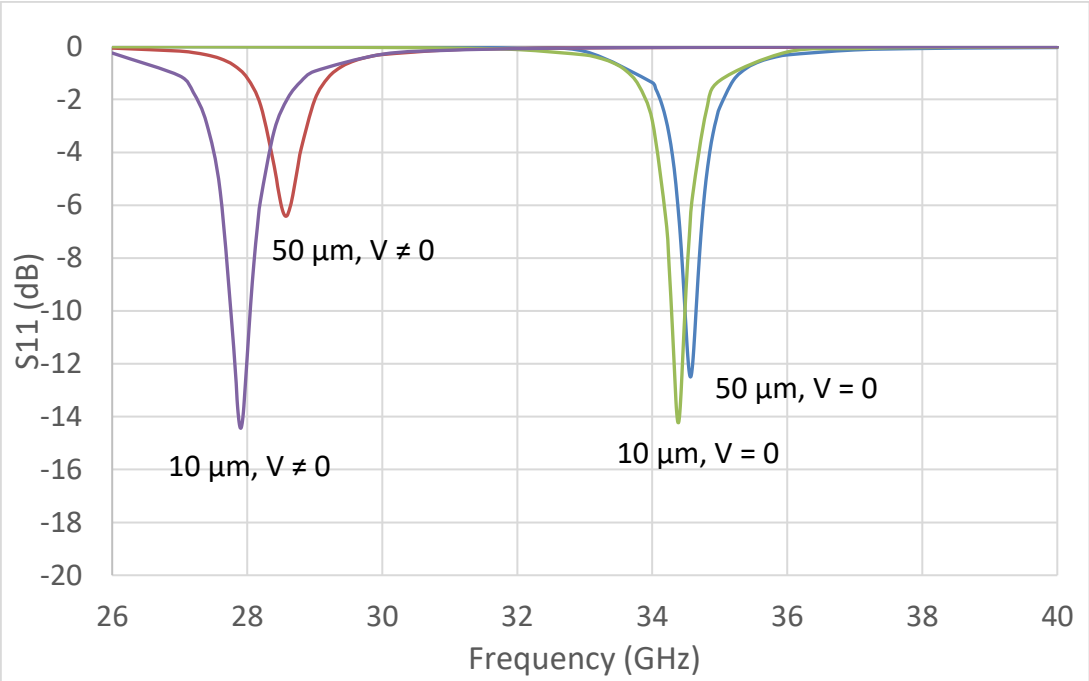

Figure 3.1.19 The frequency response of prototype 1 (50 µm) and 2 (10 µm) filled with 1825 LC

Functionality	f_r(GHz) at V = 0	f_r(GHz) at V ≠ 0	Tunability Δf_r(GHz)	Absorption (dB) at V = 0	Absorption (dB) at V ≠ 0
Prototype 1	34.44	28.65	5.79	-12.4	-6.4
Prototype 2	34.41	27.9	6.51	-13.8	-14.44

Table 8 Comparison between the different functionalities of prototypes 1 and 2 filled with 1825

3.2 TLM modeling

It is interesting to use purely or semi-analytical approaches using partial numerical simulations [8,10]. In this part, we compare the results of the TLM approach to the COMSOL simulations of our prototype. By using the analytical model of this device, the influence of different geometrical and material parameters can be better understood. This approach has a lower calculation time than full wave calculations in addition to being useful to new applications' development.

Primarily, the different parameters of the model are studied without adding neither interconnections nor a glass substrate, and after, the glass and interconnections were introduced to study their effects on the original prototype.

3.2.1 TLM Modeling of the metasurface without glass slide

The first step is the research of an equivalent electric circuit of the metasurface.

3.2.1.1 Research of the equivalent electrical circuit

Figure 3.2.1 illustrates the schematic design of the absorbing metasurface to be modelled that is made from a frequency selective surface, consisting of an array of square-metallic patches of side *a* and period *p* printed on a dielectric substrate of thickness *t*, permittivity ε, and losses factor tanδ. The surface impedance of the absorbing structure Z_s is the result of the parallel configuration of the impedance of the grounded dielectric plane Z_d 'seen' at the air-device interface level through the thickness of the dielectric *d* and the equivalent impedance of the FSS structure (Z_{FSS}).

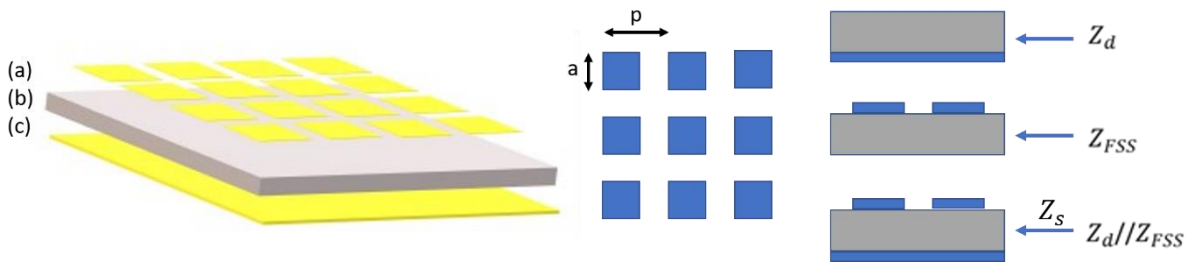

Figure 3.2.1 3D design of the absorbing metasurface and an illustration of surface impedances, where (a) is the metasurface, (b) is the dielectric, and (c) is the back metal plane.

Using transmission line theory and assuming a low-loss $\varepsilon_r'' \ll \varepsilon_r'$ regime (tgδ << 1), the real and imaginary parts of the impedance of the grounded plane Z_d is expressed generally as:

$$Z_d = \frac{Z_0}{\sqrt{\varepsilon_d}} \tanh(\gamma_d t) \text{ where } \gamma_d = \alpha_d + j\beta_d = \gamma_0 \sqrt{\varepsilon_r{}^*} = j\frac{2\pi}{\lambda_0}\sqrt{\varepsilon_r{}^*}$$

$$Re\{Z_d\} = \frac{Z_0}{\sqrt{\varepsilon_r'}}\left[\frac{\varepsilon_r''}{2\varepsilon_r'}\tan\left(\gamma_0 t\sqrt{\varepsilon_r'}\right) - \left(\gamma_0 t\frac{\varepsilon_r''}{2\sqrt{\varepsilon_r'}}\right)\left(1 + \tan\left(\gamma_0 t\sqrt{\varepsilon_r'}\right)^2\right)\right]$$

$$Im\{Z_d\} = \frac{Z_0}{\sqrt{\varepsilon_r'}}\left[\tan\left(\gamma_0 t\sqrt{\varepsilon_r'}\right)\right]$$

Where Z_0 is vacuum impedance equals to 377 Ω, γ_d is the propagation constant in the dielectric, α_d is the attenuation coefficient, β_d is the phase constant, and λ_0 is vacuum wavelength.

In our case, we have low losses and the thickness is very small compared to the wavelength, so, we find that the impedance Z_d is equivalent to an inductance L_d and becomes independent of permittivity:

$$Z_d = jL_d\omega \text{ where } L_d = Z_0\frac{t}{c} = \mu_0 t \text{ and c is the speed of light.}$$

As thickness increases, L_d increases and Z_d becomes infinite for $t = \frac{\lambda_0}{4\sqrt{\varepsilon_r'}}$ and capacitive for $t > \frac{\lambda_0}{4\sqrt{\varepsilon_r'}}$.

For the metallic patch networks considered here, it is possible to analytically express the reactive and resistive elements including ohmic and dielectric losses [1-4] of the FSS without the ground plane. Therefore, for Z_{FSS}, the impedance of the FSS is considered that of a series RLC resonant circuit as previously proposed in [11-12].

At a frequency lower than that of resonance, the FSS impedance is capacitive, whereas the ground plane's impedance is inductive when t < λ/4. By setting these two elements in parallel, the imaginary part of $Z_s = Z_d \parallel Z_{FSS}$ is cancelled at the resonance frequency F_R [13, 14]. The criterion of total absorption, however, requires to eliminate any reflection under the impedance matching condition $Re\{Z_s(F_R)\} = Z_0$. In the case of small substrate thickness with respect to the wavelength, strong coupling effect occurs between the FSS and the metal back plane yielding a magnetic resonance effect. In fact, a current loop results from the combination of displacement currents in the dielectric layer and of conduction current components in the metal layers in an antiparallel configuration. Finally, the equivalent circuit giving the surface impedance Z_s is presented in Figure 3.2.2.

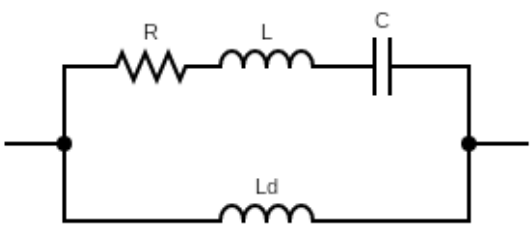

Figure 3.2.2 Preliminary equivalent circuit of the model under study, where the series RLC represents the FSS, and L_d represents the short-circuited dielectric layer.

To confirm the layout of the equivalent circuit, a simulation was done using COMSOL for a patch-type absorbing metasurface (Figure 3.2.1) with liquid crystal infiltration of relative permittivity ε_r=3 (1-j0.014) targeting an operating frequency in the Ka band. At these frequencies, the relative order

of magnitude of the overall losses due to finite conductivity and resulting from complex permittivity, show that dielectric losses dominate. For comparison, the frequency evolutions of the simulated and calculated reflection coefficients are given in Figure 3.2.3 showing resonance behavior with incident wave absorption along with the calculated reflection coefficient of the optimized preliminary equivalent circuit. From the simulated reflection coefficient, the surface impedance can be calculated using the following equation:

$$Z_s(f) = Z_0 \frac{1 + S_{11}(f)}{1 - S_{11}(f)}$$

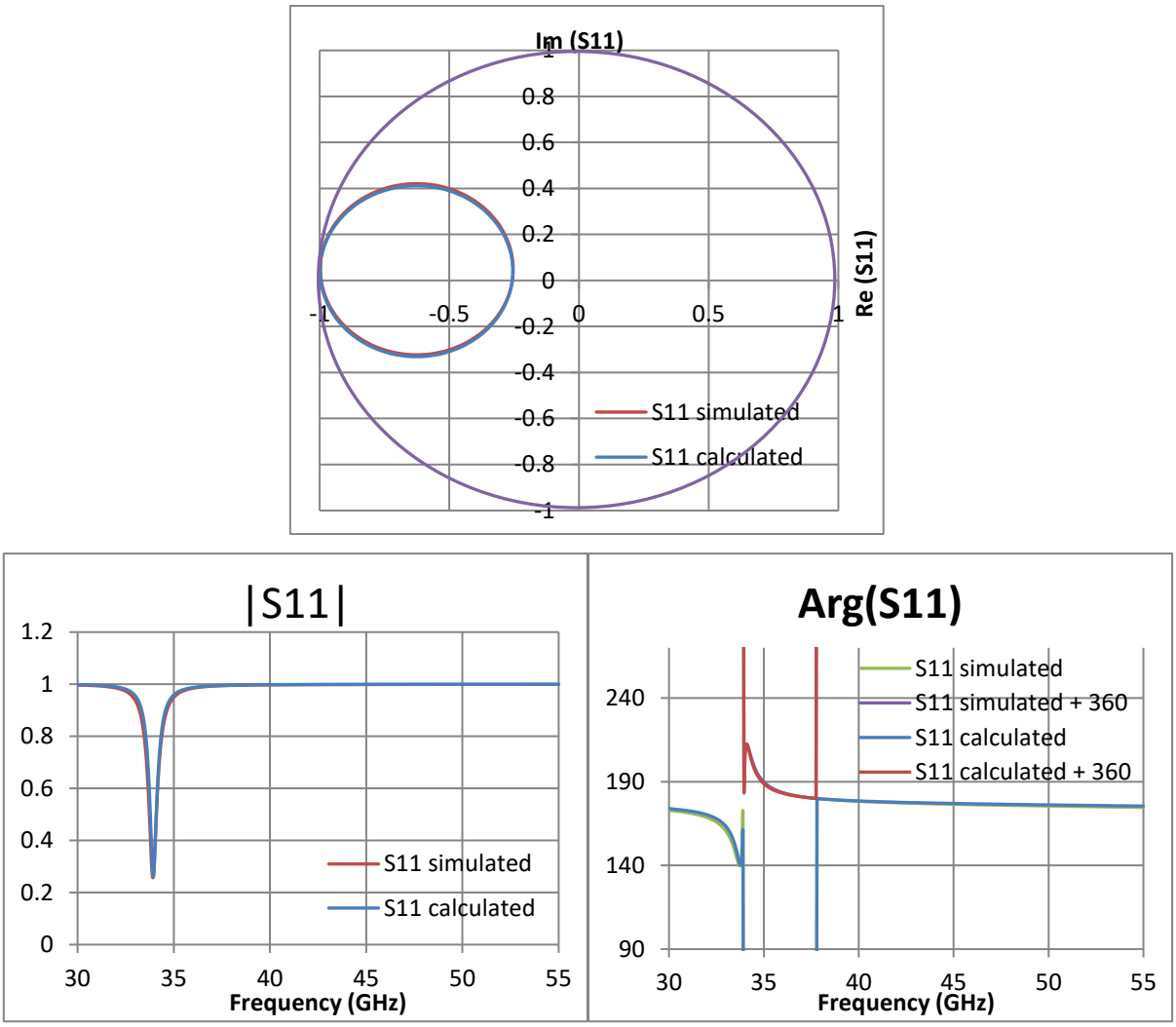

Figure 3.2.3 Frequency evolution of the reflection coefficient of the simulation (red) and the optimized equivalent circuit (blue), (a) Smith chart representation, (b) linear modulus, and (c) phase. (ε=3(1-j0.014), t=50 µm, p=5 mm, a=2.5 mm, R= 0.8 Ω, L= 251 pH, C= 69.9 fF, and L_d= 62.8 pH)

The frequency variations in the modulus of S_{11} (Figure 3.2.3b) show rejection dip ($|S_{11}|_{min}$=0.26) in the spectrum for a frequency of 33.9 GHz corresponding to a peak in absorption.

In Figure 3.2.4, the frequency dependence of the calculated impedance from both the simulated and calculated reflection coefficients are given.

As shown in Figure 3.2.4b, it is apparent that the imaginary part of the surface impedance becomes null two times in the studied frequency range showing the existence of two resonance frequencies. The lower resonance frequency corresponds to the maximum of the real part and modulus (Figure 3.2.4a and c) of the impedance which is the parallel resonance F_{r_p}=33.95 GHz. On the other hand, the higher resonance frequency corresponds to the minimum of the real part and modulus of the surface impedance which is the series resonance F_{r_s}=37.8 GHz.

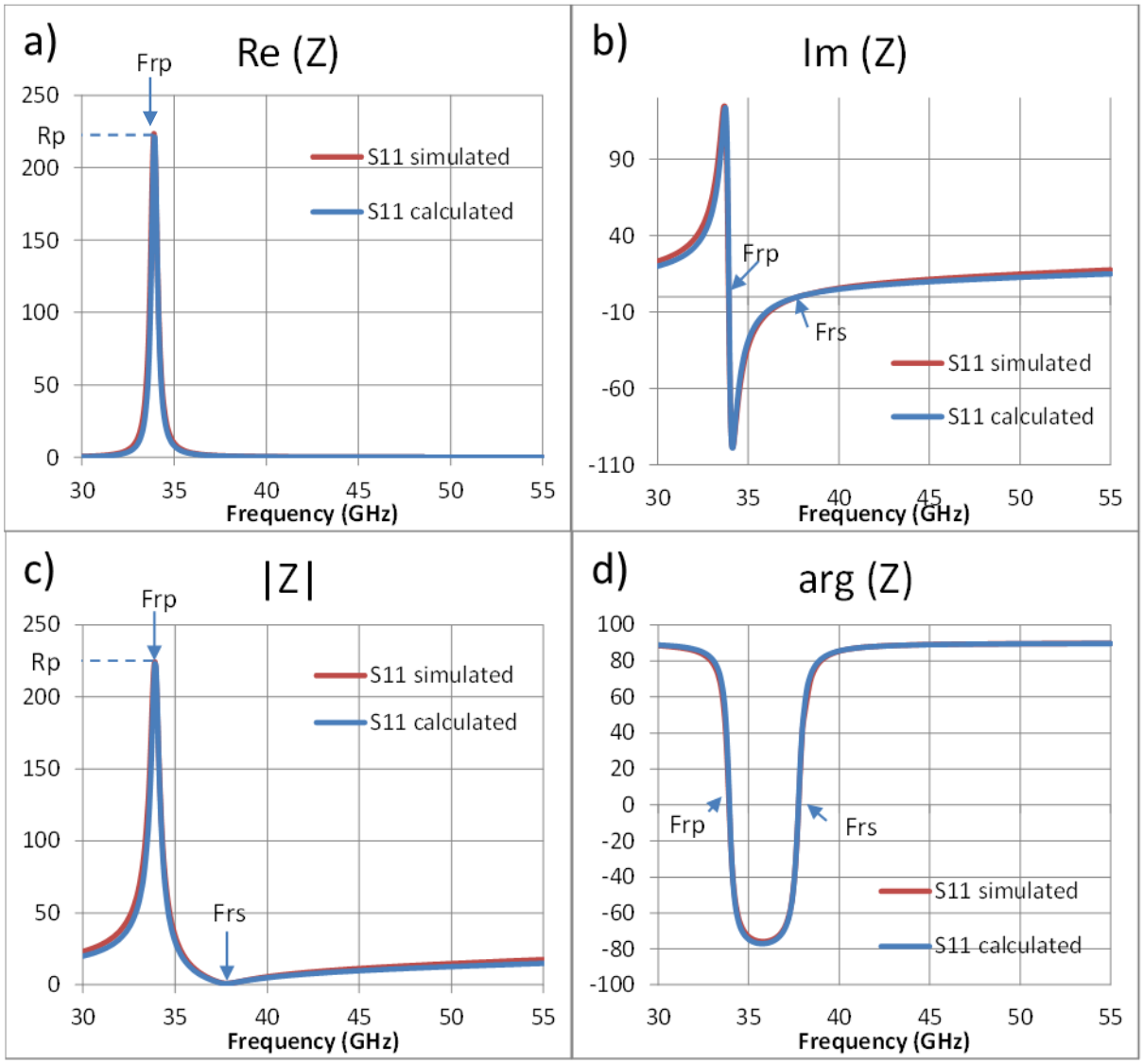

Figure 3.2.4 Frequency dependence of (a) the real part, (b) the imaginary part, (c) the modulus, and (d) the phase of the calculated surface impedance from simulation (red) and optimized equivalent circuit (blue). (ε=3(1-j0.014), t=50 µm, p=5 mm, a=2.5 mm, R= 0.8 Ω, L= 251 pH, C= 69.9 fF, and L_d= 62.8 pH)

These behaviors are in agreement with the equivalent circuit model: $Z_s = (jL_d\omega) \parallel \left(R + jL\omega + \frac{1}{jC\omega}\right) = R_{Z_s} + jX_{Z_s}$,

where $R_{Z_s} = \frac{RL_d^2\omega^2}{R^2+\left[\frac{(L+L_d)(C\omega^2-1)}{C\omega}\right]}$,and $X_{Z_s} = \frac{L_d\omega\left[R^2+\left[\frac{LC\omega^2-1}{C\omega}\right]\left[\frac{(L+L_d)(C\omega^2-1)}{C\omega}\right]\right]}{R^2+\left[\frac{(L+L_d)(C\omega^2-1)}{C\omega}\right]^2} \approx \frac{L_d\omega(LC\omega^2-1)}{(L+L_d)(C\omega^2-1)}$ (if R^2 is not taken into account because it is very small).

Which gives, $F_{r_p} = \frac{1}{2\pi\sqrt{(L+L_d)C}}$ and $F_{r_s} = \frac{1}{2\pi\sqrt{LC}}$ when $X = 0$.

From the above model we should extract the values of the different elements in the equivalent circuit, L_d, R, L and C. First, L_d can be easily calculated by knowing t, the thickness of the dielectric. To find L and C we can use the equations of $F_{r_p}$and F_{r_s} and their values. At resonance, $F = F_{r_p}$, the equivalent circuit of the model (Figure 3.2.5) is reduced to only the parallel resistance $R_{Z_{smax}} = R_p = \frac{L_d^2\omega_{R_p}^2}{R}$. This equation is used to find R, which by substitution gives $R = \frac{L_d^2\omega_{r_p}^2}{R_p}$, where R_p= 223.3 Ω. In conclusion, we have the values of the elements in the equivalent circuit to be R=0.8 Ω, L=251 pH, C=69.9 fF, and L_d= 62.8 pH.

Using the calculated values of the different elements, the blue curves that are shown in Figure 3.2.3 and Figure 3.2.4 are drawn, where a slight discrepancy is pointed out between the imaginary parts and the modulus of the calculated and simulated reflection coefficients and impedances. Moreover, by observing the Smith chart in Figure 3.2.4a, it can be seen that the blue circle's center is not aligned with the orange's one, it is slightly lower. This observation motivates the addition of an imaginary part to the calculated Z_s, which is represented as a series inductance L_s as shown in Figure 3.2.5. This additional inductance could result from the non-metallic parts of the top surface [15].

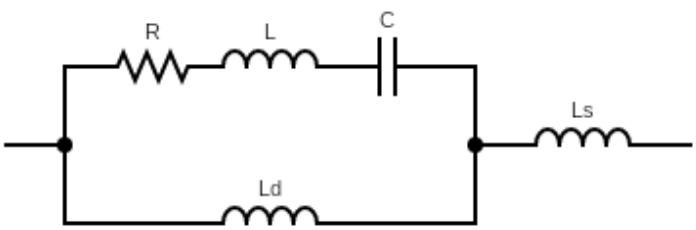

Figure 3.2.5 Final equivalent circuit of the model under study, where the series RLC represents the FSS, L_d represents the short-circuited dielectric layer and L_s represents the additional series inductance.

After the addition of L_s, the imaginary part of the impedance, changes to X'_{Z_s}. Whereas R_{Z_s} does not change, which means that at resonance, $R_{Z_s} = R_p$ and $F = F_{r_p}$ stay the same. This implies

that the value of F_{r_s} needs a re-evaluation in addition to its expression which is now equals to $\frac{1}{2\pi\sqrt{\left(L+\frac{L_s L_d}{L_s+L_d}\right)C}}$.

The new values of L and C are calculated to 220.5 pH and 77.44 fF respectively. To calculate L_s, it should be noted that at low frequency ($F < F_{r_p}$),

$$X'_{Z_s} = (L_s + L_d)\frac{\frac{\omega^2}{\omega_{R_s}^2} - 1}{\frac{\omega^2}{\omega_{R_p}^2} - 1}$$

Which gives the value of Ls=9.89 pH. These values result in a good fit between the simulation and calculated reflection coefficients' calculated impedances; this can be seen in Figure 3.2.6.

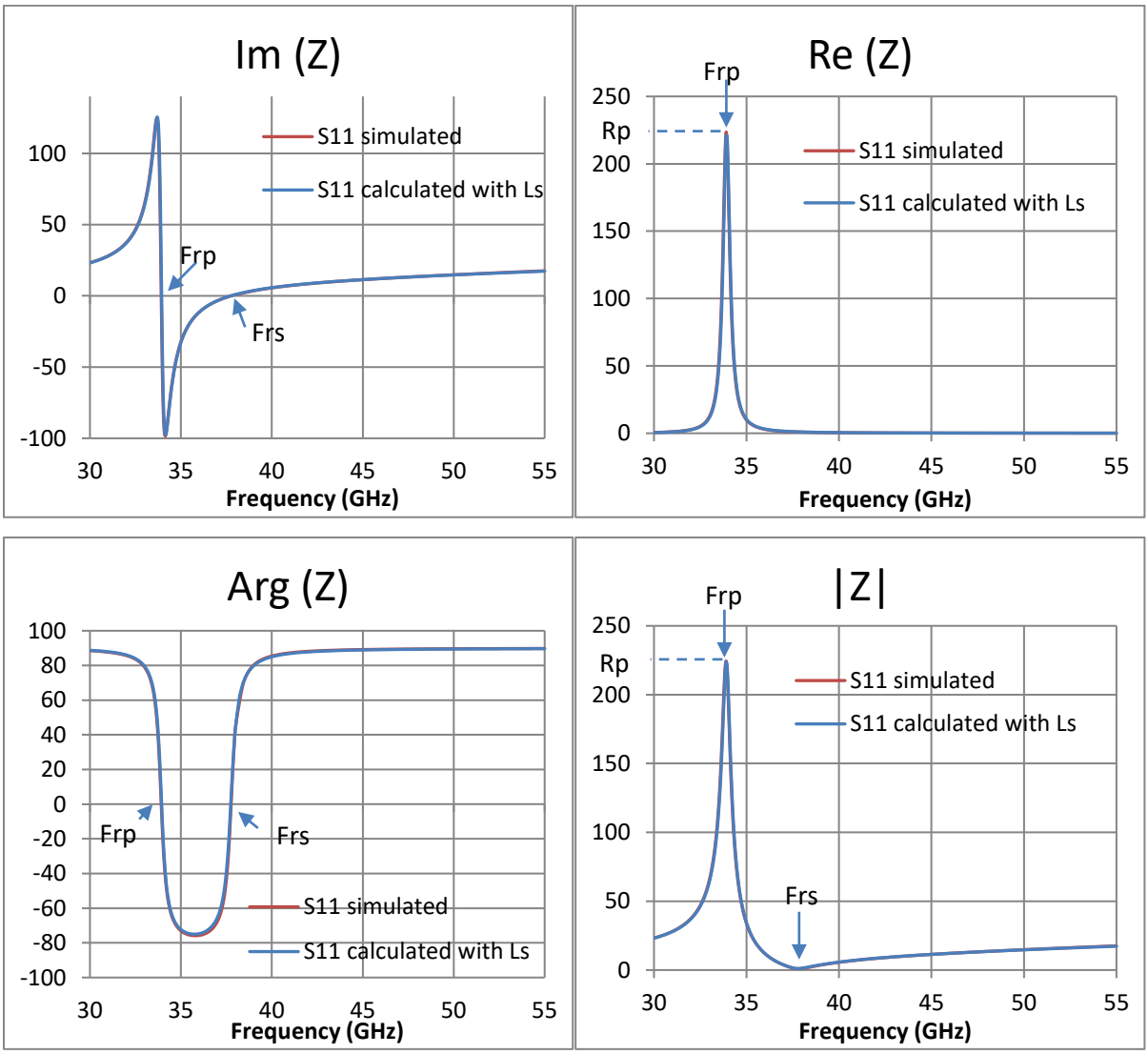

Figure 3.2.6 Comparison of impedances obtained by COMSOL simulation (red) and the final equivalent circuit analysis (blue) where L_d=62.8 pH, R=0.8 Ω, L=220.5 pH, C=77.44 fF and L_s=9.89 pH.

In the design of the final device, optimizing surface impedance also requires adjusting geometric parameters for a given dielectric thickness. In our case, the substrate consists of the liquid crystal layer infiltrated beneath the FSS recalling that the dielectric LC losses are responsible for the total absorption of incident energy under the condition of impedance matching.

The next part illustrates the influence of different parameters on the resonance frequency and the absorption level.

3.2.1.2 Parametric Study

This study consists of two stages:

- simulation (COMSOL) of the structure according to the different geometrical and material parameters.

- determination of resonance characteristics (resonance frequency, quality factor and maximum absorption) and values of the elements of the equivalent circuit elements.

3.2.1.2.1 Effect on Resonance Frequency:

Assuming that the impinging wave is trapped under the patch of side *a*, the equation usually used for the resonance frequency is the following:

$$F_{r_p} = \frac{c}{2a\sqrt{\varepsilon'}}$$

This equation gives the fact that the dielectric wavelength is equal to two times the patch size at the resonance. Based on the given equation, the resonance frequency depends mainly on the side of the patch a and the real part of the complex permittivity ε' of the liquid crystal and that it is inversely proportional to these two parameters [16]. So, we studied the influence of these two parameters.

In Figure 3.2.7 and Figure 3.2.8, the effect of the patch side *a* and the permittivity ε' of the dielectric layer on the absorption and the resonance frequency can be shown respectively, from which the evolution of frequency with respect to the size of the patch and the permittivity can be drawn (Figure 3.2.9a and Figure 3.2.9c). In addition, the two graphs show an agreement with the previous equation about F_{r_p} being inversely proportional to a and ε', where it is verified in Figure 3.2.9b and Figure 3.2.9d. As for the absorption, it can be seen that it increases with the size of the patch and decreases with the permittivity of the dielectric.

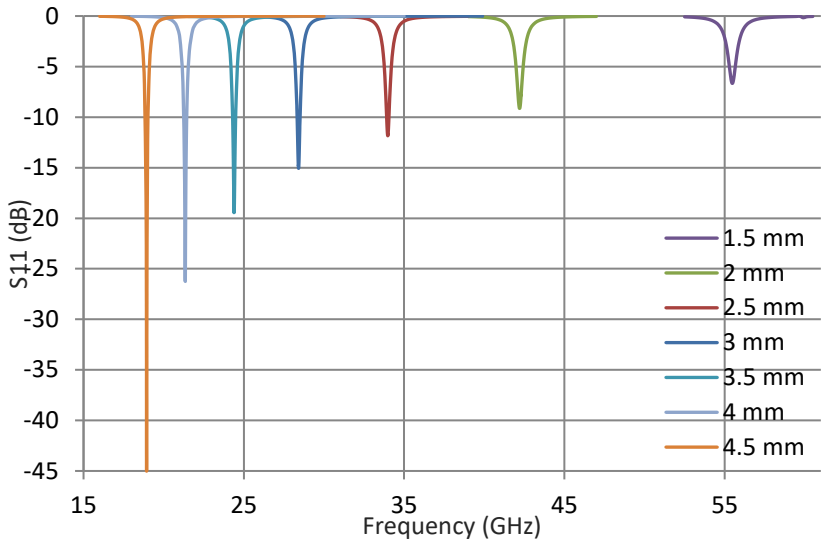

Figure 3.2.7 Influence of the patch side a on the resonance frequency and absorption of the model with the period=5 mm, the dielectric permittivity ε=3(1-j0.014) and the dielectric thickness t=50 µm.

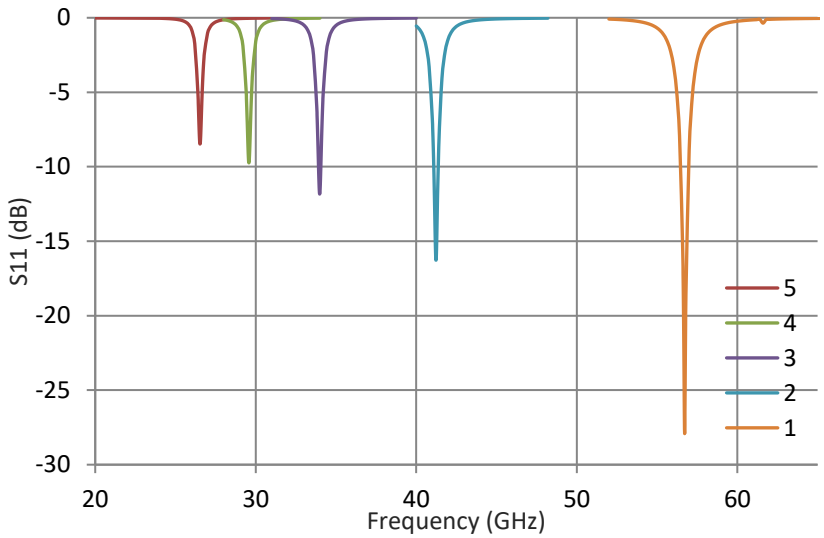

Figure 3.2.8 Influence of the dielectric permittivity on the resonance frequency and absorption of the model with p=5 mm, the patch side a=2.5 mm, the dielectric losses tanδ=0.0014 and the dielectric thickness t=50 µm.

Moreover, the theoretical behavior of the resonance frequency has been reported in Figure 3.2.9. It can be observed that the law for resonance frequency is verified with a small shift between the calculated and simulated values.

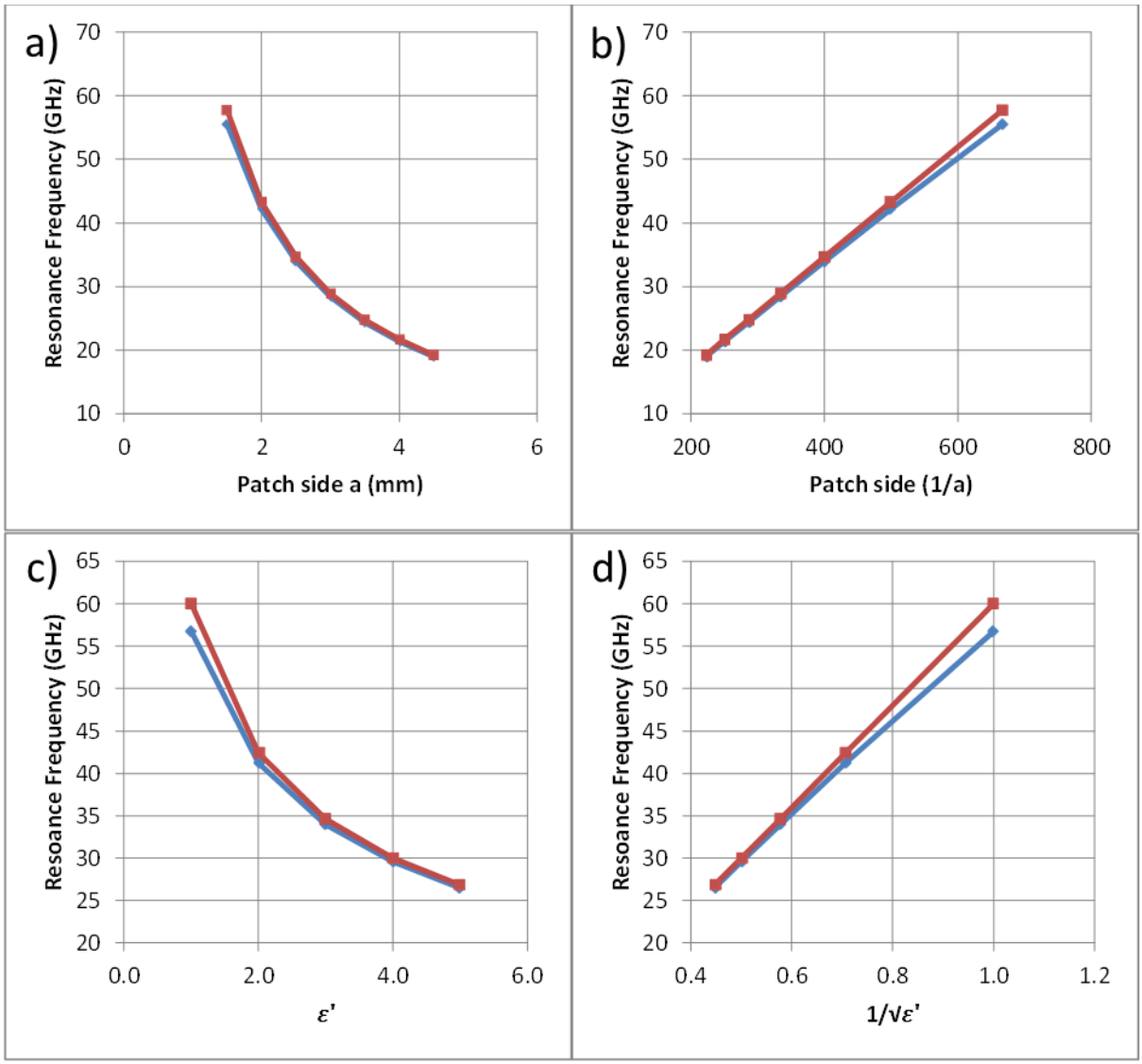

Figure 3.2.9 Variations in the resonance frequency as a function of (a) the side of the patch, (b) its inverse 1/a, (c) the real part of the LC permittivity ε' and (d) the inverse of its square root 1/√ε'. simulated (blue) vs. theoretical (red)

Although the relative error is relatively small (<6%), it is possible to reduce it to limit the frequency shift between the simulated and calculated. This phenomenon can be explained that it is due to having an effective permittivity in addition to an effective patch size due to fringing effect, so the equation of F_{r_p} becomes as following [7, Section 8.9]:

$$F_r = \frac{c}{2a_{eff}\sqrt{\varepsilon_{eff}}}$$

$$\frac{a}{t} > 1$$

$$\varepsilon_{eff}(0) = \varepsilon_{eff}(f = 0) = \frac{\varepsilon + 1}{2} + \frac{\varepsilon - 1}{2\sqrt{\left[1 + 12\frac{t}{a}\right]}}$$

$$a_{eff}(0) = a + 2\Delta a$$

$$\Delta a = \left[0.412\frac{(\varepsilon_{eff}(0) + 0.3)(\frac{a}{t} + 0.264)}{(\varepsilon_{eff}(0) - 0.258)(\frac{a}{t} + 0.8)}\right]t$$

However, with the patch having a dispersive behavior, the effective permittivity ε_{eff} depends on frequency. Knowing that $f = f_{r_p}$, the model used to calculate $\varepsilon_{eff}(f)$ is the following:

$$\varepsilon_{eff}(f) = \varepsilon - \left[\frac{\varepsilon - \varepsilon_{eff}(0)}{1 + \frac{\varepsilon_{eff}(0)}{\varepsilon}(\frac{f}{f_t})^2}\right]$$

$$f_t = \frac{Z_c(0)}{2\mu_0 t}$$

$$Z_c(0) = Z_c(f = 0) = \frac{\frac{120\pi}{\sqrt{\varepsilon_{eff}(0)}}}{\frac{a(0)}{t} + 1.393 + 0.667\ln\left[\frac{a(0)}{t} + 1.444\right]}$$

The results of using the above equations are given in Figure 3.2.10 and Figure 3.2.11, where it is shown that by taking into account a_{eff} and ε_{eff}, there is an improvement of the predicted resonance frequency values.

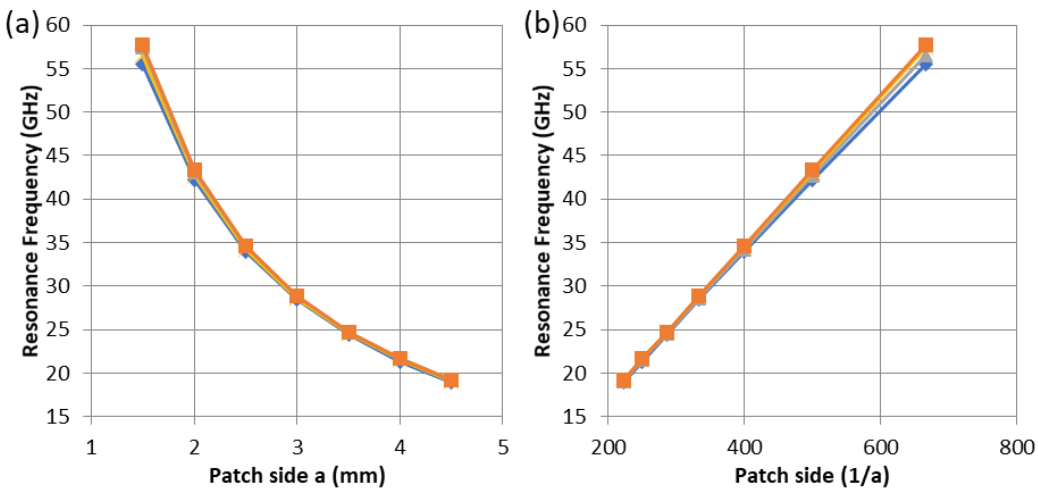

Figure 3.2.10 Variations in the resonance frequency as a function of (a) the side of the patch, (b) its inverse 1/a. Simulated (blue), calculated: ε=3, Δa=0 (orange), calculated ε=3, a=a_{eff}(f=0) (grey), and calculated ε=3, a=a_{eff}(f=f) (yellow)

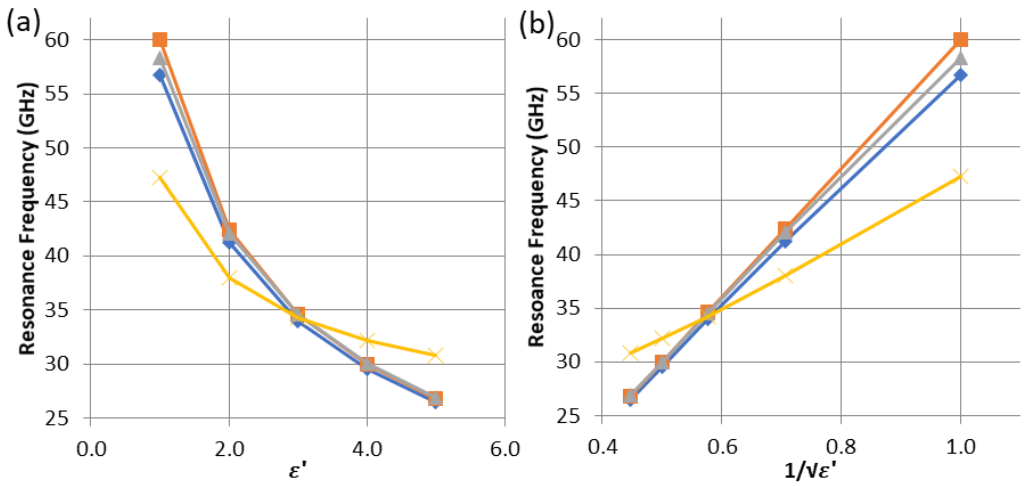

Figure 3.2.11 Variations in the resonance frequency as a function of (a) the real part of the LC permittivity ε' and (b) the inverse of its square root 1/√ε'. Simulated (blue), calculated: a=2.5 (orange), calculated a=2.5, $\varepsilon=\varepsilon_{eff}(f=0)$ (grey), and calculated a=2.5, $\varepsilon=\varepsilon_{eff}(f=f)$ (yellow)

3.2.1.2.2 Influence of thickness

Thickness is an important parameter for LC because it has to be driven with a reasonable voltage.

Figure 3.2.12 displays the frequency dependence of the modulus of the reflection coefficient of the metasurface by taking the thickness of the substrate as a parameter.

As observed in Figure 3.2.12, thickness of the dielectric layer affects the level of absorption and the resonance frequency. On the other hand, with thickness, we can find an optimum absorption in contrast with what has been presented with the variation of the patch side and the permittivity of the dielectric. For the used parameters, an optimal thickness corresponds to a near-total absorption which has a -50 dB rejection dip for a LC thickness of 80 µm.

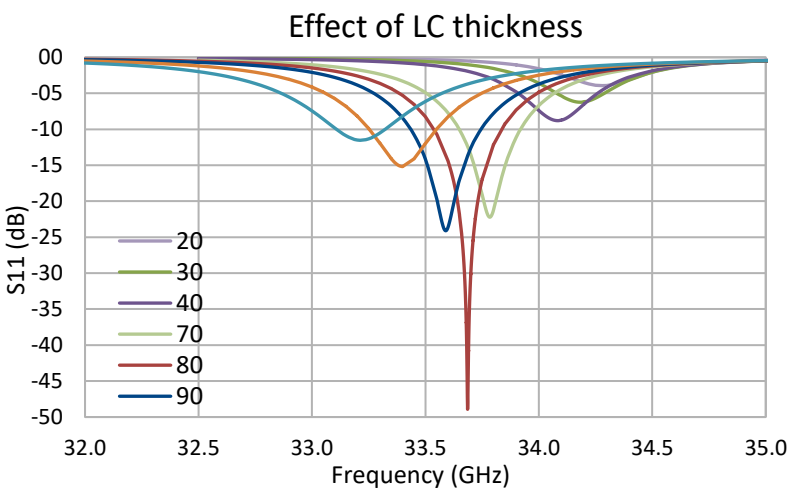

Figure 3.2.12 Influence of the dielectric thickness on the resonance frequency and absorption of the model with p=5 mm, a=2.5 mm, tanδ=0.014 and the dielectric thickness t=50µm

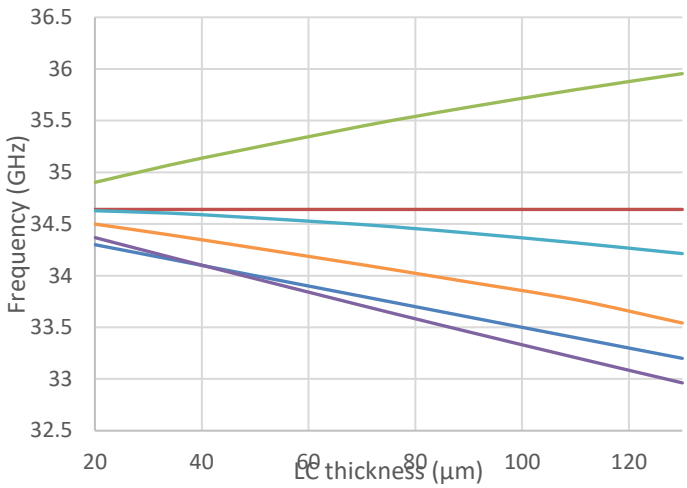

Figure 3.2.13 Effect of thickness on resonance frequency, between simulated and calculated. Simulated (blue), calculated: a=a, ε=ε (red), calculated: a=a, ε=ε_{eff}(f=0) (green), calculated: a=a_{eff}, ε=ε (purple), calculated: a=a_{eff}, ε=ε_{eff}(f=0) (cyan), calculated: a=a_{eff}, ε=ε_{eff}(f=f) (orange)

The thickness dependence of $R_p = Re\left(Z_s\left(F_{r_p}\right)\right) = \frac{L_d^2 \omega_{Rp}^2}{R}$ at the resonance frequency $(Im\left(Z_s\left(F_{r_p}\right)\right) = 0)$ and the minimum reflective coefficient modulus are shown in Figure 3.2.14. The variation in LC thickness has the effect of linearly increasing R_p passing through 377 Ω. When R_p equals the characteristic impedance of the vacuum Z_0=377 Ω , the absorption is almost total and $|S_{11}|_{min} = 0$. This behavior can be explained by the following relations between impedance and reflection coefficient:

$$Z_s\left(F_{r_p}\right) = R_p = Z_0 \frac{1 + S_{11}(F_{r_p})}{1 - S_{11}(F_{r_p})}$$

$$|S_{11}|_{min} = \frac{R_p - Z_0}{R_p + Z_0}, \text{ where } Z_0 = 377\ \Omega$$

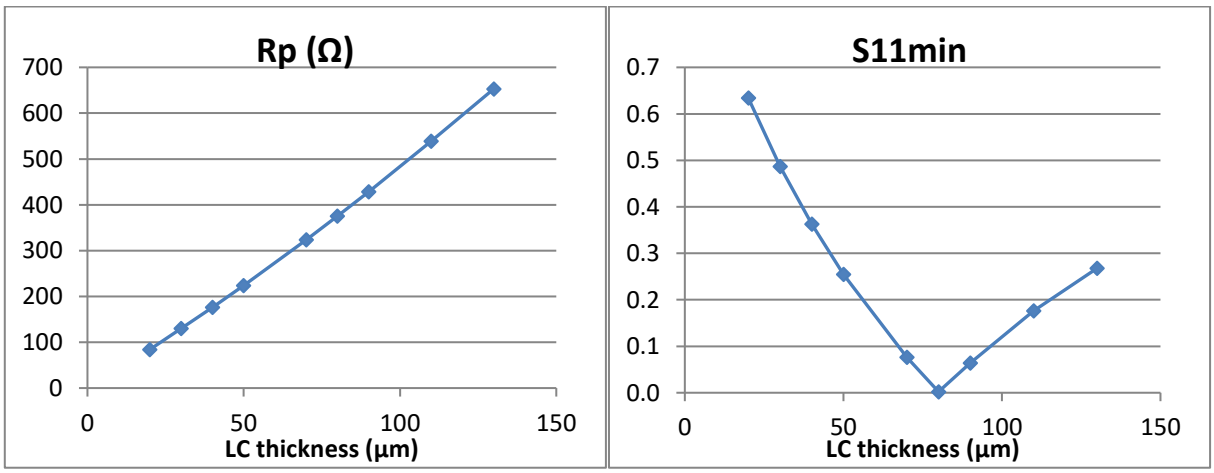

Figure 3.2.14 Effect of dielectric layer thickness on absorption: module of impedance at resonance and minimum reflective coefficient module S_{11min}

Another approach to analyze the absorption is to study the quality factors versus the thickness of the LC. The total quality factor Q_t is connected with two other quality factors which are the dissipative quality factor Q_d and the radiative quality factor Q_r with the following expression:

$$\frac{1}{Q_t} = \frac{1}{Q_r} + \frac{1}{Q_d}$$

$$Q_t = \frac{Q_d\, Q_r}{Q_d + Q_r}$$

In our case, Q_d, depends only on the dielectric losses and can also be expressed by a relation between the different elements of the equivalent circuit model because it represents the quality factor of the resonator.

$$Q_d = \frac{1}{\tan\delta} = \frac{(L + L_d)\omega_{r_p}}{R} = \frac{1}{RC\omega_{r_p}} = \frac{1}{R}\sqrt{\frac{L + L_d}{C}}$$

Where $R = \frac{{L_d}^2 {\omega_{r_p}}^2}{R_p}$.

Moreover, Q_r is the quality factor when R_p is equal to the vacuum characteristic impedance Z_0 because it represents the quality factor when there is impedance matching which means $R_0 = \frac{{L_d}^2 {\omega_{r_p}}^2}{Z_0}$.

$$Q_r = \frac{1}{R_0 C\omega_{r_p}} = \frac{Z_0}{RR_p C\omega_{r_p}} = \frac{Z_0}{R_p} Q_d$$

It can be seen in Figure 3.2.15, when the thickness increases, there is a decrease in the external quality coefficient Q_r while the intrinsic quality factor Q_d does not significantly vary. Finally, the overall Q_t quality coefficient decreases with thickness. To decide optimal thickness, the Q_r and Q_d quality factors should be equal [17],

$$Q_t = \frac{Q_d}{2} = \frac{Q_r}{2}$$

and the coupling coefficient is $\beta = \frac{Q_r}{Q_d} = \frac{Z_0}{R_p} = 1$, $(R_p = Z_0)$.

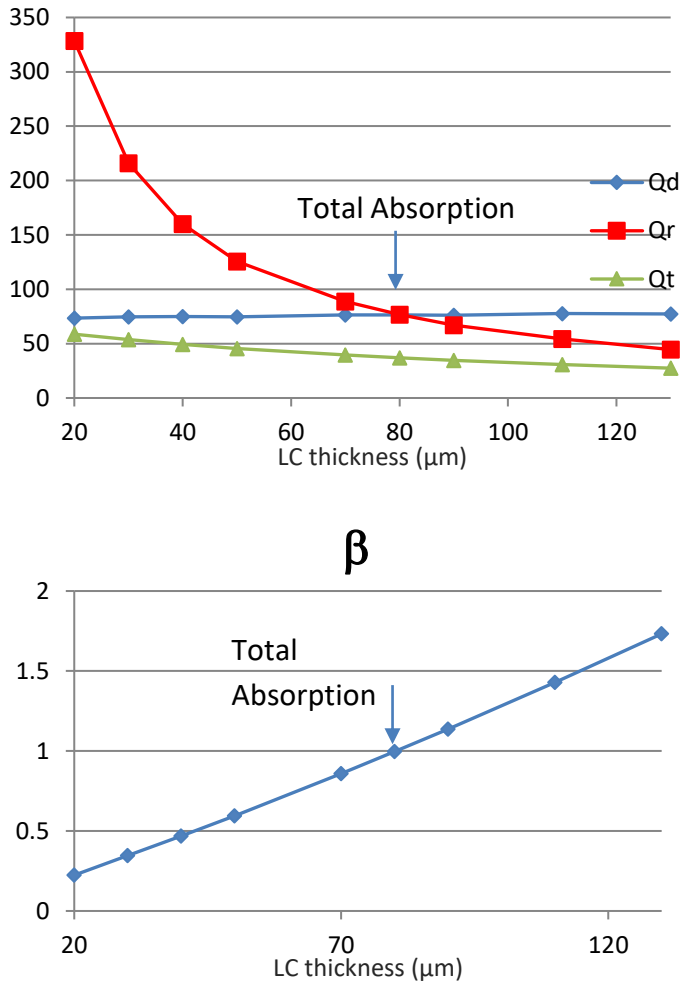

Figure 3.2.15 Effect of dielectric layer thickness on absorption: Q_d, Q_r and Q_t quality coefficients and the coupling coefficient β

Moreover, Figure 3.2.16 gives the results of the optimization of the inductance L and the capacitance C in the equivalent circuit for different dielectric thicknesses.

The inductance increases quasi linearly with the LC thickness while the capacitance decreases illustrating the influence of the ground plane on C.

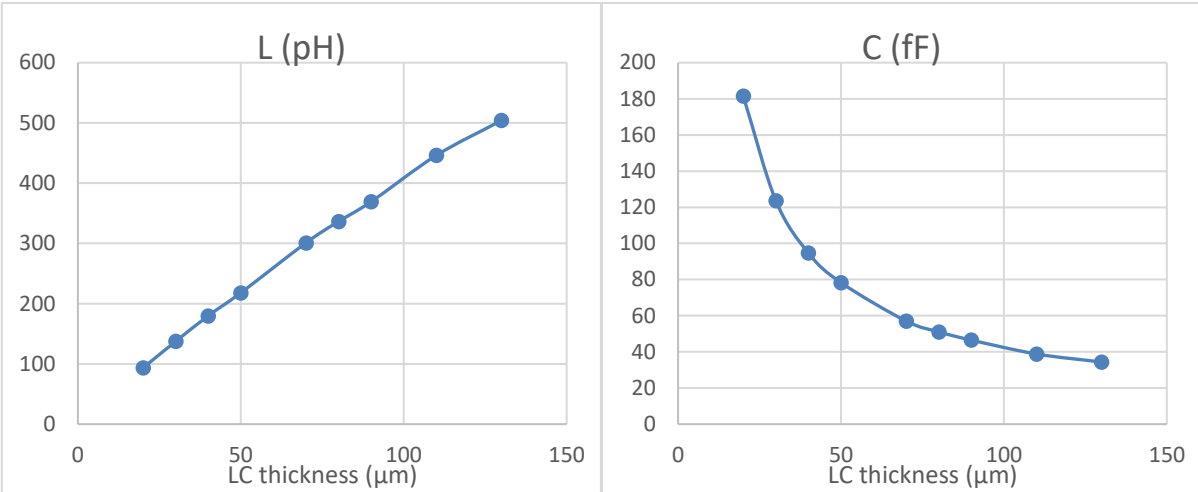

Figure 3.2.16 Variations of the inductance and the capacitance of the equivalent circuit model versus the dielectric thickness. (p=5 mm, a=2.5 mm)

3.2.1.2.3 Influence of dielectric losses

The dielectric losses tgδ modify only the absorption of the metasurface whereas it has no effect on resonance frequency (Figure 3.2.17). No absorption is observed for low and high losses materials. In the middle range, the absorption increases with losses up to total absorption (tgδ ≈ 0.009) and then decreases.

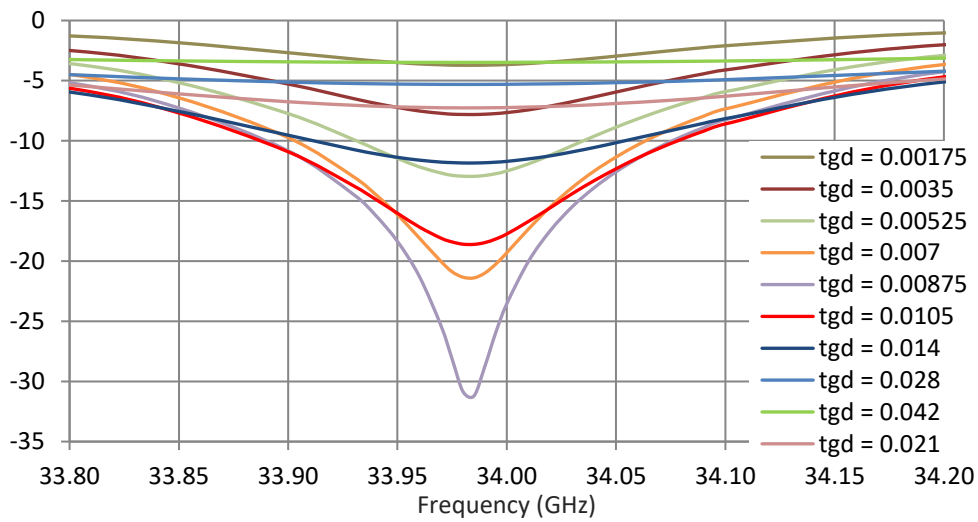

Figure 3.2.17 Influence of the LC dielectric losses tgδ on the resonance frequency and absorption of the model with p=5 mm, the dielectric permittivity ε=3(1-j0.014) and the dielectric thickness t=50 µm

A study of the equivalent circuit elements versus dielectric losses shows that these last have no effect on the inductance L and the capacity C and only the resistance depends of dielectric losses (Figure 3.2.18). The previous behavior of absorption is directly connected with the equivalent resistance Rp. This resistance is equal to the free space impedance Z_0 at total absorption.

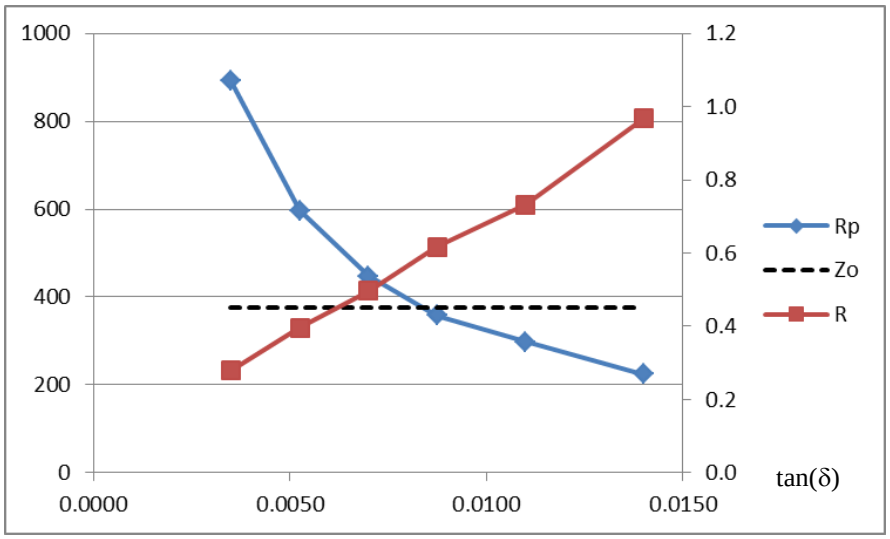

Figure 3.2.18 Influence of the LC dielectric losses tgδ on the resistance R, Rp with p=5 mm, the dielectric permittivity ε=3(1-j0.014) and the dielectric thickness t=50 µm

3.2.1.2.4 3.2.1 Influence of the glass slab

As previously reported, in our case, the substrate corresponds to a liquid crystal layer infiltrated underneath the FSS, with the aim of manufacturing a voltage controlled metasurface. In order to infiltrate the liquid crystal by capillarity and perform the surface treatment necessary for its initial orientation, the FSS consisting of patches is printed onto on a glass slab (thickness of t_{glass}, permittivity ε'_{glass}) [7]. As the impinging electromagnetic wave is transmitted through this glass layer, it is important to study the influence of this glass slab on the device performance.

Figure 3.2.19 and Figure 3.2.20 show the influence of the glass thickness t_{glass} and of its permittivity ε'_{glass} on the glass modulus of the metasurface reflection coefficient upon frequency. For the two cases, one observes a strong decrease of the resonance frequency. As for the LC thickness, an optimal value for the thickness t_{glass} and the permittivity ε_{glass} aiming quasi unit absorption can be found.

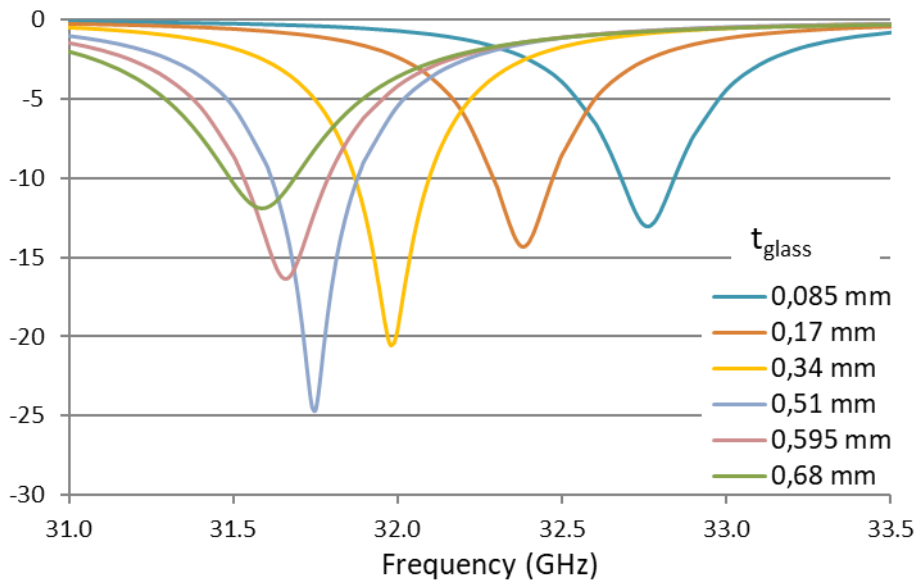

Figure 3.2.19 Modulus of the reflection coefficient as a function of the thickness of the glass blade (ε_{glass}=5)

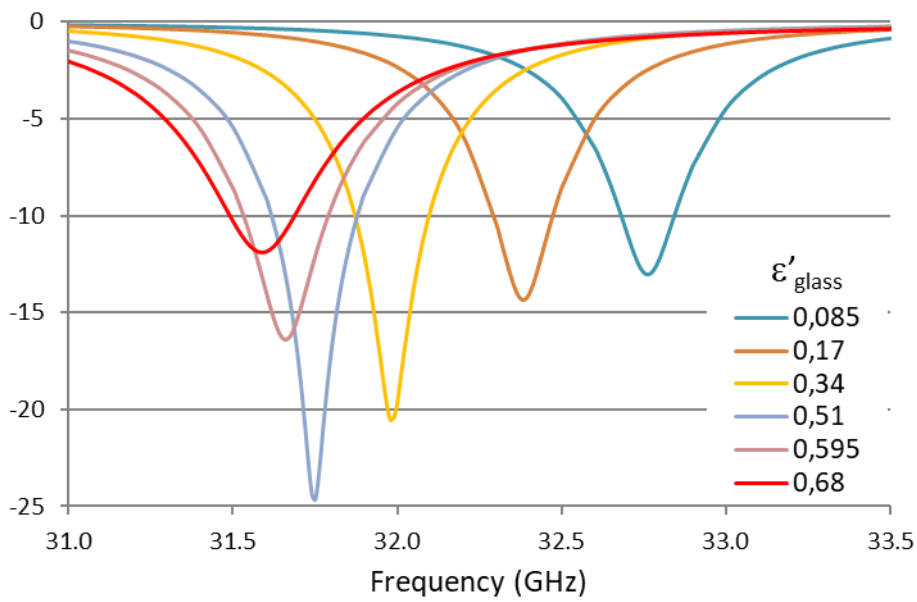

Figure 3.2.20 Modulus of the reflection coefficient as a function of the permittivity ε'_{glass} of the glass blade (t_{glass}=0.68 mm)

To model the metasurface with a glass blade, we consider the glass blade as a no losses dielectric layer of length t_g and permittivity ε'_g (characteristic impedance $Z_{cg} = \frac{Z_0}{\sqrt{\varepsilon' g}}$, wavelength $\lambda_g = \frac{\lambda_0}{\sqrt{\varepsilon' g}}$) and we suppose that the addition of the glass layer does not alter the impedance (Z_{FSS}) of the FSS structure (Figure 3.2.21).

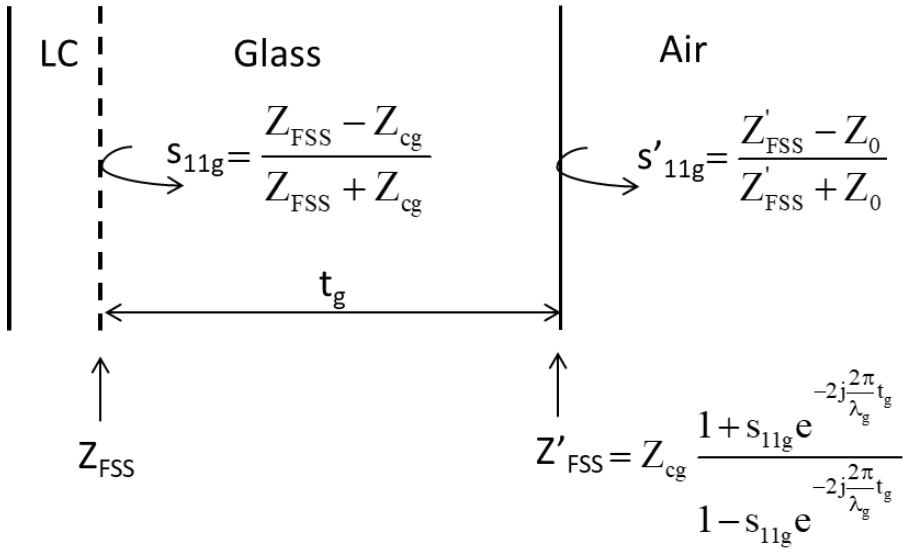

Figure 3.2.21 Model of the metasurface with a glass blade

An example of modeling is reported in Figure 3.2.22. The figure compares the reflection coefficients obtained from COMSOL simulations (red curves) and the previous model (blue curves) with (full lines) and without glass blade (dotted lines). The cases with and without glass blade are obtained in adding or suppressing the glass blade from COMSOL simulations. The results are in good agreement. In the case without glass, the difference between COMSOL simulated and calculated data is probably connected with the influence of glass on the impedance Z_{FSS}.

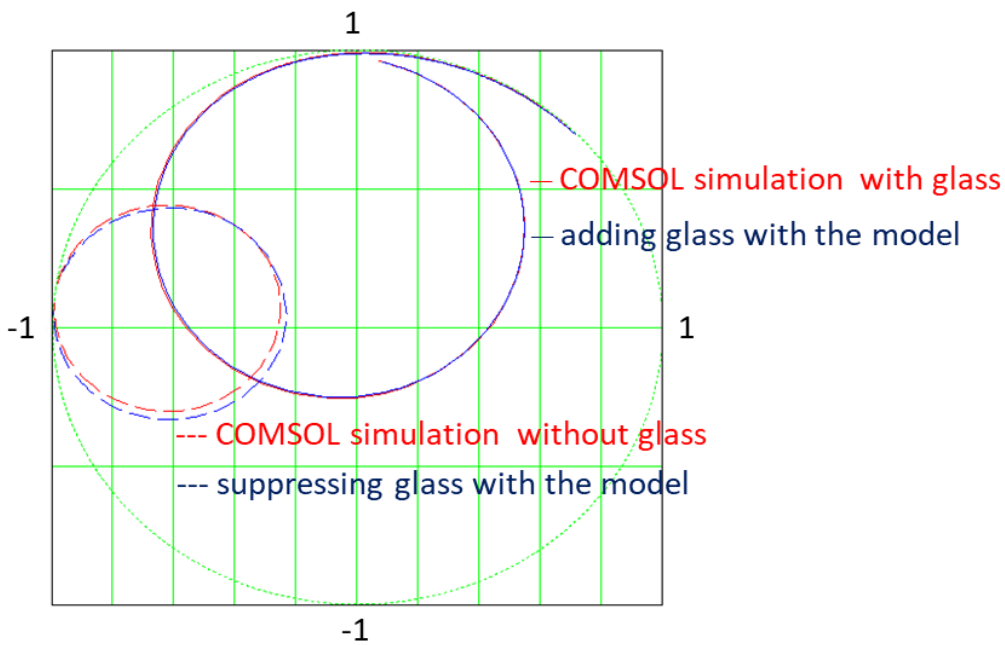

Figure 3.2.22 Comparison of the reflection coefficients (Smith chart) obtained from COMSOL simulation (red) and the previous model (blue) adding (full lines) and suppressing glass blade (dotted lines) from simulations (a=2.5 mm, p=5 mm, t=50 µm, ε=3, t_g=0.68 mm, ε_g=5

Conclusion

To sum up, full wave analysis by means of the COMSOL software allowed us to define the geometrical dimensions of the layout of the mask whose fabrication will be reported in the next chapter. The optimization of these dimensions was performed for two values of the LC layer thickness, 10 and 50 µm respectively and for a metasurface infiltrated by LC 5CB. For determined LC properties, let us emphasize that the three following geometrical characteristics: (i) patch side influencing mainly the resonant frequency and (ii) array period and LC thickness are the most relevant parameters in the achievement of a quasi-unit absorption coefficient (zero reflection and transmission). Parametric studies varying the material properties were carried out in this chapter showing as expected and in agreement with the analytical study presented in Chapter 2, a frequency dependence inversely proportional to the square root of the dielectric constant and an absorption level that is strongly dependent on the impedance matching criterion. With an average permittivity $\bar{\varepsilon} = \frac{\varepsilon_{\parallel}+\varepsilon_{\perp}}{3}$ around 2.8 and loss tangent between 1 and 2%, LC 5CB was thus chosen for further optimizing the geometrical dimensions notably by taking the glass substrate and the narrow interconnect strips into account. By post simulation, assuming the same metasurface layout infiltrated by LC 1825 instead of 5CB, it was demonstrated that high performance can be maintained without requiring the fabrication of a new mask set.

Despite their accuracy and confidence in their validity, the numerical optimization of these parameters however requires relatively massive and time-consuming calculations. Even by introducing PEC/PMC boundary conditions instead of periodic master slave boundary conditions for uniformly controlled metasurfaces and normal incidence. Therefore, the full-wave approach was completed by the development of an analytical study based on the transmission line formalism (TLM) and equivalent circuit model (FSS-type approach). Material and geometry dependence of the resonant frequency and reflectivity level, via closed forms, were reported and on the other hand allowed us to evaluate the impact of the glass supporting slab whose thickness is of the order of 1 mm. The impact of fringing field effects was also evaluated. For the deep-subwavelength LC thickness in the tens or few tens' micrometers, it appears that such TLM-FSS approach quantitatively describes the reflectivity spectra provided to drastically modify the value of the capacitance in the FSS equivalent circuit. This modification can be understood by the proximity of the ground plane that forms with the top metal array a parallel capacitance while in a FSS approach the edge capacitance is of major concern. It thus appears that an equivalent circuit description, that includes the top and rear metal plated described by a parallel LC configuration is preferable to the one based on the series FSS-type LC equivalent circuit (TLM approach is still necessary for the parallel plate configuration for describing the outer regions not

covered by metal on top). This parallel plate model is beyond the scope of this design chapter and will be one of the future developments of the present work.

Chapter 4: Realization and Characterization of LC Tunable Metasurfaces

Introduction

This chapter is devoted to the experimental assessment of the reflectivity spectra that were measured in free space in a non-anechoic environment, in the Ka band (26-40 GHz). Prior to their presentation, we first describe the technological aspects with the manufacturing by microelectronics techniques of the micro-structured top and rear glass substrates with their assembly after an alignment layer deposition. Then, the set up in a bi-static configuration is described along with calibration and measurement techniques that allow us to determine the level of absorption of equivalently of the reflection coefficient.

4.1 Fabrication and assembling

Let us recall that prototypes I and II, whose geometries were defined by means of full wave electromagnetics simulations and their expected performances explained on the basis of the TLM approach as shown previously, consist of a stack of various dielectric substrates (glass and LC layers) and metal films. For explaining the technological steps in the next sections devoted to fabrication and assembling, Figure 4.1.1 shows an expanded view of the various layers for prototype I with a patch side *a* of 2.5 mm and a period *p* of 5 mm. Interestingly, Prototype II has the same structure as Prototype I with one difference of having a period p=3.2 mm that is nearly equal to the size of the patch a=3 mm making a more compact figure. From this figure it can be seen that basically a voltage-controlled LC metasurface consists of a uniformly metallized glass substrate used as a back plane, and another glass substrate that is covered by a periodic array. The inset in this figure shows the layout of this array with the period "p" of the square lattice array and the side of the square-shaped metal patches "a" where all the patches are interconnected with very narrow strips of width "w" at a submillimeter scale equal to 150 µm (aspect ratio ≈ 17) for not disturbing the dynamic response of the system. As a consequence, it seems very tricky to manufacture such a micro-structured metallized substrate by means of conventional Printed Circuit Board (PCB) technology. In addition, for prototype II, there is an additional challenge due to the fact that the patches are in close proximity thus increasing the difficulty in the fabrication of this prototype.

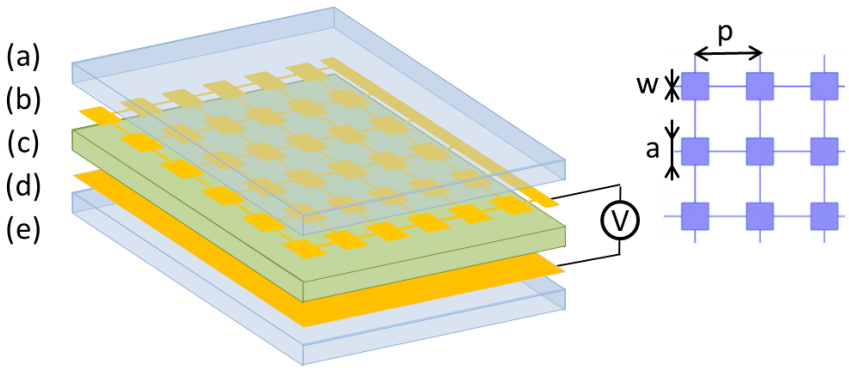

Figure 4.1.1 Expanded view of a LC controlled metasurface: (a) glass plate, (b) array of interconnected patches, (c) nematic liquid crystal (not in scale), (d) uniform metallic plate, (e) glass plate.

4.1.1 Manufacturing Techniques

The manufacturing of the two metalized glass substrates was conducted at the CMNF (Center of Micro and Nano Fabrication) in the central lab of IEMN. Such a center is one of the main laboratories of the RENATECH (Réseau National de Technologies) NETWORK. All the process described shortly below were performed by Karine Blary of the CMNF staff.

Hereafter without detailing all the technological steps, we outline the various decisions that have been taken, in particular with respect to the metal layer thickness. The latter plays a major role in the operation of the devices in addition to the concerns that were specifically developed owing to the relevant dimension here again on a micron scale whereas most of the project of the CMNF center address submicron scale.

The first decision to take concerns the glass substrate. Even if the devices are designed for operating at a relatively high frequency (Ka band) with respect to the common microwave bands such as X band, and hence small wavelength, it is imperative that the device's transverse dimension corresponds to several wavelengths by bringing to mind that at 30 GHz the wavelength is 1 cm. On the other hand, the area of the metasurface is limited by the equipment that will be used for resist spinning and metal deposition in a high vacuum deposition chamber.

In addition, the thickness of this substrate is also quite important notably with respect to its rigidity and its planarity from the mechanical point of view as well as its dielectric properties which also plays a key role in the matching conditions as seen in the design section. In fact, we used two kinds of substrate for the fabrication of prototypes I and II.

For prototype 1, an ITO glass substrate with a thickness of 680 µm that was commercially available (Military University of Technology, Warsaw, Poland) was used for the patch array. Devoted initially to the fabrication of photonic devices, the ITO layer was removed by using the following chemical etchant (Aqua Regia) for achieving bare glass slabs. The relative permittivity in microwave was assumed around 5 neglecting its losses. Moreover, a glass substrate of thickness 3 mm was used for the side having a uniform metallization representing a short circuit.

For prototype 2, a 1.1 mm glass substrate supplied by (Verre Industrie) was used for both sides, the patch array and the short circuit. Its relative permittivity in the microwave regime given by the supplier is 5.7 with no information about the loss tangent that is however presumably quite low.

For adapting the transverse dimensions of the glass substrates (Verre Industrie), it was necessary to carve them to specific dimensions and pointing out the difficulty of this technological operation for ultra-thin (~1 mm or less) glass substrates with a large area (several centimeters).

Structuring the metal pattern deposited on the top glass (Figure 4.1.1) was conducted first by fabricating a photolithography mask.

For prototype 1 with a square-shaped patch of width a=2.5 mm and a period p=5 mm, the number of the basic cells was 14x13 = 182 cells over the active area. The photolithography mask was written by e–beam lithography sequentially after deposition of E-beam resists [1,2]. The final layout of prototype I is shown in Figure 4.1.2, illustrating the top glass and rear glass substrates after undergoing selective and uniform metallization, respectively, where the un-metallized region for the rear plate was due to the clamping system for evaporation.

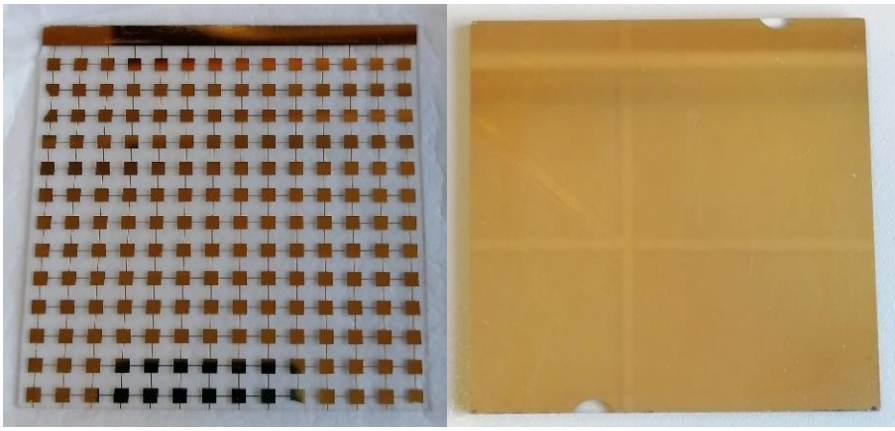

Figure 4.1.2 Photos of the top and rear metal plates for prototype I printed onto 680 µm and 3 mm glass substrates respectively. The glass area is 7x7 cm2. The patch side is 2.5 mm, the array lattice period is 5 mm

On the other hand, prototype 2 is denser. With the patch having a width of 3 mm and a period of 3.2 mm as can be seen from Figure 4.1.3, the number of the basic cells was 22x21 = 462 cells compared to that of prototype I. The fact that the array was dense also determines the choice whether to use a positive or a negative resist in order to optimize the e-beam writing time which is usually several hours.

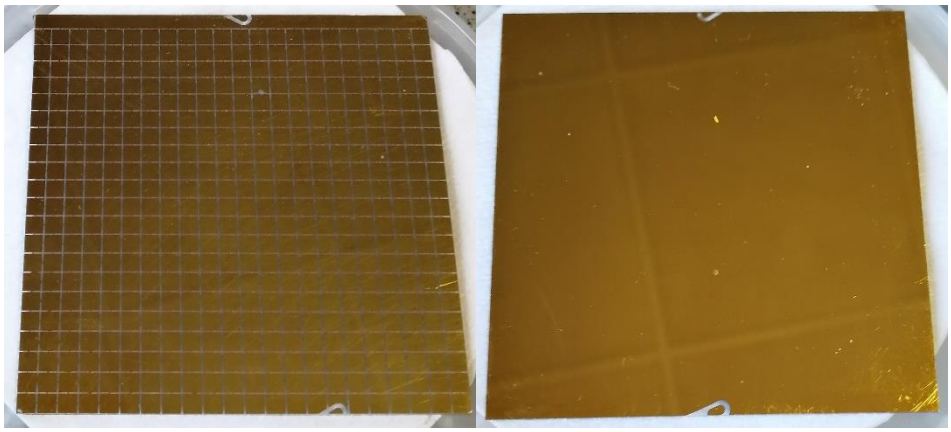

Figure 4.1.3 Photos of the top and rear metal plates for prototype II manufactured with two 1.1 mm-thick glass substrates having an area of 7x7 cm2. The patch width is 3 mm for a period equal to 3.2 mm

The selective deposition of metal, which in our case is gold with a bulk conductivity around $4x10^7$ S/m, was carried out by a lift off technique. This method allows a quite accurate definition of the

metalized patches and of the interconnecting strips that have a width of 150 µm. The targeted metal thickness was 1 µm. This thickness is a relatively big value with respect to generic metal deposition by evaporation that are used for actives devices for example such as millimeter FETs which are fabricated in the CMNF lab. As a consequence, the choice of the resists was adapted to this constraint.

Another specificity in the lift-off deposition and evaporation processes, was the use of the electron gun heating [3] in the high vacuum deposition chamber instead of the conventional Joule heated cell. Such a condition has increased the gold deposition rate dramatically by evaporation thus minimizing the processing time. In the following it will be shown by using a four probes characterization of the sheet resistivity that such a process has however not degraded the quality of the gold films.

In the next section we will explain how we assembled these two prototypes by also describing the means to have the LC molecules in planar orientation by a rubbed polymer which is one of the most critical issues for a voltage controlled metasurface to successfully operate.

4.1.2 Assembling Techniques

As portrayed before, two kinds of array patterns were manufactured either with a period equal to double the square-shaped patch or in a denser configuration with a period slightly bigger than the patch's width. The results of the full simulations indicate that by means of this two-layout set (dense or sparse) it would be possible to assess the reflectivity properties of different LCs by the ability to unmount the assembled metasurfaces for each measurement. This is the case in Chapter 3 where we consider a high birefringence (dielectric anisotropy) LC 1825 for reflectivity assessment of both prototypes.

As a consequence, prior to each assembling stage, the metallized surfaces are thoroughly cleaned with acetone and alcohol followed by subsequent deposition of an alignment polymer layer whose choice and processing conditions are shortly described in the following section.

The different steps of prototypes assembling given in Figure 4.1.4 will be successively described.

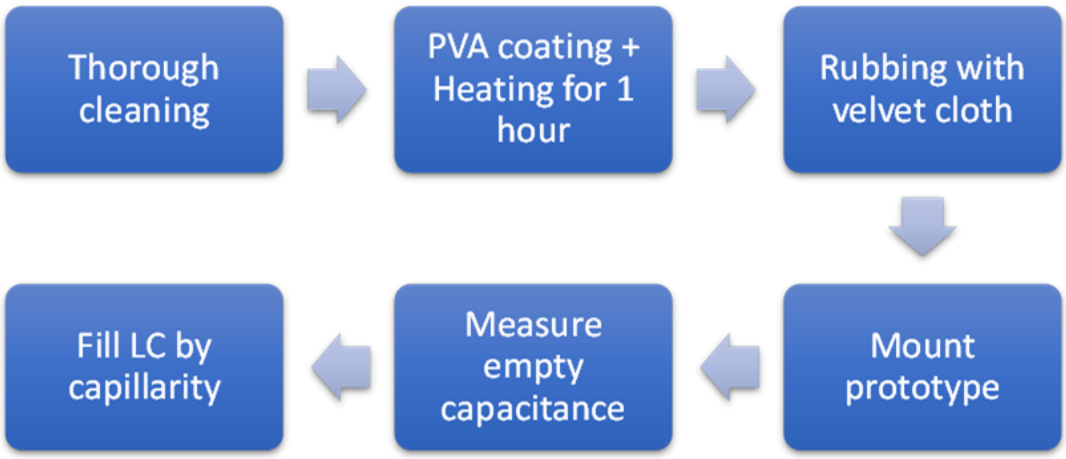

Figure 4.1.4 Different steps of prototype assembling

4.1.2.1 Alignment Layer Deposition

The next stage concerns the surface treatment of the two metalized glass substrates with an alignment layer of a rubbed polymer targeting a planar orientation of the optical axis along the transverse direction of the metasurfaces [4,5].

As already introduced in the first chapter in the section devoted to the background on LC technology, Liquid Crystal molecules can be orientated by an electric or a magnetic field or by means of a surface treatment by an alignment layer. Application of a bias voltage between the top and rear metal plates of the MIM – type capacitance – like structure creates a uniform driving field vector whose orientation is normal with respect to the electrodes. Therefore, with the application of a driving voltage, the elongated LC molecules orientate their optical axis in a normal direction to the metal LC interface (Homeotropic orientation). When the driving voltage is cut between the two electrodes, the molecules should return to their initial state with an optical axis oriented along the transverse direction. Noting that the driving voltage is a quasi-static ac-voltage with an operating frequency of 10 kHz, such a bias-less condition is equivalent to a rms value of 100 mV in order to be able to measure capacitance of the prototype in the latter situation. To achieve this no-voltage condition, the orientation of the LC is governed by the rubbing direction of the polymer layer whose role is of utmost importance for the reorientation of the LC molecules to have a successful dynamic control of the resonance frequency of the micro-resonator's arrays.

To illustrate the recent progress about such topic, let us quote the recent publication about the use of graphene 2D layer.

In the present work devoted to the use of conventional Cyano-biphenyl-type nematics, it was decided to use a PVA (Poly Vinyl Alcohol) surfactant that was used with success over the past in the lab. Moreover, it will be shown in the next section that using a PVA alignment layer is also suitable for a metasurface infiltrated by a high anisotropy LC 1825.

4.1.2.2 PVA/DI solution

For the solution preparation, we used the same composition and deposition conditions that were reported in the two following references.

This PVA solution (Sigma-Aldrich) was prepared in the chemistry lab of concentration 1mg/ml in de-ionized water (DI). PVA does not show good solubility in DI water, so this problem was resolved by the following steps to have a complete transparent solution:

1. After 1 hour of ultrasonication, we heat it up moderately to 50°C and then slowly to reach 90°C maximum.
2. We keep the isothermal state of the solution at 90°C for 1 hour.
3. Then we do another 30 minutes of ultrasonication.

4.1.2.3 Spin coating

The resulted solution is then deposited on the surface of each metallized glass substrate using a syringe and then by spin coating method it is spread evenly on each surface. The rotation speed that was used is 3000 RPM for 45 seconds. We have not checked the uniformity or the thickness of PVA on the substrates before, but we can use the profilometer to check this two information.

4.1.2.4 Thermal heating

As a final stage for applying the surfactant, both substrates are put in the oven at 100°C for 1 hour to dry completely.

4.1.2.5 Rubbing

After the substrates are dry, they are rubbed by using a clean velvet Fabric in a unidirectional manner to facilitate the orientation of the LC molecules when infiltrated between the two metallized glass substrates whose assembling is outlined in the next section. As a last comment let us mention that some references in the literature indicate that such a rubbing can be performed by rotation, but regarding the square shaped metasurface we are using, the choice of a unidirectional rubbing seems more appropriate.

4.1.2.6 Assembling:

Mica spacers (Meta fix) are positioned at each edge of the prototype to create an even cavity between the two metallized glass plates that are maintained by clamps as illustrated in Figure 4.1.5. The area of these micas is chosen such that the disturbance of the quasi-static and the microwave response of the device is decreased as much as possible. That to be done, their dimension is chosen so that they have a qualitatively low influence on the capacitance versus voltage and the reflectance spectra.

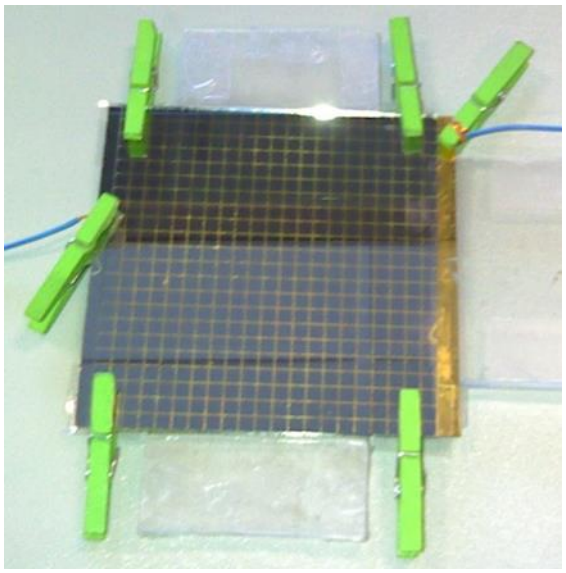

Figure 4.1.5 Photo of the complete assembled device. Wires are connected to the impedance analyzer for electrical driving and capacity measurements.

4.1.2.7 Filling

After assembling the prototype at room temperature, the nematic LC is infiltrated by capillarity through the cavity between the two metallized glass substrates [6]. This method ensured the non-formation of bubbles inside the device due to the forces of capillarity decreasing the probability of having some inaccuracy during the measurements. The filling of the prototype was done while it was positioned vertically for measurement facing the antennas and connected to the impedance analyzer.

From the simulation reported in Section 3.1.3, it was shown that prototype II was designed for a LC layer thickness ranging between 10 and 20 µm whereas prototype I concerns the LC layer with a thickness around 50 µm. In effect, obtaining a specific thickness for the LC layer depends on the choice of mica thickness to be used when working on either the dense micro-resonator array or the sparse one.

At this stage, it seems worthily to mention the technological challenge in assembling a 7x7 cm^2 device by using small mica pieces positioned at each corner. The problems were faced mostly with prototype II due to the very high aspect ratio between the thickness of the LC layer which is 10 µm, hence the thickness of the mica spacers, and the size of the metallized glass substrates. Under such a challenging configuration, the main conflict that we have faced was the presence of short circuits in the vicinity of the bias line where the clamping structures are positioned and also inside the array.

In practice, these short circuits were signaled during the conducted electric measurements, and their positioning across the metasurface were found by using infra-red imaging which detected the hot spots due to local conduction through the LC layer as illustrated in Figure 4.1.6.

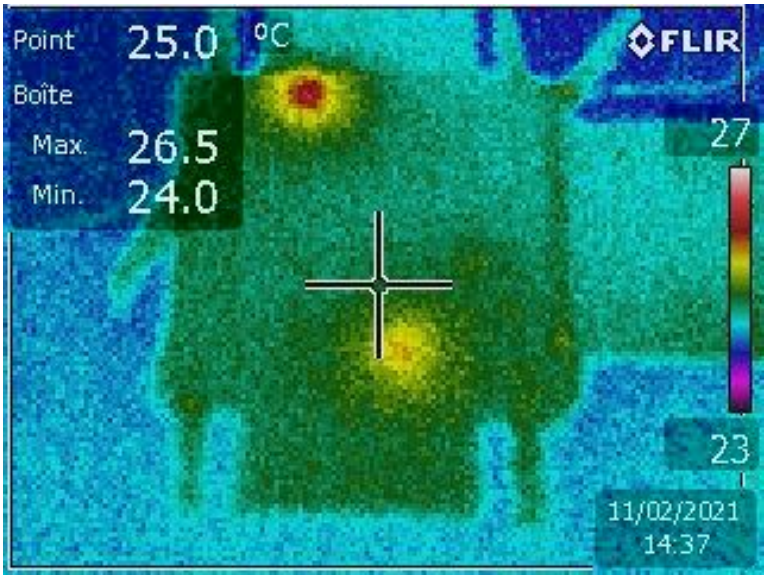

Figure 4.1.6 Illustration of the IR imaging technique that was employed for the detection of the short-circuited hot spots

4.2 Characterization Techniques of the Complex Reflectivity in Free Space

4.2.1 Experimental set-up for free space measurements

In the following sections, we will discuss the characterization techniques in free space of the complex reflectivity (*modulus and phase*). They were developed in the LEMCEL microwave lab aiming at measuring the reflectivity spectra of metasurface *without an anechoic chamber environment*.

We first discuss the bi-static configuration that will be preferred to the conventional monostatic one. Indeed, despite the fact that we solely limit the characterization stage to the *normal*

incidence condition, it will appear that such a bi-static configuration allows to dramatically increase the measurement accuracy.

In practice, we also explain (i) how we chose the distance between the metasurface under test and the two horns of the bi static set-up (ii) how the *reference test structure* and calibration stage were established so that different measurements can be carried. At last, some information is reported about the alignment techniques and the automation of this free space set up that was coupled to the quasi-static C(V) measurement that will be described in another section.

4.2.1.1 Bi-static versus mono-static configuration

The metasurfaces that are considered in the present work are all operating in a reflect-array mode. Indeed, the back-side uniformly metallized ground plane suppresses any transmission of the impinging wave and *conceptually a one-port measurement is sufficient* to assess the reflectivity properties of such a device. However, in such a one-port configuration, there are at least two contributions to the reflected wave. The first one is the spurious reflected wave that results from the impedance mismatch of the horn-free space interface. The second significant term stems from EM wave scattered by the metasurface under test. If the level of the metasurface reflected wave is low with respect to the horn mismatch contribution, the accuracy of the magnitude measurement of the reflectivity is degraded.

A solution to solve this issue is use a two-port configuration using the frequency selective metasurface as a perfect reflecting element (no transmission) so that the measurement of the S_{21} scattering parameters allows the measurement of the complex reflectivity of the metasurface with accuracy.

In practice, the PNA Network E8361C network analyzer operating between 10 MHz and 67 GHz is used to measure the complex reflectivity of the functional metasurface in the Ka band (26-40 GHz).

4.2.1.2 Calibration of the network analyzer

A vector network analyzer (VNA) requires calibration to be performed before measurements can be made. The accuracy on the measurement of the "S" parameters of microwave components depends on the calibration used to correct the errors inherent in the system. Calibration consists of measuring known “standard” elements in order to determine the systematic errors of the system before measuring the component and thus define the measurement plans. The error coefficients calculated from the calibration will be used to determine the S parameters of the DUT.

There are several methods to calibrate the network analyzer, and one of them is the TRL method. – THRU - connection of port 1 and port 2, directly or with a short length of transmission line – REFLECT - connect identical one-port high reflection coefficient devices to each port – LINE - insert a short length of transmission line between port 1 and 2 (different line lengths are required for the THRU and LINE). THRU-REFLECT-LINE is an approach to 2-Port calibration (Figure 4.2.1) that relies on transmission lines rather than a set of discrete impedance standards.

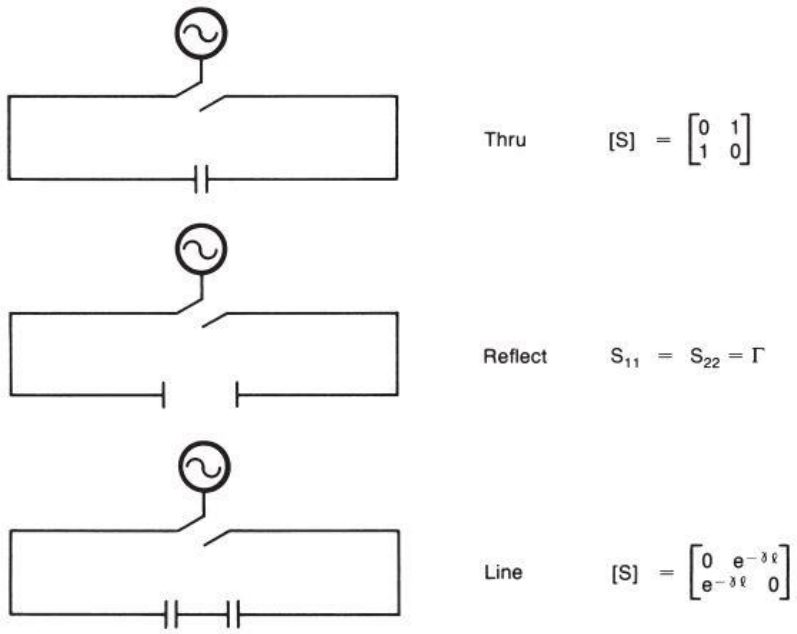

Figure 4.2.1 TRL procedure and assumed S-parameter values for each step

The TRL calibration technique relies only on the characteristic impedance of a short transmission line. From two sets of 2-port measurements that differ by this short length of transmission line and two reflection measurements, the full 12-term error model can be determined. Due to the simplicity of the calibration standards, TRL can be applied in dispersive transmission media such as microstrip, strip-line and waveguide. With precision coaxial transmission lines, TRL currently provides the highest accuracy in coaxial measurements available today.

Figure 4.2.2 contains the block diagram for a simplified 2-port measurement system. Eight of the error terms are represented by the error adapters in the figure. These errors are characterized using the basic TRL calibration.

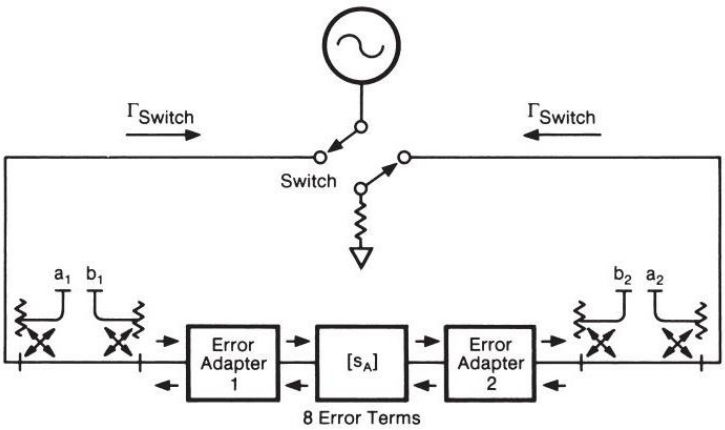

Figure 4.2.2 Functional Block diagram for a 2-port error-corrected measurement system

Two additional steps are required to complete the calibration. Forward and reverse isolation is measured as the leakage from port 1 to port 2 and from port 2 to port 1 with each port terminated. Now, all twelve terms of the 2-port error model are determined.

In the present work the horns that were used are connected to the VNA coaxial cables (K standard) via the use of coaxial/rectangular wave guides transitions. As a consequence, the calibration stage was performed between 26 GHz and 40 GHz in the flange of the output wave guides of these transition with TRL (Thru-Reflect-Line) method [7,8] with respectively a short-circuited waveguide (Reflect), a guide section of 2.48 mm length (Line) and when the two ports of the analyzer are connected (Thru). The dimensions of the wave guide section are 7.112 mm x 3.556 mm.

4.2.1.3 Free Space measurement techniques

4.2.1.3.1 Choice of the high gain horn antenna

Let us mention that the measurement of complex reflectivity of the metasurface is carried out under free space propagation condition in quasi-normal incidence, as seen later, in a bistatic configuration.

Under these conditions, one of the first important issues is the choice of the two horns that are used for transmitting the EM energy scattered by the sample and for detecting the reflected wave respectively.

The transverse dimensions of the metasurfaces are typically 7x7 cm^2 and we will see in the following section that the distance between the horn and the DUT has to be in excess of 1 meter. At last, as mentioned before, the measurements are not carried out in an anechoic chamber and special attention has to be paid to the spurious reflections from the lab environment. On the basis of these

considerations, it appears that one of the most important elements of the measurement setup is the horn and more particularly its directivity or gain having in mind that its SWR is also very important for the accuracy of the Vector analysis.

In practice, we used two identical pyramidal horn antennas (ref XB-GH28-25dB) operating in the 26-40 GHz range and with a gain of 25 dB at 26 GHz and 26 dB at 40 GHz.

These horn antennas are connected each to a rectangular waveguides section of length 10 cm (ref 33KFKF50, FF) which are connected to waveguide-coaxial transitions (28-120B-10cm-6) and Anritsu 3670K50 coaxial cables.

At last, it is worth mentioning that only the TE linear polarization is available with only one coaxial probe. However, owing to the high symmetry degree of the device under test within square-shaped patch for the basic cell and square-lattice of the periodic array, no sensitivity to the EM polarization of the metasurfaces is expected.

These transmitting and receiving horn antennas are held by tripods with the possibility to modify their radiation direction by using two turn tables fixed to the wave guides interconnecting the coaxial wave guide transition and the horn input flange as it can be seen in Figure 4.2.3.

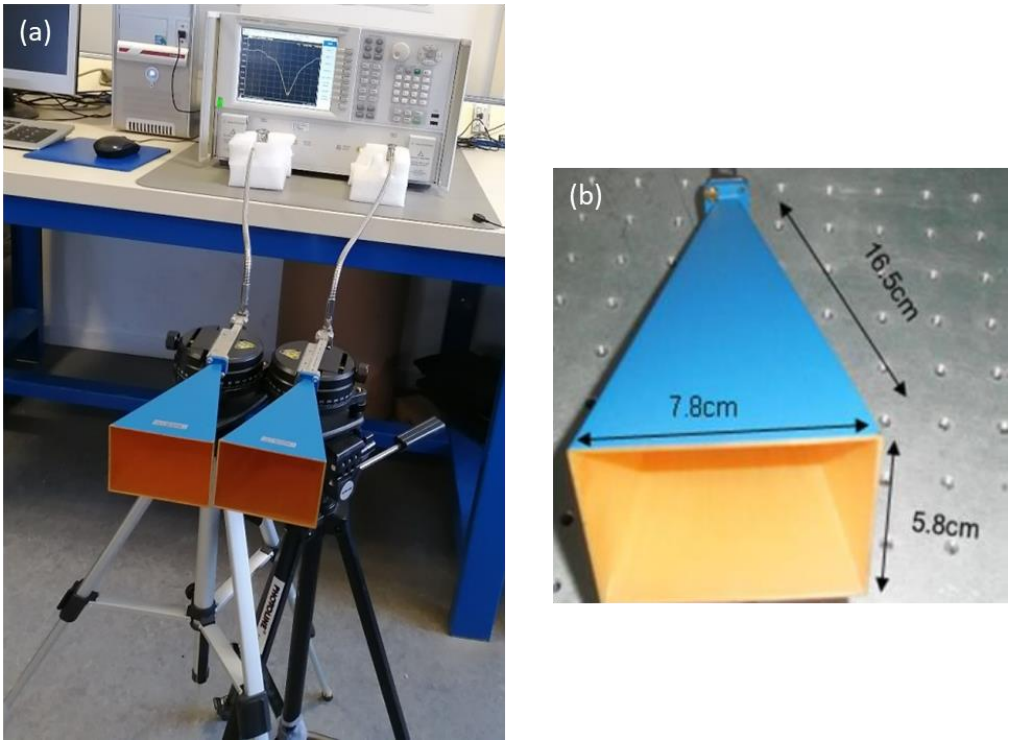

Figure 4.2.3 (a) Photo of the transmitting and receiving high gain (25 dB) antennas, (b) Relevant dimension of the radiating aperture that was used for calculating the far field condition and length of the tapering section

4.2.1.3.2 Choice of the distance between horns and DUT

As seen in the section devoted to the metasurface design (Section 3.1), the numerical calculations were conducted assuming a plane wave impinging onto the basic cell of the metasurface and by taking into account the periodicity of the array by using periodic boundary conditions.

In experiment, the condition of plane wave with a quite flat phase front will be satisfied by putting the device under test in the far field zone.

For this configuration to be functional in the far field region (Fraunhofer zone), a distance D between the horns and the DUT has to be calculated using the following equation:

$$D = \frac{2d^2}{\lambda_0}$$

Where d is the largest dimension of the radiating aperture and λ_0 is the wavelength in free space. For the Ka band of interest from 26 to 40 GHz the central frequency is 33 GHz. Therefore, a representative value of the distance Horn/DUT noted here D is 1.33 m that was calculated with d=7.8 cm (Figure 4.2.4) [9,10].

4.2.1.3.3 Horn radiation patterns alignment

As previously mentioned, the DUT transverse dimensions are of the order of a few centimeters while we just calculated that the typical distance between the horn and DUT is in excess of 1 m. Such a high aspect ratio between D and the metasurface lateral dimension requires a very careful alignment of the radiation patterns of the horn. Also Let us mention that only the EM reflection properties under normal incidence have been considered in the present work. Also, experimentally, the transmitting and receiving horns with very large radiation aperture to achieve high gain values, are set one next to the other. Under this condition of high gain with narrow pencil type radiation pattern and small area of the DUT, it appears essential to minimize as soon as possible the incidence angle that has to be close to 0° and to manage with accuracy the tilt angle of the transmitting and receiving antenna.

Figure 4.2.4 illustrates the final orientation of the two horns that was determined experimentally to have an incidence angle as close as possible to 0°. This figure illustrates ray tracing the main lobe direction of the field impinging onto the metasurface followed by a total *specular reflection* and finally the orientation of EM field that is detected via the receiving horn antenna. In practice, a distance at the backside of the horns of 9 cm was found. By recalling that the far field condition at 33 GHz corresponds to D=1.33 m, the angle was found to be $a =$

$\text{atan}\frac{9}{133} \sim 4°$ corresponding to an incidence angle defined with respect to the normal on the metasurface of 2°.

After positioning the antennas, the placement of the DUT was adjusted using an auto-balanced cross laser positioned at the level of the antennas from behind to verify that the DUT is well illuminated and probed by means of the transmitting and receiving horn antenna with the rotation of the DUT around its vertical axis to achieve the reflection of the laser beam to its source as illustrated in Figure 4.2.5.

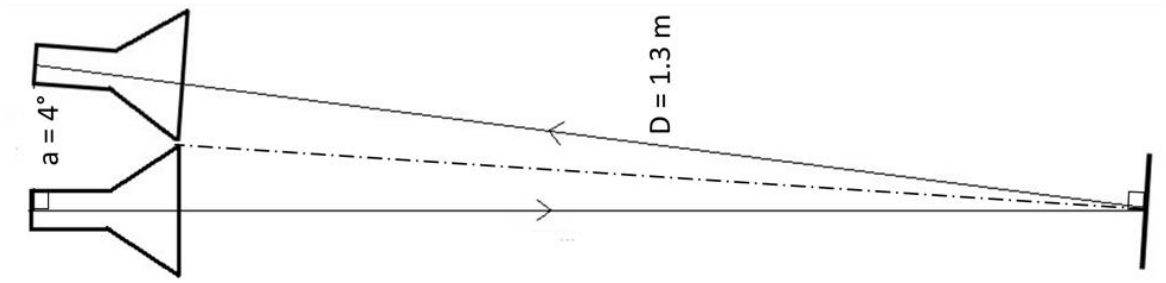

Figure 4.2.4 Illustration of the orientation of the antennas with respect to the metasurface that is set to a distance D=1.33m with a back-side distance between the two horns of 9 cm that correspond to an incidence angle around 2°

Figure 4.2.5 Illustration of the method that was used to adjust the orientation of the DUT by using laser pointer between and just behind the two horns (normal direction with respect to the DUT) with monitoring of the reflected laser spot

4.2.1.3.4 Free space losses

It was shown in the previous sections that the device under test has to be placed in the far field region with a distance of the order of 1 meter between the DUT and the Horn pairs. The EM wave propagates also twice this distance. There is no dissipation of the EM energy for the wave travelling in the lossless medium that is here air. In contrast, despite the use of high gain radiating element, the radiation beam exhibits some divergence. It results from this quite significant loss due to the propagation in free space.

An idea about the importance of these so-called free space losses can be obtained by using the Friis equation. Figure 4.2.6 illustrates the application of this formula in our case.

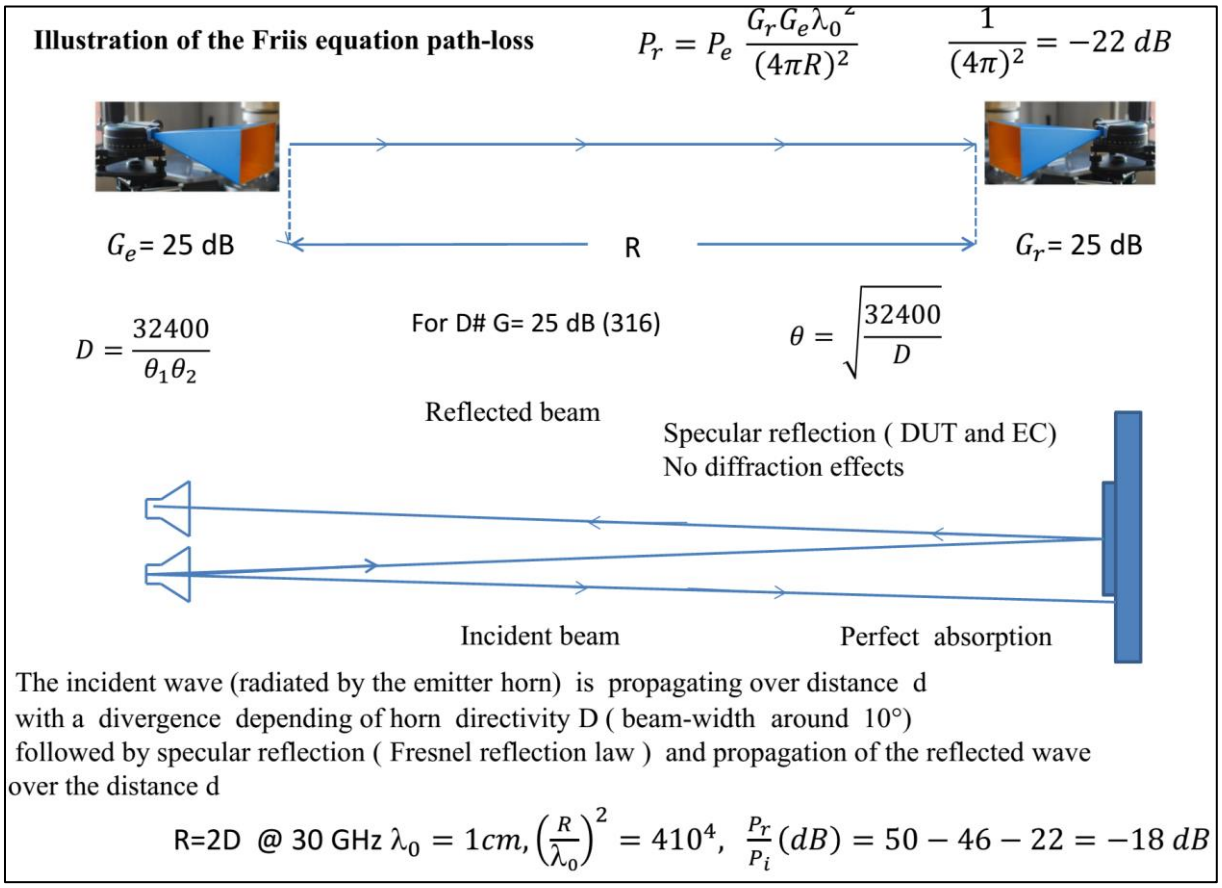

Figure 4.2.6 Illustration of the propagation loss in the case of direct link between the two horns and application of this formula to the case of reflectivity measurement of a metasurface in bistatic configuration

In this figure, the device under test (small side blue pattern) reflects totally the impinging wave according to a specular reflection process (no high order diffraction effect that could modify the direction of the reflected wave). Whatever the operating frequency, the back side metal layer cancels any transmission. The sole difference concerns the level of absorption of the DUT that is measured via the reflectance. Behind the DUT a perfect absorber (shaped as pyramids) is placed so that any side

radiation that could give spurious reflection, is totally absorbed. The calculation of the loss terms was made at 30 GHz (1 cm) for simplicity. It can be deduced assuming a horn gain of 25 dB that a typical loss propagation level is around -18 dB.

4.2.1.3.5 Reference perfect reflector

From the previous section, we learned that the baseline of the reflected wave that is detected in the receiving horn shows a relative level of the order of -20 dB with respect to the power level radiated by the emitting horn antenna. Typically, the power supplied by the VNA is -10 dBm. The losses in the coaxial cables, the coaxial/waveguide transition and as a general rule all the parts of the guiding sections are negligible with respect to the one due to the divergence of the radiated beam. On the other hand, the losses of the waveguide section are taken into account by means of the calibration technique of the VNA. In the free space section however, it is quite difficult to control the difference in the optical path characteristics. For instance, the directivity of the horn antenna that varies as a function of frequency.

A simple means to solve this issue is to do the difference between the frequency dependence of a reference perfect reflector and the frequency response of the DUT. Both devices reference test and DUT will see for each frequencies the same conditions of radiation, alignment and propagation loss provided that the reference test is exactly placed and oriented as the DUT.

As a consequence, the first goal in a reflectivity measurement is to record the reflectance of a perfect metal plate exactly with the same DUT lateral dimensions of the back side metal plate of the DUT. Under this condition and by difference analysis, it is possible to achieve the absolute value of the reflectivity of the sample under test.

Let us note that such a reference metal plate also permits one to also deduce the phase-shift between the incident and the reflected waves by suppressing the phase rotation that are due to the propagation of the wave in free space.

4.3 Reflectivity spectra measurements for the different prototypes

In the following section, we will discuss the results of the reflectivity spectra measurements in microwave range for prototypes 1 and 2 prepared with the 5CB and 1825 LCs; the prototypes 1 and 2 correspond respectively to 50 µm and 10 µm LC thickness. Before mounting the prototype, the rear metal plate is placed and the corresponding reflectance is measured and saved; this represents the reference level for total reflection. After mounting and before filling the prototype, the capacitance of

the empty device is measured to estimate the average thickness over the whole active surface. After filling, reflectance is measured in the frequency range 26-40 GHz at different values of driving voltage; simultaneously, the capacitance is measured to determine the low frequency permittivity (Section 2.4). For each device, we first give the measured reflectance in comparison with the reference; then we give the normalized reflectance and the absorbance.

4.3.1 5CB LC Based Tunable Metasurfaces

The primary measurement of the empty prototype 1 resulted in a capacitance of 353.4 pf which gives a geometrical thickness of 35.5 µm (surface area of patches + interconnections – mica=1271.5 mm^2). After filling, the device capacitance and the calculated 5CB LC permittivity were measured; then the prototype is put in place at a distance of 1.33 m from the antennas in order to start the microwave measurements of the reflectance spectra in the far field region.

As Figure 4.3.1a shows, an absorption dip is observed in the Ka band as predicted; the resonance frequency without voltage is 33 GHz and the corresponding absorption is of 12dB (Figure 4.3.1b). Moreover, the influence of the voltage on the resonance frequency is evidenced: the resonance frequency continuously decreases for increasing voltage. The lowest resonance frequency is of 31.74 GHz and is obtained for 20 Veff; the shift (1.26 GHz) corresponds to an agility of 4%. Let us notice that the absorption dip does not change with varying voltage; the absorbance near the resonance is higher than 90%. The experimental results can be compared with those obtained by simulations in chapter 3: The measured resonance frequency without voltage (33 GHz) is slightly lower (-2.4%) than the one simulated on prototype 1 (33.8 GHz); similar behavior is observed at high voltage (31.7 GHz instead of 32.3 GHz). The experimental resonant frequency shift (-1.26 GHz) is lower than the simulated one (-1.5 GHz). The measured absorption dip (-9 dB) is also lower than the simulated ones without voltage (- 13.8 dB) and at high voltage (-18 dB).

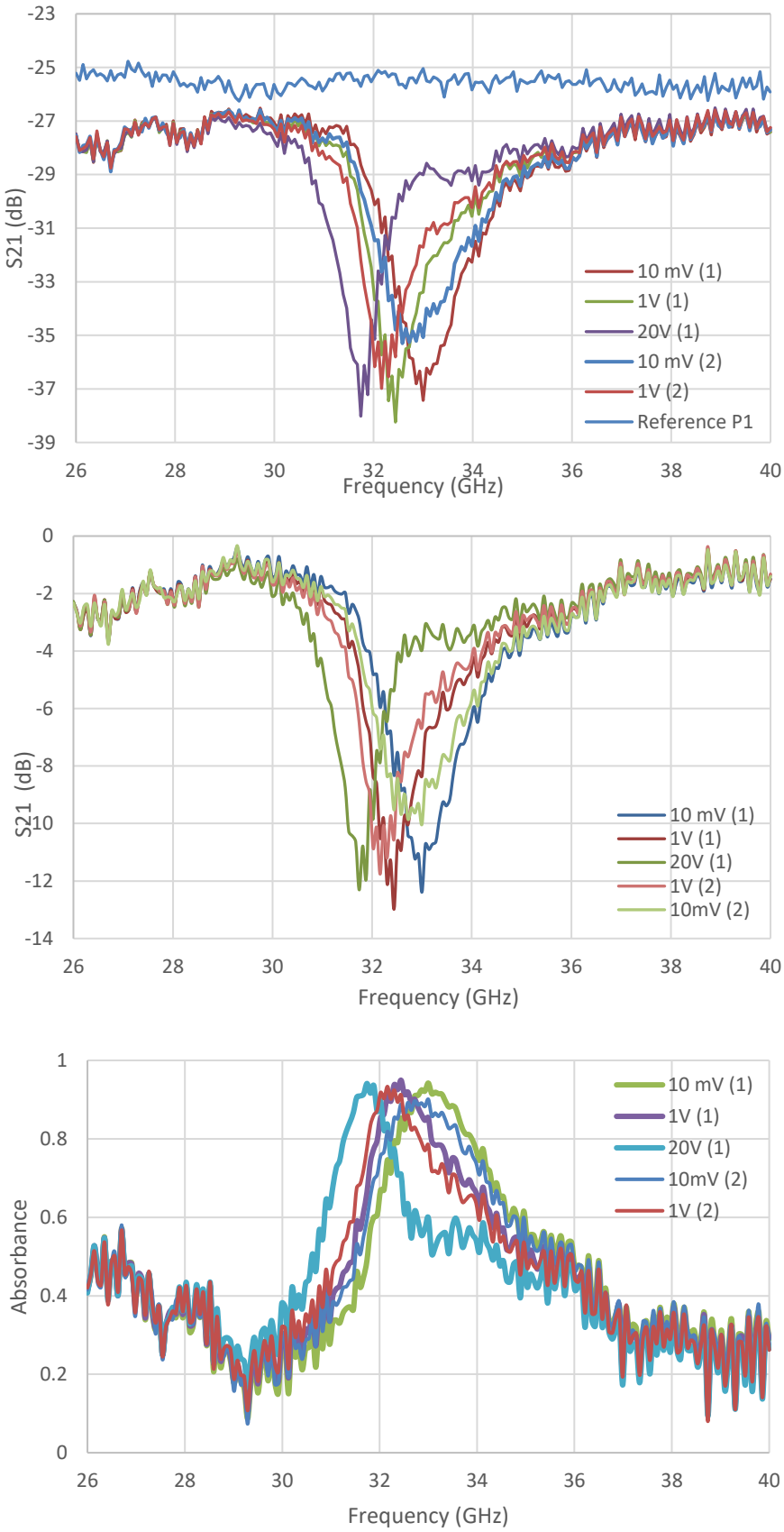

Figure 4.3.1 Reflection measurements of the prototype 1 filled with 5CB: (a) reflection at different applied voltages (increasing, decreasing) in comparison with the reference rear metal plate, (b) normalized reflection coefficient, (c) calculated absorbance vs. frequency

The reference attenuation is near -25 dB at 26 GHz and decreases of about -1 dB at 40 GHz. This value is higher than this predicted by Friis equation (-18 dB at 30 GHz). This result could result from the limited surface of the reference (7x7 cm²). Far from the resonance, there is a gap between the reference level and the attenuation observed with the prototype; such a result could be connected with a change of the reference plane when the rear metal plate is replaced by the prototype.

After switching off the voltage, the measured resonance frequency is different from that measured before applying the voltage. This is due to a change of the planar orientation which is affected by the initial applied voltage; we suppose this is linked to the quality of the coated PVA layer and the high thickness as discussed in Section 2.4. Figure 4.3.2 supports this hypothesis because the measured permittivity also changes after applying the voltage. Let us notice that the values of the permittivity obtained from the prototype with a relatively large surface (from 7.45 till 15.4, anisotropy around 8) are similar to those measured using small cells in section 2. In addition, the low number of measuring points does not show the threshold voltage effect.

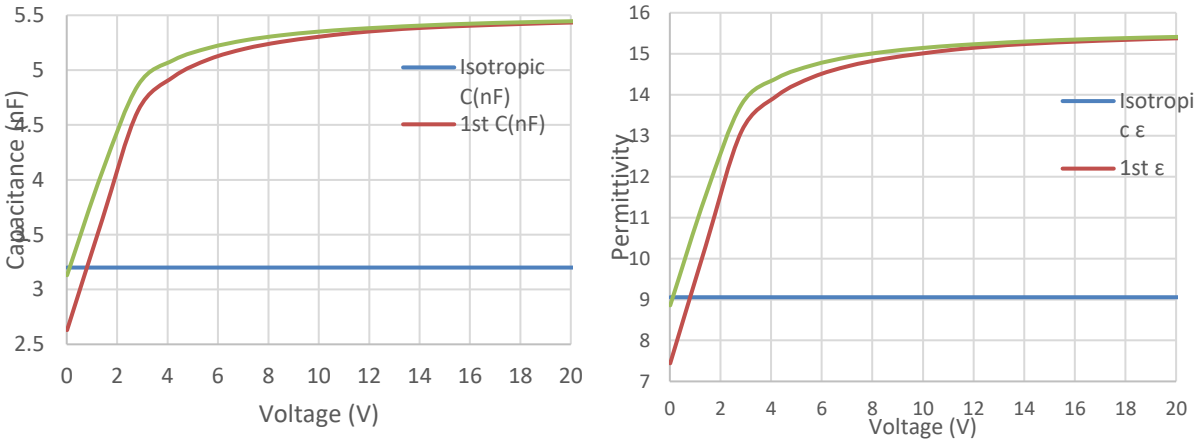

Figure 4.3.2 (a) Capacitance vs. Voltage and (b) Calculated permittivity vs. Voltage of Prototype 1 infiltrated with 5CB.

To check the reproducibility of the results, other measurements have been done on the prototype 1 with 5CB after unmounting/mounting the device and using a new PVA solution. This comparative study has shown that unmounting/mounting operation does not affect the results. However, a recently prepared PVA allows a better control of the orientation; indeed, after switching off the voltage, the measured resonance frequency is similar to that measured before applying the voltage (Figure 4.3.3).

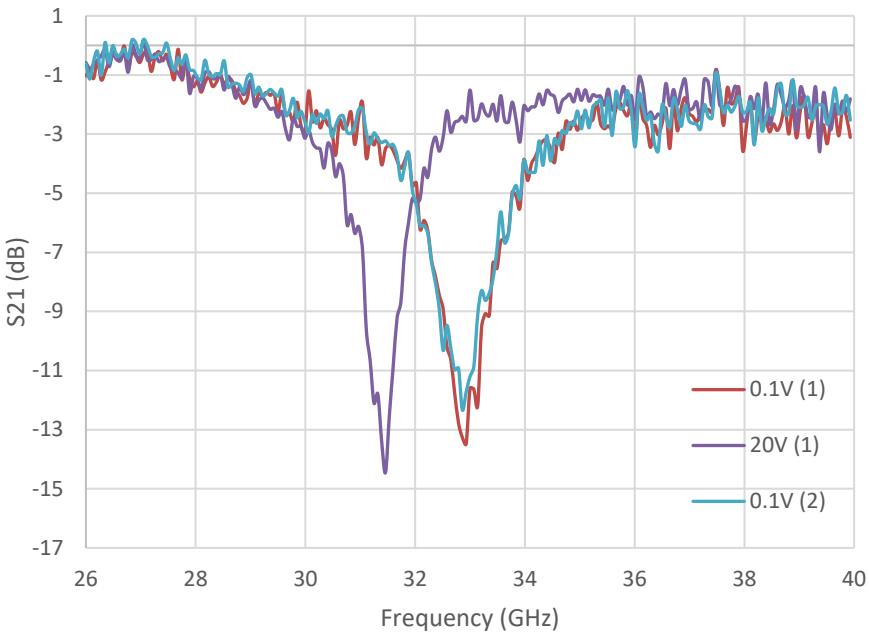

Figure 4.3.3 Normalize reflection measurements of the prototype 1 filled with 5CB after unmounting/mounting

The prototype 2 filled with 5CB was characterized using the same procedure presented above for the prototype 1. From the capacitance measurement of the empty device (2 nF), we estimated a thickness of 15 µm; the corresponding reflectance spectra are given in Figure 4.3.4. The resonance frequencies and the shift under voltage are similar to those of prototype 1. We can notice a higher absorption compared to that of prototype 1; it depends on the applied voltage. The voltage dependence of the absorption was also predicted by simulations.

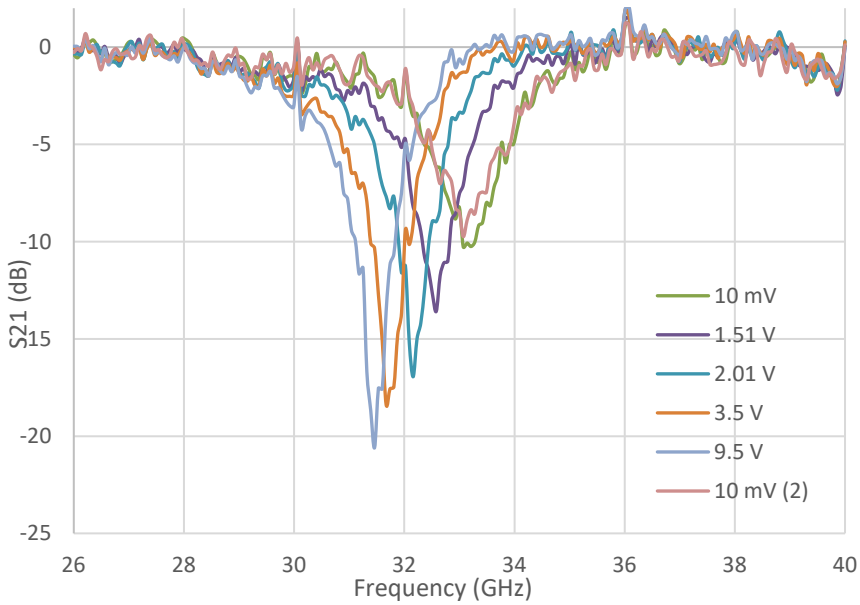

Figure 4.3.4 Normalized reflection measurements of the prototype 2 filled with 5CB

4.3.2 1825 LC Based Tunable Metasurfaces

Initially, the two studied prototypes were designed for 5CB liquid crystal. However, the two devices were also characterized after filling with the large microwave anisotropy 1825 LC.

The empty capacitance of the prototype was of 353 pF; this gives an estimated thickness of 32 µm. As presented in Figure 4.3.5a, the prototype 1 shows an absorption dip in the frequency range 26-40 GHz. The maximum of absorption (Figure 4.3.5, 7 dB) is relatively low compared to that obtained with 5CB. However, as expected, the frequency shift under high voltage (5 GHz) comparted to the value observed with 5CB (1.26 GHz); this is the largely dielectric anisotropy of 1825 LC. The absorbance is higher than 70% in the voltage range.

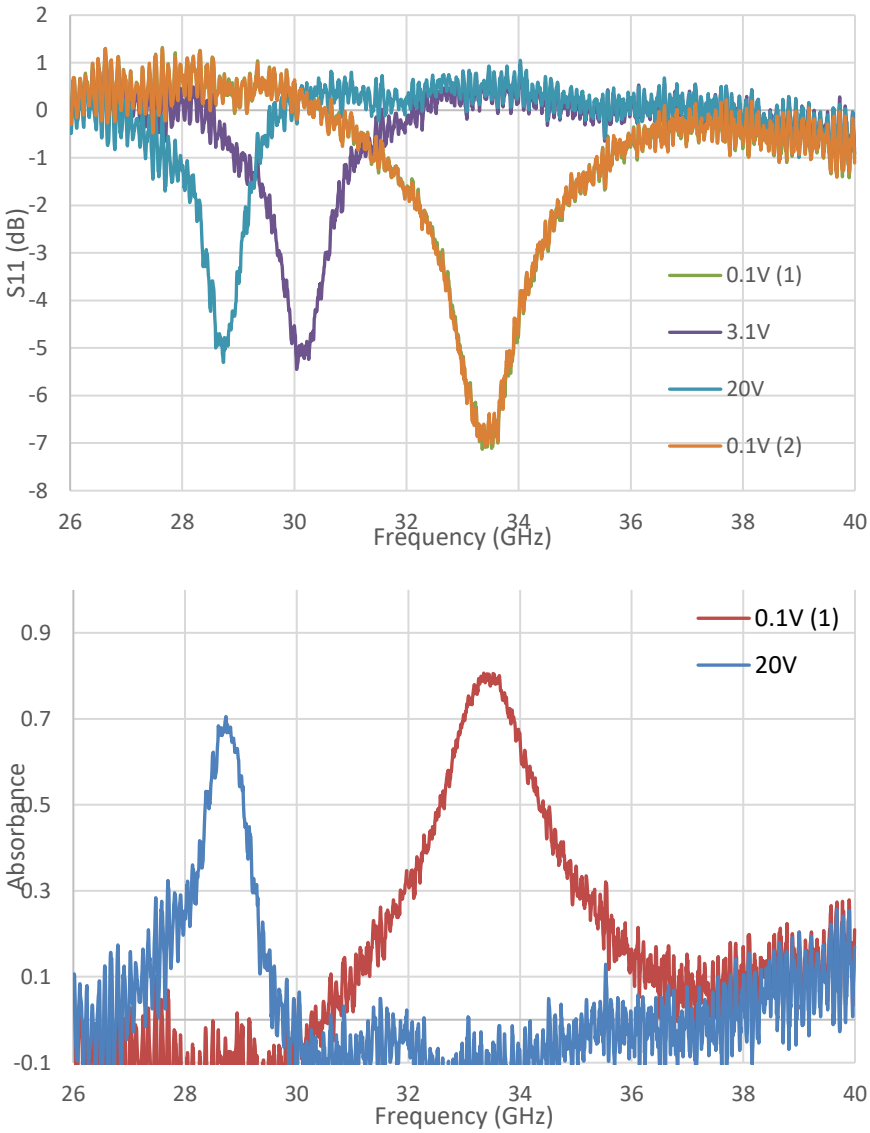

Figure 4.3.5 Reflection measurements of the prototype 1 filled with 1825 LC: (a) normalized reflection coefficient, (b) calculated absorbance versus frequency.

The permittivities measured at low and high voltage from the prototype are in agreement with those previously measured using small commercial cells. The voltage dependent permittivity curves (Figure 4.3.6) shows that the measured permittivity after switching off the voltage is similar to the initial value.

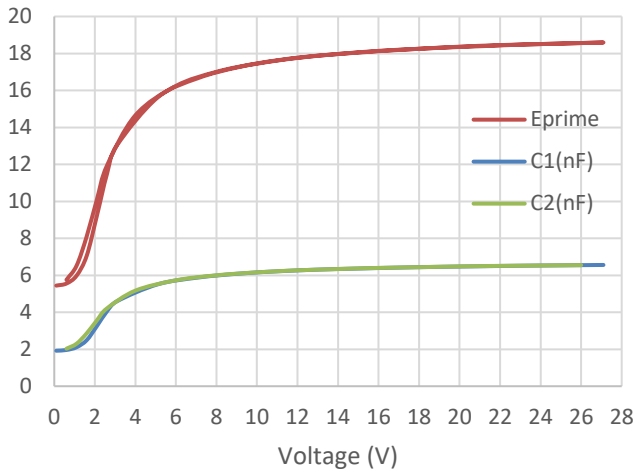

Figure 4.3.6 Capacitance vs. Voltage and Calculated permittivity vs. Voltage of Prototype 1 infiltrated with 1825

As Figure 4.3.7 shows for the prototype 2, a very large absorption is observed in the measuring frequency range with a large shift of the resonant frequency (6 GHz). The prototype behaves as a perfect tunable absorber. Maximum absorptions are observed at 0V (-50 dB) and at 20 V_{eff} (-30 dB). The experimental observed absorptions are higher than the simulated results (Section 3.1.4). In the middle of the driving voltage range, the absorption becomes minimum (-17 dB) at a driving voltage of 3 V_{eff}.

The absorbance is 100% at 0 V and 20 V_{eff} and the minimum is of 85% at 3 V_{eff}. From absorbance, we deduce the total quality factor of the prototype. The quality factor varies from 20 at low driving voltage up to 51 for a voltage of 20 V_{eff}. Some data are reported in Table 9.

V_{eff} (V)	F_R (GHz)	ΔF	$Q_t = F_0/\Delta F$
0.1	32.86	1.75	19.25
3	28.72	1.42	20.8
6	27.53	1.03	27.5
20	26.85	1.42	51

Table 9 Resonant frequency and total quality factor as a function of applied voltage amplitude for the prototype 2 filled with 1825 LC

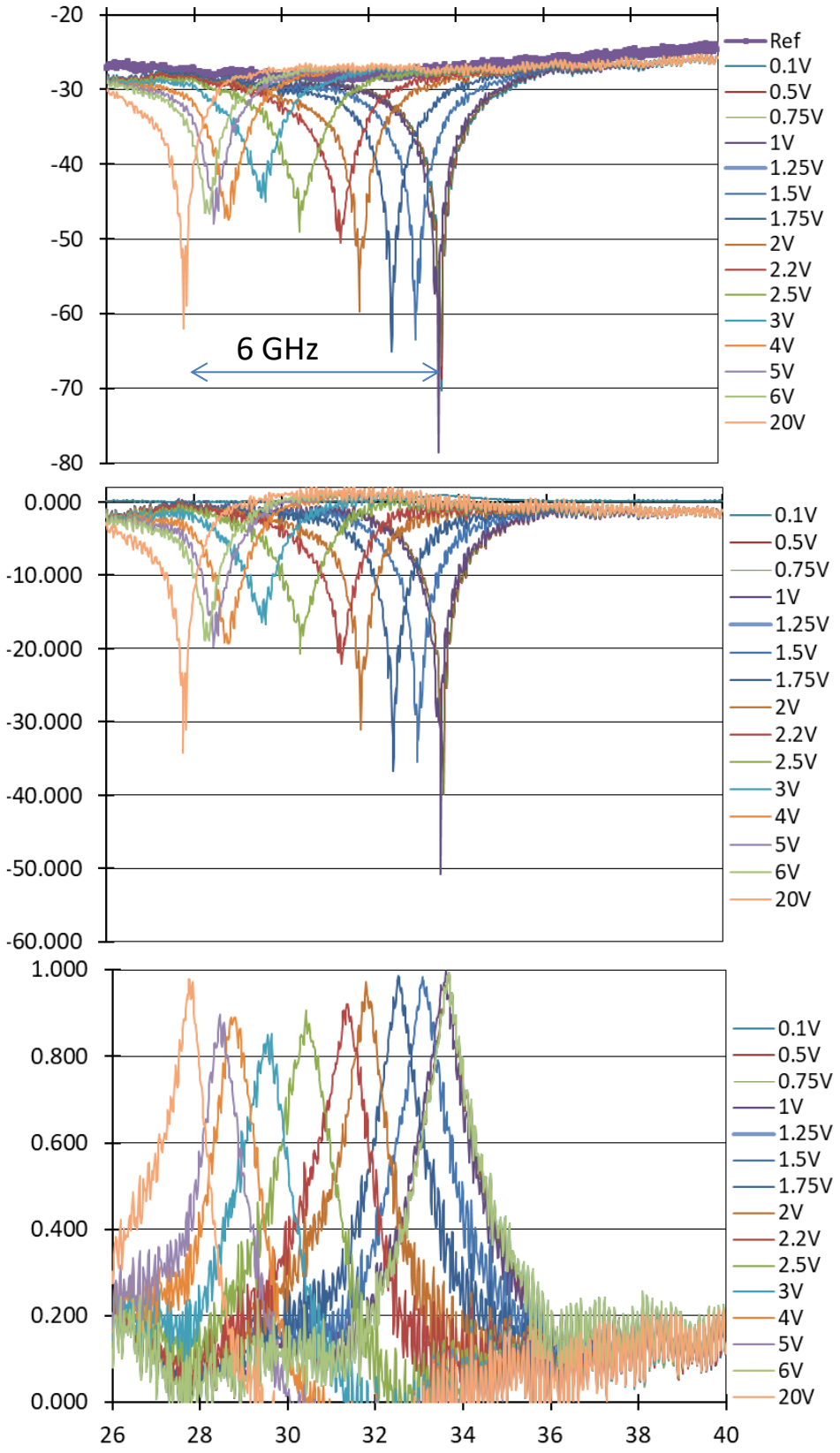

Figure 4.3.7 Reflection measurements of prototype 2 filled with 1825: (a) measured reflection at different applied increasing voltages in comparison with the reference rear metal plate, (b) normalized reflection coefficient, (c) calculated absorbance vs. frequency

The Figure 4.3.8 gives the evolution of the resonant frequency with the applied voltage amplitude. After a threshold, the resonance frequency decreases continuously from 33.7 GHz at 0 V to 27.7 GHz at 20 V_{eff}; the frequency shift and the agility are respectively 6 GHz and -17.8%; these values are in agreement with those obtained by simulations (Section 3.1.4).

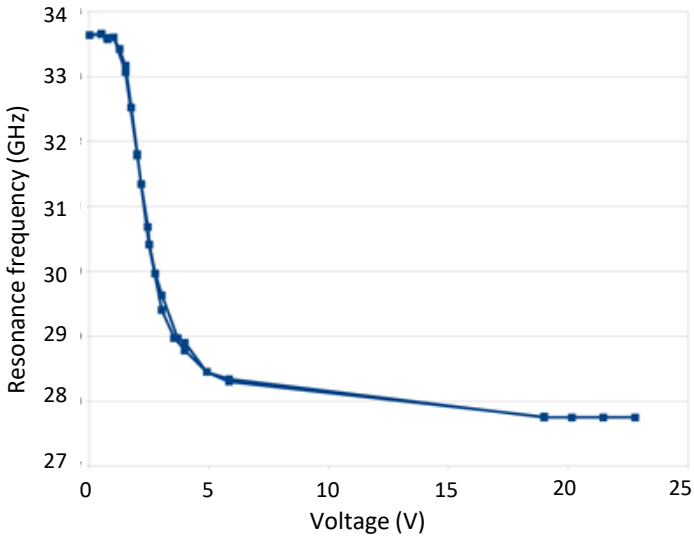

Figure 4.3.8 Evolution of the resonance frequency versus the applied voltage amplitude

4.3.3 Synthesis of the Results and Comparison with Literature

In this section, we discuss the main results achieved in the framework of this PhD work in terms of dielectric anisotropy and tunability of scattering parameters by comparing them (Table 10) to key papers reported in the literature on Liquid Crystal controlled metasurfaces (Section 1.2.3)

To make this comparison, we will define two figures of merit, one for the LC compound (FoM_{LC}) and another for the various devices that were fabricated and *experimentally assessed* for the *dynamic* control of their scattering parameters S_{ij} (FoM_D).

The structures will be defined by the LC thickness (t_{LC}). Mentioned in the table is the relative thickness normalized to the center wavelength of the operating frequency band ($\frac{t_{LC}}{\lambda}$), in addition to showing that the LC thickness is generally shrunk at increasing operating frequency.

In terms of amplitude modulation (A_m), the dynamic range will be defined as the ratio between the scattering parameters measured for the two orientations of the LC molecules.

$$A_m = \frac{S_{ij_\perp}}{S_{ij_\parallel}}$$

For the LC compound figure of merit, it was defined as:

$$FoM_{LC} = \frac{\Delta\varepsilon}{\varepsilon_{\parallel}}$$

With:

$$\Delta\varepsilon = \varepsilon_{\parallel} - \varepsilon_{\perp}$$

Here, we prefer to define the LC compound figure of merit via the permittivity rather than using the refractive index definition as often chosen for LC birefringent compounds operating on the optical regime. In case that solely the index values are reported in the publications, we deduce the corresponding permittivity values from:

$$\varepsilon_{\perp} = {n_{\perp}}^2$$

$$\varepsilon_{\parallel} = {n_{\parallel}}^2$$

For the device's figure of merit, it was calculated from the following expression:

$$FoM_D = \frac{\Delta f_r}{\bar{f_r}}$$

With:

$$\bar{f_r} = \frac{f_{r_{\perp}} + f_{r_{\parallel}}}{2}$$

And:

$$\Delta f_r = f_{r_{\perp}} - f_{r_{\parallel}}$$

Ref.+ Structure	Anisotropy	Control	Freq. (GHz)	t_{LC} (µm)	Rel.t_{LC}	FoM_{LC}	FoM_D	A_M (dB)
[11] Patch-Like	LC E3 $\Delta\varepsilon = 0.39$ $\varepsilon_{\perp} = 2.52$ $\varepsilon_{//} = 2.91$	Electric (E) V=10 V	27	110	0.016	0.13	0.018	15
[31] Broad-Side SRR	Tsinghua U. LC $\Delta n = 0.18$ $n_{\perp} = 1.5$ $n_{//} = 1.68$	Magnetic (B) Permanent Magnet >1 kG	10.85	500	0.029	0.2	0.027	20
[35] Omega-Type	Mixture Nematic LC $\Delta\varepsilon = 0.14$ $\varepsilon_{\perp} = 1.74$ $\varepsilon_{//} = 1.88$	Magnetic (B) 500 G	11.61	500	0.026	0.074	0.018	10
[36] Wire-Pair	Commercial LC TEB 30 A $\Delta n = 0.17$ $n_{\perp} = 1.65$ $n_{//} = 1.73$	Electric (E) V=100 V	9.73	600	0.033	0.09	0.037	15
[37] Fishnet	TEB 30 A measured (X-band) $\Delta\varepsilon = 0.27$ $\varepsilon_{\perp} = 2.72$ $\varepsilon_{//} = 2.99$	Electric (E) V=60 V	8.5	500	0.025	0.096	0.037	8
This work Patch-Like	LC 5CB $\Delta\varepsilon = 0.31$ $\varepsilon_{\perp} = 2.59$ $\varepsilon_{//} = 2.9$	Electric (E) V= 8 V	32.25	50	0.01	0.106	0.04	11
This work Patch-Like	LC 1825 $\Delta\varepsilon = 1.41$ $\varepsilon_{\perp} = 2.57$ $\varepsilon_{//} = 3.98$	Electric (E) V=6 V	31	14.6	0.0026	035	0.19	20

Table 10 Comparison between key papers reported in the literature on Liquid Crystal controlled metasurfaces and the results of this PhD work

From the comparison of the experimental results achieved during this thesis for LC 1825 with respect to those reported in key papers which were mentioned in the literature on LC controlled metasurface, one can note significant improvements in the amplitude modulation of the scattering

parameters that reaches minimum value of 20 dB between the data recorded for the two LC molecules orientation.

In addition, the use of LC 1825 compound with a dielectric anisotropy of 1.4, that was measured in the 26-40 GHz frequency band, improves the frequency agility dramatically with a value around 20% that compares favorably to the values recorded for generic LCs such as 5CB.

Conclusion

This chapter was devoted to the measurement in free space of the frequency dependence of the reflectance spectra for metasurfaces infiltrated either by LC 5CB or LC 1825. For both LC compounds we used the same mask sets designed in Chapter 3 and whose manufacturing techniques were here outlined along with the VNA measurement techniques of the scattering parameters. It was shown that for both LC compounds, a rejection dip in the reflectance spectra at the resonant frequency of the metasurface can be continuously down shifted by the application of a bias voltage. This shows the feasibility of an amplitude modulator by electrically controlling the orientation of the LC orientation.

The performance of this LC controlled functional metasurface, notably in terms of rejection at the resonance frequency and of insertion loss in the outer bands, depends on the LC employed by regarding the dielectric anisotropy and loss tangents and also on the LC thickness. The best results were achieved with the 10 µm-thickness metasurface infiltrated with LC 1825. In that case rejection level of the order of 30 dB was achieved while the reflection is close to unity when the resonant frequency is shifted by 6 GHz.

General Conclusion

The goal to *dynamically control* the reflectivity of a metasurface, in a reflect-array operating mode, with a high contrast ratio between quasi total absorption and low reflection, aiming the realization of an amplitude modulator, was reached. For the demonstration of this first proof principle, a square patch array with a square lattice, was (i) designed by full wave numerical analysis and analytical transmission line approach and (ii) experimentally assessed by free space reflectance measurements in the 26-40 GHz frequency band. Their manufacturing was performed in the frame work of RENATEC (French network of high-end facilities in the field of micro & nanotechnology coordinated by CNRS) at IEMN notably using E-beam pattering of the photolithography masks and electron gun gold evaporation. The results achieved for the two LC compounds (5CB and 1825) infiltrated in between the top and rear metal plates of the basic cells for two LC thicknesses (10 µm and 50 µm) shows state of the art results in terms of frequency agility and reflectivity contrast for the ultra-thin (10 µm) high anisotropy LC 1825 prototype. Therefore, a frequency shift of more than 17% yielding to a reflectivity ratio of ~30 dB was obtained when the LC 1825 molecules have their optical axis oriented along the transverse directions with an ordinary permittivity value of 2.57 (orientation resulting from the rubbed PVA alignment layer) or when a quasi-static electric field resulting from a low bias applied voltage (Vsat< 5 V) aligns the molecule in the longitudinal direction with an extra-ordinary permittivity value of 3.98.

From the theoretical point of view, special attention was paid on the design rules targeting a specific operating frequency that depends mainly of the lateral dimensions of the resonator while the incident wave is impinging under normal incidence. On the other hand, we pointed the importance of the critical coupling condition. The latter corresponds to the equality of the radiative and dissipation quality factors being the necessary condition for impedance matching and total absorption.

From the experimental side, two essential contributions were introduced: first of all, with the experimental determination of the complex valued permittivity values (real part and loss tangent) of LC 1825 in the 26-40 GHz frequency band. Indeed, while some information can be found in the literature in the optical regime by listing optical index and birefringence, the data at microwave frequency bands are still missing. For this experimental determination, we have used a hollow short (2.6 mm-long for avoiding spurious resonance) rectangular waveguide whose complex propagation constant can be determined accurately with or without the infiltration of LC 1825. The retrieval of the complex permittivity values, here at constant wav guide length with respect to the NIST approach, was conducted by means of ABCD transfer matrix manipulation and retrieval of the effective (waveguide dispersion taken into account) permittivity values. The second salient contribution concerns the

reflectance measurements that were performed in the UDSMM lab in Calais without an anechoic chamber. For these measurements, a bi-static set up configuration using high gain horn antennas and large area metasurfaces under test placed in the far field region was implemented. It was shown that normalized values of the reflectance can be accurately determined with proper calibration techniques of the VNA and differential measurements between the reflection properties of the metasurface and of a reference mirror-like sample of the same area. In particular, post calculation of the absorbance from the reflectance validates an absorption level greater than 90% by sweeping the quasi-DC controlling voltage between V = 0 and Vsat.

What could be the prospects of this thesis work?

First of all, it is believed that the engineering of the phase of the reflection coefficient of the metasurfaces would be the next development stage targeting the real time manipulation of the Electro-Magnetic wave front. Toward reflection phase engineering, the basic principle would be, as shown in the theoretical section of this thesis, a shift of the resonant frequency. At the operating frequency chosen for the foreseen application, this resonant frequency shift could dynamically modify the equivalent impedance of the metasurface that can change in case of a sufficient large shift from pure inductive to capacitive terms. As a consequence, a 2π jump could be introduced for the argument of the complex reflection coefficient. In that case of phase modulation, contrary to the absorption rules that were presented in the present work, it is however worth-mentioning that the main requirement would be to preserve high reflection level whatever the frequency. In this thesis dissertation, this possibility, with only a few dB of loss, was already pointed out by numerical simulations for strongly mismatched metasurfaces.

The second innovative route would be to develop a pixelated metasurface for producing local variations of the reflection coefficient by a proper addressing system. On can think in that case to develop gradient index metasurfaces that are implemented for instance in radiation pattern engineering in particular for beam steering, deflecting and scanning.

Bibliography

Chapter 1

[1] P. G. De Gennes, J. Prost, "The Physics of Liquid Crystals (2nd ed.)", Oxford University Press ISBN 0-19-851785-8.

[2] P. J. Collings, J. W. Goodby, “Introduction to liquid crystals: chemistry and physics", 2019.

[3] Wikipedia, “Liquid crystals.”, pp. 1-23, 2020.

[4] U. K. Essays, “Phases of Liquid Crystals,” Nov-2018, https://www.ukessays.com/essays/chemistry/liquid-crystals.php#citethis

[5] “Introduction to Liquid Crystals.” https://web.archive.org/ web/20070704173304/ http://plc.cwru.edu /tutorial/enhanced/files/lc/Intro.htm

[6] D. Pesce, “Thermotropic Liquid Crystals from Engineered Polypeptides,” pp. 11-12, 2015.

[7] I-C Khoo, *Liquid crystals*, vol. 110, no. 9., 2017.

[8] W. Maier, A. Saupe, *Z.Naturf.*, A13, pp. 564 (1958), A14, pp. 882 (1959), A15, pp.287 (1960).

[9] G. W. *Gray, "Molecular Structure and the Properties of Liquid Crystals", Academic Press (1962)*

[10] A. Bendahou, Z. Khouba, T. Benabdallah, U. Maschke, “Mesophase study of pure and doped cyanobiphenyl liquid crystals with salen-type systems,” *Liq. Cryst.*, vol. 45, no. 9, pp. 1312–1323, 2018.

[11] S. E. E. Profile, “Dielectric Properties and Orientational Order of 4- (w -Hydroxyalkoxy) -4 ’ -Cyanobiphenyls,” no. March, 2016.

[12] J. A. N. G. W. Gray, K. J. Harrison, “New Family of Nematic Liquid Crystals for Displays,” *Electron. Lett.*, vol. 9, no. 6, 1973.

[13] S. Jen, N. A. Clark, P. S. Pershan, and E. B. Priestley, “Polarized Raman scattering studies of orientational order in uniaxial liquid crystalline phases,” *J. Chem. Phys.*, vol. 66, no. 10, pp. 4635–4661, 1977.

[14] L. T. Creagh and A. R. Kmetz, “Mechanism of Surface Alignment in Nematic Liquid Crystals.,” *Mol Cryst Liq Cryst*, vol. 24, n° 1-2, pp. 59-68, 1973.

[15] C. J. F. Böttcher, P. Bordewijk, "Theory of Electric Polarization"**,** Volume 2, Elsevier, 1978.

[16] Y. P. Kalmykov (ed.), "Recent Advances in Broadband Dielectric Spectroscopy", Springer, Berlin, 2013.

[17] J.P. Parneix, "Propriétés diélectriques de cristaux liquides nématiques", *Thèse d'état*, Université de Lille1, 1982

[18] W. Maier, G. Meier, *Z. Naturf.*, 16a, pp. 262, 1961.

[19] J. Jadzyn, G. Czechowski, R. Douali, C. Legrand, “Molecular model of the dielectric relaxation in nematic liquid crystals”, Liquid Crystals: Chemistry, Physics, and Applications, *Proceedings of SPI*, 4147, pp. 176-183, 2000.

[20] P. Oswald and P. Pieranski, "Nematic and Cholesteric Liquid Crystals", 2005

[21] F. J. Kahn, “Electric-field-induced orientational deformation of nematic liquid crystals: Tunable birefringence”, *Appl. Phys. Lett.*, vol. 20, no. 5, pp. 199–201, 1972.

[22] P. Oswald, G. Poy, and F. Vittoz, “Fréedericksz transition under electric and rotating magnetic field: application to nematics with negative dielectric and magnetic anisotropies,” *Liq. Cryst.*, vol. 44, no. 8, pp. 1223–1230, 2017.

[23] N. Fabvre, L. Lalouat, B. Cluzel, X. Mélique, D. Lippens, F. De Fornel, O. Vanbésien, "Optical near-field microscopy of light focusing through a photonic crystal flat lens", *Phys. Rev Lett.*, 101, 073901, 2008.

[24] E. Lheurette, G. Houzet, J. Carbonell, F. Zhang, O. Vanbésien, D. Lippens, "Omega –type balanced composite negative refractive index materials", *IEEE Transactions on Antenna and Propagation*, 56, 11, pp. 3462-3469, 2008.

[25] E. Lheurette et al., IEEE Transactions on Antennas and Propagation, 56, 11, pp. 3462-3469, 2008

[26] B. A. Munk, "Frequency selective surfaces theory and design", Wiley-inter science publication John Wiley and Sons, Inc. 2000.

[27] C. Croenne, PhD thesis of the University of Lille, 2009

[28] E.F. Knott, "the thickness criterion for single layer radar absorbents", *IEEE Transactions on Antennas and Propagation*, 27, n°5, pp. 698-701, 1979.

[29] H. Hartmunt, "On the effect of absorbing materials on electromagnetic waves with large relative bandwidth", EMC-25, n°1, p. 32-29,1983.

[30] F. Zhang, Thesis of the University of Lille, "Electromagnetic bulk metamaterial technologies application to microwave guiding and radiating elements", 2009.

[31] F. Zhang, Q. Zhao, L. Kang, D. P. Gaillot, X. Zhao, J. Zhou, D. Lippens, "Magnetic control of negative permeability metamaterials based on liquid crystals", *Appl. Phys. Lett.*, 2008, 92:193104. doi: 10.1063/1.2926678

[32] J. Xu et al., "A review of tunable electromagnetic metamaterial with anisotropic liquid crystals", Frontiers in physics, 9, 2021, 633104 Doi: 10.3389/fphy.2021.633104

[33] IC Khoo, "Nonlinear optics of liquid crystalline materials", *Phys. Rep.*, pp. 471-221, 67,2009, Doi: 10.1016/jphysrep.2009.01.001

[34] X. Wang, D. H. Kwon, DH Werner, IC Khoo, AV Kildishev, VM Shalaev, "Tunable optical negative index metamaterials employing anisotropic liquid crystals", *Appl. Phys. Lett.*, 2007, 91:143122, doi:10.1063/1.2795345

[35] F. Zhang, L. Kang, Q. Zhao, J. Zhou, X. Zhao, D. Lippens, "Magnetically tunable left-handed metamaterials by liquid crystal orientation", *Opt. Express*, 17, Issue 6, pp. 4360-4366, 2009, doi: 101364/OE.17.004360

[36] F. Zhang, Q. Zhao, W. Zhang, J. Sun, J. Zhou, and D. Lippens, "Voltage tunable short wired pair type of metamaterial infiltrated by nematic Liquid crystals", *Appl. Phys. Lett.*, 97, 134103, 2010

[37] F. Zhang, W. Zhang, Q. Zhao, J. Sun, K. Qiu, J. Zhou, D. Lippens, "Electrically controllable fishnet metamaterial based on nematic liquid crystal", *Optics Express*, 19, 2, pp. 1563-1568, 2011.

Chapter 2

[1] D. Headland Y. Monnai, D. Abbott, C. Fumeaux and W. Withayachumnankul, Tutorial Terahertz beam forming: “from concepts to realizations”, *APL Photonics* ,3, 051101, 2018.

[2] C. Qu, S. Ma, J. Hoa, M. Qiu, X. Lim, S. Xiao, Z. Miao, N. Dai, Q. He, S. Sun and L. Zhou,” Tailor the functionalities of metasurfaces based on a complete phase diagram”, Phys. *Rev Lett.*, p. 115, 235503, 2015.

[3] G. Isic, B. Vsic, D. Zografpoulos, R. Beccerelli and R. Gajié, “Electrically tunable critically coupled Terahertz metamaterial absorber based on nematic liquid crystals”, *Phys. Rev. Appl.*, 3, 064007, 2015.

[4] A. Bogi, S. Faetti, “Elastic, dielectric and optical constants of 4'-pentyl-4-cyanobiphenyl”, *Liquid Crystals*, Vol. 28 (25), pp. 729-739, 2001.

[5] R. Dabrowski, P. Kula, J. Herman, “High Birefringence Liquid Crystals”, *Crystals*, Vol. 3, pp. 443-482, 2013.

[6] D. C. Zografopoulos, A. Ferraro, and R. Beccherelli, “Liquid-Crystal High-Frequency Microwave Technology: Materials and Characterization,” *Adv. Mater. Technol.*, vol. 4, no. 2, pp. 1–22, 2019.

[7] A. Lapanik, “Liquid crystal systems for microwave applications : single compounds and mixtures for microwave applications ; Dielectric, microwave studies on selected systems”, *PhD Tech. Univ. Darmstad*, 114, 2009.

[8] T.-R. Tsai, C-Y Chen, C-L Pan,R-P Pan, X.-C. Zhang, “Terahertz time-domain spectroscopy studies of the optical constants of the nematic liquid crystal 5CB”, *Applied Optics*, p. 42, n°13, 2003.

[9] R. Douali, “Contribution à l'étude des propriétés électriques de cristaux liquides antiferroélectriques”, *Thèse de Doctorat*, Université du Littoral Côte d’Opale, 2000.

[10] A. Mikulko, M. Fras, M. Marzec, S. Wröbel, M.D. Ossowska-Chrusciel and J. Chrusciel, “Dielectric and Conductivity Anisotropy in Liquid Crystalline Phases of Strongly Polar Thioesters”, *Acta Physica Polonica*, Vol. 113 (4), pp. 1155-1160, 2008.

[11] J. Jadzyn, G. Czechowski, R. Douali, C. Legrand, “On the molecular interpretation of the dielectric relaxation of nematic liquid crystals”, *Liquid Crystals*, 26(11), pp. 1591-1597, 1999.

[12] J. Jadzyn, G. Czechowski, R. Douali, C. Legrand, “Molecular model of the dielectric relaxation in nematic liquid crystals”, Liquid Crystals: Chemistry, Physics, and Applications, Proceedings of SPI, 4147, pp. 176-183, 2000.

[13] M. Munna, F. Anwar, R. Coutu, “Nematic Liquid Crystal Composite Materials for DC and RF Switching,” *Technologies*, 7, n°2, p. 32, 2019.

[14] F. Dubois, F. Krasinski, B. Splingart, N. Tentillier, C. Legrand, A. Spadlo, R. Dabrowski, “Large microwave birefringence liquid-crystal characterization for phase-shifter applications”, *Japanese Journal of Applied Physics*, 47, p. 3564, 2008.

[15] N. Tentillier, F. Krasinski, R. Sauleau, B. Splingart, H. Lhermite, P. Coquet, “A liquid-crystal, tunable, ultra-thin Fabry-Perot resonator in Ka band”, *IEEE Antennas and Wireless Propagation Letters*, 8, pp. 701-704, 2009.

[16] N. Tentillier, “Contribution à la caractérisation diélectrique micro-onde de cristaux liquides-Application aux circuits agiles en fréquence”, *Thèse de Doctorat*, Université des Sciences et Techniques de Lille, 2003.

[17] A-H. Boughriet, C. Legrand, A. Chapoton, “Non iterative stable transmission/reflexion method for low loss material complex permittivity determination”, *IEEE Trans. on Microwave and Techniques*, 45, n°1, pp. 52-57, 1997.

[18] M. D. Janezic, J. A. Jargon, “Complex permittivity determination from propagation constant measurements”, *IEEE Microwave and Guided Wave Letters*, 9, n°2, pp. 76-78, 1999.

[19] D. M. Pozar, “Microwave Engineering”, John Wiley & Sons; 4th Edition, 2011.

Chapter 3

[1] K. Luo, S. Ge, L. Zhang, H. Liu and J. Xing, "Simulation Analysis of Ansys HFSS and CST Microwave Studio for Frequency Selective Surface", International Conference on Microwave and Millimeter Wave Technology (ICMMT), pp. 1-3, 2019, doi: 10.1109/ICMMT45702.2019.8992280

[2] https://www.comsol.fr/multiphysics

[3] “The Finite Element Method in Electromagnetics”, 3rd Edition, Jian-Ming Jin, Wiley-IEEE Press, 2014

[4] “Integral Equation Methods for Electromagnetics”, Joseph R. Mautz, Nagayoshi Morita, Artech House, 1991.

[5] Ismo V. Lindell, Ari Sihvola, “Boundary Conditions in Electromagnetics”, *IEEE Press Series on Electromagnetic Wave Theory*, Wiley-IEEE Press; 1st edition, 2019.

[6] I.V. Lindell and A.H. Sihvola, “Electromagnetic Boundary Conditions Defined in Terms of Normal Field Components”, http://arxiv.org/abs/0904.2951v2

[7] C.A. Balanis, “Antenna Theory Analysis and Design”, 2nd Ed, John Wiley & Sons, 1997.

[8] S. Tretyakov, “Analytical-Modeling-in-Applied-Electromagnetics”, Artech House, 2003.

[9] C. Caloz, T. Itoh, “Electromagnetic metamaterials: transmission line theory and microwave applications”, Wiley-Interscience, Wiley & Sons, 2006.

[10] D. F. Sievenpiper, “High-Impedance Electromagnetic Surfaces”, *PhD dissertation*, 1999.

[11] O. Luukkonen, C. Simovski, G. Granet, G. Goussetis, D. Lioubtchenko, A.V. Räisänen, S. A. Tretyakov, “Simple and Accurate Analytical Model of Planar Grids and High-Impedance Surfaces Comprising Metal Strips or Patches”, *IEEE Transactions on Antennas and Propagation*, Vol. 56, No. 6, pp.1624-1632, 2008.

[12] F. Costa, A. Monorchio, G. Manara, “An Overview of Equivalent Circuit Modeling Techniques of Frequency Selective Surfaces and Metasurfaces”, *ACES Journal*, 29, no. 12, pp. 960-976, 2014.

[13] F. Costa, A. Monorchio, G. Manara, “Analysis and Design of Ultra-Thin Electromagnetic Absorbers Comprising Resistively Loaded High Impedance Surfaces”, *IEEE Transactions on Antennas and Propagation*, vol. 58, no. 5, pp. 1551-1558, 2010.

[14] F. Costa, S. Genovesi, A. Monorchio, G. Manara, “A Circuit-based Model for the Interpretation of Perfect Metamaterial Absorbers", *IEEE Transactions on Antennas and Propagation*, 2012.

[15] N. Fernez, L. Burgnies, J. Hao, C. Mismer, G. Ducournau, D. Lippens, E. Lheurette, “Radiative quality factor in thin resonant metamaterial absorbers”, *IEEE Transactions on Microwave Theory and Techniques*, 66 (4), pp. 1764-1772, 2018.

[16] C.A. Balanis, “Advanced Engineering Electromagnetics”, 2nd Ed,John Wiley & Sons, section 8.9, pp. 455-466, 2012.

[17] A. Sellier, T.V. Teperik, A. de Lustrac, “Resonant circuit model for efficient metamaterial absorber”, *Optics Express*, 21, no S6, pp. 998-1005, 2013.

Chapter 4

[1] P. Rai-Choudhury, “Handbook of Microlithography, Micromachining, and Microfabrication”, Volumes 1 & 2: Microlithography, 1997.

[2] *A.N. Broers and al., "Electron beam lithography—Resolution limits", Microelectronic Engineering, 32 (1–4), pp. 131–142, 1996.*

[3] P. K. Roy, A. Moon, K. Mima, S. Nakai, "Study of a laser-heated electron gun", *Review of Scientific Instruments*, 67, p. 4098, 1996.

[4] J. Stöhr, M.G. Samant, "Liquid crystal alignment by rubbed polymer surfaces: a microscopic bond orientation model", *Journal of Electron Spectroscopy and Related Phenomena*, 189–207, 1999.

[5] S.-C. Jeng, S.-J. Hwang, "Controlling the Alignment of Polyimide for Liquid Crystal Devices", High Performance Polymers Polyimides Based from Chemistry to Applications, Edited by M. J. Médard Abadie, Chapter 4, 2012.

[6] D.V. Shmeliova, S.V. Pasechnik, S.S. Kharlamov, A. V. Zakharov, E.P. Pozhidaev, V.A. Barbashov, T.P. Tkache, "Capillary Flows of Nematic Liquid Crystal", *Crystals*, 10, p. 1029, 2020.

[7] G. Dambrine, « Caractérisation des transistors à effet de champ: mesure précise de la matrice de répartition et détermination directe du schéma équivalent », *Thèse de Doctorat*, Université de Lille 1, 1989.

[8] G.F. Engen, C.A. Hoer, "Thru-Reflect-Line: An improved technique for calibrating the dual six port automatic network analyzer", *IEEE Microwave Technology and Technics*, no. 12, pp. 987-993, 1979.

[9] L. Pometcu, A. Sharaiha, R. Benzerga, R.D. Tamas, P. Pouliguen, "Method for Material Characterization in Non-Anechoic Environment", *Appl. Phys. Lett.*, 108, 161604, 2016. https://doi.org/10.1063/1.4947100

[10] D.K. Deepak, V.V. Varadan, V.K. Varadan, "A free-space method for measurement of dielectric constants and loss tangents at microwave frequencies", *IEEE Transactions on Instrumentation and Measurements*, 37, no. 3, pp. 789-793, 1989.

[11] N. Tentillier, F. Krasinski, R. Sauleau, B. Splingart, H. Lhermite, Ph. Coquet, "A liquid crystal, tunable, ultra-thin Fabry-Perot resonator in Ka Band", IEEE Antennas and Wireless Propagation Letters, 8, 701-704, 2009

In addition to [31], [35], [36] and [37] from Chapter 1

Work Development

1. Oral Communications

- ✓ 16th Journées de Caractérisation Micro-ondes et Matériaux (JCMM), Toulouse, France, March 30 - April 1 2020: "Functional Meta-Surfaces Controlled by Liquid Crystals"
  R. Chamseddine, P. Ropa, K. Blary, R. Douali, C. Legrand, and D. Lippens

- ✓ 16th Journées de Caractérisation Micro-ondes et Matériaux (JCMM), Toulouse, France, March 30 - April 1 2020: "Métasurfaces Absorbantes Sélectives en Fréquences"
  P. Ropa, R. Chamseddine, C. Legrand et D. Lippens

- ✓ 20th conference on self-organized anisotropic systems (CFCL), Calais, France, August 31 - September 2 2021: "Functional Meta-Surfaces Controlled by Liquid Crystals"
  R. Chamseddine, P. Ropa, N. Tentillier, K. Blary, P. Kula, C. Legrand, and D. Lippens

2. Posters

- ✓ Workshop Gradient, IEMN, Lille, France, 18-19 October 2018: "RCS Computation and Analysis of Different Metamaterial Inclusions Using 3D-EM Simulator"
  R. Chamseddine, Prof. J. Jomaa, and Dr. H. Ayad

- ✓ Meeting of new entrants, IEMN, Lille, France, 26 November 2019: "Liquid Crystal Controlled Electro-Magnetic Functional Meta-Surface"
  R. Chamseddine, P. Ropa, K. Blary, R. Douali, V. Sadaune, C. Legrand and D. Lippens

- ✓ 19th conference on self-organized anisotropic systems (CFCL), Sète, France, 3-6 September 2019: "Métasurfaces fonctionnelles accordables par cristaux liquides"
  R. Djouadi, P. Ropa, R. Chamseddine, V. Sadaune, K. Blary, R. Douali, C. Legrand et D. Lippens

Abstract

The main goal of this thesis was to *dynamically* control the reflectivity of a metasurface using LC technologies. The metasurfaces, tunable by voltage-controlled LC orientation, operate in a reflect-array mode and exhibit a high contrast ratio between quasi total absorption and low reflection, aiming the realization of an *amplitude modulator*. Square patch periodic arrays were first designed by full wave numerical analysis and analytical transmission line approach and then experimentally assessed by reflectance measurements, with and without control voltage in the 26-40 GHz frequency band. A frequency shift of more than 5.8 GHz (17 %) yielding a reflectivity ratio of ~30 dB was obtained when using a high anisotropy LC compound with an ordinary permittivity value of 4 (orientation resulting from a rubbed PVA alignment layer) or when a quasi-static electric field resulting from a low bias applied voltage (Vsat< 5 V) aligns the molecule in the longitudinal direction with an extra-ordinary permittivity value of 2.6.

From the design point of view, special attention was paid one on the array resonant frequency that depends mainly on the *lateral* dimensions of the patch and on the *critical coupling* condition for impedance matching corresponding to the equality of the radiative and dissipative quality factors. From the experimental side, two essential contributions were brought by implementing hollow metal waveguide measurements of the LC dielectric properties with magnetic field orientation and free space set ups in a bi-static configuration for the measurements of the complex valued scattering parameter both in the Ka band.

It is believed that the engineering of the phase of the reflection coefficient of the metasurfaces would be the next development stage targeting the *real time* manipulation of the Electro-Magnetic wave front. The second innovative route would be to develop pixelated metasurface with *local* variations of the reflection coefficient targeting the engineering of radiation patterns.

Key words: Liquid Crystals, dielectric anisotropy, microwave, tunable metasurfaces, dielectric measurements, scattering parameters.

Résumé

Le but principal de cette thèse a été de contrôler *dynamiquement* la réflectivité d'une métasurface par cristaux liquides. Les métasurfaces, dont les propriétés électromagnétiques sont contrôlées électriquement par l'orientation des molécules LC, fonctionnent en réflexion et présentent un très fort contraste entre une absorption quasi-totale et un faible niveau de réflexion, dans le but de réaliser un *modulateur d'amplitude*. Des réseaux périodiques de type 'patchs' ont été optimisés par simulation numérique de type ' full wave' et à l'aide d'une approche analytique de type lignes de transmission. Leurs propriétés électromagnétiques ont ensuite été validées expérimentalement par des mesures de spectres de réflectivité, sans ou avec tension de commande, dans la bande 26-40 GHz. Un décalage fréquentiel de la fréquence de résonance du réseau de plus de 5.8 GHz, correspondant à une agilité en fréquence de 17 %, à l'origine d'un contraste de plus de 30 dB, a ainsi pu être démontré par l'infiltration d'un cristal liquide de forte anisotropie avec des valeurs de permittivité longitudinale de 4 et transversale de 2. 6.

Pour le travail de conception, une attention particulière a été portée à la condition de résonance des réseaux qui dépend principalement de la dimension latérale des patchs et à celle de couplage critique qui correspond à l'égalité des coefficients de radiation et de dissipation. Au plan expérimental, deux contributions essentielles ont été apportées avec d'une part la caractérisation des propriétés diélectriques des LC dans la bande 26-40 GHz à l'aide d'une cellule guides d'onde, les cristaux liquides étant orientés sous champ magnétique et la mise en œuvre d'un banc bi-statique de mesure en espace libre des paramètres de la matrice de répartition dans cette même bande.

L'ingénierie de phase par le contrôle de l'argument du coefficient complexe ainsi que l'introduction de variations locales grâce à des métasurfaces pixélisées, en vue de contrôler en *temps réel* les diagrammes de rayonnement, à l'aide de métasurfaces, constituent les prochaines étapes de ce travail.

Mots clés : cristaux liquides, anisotropie diélectrique, métasurfaces accordables, mesures diélectriques, matrice de répartition.